Upconversion Luminescence and Optical Temperature Sensing of $Er^{3+}/Yb^{3+}/W^{6+}$ Doped $BaBi_2Nb_2O_9$ Ferroelectric Ceramic

Thesis Submitted by

ANKITA BANWAL

In Fulfillment of the Requirements for the Degree of

DOCTOR OF PHILOSOPHY

Under the Supervision of

DR. RENUKA BOKOLIA

DEPARTMENT OF APPLIED PHYSICS

DELHI TECHNOLOGICAL UNIVERSITY, DELHI, INDIA

APRIL 2024

Dedicated to

Radharaman Lal Ju

Delhi Technological University

(Govt. of National Capital Territory of Delhi)
Bawana Road, Delhi-110042

CERTIFICATE

This is to certify that the thesis titled "***Upconversion Luminescence and Optical Temperature Sensing of $Er^{3+}/Yb^{3+}/W^{6+}$ Doped $BaBi_2Nb_2O_9$ Ferroelectric Ceramic***" is being submitted by ***MS. ANKITA BANWAL*** with registration number ***2K18/PHD/AP/505*** to the Delhi Technological University for the award of the degree of Doctor of Philosophy in Physics. The work embodied in this thesis is a record of bonafide research work carried out by me in the Computational and Functional Material Research Lab, Department of Applied Physics, Delhi Technological University (Formerly Delhi College of Engineering), New Delhi, under the guidance of ***DR. RENUKA BOKOLIA***. It is further certified that this work is original and has not been submitted in part or fully to any other University or Institute for the award of any degree or diploma.

Ankita Banwal
Roll No.2K18/PHD/AP/505

This is to certify that the above statement made by the candidate is correct to the best of our knowledge.

Dr. Renuka Bokolia
Supervisor (Assistant Professor)
Department of Applied Physics
Delhi Technological University
Delhi, India

Prof. A. S. Rao
Head & DRC Chairman
Department of Applied Physics
Delhi Technological University
Delhi, India

ACKNOWLEDGMENTS

Throughout my Ph.D. journey, I had the opportunity to interact with a variety of individuals. Each encounter has left an indelible mark on my personal and professional development with unique lessons and experiences. Therefore, I sincerely appreciate each person who has contributed to my life.

First and foremost, I humbly offer my obeisance to the ***Supreme Personality of Godhead****,* ***Kṛṣṇa****, who is the supreme cause of all causes. By His grace, I have been blessed with the privilege of expressing my devotion. I acknowledge with utmost humility that whatever I am today, every blessing and accomplishment is a manifestation of His divine will. So, as we traverse the path of life, it is our sacred duty to chant His holy name to accomplish the purpose of this human life.*

I would like to express my heartfelt gratitude to my supervisor, ***Dr. Renuka Bokolia****. The successful completion of this challenging academic endeavor would not have been possible without her affection, unwavering guidance, and support. Her belief in my abilities, even when I doubted myself, has been a tremendous source of motivation. I am particularly grateful for her fast assessment of my manuscripts and thesis chapters. Her punctuality has greatly facilitated the timely completion of my Ph.D. work with a considerable number of publications.*

I thank ***Prof. A. S. Rao*** *(DRC Chairman and HoD, Applied Physics, DTU) and* ***Prof. Prateek Sharma*** *(Vice Chancellor, DTU) for providing the necessary resources to facilitate the research activity. I further thank the experts and members of the SRC and DRC for generously dedicating their valuable time to provide their invaluable support to my thesis. Also, I thank all the faculty and staff members of the Department.*

I show my gratitude to someone special, ***Dr. Bhavya Kumar****. He has been my firm support through thick and thin, standing with me in moments of happiness and consoling me in times of sorrow. Furthermore, I thank my dear friends* ***Rohit Vashisht****,* ***Parul Mandla****,* ***Ruby Chauhan****,* ***Ankita Sharma****, and* ***Dr. Megha Sharma*** *for their love and support. I would like to thank my juniors* ***Megha Narwan****,* ***Rashi Mann****,* ***Shilpa Rana****,* ***Sheetal Kumari****,* ***Anshul****,*

***Yakshansh**, **Yash Pathak, Surya Pratap Singh Shekhawat**, **Muskan Varshney**, **Shreya Soni**, **Abdul Basith**, and **Shobhangana Singh** for their respect and help. I'm grateful for their presence in my life.*

*I owe everything to my late grandparents, **Mohan Lal** and **Suniti Devi,** whose profound love has shaped me into a compassionate and responsible individual. The void left by their absence is deeply felt, and I cherish their memory with utmost reverence. I express my heartfelt gratitude to my father, **Surinder Kumar**, who has always been a pillar of support, encouraging me to pursue and achieve each of my dreams. I thank my mother, **Rajni Devi,** for instilling in me a set of invaluable ethical principles that have been integral to my Ph.D. journey. Special thanks go to my chachu, **Yoginder Kumar**, and chachi, **Pooja Banwal**, who have treated me like their own daughter and consistently motivated me to reach new heights. I am immensely grateful to my brother, **Sanchit Banwal**, for his abundant love, respect, and care throughout the journey. I also extend my gratitude to God for blessing me with my little cousins, **Arnav Banwal** and **Arpan Banwal**. Their constant love and respect and their innocent laughter never fail to uplift my spirits. I am thankful to have a brother from another mother, **Bunty Rana**, for his love and care. I warmly thank my cousins, **Dr. Ankush Kaundal**, **Ritika Kalia**, **Nitika Kalia**, **Mona Chauhan**, **Parthik Kalia**, **Avantika Banwal**, **Abhay Banwal**, and **Vishaka Jaswal**, for their continuous mental and emotional support.*

*Last but not least, I heartily thank my spiritual mentors (**HG Paresh Das**) and (**HG Jahanva Devi Dasi**), who helped me discover the Absolute Truth (**Lord Kṛṣṇa**) and understand the purpose of life. I pray to the Divine to bestow upon me the strength and ability to serve them. Also, I want to thank **HG Radharaman Das**, **HG Antaryami Krishna Das**, **HG Kamal Kishori Devi Dasi**, **Ishika Bhandari**, **Krishna Bhandari**, and **HG Kajal** for their kindness and the genuine way in which they made me feel comfortable, which is truly remarkable. All glories to **HDG AC Bhaktivedanta Swami Srila Prabhupada** and **Guru Maharaj**.*

(Ankita Banwal)

New Delhi, April 2024

ABSTRACT

Upconversion Luminescence and Optical Temperature Sensing of $Er^{3+}/Yb^{3+}/W^{6+}$ Doped $BaBi_2Nb_2O_9$ Ferroelectric Ceramic

The host material doped with various trivalent rare earth ions (RE^{3+}) shows upconversion luminescence in which lower energy NIR radiation is converted into high energy visible radiation. This phenomenon can be stimulated using an inexpensive laser source. The upconversion luminescent materials have wide applications in the fields of solid-state lasers, white light-emitting diodes, biological imaging systems, infrared detectors, and diverse medical diagnostic techniques. Ferroelectric materials possess advantageous properties that make them well-suited as host materials for luminescence.

This thesis investigates the simultaneous effects of doping the $BaBi_2Nb_2O_9$ (BBN) system with Er^{3+}, Er^{3+}/Yb^{3+}, and $Er^{3+}/Yb^{3+}/W^{6+}$ on its structural, upconversion luminescence, temperature sensing, dielectric, ferroelectric and energy storage properties. In the Er^{3+} doped $BaBi_2Nb_2O_9$ system, the symmetry (orthorhombic geometry) and phase group (Fmmm) of prepared samples are confirmed from XRD analysis. The Raman spectra are recorded under the excitation of 785 nm, and four intense modes at 164, 225, 560, and 860 cm^{-1} are identified for undoped $BaBi_2Nb_2O_9$. The modes suppressed in undoped $BaBi_2Nb_2O_9$ ceramics can be easily observed in Er^{3+} doped compositions. However, in Er^{3+} doped $BaBi_{2-x}Er_xNb_2O_9$ composition, some less intense modes near 370, 389, 419, 437, 691, 730, and 771 cm^{-1} have been observed that might be associated with the degree of the structural disorder. The light upconversion luminescence (UCL) spectra are traced under 980 nm excitation. For an Er^{3+} content x = 0.04, the highest UCL emission intensity is obtained; beyond this content, the quenching concentration occurs. The sensitivity of the optimized prepared ceramic ($BaBi_{2-x}Nb_2Er_xO_9$: x = 0.04) is measured using the FIR technique. The absolute sensitivity (S_a) comes out to be 0.99% K^{-1} at 483 K, and the relative sensitivity (S_r) is approximately 0.40% K^{-1} at 300 K. Furthermore, the ferroelectric properties of Er^{3+} doped BBN ferroelectric ceramic degrades as compared to undoped BBN ceramic.

Further, in Er^{3+}/Yb^{3+} co-doped $BaBi_{2-x-y}Nb_2Er_xYb_yO_9$ ferroelectric ceramic, the Er^{3+} content is fixed at an optimized value (x = 0.04), and Yb^{3+} is varied from y = 0.00 to 0.12 at A-site of the perovskite structure. The SEM images of prepared ceramics resemble plate-like formations and comprise non-uniform grains with irregular orientation. An increase in grain size with Yb^{3+} content up to y = 0.10 was found to promote upconversion luminescence. Two bright green bands at 535 nm and 557 nm and a detectable red spectrum near 672 nm were observed in UCL spectra, corresponding to an excitation wavelength of 980 nm. The effective energy transfer process from Yb^{3+} to Er^{3+} ions is supported by decay time measurements, which increase with increasing Er^{3+}/Yb^{3+} content because of the non-radiative transition at higher doping concentrations. The pump power dependence upon the UCL intensity for an optimum Yb^{3+} content y = 0.10 reveals that green and red UC emissions involve two photons. Er^{3+}/Yb^{3+} co-doped $BaBi_{2-0.04-y}Nb_2Er_{0.04}Yb_yO_9$ ceramic system with y = 0.06 and 0.10 exhibit a S_a of 0.69% K^{-1} and 0.58% K^{-1} at maximum absolute temperature (T_a) = 523 K and 463 K, respectively, and S_r of 1.10% and 1.01% at maximum relative temperature (T_r) = 303 K.

Moreover, the structural and electrical properties are investigated after exploring the optical properties of Er^{3+}/Yb^{3+} co-doped $BaBi_{2-x-y}Nb_2Er_xYb_yO_9$ ferroelectric ceramic. FTIR spectra showed characteristic peaks of the Aurivillius phase at 619 cm^{-1} and 822 cm^{-1}. Four Raman modes are visible in undoped BBN, whereas 12 modes have been observed in doped BBN compositions. Temperature-dependent dielectric tests reveal significant dispersion below and above the maximum temperature (T_m), and the dielectric constant (ε') decreases with increasing frequency. The dielectric loss (ε") curves are diffused, and variations in the maxima with frequency have been detected, demonstrating the relaxor behavior of all produced BBN compositions. The thinner PE loops were achieved under applied electric fields between 75 kV/cm and 100 kV/cm. The remnant polarization (P_r) and maximum polarization (P_m) were used to calculate the energy storage parameters (W, W_{rec}, η) of each ceramic composition. The energy storage parameters improve as the applied electric field increases. It can be concluded that the efficiency (η) of undoped, Er^{3+} doped, and Er^{3+}/Yb^{3+} co-doped $BaBi_{2-x-y}Nb_2Er_xYb_yO_9$ ceramics increased with doping concentrations. In contrast, the energy storage density (W) and recoverable energy storage density (W_{rec}) of Er^{3+} doped and Er^{3+}/Yb^{3+} co-doped BBN ceramic are comparable with undoped BBN.

Lastly, the effect of transition metal ion (W^{6+}) in the tri-doped $BaBi_{2-0.04-0.10}Nb_{2-z}Er_{0.04}Yb_{0.10}W_zO_9$ ferroelectric ceramic on the structural, upconversion luminescence, temperature sensing, ferroelectric and energy storage density characteristics are discussed. The Er^{3+} and Yb^{3+} concentrations are fixed at the optimized values, and the transition metal ion W^{6+} varies from z = 0.01 to z = 0.04. The UCL emission intensity increases with the incorporation of W^{6+} ions and increases up to z = 0.02. Time decay analysis is conducted for the green and red emission bands, corresponding to transitions from $^2H_{11/2}$ to $^4I_{15/2}$ and $^4S_{3/2}$ to $^4I_{15/2}$ energy levels, respectively. The S_a of the $Er^{3+}/Yb^{3+}/W^{6+}$ tri-doped BBN system yields a result of 0.91% K^{-1} at a temperature of 573 K, which is higher than the Er^{3+}/Yb^{3+} co-doped BBN system and comparable with the Er^{3+} doped BBN system. The S_r achieved for the $Er^{3+}/Yb^{3+}/W^{6+}$ tri-doped BBN system is 1.32% at 303 K, the highest among the three BBN systems. The PE loops have improved and reached their maximum P_m value at 9.719 $\mu C/cm^2$ for z = 0.02. The W, W_{rec}, and η for undoped BBN ceramics are 0.662 J/cm^3, 0.518 J/cm^3, and 78.25% and for tri-doped BBN ceramics are 0.874 J/cm^3, 0.792 J/cm^3, and 90.53%.

In conclusion, the synthesized $BaBi_2Nb_2O_9$ (BBN) ceramic demonstrates promising properties for multifunctional applications, including optical sensors, energy storage devices, and tunable light sources.

LIST OF FIGURES

LIST OF TABLES

PUBLICATIONS RESULTING FROM THIS THESIS WORK (8)

ARTICLES IN INTERNATIONAL JOURNALS (3):

1. **A. Banwal** and R. Bokolia, "Enhanced upconversion luminescence and optical temperature sensing performance in Er^{3+} doped $BaBi_2Nb_2O_9$ ferroelectric ceramic," *Ceramics International*, vol. 48, no. 2, pp. 2230-2240, 2022. **(IF – 5.2)**
2. **A. Banwal** and R. Bokolia, "Efficient tunable temperature sensitivity in thermally coupled levels of Er^{3+}/Yb^{3+} co-doped $BaBi_2Nb_2O_9$ ferroelectric ceramic," *Journal of Luminescence*, vol. 263, 120071, 2023. **(IF – 3.6)**
3. **A. Banwal**, M. Verma, B. Singh, and R. Bokolia, "Temperature stability and improved energy storage efficiency of $BaBi_2Nb_2O_9$: Er^{3+}/Yb^{3+} relaxor ferroelectric ceramic under moderate electric fields," *Applied Physics A*, vol. 130, no. 334, 2024. **(IF – 2.7)**

ARTICLES IN INTERNATIONAL CONFERENCES (3):

1. **A. Banwal** and R. Bokolia, "Phase evolution and microstructure of $BaBi_2Nb_2O_9$ ferroelectric ceramics," *Materials Today: Proceedings*, vol. 46, part 20, pp. 10121-10124, 2021.
2. **A. Banwal** and R. Bokolia, "Effect of Er^{3+} ion doping on structural, ferroelectric and up/down conversion luminescence in $BaBi_2Nb_2O_9$ ceramic," *Materials Today: Proceedings*, vol. 47, part 14, pp. 4692-4695, 2021.
3. **A. Banwal** and R. Bokolia, "Preparation and characterizations of Yb^{3+} substituted $BaBi_{2-y}Nb_2Yb_yO_9$ ferroelectric ceramic," *Materials Today: Proceedings*, vol. 62, part 6, pp. 3782-3785, 2022.

ARTICLES COMMUNICATED IN INTERNATIONAL JOURNALS (2):

1. **A. Banwal**, M. Verma, and R. Bokolia, "Effect of transition metal ion (W^{6+}) on light upconversion and optical thermal sensitivity of Er^{3+}/Yb^{3+} doped $BaBi_2Nb_2O_9$ ferroelectric ceramic", in ***Ceramics International***.
2. **A. Banwal**, M. Verma, and R. Bokolia, "High energy-storage properties of $Er^{3+}/Yb^{3+}/W^{6+}$ doped $BaBi_2Nb_2O_9$ ferroelectric ceramic", in ***Journal of Alloys and Compounds***.

PUBLICATIONS OTHER THAN THIS THESIS WORK (6)

ARTICLES IN INTERNATIONAL JOURNALS (3):

1. **A. Banwal** and R. Bokolia, "Thermometric sensing performance in erbium modified $SrBi_{2-x}Nb_2Er_xO_9$ ferroelectric ceramic for optoelectronic devices," *Ceramics International*, vol. 48 part 23A, pp. 34405-34414, 2022. **(IF – 5.2)**

2. M. Narwan, **A. Banwal**, R. Sharma, and R. Bokolia, "Non-invasive thermal sensing and improved recoverable energy storage density of $Bi_{0.5}Na_{0.5}TiO_3$: Er^{3+} doped multifunctional ferroelectric ceramic", *Journal of Luminescence,* vol. 265, 120236, 2024. **(IF – 3.6)**

3. M. Varshney, S. Soni, **A. Banwal**, M. Narwan, M. Verma, and R. Bokolia, "Effect of Er^{3+} ion incorporation on the structural, photoluminescence, and ferroelectric properties of $K_{0.5}Na_{0.5}NbO_3$ ceramic for optoelectronic applications," *Applied Physics A*, vol. 130, no. 267, 2024. **(IF – 2.7)**

ARTICLES COMMUNICATED IN INTERNATIONAL JOURNALS (1):

1. A. Basith, S. Singh, **A. Banwal**, M. Narwan, M. Verma, and R. Bokolia, "Colour alteration due to fusion of Yb^{3+} ions in Er^{3+} doped $SrBi_2Nb_2O_9$ ferroelectric ceramic", in ***Ceramics International***.

ARTICLES COMMUNICATED IN INTERNATIONAL CONFERENCES (2):

1. A. Basith, S. Singh, **A. Banwal**, M. Narwan, M. Verma, and R. Bokolia, "Structural, photoluminescence, and ferroelectric behaviour of Er^{3+}/Yb^{3+} co-doped $SrBi_2Nb_2O_9$ ferroelectric ceramic for multifunctional device", in ***International Conference on Atomic, Molecular, Material, Nano and Optical Physics with Applications (ICAMNOP)****, Delhi, India, 2023*.

2. M. Narwan, **A. Banwal**, and R. Bokolia, "Comparative study of structural, upconversion, and ferroelectric properties in Er doped and Er/Yb co-doped BNT ceramic", in ***International Conference on Atomic, Molecular, Material, Nano and Optical Physics with Applications (ICAMNOP)****, Delhi, India, 2023*.

TABLE OF CONTENTS

1

CHAPTER

Introduction

- *This chapter offers a comprehensive overview of luminescence, including an introduction to its fundamental principles and its types. This chapter primarily centers on the phenomenon of photoluminescence, mainly upconversion (UC) photoluminescence.*
- *The relevant UC processes and advancements in materials doped with lanthanide and non-lanthanide dopants are discussed. The significance of the host lattice, its energy storage behavior, and performance with various rare earth ion dopants are examined.*
- *The optical temperature sensing method of fluorescence intensity ratio (FIR) and the importance of ferroelectric host materials replaced with rare earth ions are discussed.*

1.1 LUMINESCENCE

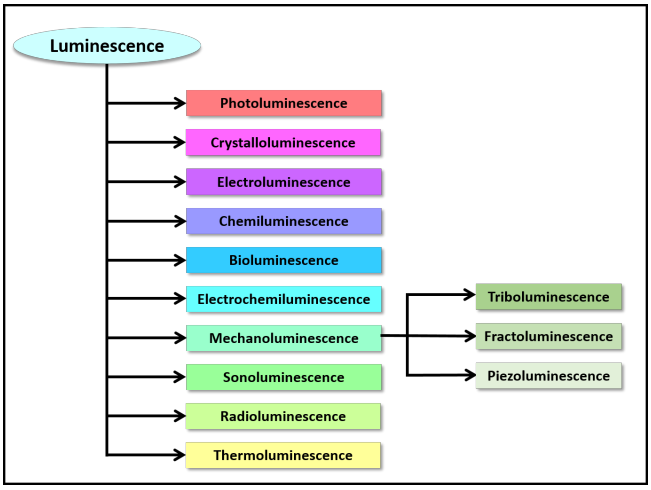

Figure 1.1: Luminescence based on modes of excitations.

The radiative photon emission from a material due to an excitation is known as luminescence. Since thermal excitations do not start the radiative emission, this is often called cold body radiation. Various excitation mechanisms may produce luminescence, and there are several kinds of luminescence based on the modes of excitation (**Figure 1.1**). Photoluminescence refers to the emission of light resulting from the absorption of photons. When crystals form, they exhibit a captivating luminescence known as crystalloluminescence. Electroluminescence generates light when an electric current passes through a substance. The enchanting display of light during chemical reactions characterizes chemiluminescence. Bioluminescence is a fascinating natural phenomenon in which living organisms produce light through chemical reactions. Electrochemiluminescence occurs when an electric current triggers a chemical reaction in a solution, leading to light emission. Mechanoluminescence results when a material is subjected to mechanical stress or deformation. This is further categorized as triboluminescence, which emerges when materials are rubbed or crushed; fractoluminescence, which illuminates during material breakage; and piezoluminescence,

which shines under pressure. Sonoluminescence occurs when light emitted from a liquid is stimulated by sound waves. Radioluminescence occurs when ionizing radiation bombards a substance, and in thermoluminescence, light emerges due to high-energy radiation exposure. This thesis focuses on photoluminescence; hence, it is essential to specify the different forms of photoluminescence. It is further categorized into two distinct components: fluorescence and phosphorescence. Depending upon the conversion of light, photoluminescence is divided into two processes: downconversion photoluminescence and upconversion photoluminescence.

1.1.1 Fluorescence and Phosphorescence

Fluorescence is a kind of photoluminescence that occurs when there is a transition from the singlet (S_1) to singlet (S_0) electronic states, as shown in **Figure 1.2**. The average lifespan under this scenario is around 10^{-4} to 10^{-8} seconds. The phosphorescence is sometimes referred to as delayed fluorescence. The phenomenon occurs when an electron is stimulated to a higher energy level (S_1), transits to the triplet (T_1), and then falls to singlet (S_0) energy levels, as shown in **Figure 1.2**. The phosphorescence duration is prolonged and may range from milliseconds to minutes, depending on the luminescent materials used.

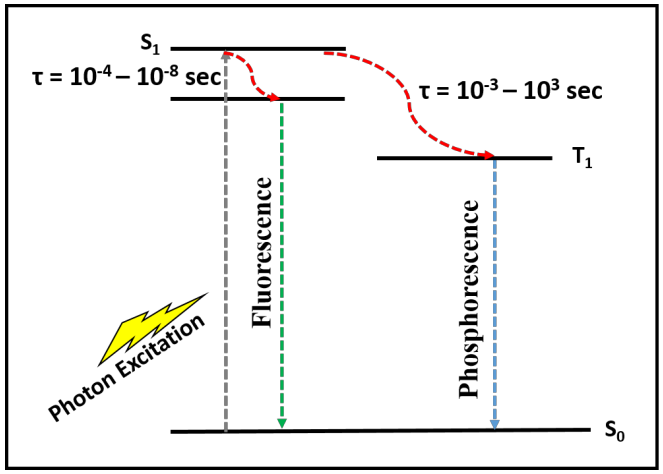

Figure 1.2: Schematics of fluorescence and phosphorescence.

1.1.2 Downconversion and Upconversion Luminescence

Downconversion photoluminescence refers to a process in which a material absorbs photons of higher energy (shorter wavelength) and emits lower energy photons (longer wavelength). In practical applications, downconversion photoluminescence is often utilized in technologies like phosphors in light-emitting diodes (LEDs). In this case, higher-energy photons from the LED source are absorbed by the phosphor material, and the material then emits lower-energy photons, effectively converting some of the energy to a different, more desirable wavelength. This process can enhance the color quality and efficiency of the emitted light. On the other hand, upconversion photoluminescence is a process in which a material absorbs photons of lower energy (longer wavelength) and then emits photons of higher energy (shorter wavelength). It is a nonlinear mechanism involving the sequential absorption of photons. In practical applications, upconversion photoluminescence is of interest in various technologies, including certain types of solar cells and biomedical imaging. The schematics of upconversion and downconversion photoluminescence are given in **Figure 1.3**. This thesis primarily focuses on upconversion luminescence (UCL); therefore, the various UCL mechanisms are discussed in the next section.

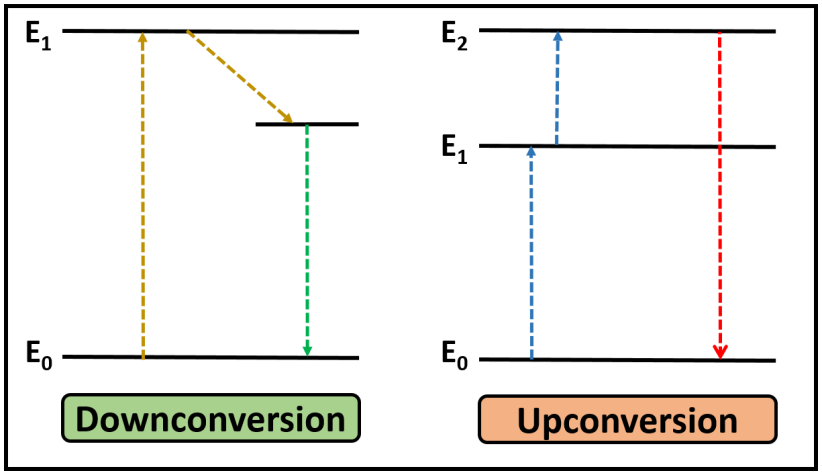

Figure 1.3: Schematics of downconversion and upconversion luminescence.

1.1.3 Upconversion Luminescence Mechanism

The upconversion luminescence phenomenon was first observed by F. Auzel in 1966 [1]. The lanthanide-doped luminous materials can undergo this process and are called upconverters. The lanthanide elements are crucial in initiating the upconversion process in these materials. The various UCL mechanisms are:

1.1.3.1 Excited State Absorption Process

The mechanism of excited state absorption (ESA) was initially proposed by N. Bloembergen [2]. The ion in its lowest energy state (E_0) absorbs energy from a photon and becomes stimulated to an intermediate energy level (E_1) via a process called ground state absorption (GSA) (**Figure 1.4**). The ion undergoes further excitation by absorbing an additional photon, resulting in a higher energy emission level (E_2) via the process of excited state absorption (ESA). Ultimately, the ion originating from the highly energized state (E_2) transitions to the lowest energy level (E_0), resulting in up-conversion emission. ESA is a process that uses a single optically active ion to increase the population of a higher emitting level via resonant energy absorption.

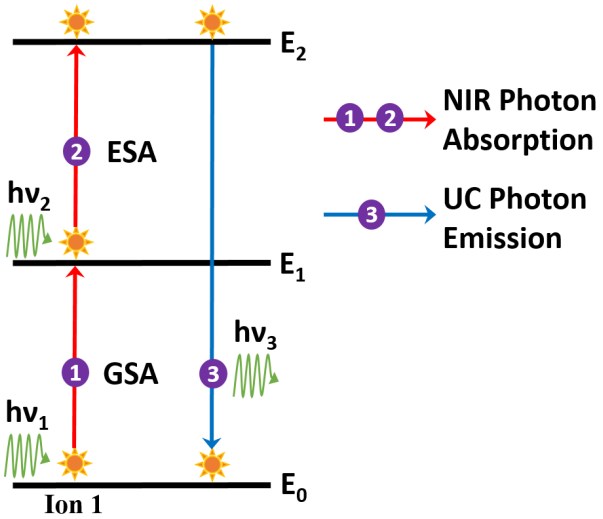

Figure 1.4: Schematics of excited state absorption process.

1.1.3.2 Energy Transfer Process

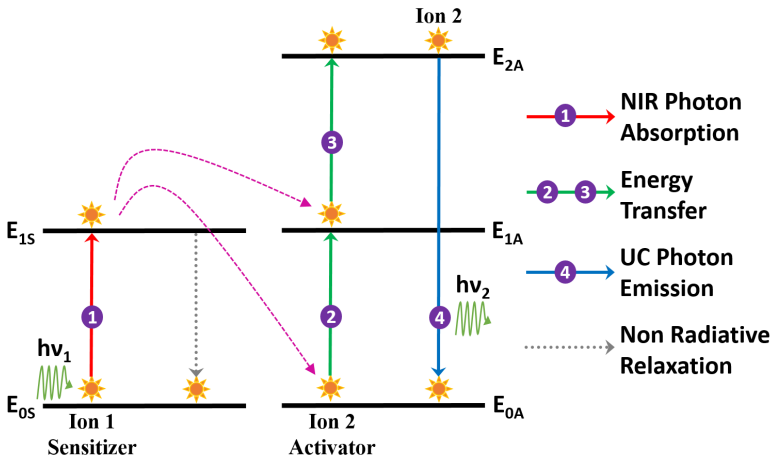

Figure 1.5: Schematics of energy transfer process.

In the energy transfer process (ET), two neighboring ions are necessary, one serving as a sensitizer and the other as an activator, as shown in **Figure 1.5**. The first photon absorption stimulates the sensitizer ion (ion 1) from its ground state (E_{0S}) to a higher energy metastable state (E_{1S}). Before undergoing non-radiative relaxation to E_{0S}, the sensitizer transmits its energy to the activator ion (ion 2) in the ground state (E_{0A}), promoting the ion 2 to E_{1A}. Once the sensitizer and activator reach their metastable states, E_{1S} and E_{1A}, respectively, another energy transfer takes place in the metastable state. This energy transfer causes the activator ion 2 to move to its higher excited state, E_{2A}, while the sensitizer ion returns to E_{0S}. The UC emission will occur from the higher energy state E_{2A} via a radiative transition to the ground state (E_{0A}). The average distance between the sensitizer and activators is a crucial component that significantly impacts the upconversion efficiency in ET [3-6].

1.1.3.3 Cooperative Process

The cooperative process has three ion centers, having two identical ions (ion 1 and ion 3). In **Figure 1.6**, when the excitation photons are absorbed, ions 1 and 3 can get excited and enter the metastable state (E_{1S}). Both ion 1 and ion 3 may concurrently and cooperatively

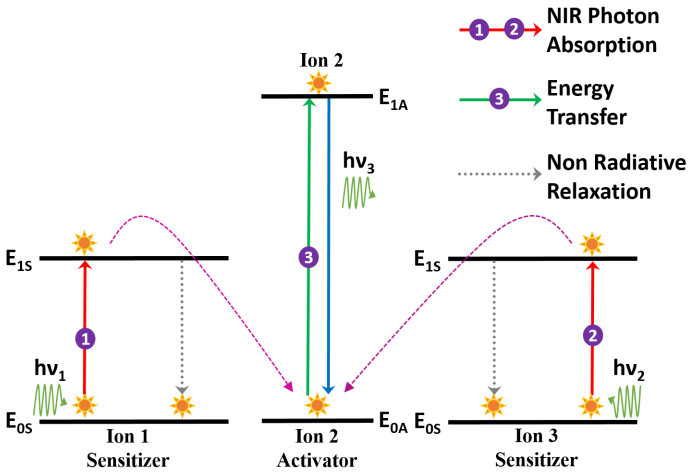

Figure 1.6: Schematics of cooperative process.

interact with ion 2, transferring the absorbed energy to stimulate ion 2 from its ground state (E_{0A}) to a higher state (E_{1A}). The ion in the E_{1A} state undergoes relaxation to the E_{0A} state by producing an upconverted photon. In this context, ions 1 and 3 function as sensitizers, meaning they absorb the energy from the incoming NIR photon and transmit it to ion 2. Ion 2, in turn, functions as an activator, resulting in the production of an upconverted photon. The cooperative process is less efficient than ESA or ET due to the involvement of quasi-virtual pair levels during transitions [4, 6, 7].

1.1.3.4 Cross Relaxation Process

Figure 1.7 depicts the cross-relaxation (CR) process, which takes place when ion 1 imparts a portion of its energy to ion 2 through the following cycle: E_2 (ion 1) + E_0 (ion 2) → E_1 (ion 1) + E_1 (ion 2). Ion 1 or ion 2 may have identical or distinct properties, and ion 2 may also exist in its higher energy form. The efficiency of the charge recombination of the CR process relies heavily on the concentration of dopants since the interaction between ions forms the CR loop. The "concentration quenching mechanism" phenomenon in emission is mostly caused by cross-relaxation. However, it is feasible to intentionally use it to manipulate the color of UC emission or initiate a potent photon avalanche process [6, 7].

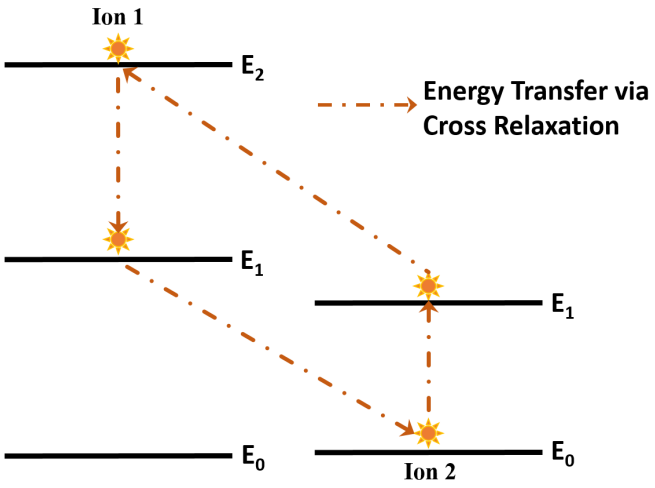

Figure 1.7: Schematics of cross-relaxation process.

1.1.3.5 Photon Avalanche Process

Photon avalanche upconversion was first noticed in infrared quantum counters doped with Pr^{3+} [8]. Only a small amount is detectable when the UC luminescence is below a certain threshold. However, when it exceeds, the intensity of UC luminescence rises significantly [9]. The photon avalanche is a loop control mechanism that utilizes ESA and efficient CR for photon excitation (**Figure 1.8**). The pump photons resonate solely with the transition from the E_1 to E_2 level of ion 2. Non-resonant ground state absorption occurs at the E_1 level of ion 2. Due to the resonance between the pump photons and the $E_1 \rightarrow E_2$ transition, ESA can elevate ion 2 to the E_2 level. A successful CR process occurs between ions 1 and 2; the energy possessed by ion 1 is transferred to ion 2 to populate the metastable state E_1 of ion 2. The iterative process begins with a single ion 2 and concludes with two ions 2 in the same metastable state (E_1). Therefore, two ions in the E_1 metastable state generate four ions via successive iterations, and this progression continues. The avalanche effect happens when the amount of energy stored in state E_1 exceeds the amount of energy lost. The avalanche effect amplifies the number of ion 2 in the metastable state E_1, resulting in population amplification, which leads to up-conversion from the emitting level E_2 [5, 7].

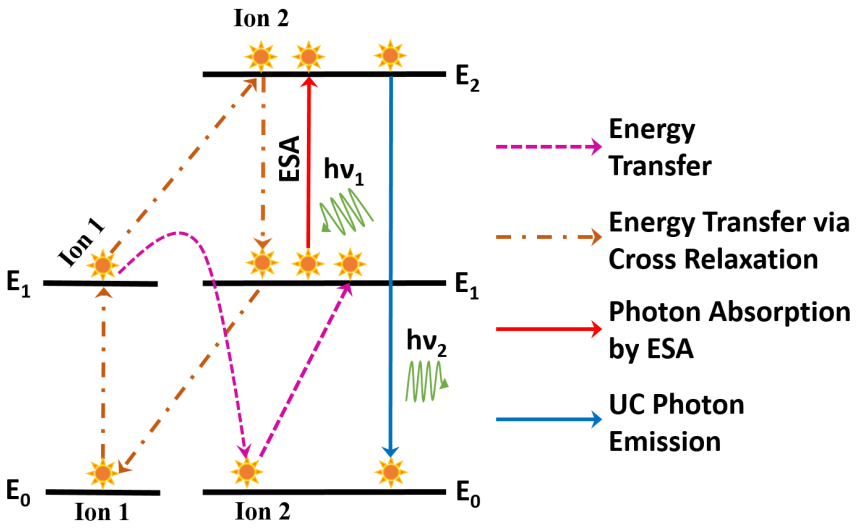

Figure 1.8: Schematics of photon avalanche process.

1.2 SELECTION OF HOST MATERIALS

The host materials offer a suitable lattice structure that creates the appropriate conditions for the dopants and customizes the luminescent characteristics of the materials. The choice of suitable host material is a crucial component that promotes the development of novel and exceptionally effective luminescent materials. Researchers have explored various inorganic host matrices, such as halides, oxides, silicates, nitrides, sulphides, and phosphates [10, 11]. The careful choice of host matrices is essential for obtaining optimal luminescence. The chosen host should have a low cut-off frequency, enhancing its optical efficiency and adaptability. Additional crucial factors significantly influencing luminescence characteristics include excellent thermal and chemical stability, a broad transparency range, a high refractive index, easy solubility, and minimal toxicity levels. The halides are intriguing due to their low phonon frequency and higher toxicity [5]. The phonon frequencies of some complex hosts and certain traditional hosts are often employed to create luminescent materials.

1.2.1 Ferroelectric Host Materials

Ferroelectric materials are a class of materials that exhibit a spontaneous electric polarization that can be reversed by applying an external electric field. This unique property distinguishes them from other dielectric materials. These materials allow structural alteration due to the presence of foreign dopants. They also exhibit reduced phonon energy and higher solubilities of both lanthanide and non-lanthanide ions [10-12]. This thesis primarily concentrates on a specific category of ferroelectrics known as bismuth layered structure ferroelectric (BLSF), which is briefly addressed in the next section.

1.2.1.1 Bismuth Layered Structure Ferroelectric

Aurivillius developed a class of compounds with a bismuth-layered structure in 1949 [13], and initially, $PbBi_2Nb_2O_9$ was discovered to be ferroelectric [14, 15]. Later on, numerous compositions of lead-free BLSFs were found to display ferroelectric properties. These compositions were distinguished by their elevated Curie temperature, reduced dielectric constant, reliable anisotropic electromechanical coupling factor, and minimal temperature coefficient of the resonant frequency. Their exceptional temperature stability, slow rate of aging, and improved fatigue properties were highly appealing from an application aspect. The features of these compositions have sparked growing interest in their development for high-temperature piezoelectric applications.

The BLSFs are characterized by the formula $(A_{m-1}B_mO_{3m+1})^{2-}$. The compound $(A_{m-1}B_mO_{3m+1})^{2-}$ represents a perovskite block with m octahedral layers stacked inside $(Bi_2O_2)^{2+}$ layers. A represents trivalent, divalent, monovalent cations, or a mixture, such as Bi^{3+}, Na^{+}, Pb^{2+}, Ba^{2+}, etc., while B denotes hexavalent, pentavalent, or tetravalent ions, such as W^{6+}, Ta^{5+}, Nb^{5+}, Ti^{4+} [16-20]. Here are several examples of BLSF with various values of m:

(i) Bi_2WO_6 (m = 1) [21], (ii) $BaBi_2Nb_2O_9$ (m = 2) [22], (iii) $Bi_4Ti_3O_{12}$ (m = 3) [23], (iv) $BaBi_4Ti_4O_{15}$ (m = 4) [24, 25].

1.2.1.2 Energy Storage Density Properties in Ferroelectrics

Scientific and technological advancements have significantly increased life expectancy and improved quality of life. However, these positive outcomes come hand in hand with two interconnected challenges: overpopulation and energy scarcity. The widespread use of electrical energy has contributed to issues like air pollution and global warming, while traditional fossil fuels are nearly depleted. However, only focusing on energy conservation without considering the emission of lead would cause more harm to the environment. Consequently, lead-free systems have emerged as the primary approach to address the energy problem while preventing secondary lead contamination efficiently. Currently, the primary types of energy storage devices consist of batteries, dielectric capacitors, electrochemical capacitors, fuel cells, etc. Dielectric capacitors have become essential components in pulse power equipment because of their rapid charge-discharge speeds (about nanoseconds) and remarkably high power density (up to 10^8 watts per kilogram). Scientists have created many energy storage materials for dielectric capacitors, including polymers, ceramic polymer composites, glass, glass ceramics, and ceramics. Dielectric ceramics have moderate breakdown field strength, little dielectric loss, and anti-fatigue properties compared to other dielectric materials. For high-temperature applications, dielectric ceramics are distinguished by their remarkable thermal stability. The diverse characteristics of dielectric ceramics provide great potential for using energy storage capacitors in aviation, oil drilling, electromagnetic pulse warfare, and other applications [26, 27].

Based on the polarization variation with the electric field, energy storage dielectric materials may be classified into two distinct categories: nonlinear dielectrics and linear dielectrics [28]. The dielectric constant of linear dielectrics remains constant regardless of the electric field. The polarization strength is directly proportional to the electric field strength. Meanwhile, nonlinear dielectric materials have a pattern of polarization where they first grow to their maximum value (P_m) during the charging process. This occurs when the electric field reaches its breakdown electric field (E_b). Subsequently, during the discharging process, when the electric field reduces to zero, the polarization lowers to a non-zero residual polarization (P_r), often referred to as the PE hysteresis loop. A schematic diagram of nonlinear dielectrics is given in **Figure 1.9**. The total energy stored throughout the charging process equals the combined value of the purple and the shaded region (**Figure 1.9)**. The energy storage density (W) in a system is determined by calculating the integral area of the P-E loop to the polarization (P) and is denoted by Eq. (1.1) [26]:

$$W = \int_0^{P_m} EdP \tag{1.1}$$

The energy that may be released is the recoverable energy storage density (W_{rec}). The area under the vertical lines shows W_{rec} and can be defined by Eq. (1.2) [27]:

$$W_{rec} = \int_{P_r}^{P_m} EdP \tag{1.2}$$

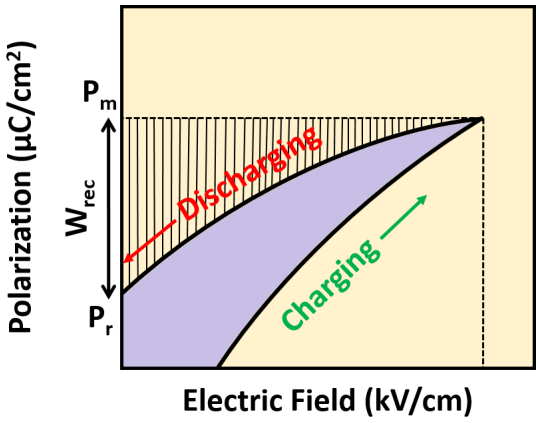

Figure 1.9: Schematic diagram of nonlinear dielectrics.

The energy that remains unreleased is defined as the loss energy density (W_{loss}). The energy storage efficiency (η) of the dielectric material can be expressed by Eq. (1.3) [26, 27]:

$$\eta = \frac{W_{rec}}{W} = \frac{W_{rec}}{W_{rec} + W_{loss}} \tag{1.3}$$

There are different types of nonlinear dielectrics, such as (1) ferroelectric, (2) relaxor ferroelectrics, (3) anti-ferroelectrics, and (4) anti-relaxor ferroelectric. **Figure 1.10(a-d)** represents types of nonlinear dielectric. The red and pink regions represent the W_{rec} and W_{loss}, respectively. Ferroelectrics have a substantial maximum polarization and a low breakdown strength. However, their significant residual polarization reduces the recoverable energy storage and efficiency. On the other hand, relaxor ferroelectrics and antiferroelectrics exhibit greater saturation polarizations and lower residual polarizations, making them suitable for applications requiring significant energy storage. Anit-relaxor ferroelectrics include relaxors with antiferroelectrics, resulting in a material that exhibits both a beam-waisted hysteresis loop and a significant polarization [26-28].

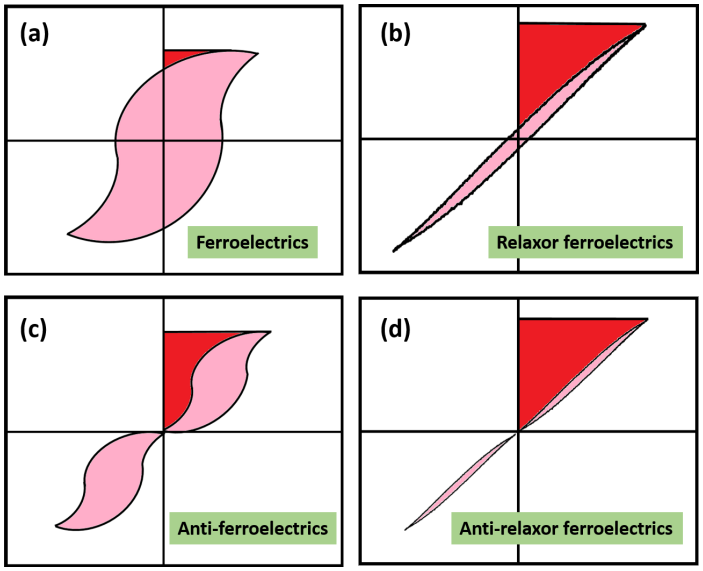

Figure 1.10: Types of non-linear dielectrics (a) Ferroelectric (b) Relaxor ferroelectric (c) Anti-ferroelectric (d) Anti-relaxor ferroelectric.

This thesis comprehensively investigates a relaxor ferroelectric material, $BaBi_2Nb_2O_9$, that belongs to the BLSF family. $BaBi_2Nb_2O_9$ is chosen as a host material for upconversion because it is chemically and thermally stable, has lower phonon energy (860 cm^{-1}), and allows modifications in its crystal structure with additional dopants. Furthermore, its inherent electrical properties make it a suitable material for further investigation. According to the general BLSF formula, the perovskite layer is $(BiNb_2O_7)^{2-}$ where the A-site is occupied by bismuth ions and the B-site by niobium ions, and the number of octahedral layers is m = 2.

1.2.1.3 Recent Studies on BLSF

Table 1.1 provides brief details of recent studies on BLSF materials, and it can be seen that the BLSF is a potential host material for multifunctional applications.

Table 1.1: Recent studies on different BLSF doped with different dopants.

Host Material	Dopant	Work Presented	Year	Ref.
$BaBi_2Nb_2O_9$	Er/Yb	Strong UC green emission of powdered BBN	2017	[29]
$Na_{0.5}Bi_{4.5}Ti_4O_{15}$	K/Er	Green upconversion emission and a good electrical performance	2019	[30]
$CaBi_4Ti_4O_{15}$	Tm/Yb	A strong blue light and a weaker red UC emission band along with maximum sensitivity 0.016 K^{-1} at 503 K	2020	[31]
$SrBi_2Nb_2O_9$	Er	Two green emission band and maximum sensitivity of 0.0086 K^{-1} at 443 K	2022	[32]
$SrBi_2Nb_2O_9$	Er/Yb	Theoretical and experimental analysis of photoluminescence and electrical properties	2022	[33]
$Bi_4Ti_3O_{12}$-$xNa_{0.5}Bi_{2.5}Nb_2O_9$	Sm	Microstructure, electrical, photoluminescence and photochromic properties of the ceramics	2022	[34]
$Ba_2NaNb_5O_{15}$	Er/Yb	Up-conversion luminescence, temperature sensing and energy storage performance of transparent glass ceramic	2022	[35]
$Na_{0.5}Bi_{2.5}Ta_2O_9$	Er/Yb	Relative sensitivity of 5.99% K^{-1} at cryogenic temperature of 153 K. After irradiation with commercial laser of 405 nm for 30 s, the relative sensitivity is increased to 6.81% K^{-1}	2023	[36]

1.3 SELECTION OF SUITABLE DOPANTS

Inorganic upconversion phosphors consist of a crystalline host and a dopant, often lanthanide ions, which are present in low concentrations. The dopant acts as a luminous core, while the host lattice and crystal structure serve as a framework to put these cores in the most favorable location. The precise spacing between rare earth ions and their spatial arrangement are crucial factors in sensitive luminescence. When stimulated by NIR, several host materials infused with lanthanide ions can generate visible light [37, 38].

1.3.1 Lanthanide Dopants

The observed luminescence behavior is mainly attributed to the lanthanide elements. To fully grasp the performance of various lanthanide elements, it is crucial to have a deep understanding of their energy level structure. The elements referred to as "rare earth elements" are part of the 6^{th} period and 3^{rd} group of the periodic table. They have atomic numbers ranging from 57 to 71. These elements have an incompletely filled 4f shell and are protected by the nearby $5s^2$ and $5p^6$ orbitals. As a result, their energy levels are minimally influenced by the surrounding environment and remain relatively constant in doped systems, regardless of the host matrices. The neutrally charged lanthanide elements have the electronic configuration $[Xe]5d6s^2 4f^n$ (n = 0 to 14). The 4f orbital is occupied successively from 0 to 14 as the elemental series progresses from Lanthanum to Lutetium. When introduced into specific host matrices, lanthanide elements are most stable in the triply ionized state, where their electronic configuration is $[Xe]4f^n$ [39].

The energy level of a material is denoted by total spin angular momentum (S), total orbital angular momentum (L), and total angular momentum (J). Energy level splitting

occurs as a result of three distinct types of interaction occurring within the host lattice (**Figure 1.11**), which are elaborated in the following sections:

I. **Electronic interaction:** The transition from $4f^n$ to $4f^{n-1}5d$ is due to the $4f^{n-1}$ and 5d electrons, typically observed in divalent lanthanides [40, 41]. The energy difference between these energy levels is quite significant (> 10^4 cm^{-1}); therefore, the possibility of this interaction is extremely low.

II. **Coulombic interaction:** The next strongest interaction is the Coulombic interaction, which arises due to the electrostatic repulsion between electrons occupying the 4f orbitals of the lanthanide element. This repulsion causes the energy levels of the free ion to split into several levels, characterized by ^{2S+1}L energy levels. The split levels exhibit a degeneracy of (2L+1)(2S+1) fold. The splitting of the ^{2S+1}L term levels is around 10^4 cm^{-1} and is particularly noticeable compared to other types of interactions [42, 43].

III. **Spin-orbit interaction:** In accordance with the Russel-Saunders scheme, the combined effect of the strong Coulombic contact results in the coupling of the L and S to produce J. Due to the spin-orbit interaction, the Coulomb-split levels further split into a manifold of (2J+1) levels. These levels are denoted as $^{2S+1}L_J$ levels. The splitting order is approximately 10^3 cm^{-1} [42, 43].

IV. **Crystal field interaction:** The Stark splitting of $^{2S+1}L_J$ levels is induced by the interaction between the ion and its surrounding crystal field, further dividing the energy manifolds. The crystal-field interaction modifies the (2J+1) degeneracy by (J+1/2) for ions possessing an odd n configuration. However, for ions with an even n configuration, the degeneracy remains unchanged at (2J+1), denoted as $^{2S+1}L_{J,\mu}$. In this instance, energy levels are split by 10^2 cm^{-1}.

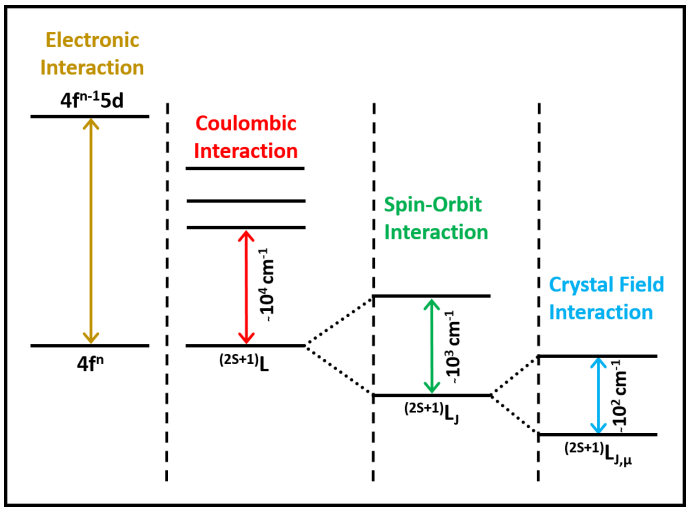

Figure 1.11: Types of energy level splitting due to various interactions within the host.

The optical transitions shown by rare-earth ions are categorized according to their outer electronic configuration:

i. **f-f transition:** The phenomenon occurs inside the 4f orbitals of the same lanthanide ion. This transition is prohibited due to the electric dipole process since both states have the same parity. This phenomenon occurs due to the merging of states, which is generated by the contact between the lanthanide ions and either the crystal field or the lattice vibrations. This interaction relaxes the selection rules, enabling electric dipole transitions [44].

ii. **f-d transition:** The $4f^n \rightarrow 4f^{n-1}5d$ transition refers to the process in which an electron is elevated from the 4f orbital to the 5d orbital. The reported transitions for (Ce^{3+}, Pr^{3+}, Tb^{3+}, Yb^{2+}) rare-earth ions are spin-permitted and exhibit greater strength and larger spectral range than f-f transitions [44].

iii. **Charge transfer transition:** This excitation involves the participation of two or more molecules, where a portion of charge is transferred from one molecule to another. However, these transitions have large energies and are only seen in certain lanthanides [44].

1.3.2 Non-Lanthenide Dopants

In order to refine the luminescent characteristics of materials doped with a lanthanide, it is possible to alter the external environment of the emission centers. Including some non-lanthanide elements has shown encouraging outcomes in effectively altering the local crystal field around the rare-earth ions. Several non-lanthanide elements, including Li^{+}, Mg^{2+}, Zn^{2+}, Mo^{3+}, Bi^{3+}, and W^{6+}, have been shown to enhance the luminescent properties [44-47].

1.4 OPTICAL TEMPERATURE SENSING

Lanthanide-doped materials are gaining attention for temperature sensing applications due to the temperature-dependent nature of their emission intensity. One notable advantage of these sensors is their ability to operate without physical contact. This feature proves particularly beneficial in various scenarios where traditional temperature sensors face limitations. Temperature sensing in RE-doped materials is often achieved by analyzing decay time and fluorescence intensity ratio (FIR). Fluorescence lifetime decay requires pulsed excitation and the measurement of temperature-dependent fluorescence decay curves originating from two higher stimulated energy levels. Using the FIR approach, two energy levels near each other are merged into a single lower level to monitor temperature. As the population of each energy level is proportional to the emission intensity of thermally coupled levels (TCLs), their temperature-dependent ratio is unaffected by the intensity of the source. A well-established theory of thermally coupled fluorescence states that thermally coupled levels emit fluorescence, with the population of these levels being directly proportional to the total population. On average, FIR techniques are more effective than lifetime-based approaches [48, 49].

1.4.1 Fluorescence Intensity Ratio

The fluorescence intensity ratio (FIR) technique utilizes two thermally coupled levels of rare-earth ions within the material. A crucial criterion for its effectiveness is that the energy separation between these adjacent levels must be sufficiently large (> 200 cm^{-1}) to prevent the overlap of two emissions. Simultaneously, it needs to be small enough (< 2000 cm^{-1}) to ensure the population of the upper level is within the temperature range of interest [50]. Trivalent rare earth ions are appealing for temperature sensing, given their abundant energy levels distributed across a broad wavelength range from ultraviolet to infrared [51, 52]. This thesis focuses on the electronic states of Er^{3+} ions, specifically the $^2H_{11/2}$ and $^4S_{3/2}$ states. These states are thermally linked, and their populations follow the Boltzmann distribution. In **Figure 1.12**, the intensity I_H is associated with the transition from $^2H_{11/2}$ to $^4I_{15/2}$, and the intensity I_S is related to the transition from $^4S_{3/2}$ to $^4I_{15/2}$ of two green emission bands. The FIR of the green emissions may be determined by neglecting the effects of self-absorption of emission and considering the thermalization of the population at the levels. This relationship is provided by Eq. (1.4) [53]:

$$FIR = \frac{I_H}{I_S} = \frac{N(^2H_{11/2})}{N(^4S_{3/2})} = \frac{A_H g_H \sigma_H \omega_H}{A_S g_S \sigma_S \omega_S} \exp\frac{-\Delta E}{K_B T} = C \exp\frac{-\Delta E}{K_B T} \quad (1.4)$$

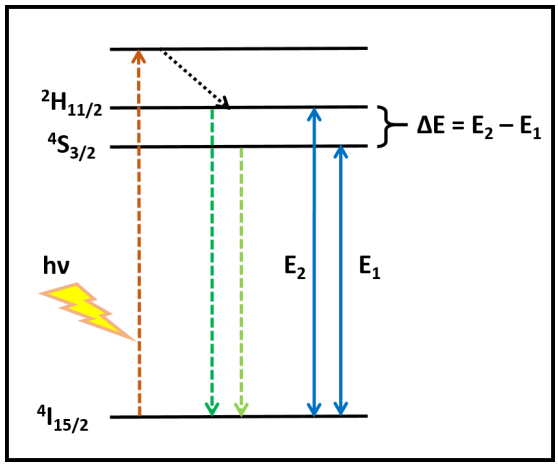

Figure 1.12: Diagrammatical illustration of optical temperature sensing of TCL of Er^{3+} ions.

where $N(^2H_{11/2})$ and $N(^4S_{3/2})$ are the population number of H and S levels, respectively. The σ values correspond to the detection system's response at the emission angular frequency ω, A is the impulsive radiative rate, g is TCL degeneracy, ΔE is the energy gap, K_B is the Boltzmann constant, T is the absolute temperature, and C is the exponential coefficient. To effectively measure temperature sensitivity (S_a) using the FIR method, it is crucial to comprehend the rate at which the fluorescence intensity ratio (I_H/I_S) varies in response to a certain temperature change (T) and is given by Eq. (1.5) [53]:

$$S_a = \frac{d(FIR)}{dT} = FIR\ \frac{\Delta E}{K_B T^2} = \ C\left(\frac{\Delta E}{K_B T^2}\right) \exp \frac{-\Delta E}{K_B T} \tag{1.5}$$

Collins et al. and Brites et al. propose that the calculation of relative sensitivity (S_r) is a more valuable method for comparing the effectiveness of various temperature sensors and is presented by Eq. (1.6) [53, 54]:

$$S_r = \frac{1}{FIR}\frac{d(FIR)}{dT} = \frac{\Delta E}{K_B T^2} \tag{1.6}$$

Eq. (1.6) states that the relative sensitivity is determined by the percentage change in FIR values resulting from a 1 K temperature shift. The sensitivity relies upon the variation in energy between the thermally connected levels. The accuracy of the calculated sensitivity becomes satisfactory if the theoretical energy gap (ΔE_{th}) roughly corresponds to the energy gap observed via experimentation (ΔE_{ex}). Error (δ) is a crucial metric used to assess the level of agreement between the ΔE_{th} and ΔE_{ex}. It is mathematically represented by Eq. (1.7):

$$\delta = \frac{|\Delta E_{th} - \Delta E_{ex}|}{\Delta E_{ex}} \times 100\% \tag{1.7}$$

The uncertainty in temperature measurement is the smallest temperature that can be measured. Baker et al. and Brite et al. proposed a method for estimating δT with δ_Δ/Δ as device precision (Eq. 1.8) [55, 56]:

$$\delta T = \frac{1}{S_r}\frac{\delta_\Delta}{\Delta} \quad (1.8)$$

The precision of every measurement is determined by its repeatability and reproducibility. A negligible difference in repeated measurements under the same circumstances indicates high repeatability. Using the same equipment and maintaining consistent geometrical dimensions of the sample, excitation source, and detector is advisable throughout the tests. The time allocated for sample temperature stabilization and data capture are crucial during calibration experiments. The repeatability can be expressed by Eq. (1.9) [55, 56]:

$$R = 1 - \max\frac{(\Delta_{Av} - \Delta_{Sp})}{\Delta_{Av}} \quad (1.9)$$

where Δ_{Av} is the mean value of FIR and Δ_{Sp} is the specific value of FIR at each temperature. A minimum of 10-20 consecutive cycles is required for statistical significance.

1.4.2 Factors Affecting FIR

The factors significantly influence the suitability of a material for temperature sensing:

i. Cost-effectiveness and availability of materials.

ii. The operational temperature range of the material and instrument should be comparable.

iii. ΔE should be more than 200 cm^{-1} to prevent overlap of TCLs and less than 2000 cm^{-1} to maintain the population of the upper level.

iv. Typically, detectors need fluorescence transitions between 6000 to 25000 cm^{-1}.

v. Radiative transitions should have a greater impact than non-radiative transitions.

vi. The excitation sources should be matched and miniaturized for seamless integration of the sensing material onto the optical fiber tip.

1.5 APPLICATIONS

Upconversion materials are used in bio-imaging applications, particularly for deep-tissue imaging. The ability to convert low-energy NIR light to higher-energy visible or ultraviolet light allows for enhanced penetration into biological tissues. In medicine, upconversion luminescence is employed for both imaging and therapeutic purposes. It can be used for imaging-guided drug delivery and therapy. Upconversion materials are explored to improve the efficiency of solar cells. By converting low-energy photons into higher-energy photons, they can harvest a broader spectrum of sunlight, increasing energy conversion efficiency. Upconversion materials find applications in security inks and anti-counterfeiting technologies. Their unique emission properties can be employed to create invisible or hard-to-replicate markings.

Upconversion materials are utilized in sensing applications like temperature sensing and environmental monitoring. The response of upconversion luminescence to changes in temperature or the presence of specific substances makes them valuable in sensor technologies. In medical applications, such as surgical therapy, non-contact temperature sensors can accurately measure ambient temperatures without direct contact with the patient. Additionally, in industrial settings, these sensors can remotely assess the temperatures of concealed objects in challenging environments, such as high-pressure nuclear power plants and coal fields. Upconversion materials are being explored for applications in data storage. The ability to switch between different luminescent states under different excitation conditions can be harnessed for data encoding. Upconversion materials are explored for potential applications in display technologies, including color display and light-emitting devices.

1.6 THESIS OBJECTIVES

The following are the key objectives of the thesis:

- To study the effect of the Er^{3+} ions in $BaBi_2Nb_2O_9$ ferroelectric ceramic on the upconversion luminescence, optical temperature sensing, and ferroelectric properties.
- To investigate the impact of Yb^{3+} ions on upconversion luminescence spectra and optical temperature sensing properties in optimized Er^{3+} doped $BaBi_2Nb_2O_9$ ferroelectric ceramic.
- To discuss the dielectric, ferroelectric, and energy storage properties of Er^{3+}/Yb^{3+} co-doped $BaBi_2Nb_2O_9$ ferroelectric ceramic.
- To explore the effect of W^{6+} ions in $Er^{3+}/Yb^{3+}/W^{6+}$ tri-doped $BaBi_2Nb_2O_9$ ferroelectric ceramic on upconversion luminescence, temperature sensing, and ferroelectric performance.
- To examine the energy storage density, recoverable energy storage density, and efficiency of undoped, Er^{3+} doped, Er^{3+}/Yb^{3+} co-doped, and $Er^{3+}/Yb^{3+}/W^{6+}$ tri-doped $BaBi_2Nb_2O_9$ ferroelectric ceramic.

1.7 THESIS ORGANIZATION

Chapter 1 thoroughly examines several forms of photoluminescence and their classifications. The significance of choosing $BaBi_2Nb_2O_9$ ferroelectric materials as a host material is being addressed. The energy storage characteristics of ferroelectric material are examined in detail. This chapter emphasizes the significance of rare earth ions in upconversion luminescence. A brief discussion is given on the applications of upconversion luminescent materials in several domains. Furthermore, this chapter offers concise information on the thesis's objectives and briefly details the thesis layout.

Chapter 2 outlines the synthesis process and various characterization techniques in detail. The solid-state method is used to synthesize the $BaBi_2Nb_2O_9$ ceramic. Furthermore, the characterization procedures that are employed to analyze the synthesized ceramic are detailed in this chapter. The structural analysis is studied using X-ray diffraction (XRD), scanning electron microscopy (SEM), Fourier transform infrared spectroscopy (FTIR), and Raman spectroscopy. The photoluminescence properties are discussed using upconversion luminescence (UCL) spectra, pump power analysis, and time-resolved fluorescence spectroscopy. The fluorescence intensity ratio (FIR) technique studies the temperature-dependent UCL spectra. The ferroelectric properties are explored by polarization vs electric field (PE) loops. The temperature-dependent dielectric studies reveal the dielectric constants of prepared ceramics. The strategies mentioned above are thoroughly explained in this chapter.

Chapter 3 investigates the synthesis and characterization of Er^{3+} doped $BaBi_{2-x}Er_xNb_2O_9$ ceramic composition. The structural analysis of $BaBi_2Nb_2O_9$ ceramic is performed by X-ray diffraction and Raman spectroscopy. PE hysteresis loops have measured ferroelectric properties at room temperature. The UCL spectra and time-resolved photoluminescence were obtained under the excitation of 980 nm. The FIR technique is used to study the temperature sensing behavior of optimized Er^{3+} doped $BaBi_2Nb_2O_9$ ferroelectric ceramic.

Chapter 4 discusses the preparation of Er^{3+}/Yb^{3+} co-doped $BaBi_2Nb_2O_9$ ceramic by keeping the Er^{3+} content constant at optimized value and varying the Yb^{3+} concentration. The XRD and SEM studies comprehensively describe the pure perovskite phase formation and the dense microstructure. This chapter focuses on the UCL properties of Er^{3+}/Yb^{3+} co-doped $BaBi_2Nb_2O_9$ ceramic. The pump power variation on UCL spectra gives information

about the number of photons involved in the UC process. The time decay analysis is conducted for all the Er^{3+}/Yb^{3+} co-doped $BaBi_2Nb_2O_9$ under the stimulation of 980 nm wavelength. Furthermore, the effect of tuning Yb^{3+} concentration in optical temperature sensing is addressed in this chapter.

Chapter 5 addresses the structural, dielectric, ferroelectric, and energy storage properties of undoped, Er^{3+} doped, and Er^{3+}/Yb^{3+} co-doped $BaBi_2Nb_2O_9$ ceramic. FTIR and Raman spectra provide information about the various vibrational modes of $BaBi_2Nb_2O_9$ ceramic. FTIR and Raman spectra provide insights into the many vibrational modes shown by $BaBi_2Nb_2O_9$ ceramic. An in-depth analysis is provided on the shifts of FTIR and Raman bands caused by dopant ions. The temperature-dependent dielectric studies are performed at various frequencies (1 kHz to 1 MHz). The ferroelectric properties are explored by polarization versus electric fields (PE) loops at various applied electric fields. The energy storage performance of undoped, Er^{3+} doped, and Er^{3+}/Yb^{3+} co-doped $BaBi_2Nb_2O_9$ ceramic is investigated using PE loops parameters. Additionally, the temperature-dependent energy storage parameters are also discussed in this chapter.

Chapter 6 focuses on the controlled variation of W^{6+} ions in $BaBi_2Nb_2O_9$ ceramic while maintaining Er^{3+} and Yb^{3+} ions at optimized levels. The objective is to investigate the influence of W^{6+} ions on the structural, UCL, sensing, and ferroelectric properties of the material. The chapter discusses the effects of different doping configurations, including undoped, singly Er^{3+} doped, Er^{3+}/Yb^{3+} co-doped, and $Er^{3+}/Yb^{3+}/W^{6+}$ tri-doped $BaBi_2Nb_2O_9$ ceramics, on their optical and electrical characteristics. XRD spectra analyze the structural changes induced by tri-doping in the host material. The UCL spectra are examined to determine the optimal W^{6+} content for enhanced luminescence efficiency. Time decay analysis is conducted for the green and red emission bands, corresponding to transitions

from $^2H_{11/2}$ to $^4I_{15/2}$ and $^4S_{3/2}$ to $^4I_{15/2}$ energy levels, respectively. Moreover, the optimized W^{6+} content is employed for optical temperature sensing in the 303 K to 623 K temperature range. The ferroelectric behavior of the ceramics is investigated using PE loops, while the energy storage performance is assessed through PE loop parameters.

Chapter 7 serves as a comprehensive summary of the research findings presented in this thesis. It highlights the outcomes of the analysis performed in each chapter. Additionally, the chapter delineates the future scope of this research, identifying potential avenues for further exploration and development.

1.8 REFERENCES

[1] F. Auzel, "Upconversion and anti-stokes processes with f and d ions in solids," *American Chemical Society*, vol. 104, pp. 139-174, 2004.

[2] N. Bloembergen, "Solid state infrared quantum counters," *Physical Review Letters*, vol. 2, no. 3, pp. 84-85, 1959.

[3] F. Zhang, "General introduction to upconversion luminescence materials, in Photon upconversion nanomaterials," *NanoScience and Technology*, Springer, pp. 1-20, 2015.

[4] J. Zhou, Q. Liu, W. Feng, Y. Sun, and F. Li, "Upconversion luminescent materials: Advances and applications," *Chemical Reviews*, vol. 115, pp. 395-465, 2015.

[5] K. L. Reddy, R. Balaji, A. Kumar, and V. Krishnan, "Lanthanides doped near-infrared upconversion nanophosphors: Fundamental concepts, synthesis strategies and technological applications," *Small*, vol. 14, 1801304, 2018.

[6] E. Hong, L. Liu, L. Bai, C. Xia, L. Gao, L. Zhang, and B. Wang, "Control synthesis, subtle surface modification of rare-earth doped upconversion nanoparticles and their application in cancer diagnosis and treatment," *Materials Science and Engineering C*, vol. 105, 110097, 2019.

[7] H. Dong, L. D. Sun, and C. H. Yan, "Basic understanding of the lanthanides related upconversion emission," *Nanoscale*, vol. 5, pp. 5703-5714, 2013.

[8] J. S. Chivian, W. E. Case, and D. D. Eden, "The photon avalanche: A new phenomenon in Pr^{3+}-based infrared quantum counters," *Applied Physics Letters*, vol. 35, 124-125, 1979.

[9] M. F. Joubert, "Photon avalanche upconversion in rare earth laser materials," *Optical Materials*, vol. 11, pp. 181-203, 1999.

[10] R. Bokolia, O. P. Thakur, V. K. Rai, S. K. Sharma, and K. Sreenivas, "Electrical properties and light upconversion effects in $Bi_{3.79}Er_{0.03}Yb_{0.18}Ti_{3-x}W_xO_{12}$ ferroelectric ceramics," *Ceramics International*, vol. 42, no. 5, pp. 5718-5730, 2016.

[11] M. Varshney, S. Soni, A. Banwal, M. Narwan, M. Verma, and R. Bokolia, "Effect of Er^{3+} ion incorporation on the structural, photoluminescence, and ferroelectric properties of $K_{0.5}Na_{0.5}NbO_3$ ceramic for optoelectronic applications," *Applied Physics A*, vol. 130, no. 267, 2024.

[12] R. Sahu and P. Kumar, "Microstructural, dielectric and ferroelectric properties of $Sr_{0.8}Bi_{2.15}Ta_2O_9$ ceramics synthesized by microwave processing technique," *Phase Transitions*, vol. 93, no. 1, pp. 91-99, 2020.

[13] Y. Liu, M. Chen, T. Cao, Y. Sun, C. Li, Q. Liu, T. Yang, L. Yao, W. Feng, and F. Li, "A cyanine-modified nanosystem for in vivo upconversion luminescence bioimaging of methylmercury," *Journal of the American Chemical Society*, vol. 135, pp. 9869-9876, 2013.

[14] K. Zheng, Z. Liu, C. Lv, and W. Qin, "Temperature sensor based on the UV upconversion luminescence of Gd^{3+} in Yb^{3+}-Tm^{3+}-Gd^{3+} co-doped $NaLuF_4$ microcrystals," *Journal of Materials Chemistry C*, vol. 1, pp. 5502-5507, 2013.

[15] B. I. Lee, E. Lee, and S. H. Byeon, "Assembly of layered rare-earth hydroxide nanosheets and SiO_2 nanoparticles to fabricate multifunctional transparent films capable of combinatorial color generation," *Advanced Functional Materials*, vol. 22, pp. 3562-3569, 2012.

[16] M. X. Façanha, F. F. do Carmo, J. P. C. doNascimento, T. O. Sales, W. Q. Santos, A. S. Gouveia-Neto, C. J. da Silva, and A. S. B. Sombra, "A novel white-light emitting $BaBi_2Nb_2O_9$: $Li^+/Tm^{3+}/Er^{3+}/Yb^{3+}$ upconversion phosphor," *Journal of Luminescence*, vol. 204, pp. 539-547, 2018.

[17] T. Wei, C. Z. Zhao, Q. J. Zhou, Z. P. Li, Y. Q. Wang, and L. S. Zhang, "Bright green upconversion emission and enhanced ferroelectric polarization in $Sr_{1-1.5x}Er_xBi_2Nb_2O_9$," *Optical Materials*, vol. 36, pp. 1209-1212, 2014.

[18] A. Banwal and R. Bokolia, "Phase evolution and microstructure of $BaBi_2Nb_2O_9$ ferroelectric ceramics," *Materials Today: Proceedings*, vol. 46, part 20, pp. 10121-10124, 2021.

[19] Z. Chen, L. Sheng, X. Li, P. Zheng, W. F. Bai, L. Li, F. Wen, W. Wu, L. Zheng, and J. Cui, "Enhanced piezoelectric properties and electrical resistivity in W/Cr co-doped $CaBi_2Nb_2O_9$ high-temperature piezoelectric ceramics," *Ceramics International*, vol. 45, no. 5, pp. 6004-6011, 2019.

[20] H. Zou, Y. Yu, J. Li, Q. Cao, X. Wang, and J. Hou, "Photoluminescence, enhanced ferroelectric, and dielectric properties of Pr^{3+}-doped $SrBi_2Nb_2O_9$ multifunctional ceramics," *Materials Research Bulletin*, vol. 69, pp. 112-115, 2015.

[21] X. Hui, D. Peng, H. Zou, J. Li, Q. Cao, Y. Li, X. Wang, and X. Yao, "A new multifunctional aurivillius oxide $Na_{0.5}Er_{0.5}Bi_4Ti_4O_{15}$: Up-conversion luminescent,

dielectric, and piezoelectric properties," *Ceramics International*, vol. 40, no. 8, part A, pp. 12477-12483, 2014.

[22] A. Banwal and R. Bokolia, "Effect of Er^{3+} ion doping on structural, ferroelectric and up/down conversion luminescence in $BaBi_2Nb_2O_9$ ceramic," *Materials Today: Proceedings*, vol. 47, part 14, pp. 4692-4695, 2021.

[23] Z. Peng, Q. Chen, Y. Chen, D. Xiao, and J. Zhu, "Microstructure and electrical properties in W/Nb co-doped aurivillius phase $Bi_4Ti_3O_{12}$ piezoelectric ceramics," *Materials Research Bulletin*, vol. 59, pp. 125-130, 2014.

[24] S. Kojima, R. Imaizumi, S. Hamazaki, and M. Takashige, "Raman scattering study of bismuth layer-structure ferroelectrics," *Japanese Journal of Applied Physics*, vol. 33, no. 9, pp. 5559-5564, 1994.

[25] J. D. Bobić, M. M. V. Petrović, and B. D. Stojanović, "Aurivillius $BaBi_4Ti_4O_{15}$ based compounds: Structure, synthesis and properties," *Processing and Application of Ceramics*, vol. 7, no. 3, pp. 97-110, 2013.

[26] Z. Sun, Z. Wang, Y. Tian, G. Wang, W. Wang, M. Yang, X. Wang, F. Zhang, and Y. Pu, "Progress, outlook, and challenges in lead-free energy-storage ferroelectrics," *Advanced Electronic Materials*, vol. 6, 1900698, 2020.

[27] A. R. Jayakrishnan, J. P. B. Silva, K. Kamakshi, D. Dastan, V. Annapureddy, M. Pereira, and K. C. Sekhar, "Are lead-free relaxor ferroelectric materials the most promising candidates for energy storage capacitors?" *Progress in Materials Science*, vol. 132, 101046, 2023.

[28] H. Zhang, W. Tian, Q. Zhang, W. Ma, P. Fan, D. Salamon, S. Zhang, B. Nan, H. Tan, and Z. Ye, "Review on the development of lead-free ferroelectric energy-storage ceramics and multilayer capacitors," *Journal of Materials Chemistry C*, vol. 8, pp. 16648-16667, 2020.

[29] M. X. Façanha, J. P. C. do Nascimento, M. S. Silva, M. Filho, A. L. B. Marques, A. G. Pinheiro, and A. S. B. Sombra, "Up-conversion emission of Er^{3+}/Yb^{3+} co-doped $BaBi_2Nb_2O_9$ (BBN) phosphors," *Journal of Luminescence*, vol. 183, pp. 102-107, 2017.

[30] Z. Zhang, J. Li, L. Liu, J. Sun, J. Hao, and W. Li, "Upconversion luminescence and electrical properties of (K, Er) co-modified $Na_{0.5}Bi_{4.5}Ti_4O_{15}$ high-temperature piezoceramics," *Physica B: Condensed Matter*, vol. 580, 411920, 2020.

[31] T. Fu, X. Wang, H. Ye, Y. Le, and X. Yao, "Up-conversion luminescence and temperature sensing properties of $CaBi_4Ti_4O_{15}$: Tm^{3+}, Yb^{3+} Ceramics," *Journal of Electronic Materials*, vol. 49, pp. 5047-5052, 2020.

[32] A. Banwal and R. Bokolia, "Thermometric sensing performance in erbium modified $SrBi_{2-x}Nb_2Er_xO_9$ ferroelectric ceramic for optoelectronic devices," *Ceramics International*, vol. 48, part 23A, pp. 34405-34414, 2022.

[33] Y. Zhang, Y. Wei, A. Zhang, R. Chu, G. Li, C. Zhang, and Z. Xu, "High electrical properties and good upconversion luminescence in $SrBi_{1.94-x}Er_{0.06}Yb_xNb_2O_9$ lead-

free piezoelectric ceramics," *Journal of Alloys and Compounds*, vol. 923, 166432, 2022.

[34] J. Yao, X. Rao, P. Du, W. Li, X. Mao, and L. Luo, "The electric and optical properties of $Bi_4Ti_3O_{12}$-$Na_{0.5}Bi_{2.5}Nb_2O_9$: Sm composite ceramics," *Ceramics International*, vol. 48, pp. 37039-37048, 2022.

[35] F. Luo, J. Xing, Y. Qin, Y. Zhong, F. Shang, and G. Chen, "Up-conversion luminescence, temperature sensitive and energy storage performance of lead-free transparent Yb^{3+}/Er^{3+} co-doped $Ba_2NaNb_5O_{15}$ glass-ceramics," *Journal of Alloys and Compounds*, vol. 910, 164859, 2022.

[36] P. Li, Z. Zhang, Z. Xu, H. Sun, Q. Zhang, and X. Hao, "Photomodulated cryogenic temperature sensing through a photochromic reaction in $Na_{0.5}Bi_{2.5}Ta_2O_9$: Er/Yb multicolour upconversion," *Optics Express*, vol. 31, pp. 7047-7059, 2023.

[37] K. W. Krämer, D. Biner, G. Frei, H. U. Güdel, M. P. Hehlen, and S. R. Luthi, "Hexagonal sodium yttrium fluoride based green and blue emitting upconversion phosphors," *Chemistry of Materials*, vol. 16, pp. 1244-1251, 2004.

[38] A. Aebischer, M. Hostettler, J. Hauser, K. Krämer, T. Weber, H. U. Güdel, and H. B. Burgi, "Structural and spectroscopic characterization of active sites in a family of light-emitting sodium lanthanide tetrafluorides," *Angewandte Chemie*, vol. 118, 2802-2806, 2006.

[39] K. N. R. Taylor and M. I. Darby, "Physics of rare earth solids," *Chapman and Hall Ltd: England*, 1972.

[40] J. Rubio O., "Doubly valent rare-earth ions in halide crystals," *Journal of Physics and Chemistry of Solids*, vol. 52, pp. 101-174, 1991.

[41] P. S. Peijzel, A. Meijerink, R. T. Wegh, M. F. Reid, and G. W. Burdick, "A complete $4f^n$ energy level diagram for all trivalent lanthanide ions," *Journal of Solid State Chemistry*, vol. 178, pp. 448-453, 2005.

[42] C. K. Duan and M. F. Reid, "A simple model for f-d transitions of rare-earth ions in crystals," *Journal of Solid State Chemistry*, vol. 171, pp. 299-303, 2003.

[43] L. Ning, C. Duan, S. Xia, and M. F. Reid, "A model analysis of $4f^N$-$4f^{N-1}5d$ transitions of rare-earth ions in crystals," *Journal of Alloys and Compounds*, vol. 366, pp. 34-40, 2004.

[44] J. C. G. Bünzli and S. V. Eliseeva, "Basics of lanthanide photophysics," *Springer-Verlage: Berlin.*, pp. 1-45, 2010.

[45] G. Chen, H. Liu, H. Liang, G. Somesfalean, Z. Y. Bai, Y. Wang, K. Yang, X. Zhang, Y. Song, C. H. Wang, and Z. Zhang, "Upconversion emission enhancement in Yb^{3+}/Er^{3+}-codoped Y_2O_3 nanocrystals by tridoping with Li^+ ions," *Journal of Physical Chemistry A*, vol. 112, 12030, 2008.

[46] Y. Bai, Y. Wang, K. Yang, X. Zhang, Y. Song, and C. H. Wang, "Enhanced upconverted photoluminescence in Er^{3+} and Yb^{3+} co-doped ZnO nanocrystals with and without Li^+ ions," *Optics Communications*, vol. 281, pp. 5448-5452, 2008.

[47] Y. Bai, Y. Wang, K. Yang, X. Zhang, G. Peng, Y. Song, Z. Pan, and C. H. Wang, "The effect of Li on the spectrum of Er^{3+} in Li- and Er-codoped ZnO nanocrystals," *Journal of Physical Chemistry C*, vol. 112, no. 32, pp. 12259-12263, 2008.

[48] X. Wang, Q. Liu, Y. Bu, C. S. Liu, T. Liu, and X. Yan, "Optical temperature sensing of rare-earth ion doped phosphors," *RSC Advances*, vol. 5 pp. 86219-86236, 2015.

[49] Y. Zhao, X. Wang, Y. Zhang, Y. Li, and X. Yao, "Optical temperature sensing of up-conversion luminescent materials: Fundamentals and progress," *Journal of Alloys and Compounds*, vol. 817, 152691, 2020.

[50] S. A. Wade, S. F. Collins, and G. W. Baxter, "Fluorescence intensity ratio technique for optical fiber point temperature sensing," *Journal of Applied Physics*, vol. 94, pp. 4743-4756, 2003.

[51] H. Dong, L. D. Sun, and C. H. Yan, "Energy transfer in lanthanide upconversion studies for extended optical applications," *Chemical Society Reviews*, vol. 44, pp. 1608-1634, 2015.

[52] P. Du and J. S. Yu, "Effect of molybdenum on upconversion emission and temperature sensing properties in $Na_{0.5}Bi_{0.5}TiO_3$: Er/Yb ceramics," *Ceramics International*, vol. 41, pp. 6710-6714, 2015.

[53] S. F. Collins, G. W. Baxter, S. A. Wade, T. Sun, K. T. V. Grattan, Z. Y. Zhang, and A. W. Palmer, "Comparison of fluorescence-based temperature sensor schemes: Theoretical analysis and experimental validation," *Journal of Applied Physics*, vol. 84, pp. 4649-4654, 1998.

[54] C. D. S. Brites, P. P. Lima, N. J. O. Silva, A. Millan, V. S. Amaral, F. Palacio, and L. D. Carlos, "Thermometry at the nanoscale," *Nanoscale*, vol. 4, pp. 4799-4829, 2012.

[55] S. N. Baker, T. M. McCleskey, and G. A. Baker, "An ionic liquid-based optical thermometer," *Ionic Liquids IIIB: Fundamentals, Progress, Challenges, and Opportunities*, vol. 15, pp. 171-181, 2005.

[56] C. D. S. Brites, A. Millan, and L. D. Carlos, "Lanthanides in luminescent thermometry," *Handbook of the Physics and Chemistry of the Rare Earths*, vol. 49, pp. 339-427, 2016.

2

CHAPTER

Synthesis and Characterization Details

- *This chapter provides specific information on the synthesis of undoped and doped $BaBi_2Nb_2O_9$ ferroelectric ceramic compositions using the solid-state reaction method.*
- *The experimental methodologies used in the current thesis are outlined, and their operational principles and apparatus are concisely explained.*
- *This chapter also discusses many experimental approaches for analyzing the structure, microstructure, ferroelectric, and luminescence properties and measures associated with luminescence thermometry and ferroelectric properties.*

2.1 SYNTHESIS PROCESS

Most inorganic powder-based bulk ceramics are synthesized using the solid-state reaction process. The selection of this process is based on its ability to be replicated, its cost-effectiveness, and its capacity to easily generate a substantial amount of powder. The initial precursor materials are heated to high temperatures and undergo a simple chemical reaction. Under normal conditions, the reaction will not take place until the temperature of the reaction reaches a minimum of two-thirds of the melting point of the reactants, and this rate increases dramatically as the temperature rises [1]. To overcome the lattice energy and enable a cation or anion to penetrate another site for the solid-state reaction to continue, temperatures ranging from 500°C to 2000°C are necessary. The reaction might take a long time to complete, but it can be sped up by raising the temperature since the diffusion rate increases. Furthermore, reactions are often placed in solid form since solids are seldom heated to their melting point.

The preparation of $BaBi_2Nb_2O_9$ ceramic is carried out using a solid-state method. Raw high-purity powders purchased from Sigma Aldrich and Alfa Aesar were weighed in stoichiometric amounts and mixed in a mortar pestle with ethanol for 8 hours. The mixed raw powders were kept at a temperature of 950°C for 3 hours for calcination. The calcined powder samples were then given a circular disc shape of 10 mm diameter after rigorously mixing with 5 wt% polyvinyl alcohol (PVA). The circular discs were sintered in a high-temperature furnace at 1050°C in two steps, first with intermittent heat treatment at 500°C for 1 hour for removal of the PVA binder, and then the temperature was raised to 1050°C for a dwell time of 3 hours. The schematic description of the synthesis method is represented in **Figure 2.1.**

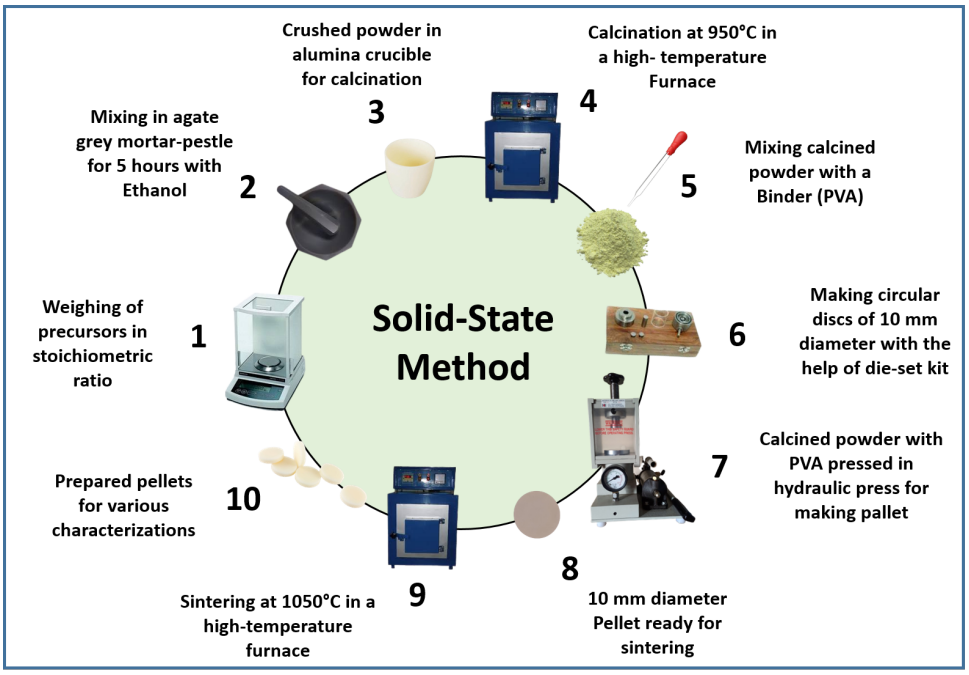

Figure 2.1: Steps involved in the synthesis of ceramic using solid-state method.

2.1.1 Selection of Raw Materials

The solid-state reaction technique generally employs inorganic oxides and carbonates as the primary raw ingredients for ceramic production. The selected raw materials comprise high-grade powders with excellent purity and low moisture content. Smaller particle sizes are recommended to increase reactivity and avoid agglomeration. Table 2.1 includes the initial raw materials for producing undoped and doped $BaBi_2Nb_2O_9$ compositions.

Table 2.1: Details of precursor powders used for preparing undoped and doped $BaBi_2Nb_2O_9$ ceramic.

Precursors	Brand	Purity (%)	Molecular Weight (g/mol)	Density (g/cc)
$BaCO_3$	Sigma Aldrich	99.00	197.34	4.29
Bi_2O_3	Alfa Aesar	99.00	465.96	8.90
Nb_2O_5	Sigma Aldrich	99.90	265.81	4.47
Er_2O_3	Alfa Aesar	99.99	382.56	8.64
Yb_2O_3	Sigma Aldrich	99.90	394.08	9.20
WO_6	Alfa Aesar	99.80	231.85	7.16

2.1.2 Calculations, Weighing, and Mixing of Precursor Powders

Eqs. (2.1 - 2.4) represent the synthesis reaction for undoped, Er^{3+} doped, Er^{3+}/Yb^{3+} doped, and $Er^{3+}/Yb^{3+}/W^{6+}$ doped $BaBi_2Nb_2O_9$ ferroelectric ceramic, respectively.

$$BaCO_3 + Bi_2O_3 + Nb_2O_5 \rightarrow BaBi_2Nb_2O_9 + CO_2 \uparrow \quad (2.1)$$

$$BaCO_3 + \frac{2-x}{2}Bi_2O_3 + Nb_2O_5 + \frac{x}{2}Er_2O_3 \rightarrow BaBi_{2-x}Nb_2Er_xO_9 + CO_2 \uparrow \quad (2.2)$$

$$BaCO_3 + \frac{2-x-y}{2}Bi_2O_3 + Nb_2O_5 + \frac{x}{2}Er_2O_3 + \frac{y}{2}Yb_2O_3 \rightarrow BaBi_{2-x-y}Nb_2Er_xYb_yO_9 + CO_2 \uparrow \quad (2.3)$$

$$BaCO_3 + \frac{2-x-y}{2}Bi_2O_3 + \frac{2-z}{2}Nb_2O_5 + \frac{x}{2}Er_2O_3 + \frac{y}{2}Yb_2O_3 + \frac{z}{2}WO_6 \rightarrow BaBi_{2-x-y}Nb_{2-z}Er_xYb_yW_zO_9 + CO_2 \uparrow \quad (2.4)$$

Table 2.2 describes elements present in the precursors to synthesize undoped and doped $BaBi_2Nb_2O_9$ ceramic compositions. The precursor powders were weighed in a stoichiometric amount using Eqs. (2.1 - 2.4). For example, the calculation for 10 g of Er^{3+}/Yb^{3+} co-doped $BaBi_{2-x-y}Nb_2Er_xYb_yO_9$ ceramic (x = 0.04 and y = 0.02) is demonstrated. The total mass of the product can be calculated by:

$$A_{Ba} + (2 - x - y)A_{Bi} + 2A_{Nb} + xA_{Er} + yA_{Yb} + 9A_O = \text{Mass of Product (g/mol)} \quad (2.5)$$

Table 2.2: Details of elements present in the precursors.

Element	Symbol	Atomic Number	Atomic Mass (g/mol)	Stable Oxidation State
Barium	Ba	56	137.327	+2
Bismuth	Bi	83	208.98	+3
Niobium	Nb	41	92.906	+5
Erbium	Er	68	167.259	+3
Ytterbium	Yb	70	173.04	+3
Tungsten	W	74	183.84	+6
Oxygen	O	8	15.999	-2

After substituting the values of the atomic mass of each element in Eq. (2.5) using Table 2.2, the mass of the product comes out to be 882.73 g/mol. Now, the molecular weight (MW) value obtained from Table 2.1 is used to calculate the mass of precursors in grams and is represented in Eqs. (2.6 - 2.10).

$$BaCO_3 = \left(\frac{\text{no. of mol} \times MW_{BaCO_3}}{\text{Mass of Product}}\right) \times 10\ \text{g} = \left(\frac{1 \times 197.34\left(\frac{\text{g}}{\text{mol}}\right)}{882.73\left(\frac{\text{g}}{\text{mol}}\right)}\right) \times 10\ \text{g} = 2.2356\ \text{g} \quad (2.6)$$

$$Bi_2O_3 = \left(\frac{\text{no. of mol} \times MW_{Bi_2O_3}}{\text{Mass of Product}}\right) \times 10\ \text{g} = \left(\frac{1.94 \times 465.96\left(\frac{\text{g}}{\text{mol}}\right)}{2 \times 882.73\left(\frac{\text{g}}{\text{mol}}\right)}\right) \times 10\ \text{g} = 5.1203\ \text{g} \quad (2.7)$$

$$Nb_2O_5 = \left(\frac{\text{no. of mol} \times MW_{Nb_2O_5}}{\text{Mass of Product}}\right) \times 10\ \text{g} = \left(\frac{1 \times 265.81\left(\frac{\text{g}}{\text{mol}}\right)}{882.73\left(\frac{\text{g}}{\text{mol}}\right)}\right) \times 10\ \text{g} = 3.0112\ \text{g} \quad (2.8)$$

$$Er_2O_3 = \left(\frac{\text{no. of mol} \times MW_{Er_2O_3}}{\text{Mass of Product}}\right) \times 10\ \text{g} = \left(\frac{0.04 \times 382.56\left(\frac{\text{g}}{\text{mol}}\right)}{2 \times 882.73\left(\frac{\text{g}}{\text{mol}}\right)}\right) \times 10\ \text{g} = 0.0866\ \text{g} \quad (2.9)$$

$$Yb_2O_3 = \left(\frac{\text{no. of mol} \times MW_{Yb_2O_3}}{\text{Mass of Product}}\right) \times 10\ \text{g} = \left(\frac{0.02 \times 394.08\left(\frac{\text{g}}{\text{mol}}\right)}{2 \times 882.73\left(\frac{\text{g}}{\text{mol}}\right)}\right) \times 10\ \text{g} = 0.0446\ \text{g} \quad (2.10)$$

In this manner, the calculations for all the compositions of $BaBi_2Nb_2O_9$ ceramic are carried out. After this, the precursors are weighed using the Shimadzu weighing balance. Then, the weighed powder is mixed in agate grey mortar-pestle for 8 hours with ethanol as solvent. During this phase, it is crucial to exercise caution to prevent contamination while crushing and mixing the agglomerates. Additionally, measures should be taken to minimize any spillage that might lead to the combined powder loss.

2.1.3 Calcination of Mixed Precursor Powder

Calcination is a chemical process in which a compound undergoes a reaction, creating either a partial or complete component phase. The uniformly mixed raw materials are subjected to high temperatures to commence the chemical reaction and eliminate any carbonates and sulphates. It can remove volatile substances, such as water or certain gases,

from a material. The production of the compound occurs when the components decompose and diffuse among the grains at temperatures lower than the melting points of the raw elements. After homogeneously mixing the raw powders, they are treated at 950°C for 3 hours for calcination. A high-temperature muffle furnace with a precision of ±1°C is used, as displayed in **Figure 2.2**.

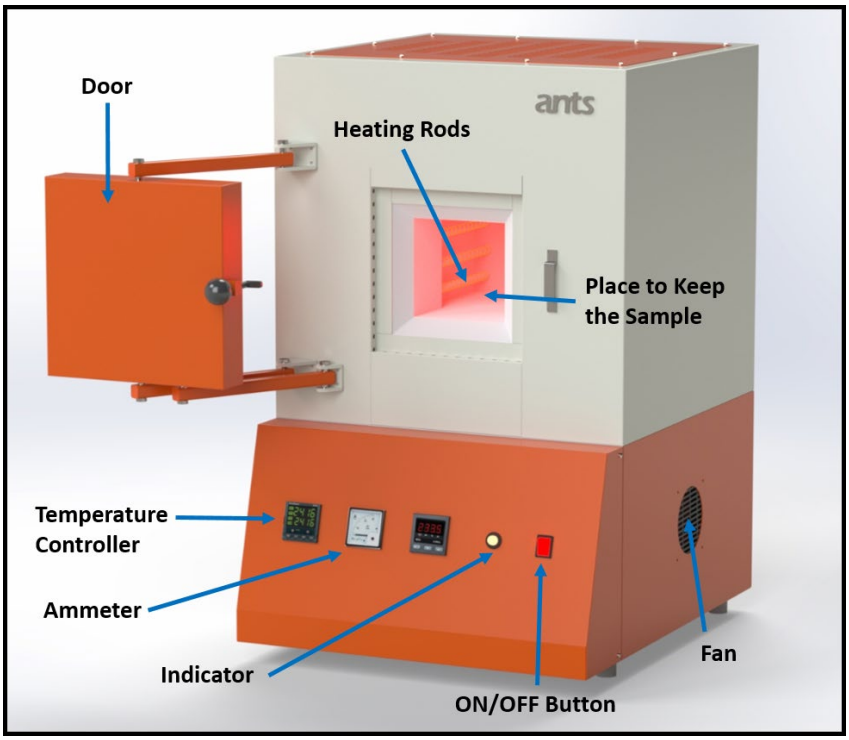

Figure 2.2: Temperature-controlled, high-temperature furnace for calcination of the prepared sample.

2.1.4 Formation of Pellets

The pellets of calcined powders are made by adding polyvinyl alcohol (PVA), which acts as a binder. The PVA is prepared by dissolving 5 g of PVA powder in 100 ml of distilled water. The distilled water is heated, and the PVA powder is gradually added. As the mixture is heated, it gradually reduces in volume, and when it reaches half of the original volume, the resulting solution becomes sticky. This indicates that the PVA has successfully dissolved in the water **Figure 2.3(a)**. The prepared PVA solution is added drop by drop to

calcined powder and thoroughly ground with calcined powder using a mortar and pestle. The powder gradually dries up during mixing, producing fine calcined powder. The fine powder is placed into a dieset to form a circular shape with a diameter of 10 mm and a thickness of 1 mm. Subsequently, the dieset is introduced into a manual hydraulic press, which undergoes compression under a pressure of 5 MPa, as shown in **Figure 2.3(b)**.

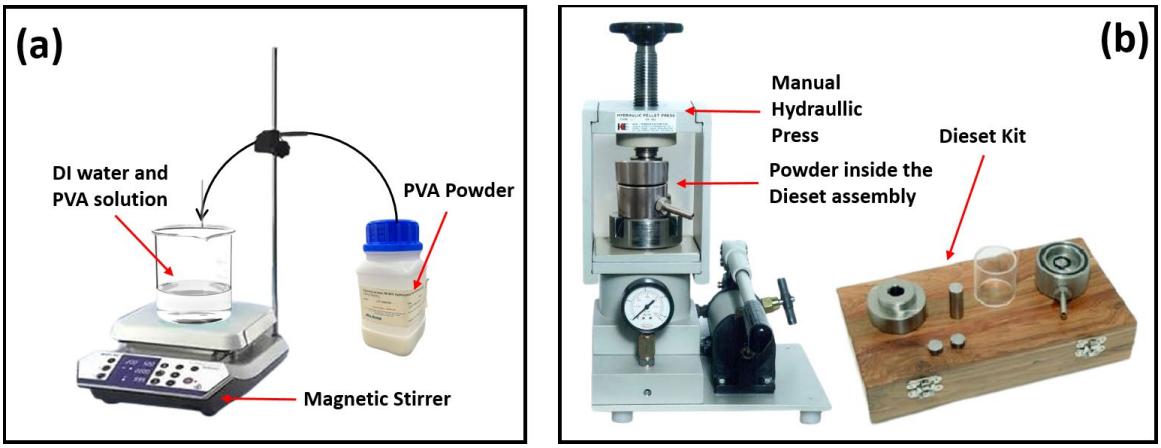

Figure 2.3: (a) Preparation of PVA in distilled water (b) Apparatus for pellet making.

2.1.5 Sintering

The sintering involves subjecting the powdered substance to high temperatures below its melting point but sufficiently enough to promote particle bonds. The heat applied during sintering encourages the particles to move and merge with adjacent particles. This movement and bonding process helps to minimize the total surface area of the particles. Since the particles seek a lower energy state, reducing the surface area reduces the overall energy associated with the system. This energy reduction is the driving force that promotes the formation of a denser ceramic structure during the sintering process. As the particles undergo sintering, the average size of the grains grows [2]. This growth is a key mechanism for minimizing the overall energy, as larger grains mean fewer grain boundaries and, consequently, a reduced surface area. The reduction in solid-gas interfaces is a

manifestation of this process, ultimately resulting in the creation of well-defined grains with clear boundaries during the sintering operation. Before sintering, the material has internal strains due to grinding and shaping. When sintering begins, the high temperature helps reduce these strains through atomic diffusion. As the temperature rises, atoms move more freely, increasing contact between grains. This enhanced contact, especially on the grain surfaces, allows atoms to pack closely together in all directions. This process, known as densification, leads to a more compact and solid ceramic structure. In simpler terms, sintering at higher temperatures helps align and pack atoms tightly, reducing internal strains and improving the density and properties of the material [3].

The prepared pellets are subjected to a two-step heat treatment process at 1050°C. In the initial step, the temperature is raised to 500°C and maintained for 1 hour to eliminate PVA. Following this, the temperature is further increased to 1050°C for an additional 2 hours to facilitate the sintering of the pellets. **Figure 2.4** provides a visual representation of this sequential process.

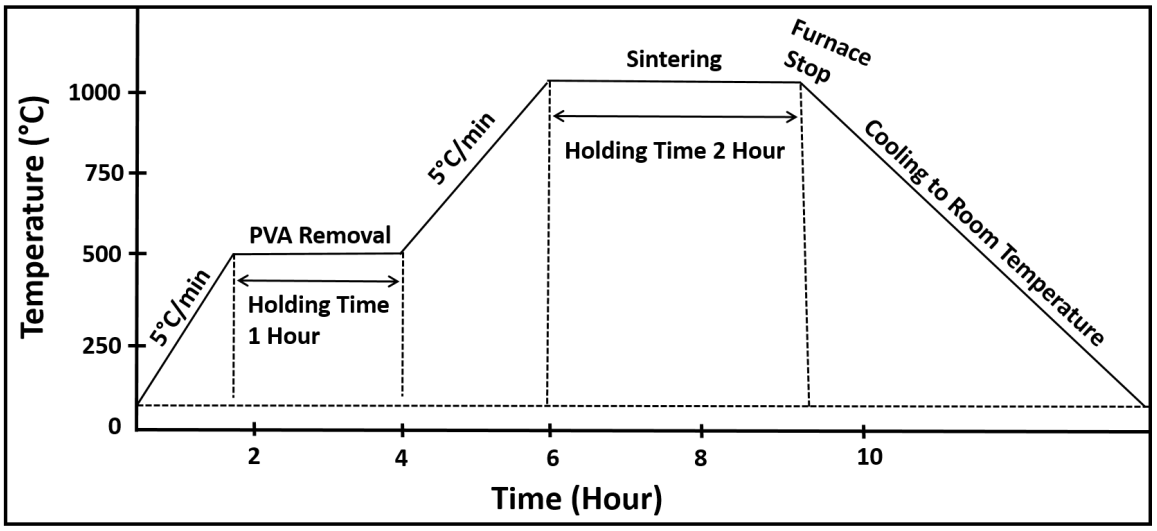

Figure 2.4: Two-step sintering process.

2.1.6 Density Measurements

The density and porosity of the material affect its electrical characteristics. The existence of crystal defects, such as vacancies, the method of solid-state solution generation, and the porosity of ceramic materials may be inferred from density measurements of samples. The lattice parameters from XRD spectra give the theoretical density (ρ_{th}) using Eq. (2.11) [4]:

$$\rho_{th} = \left(\frac{ZM}{NV}\right) g/cc \tag{2.11}$$

where Z = atomic number, M = molecular weight, N = Avogadro's number, and V = unit cell volume. The experimental density (ρ_{ex}) is evaluated using Shimadzu specific gravity measurement kit, as displayed in **Figure 2.5(a).** An overview of the procedure for ascertaining the density of synthesized ceramics is shown in **Figure 2.5(b)**. The ρ_{ex} is calculated by Archimedes' technique using Eq. (2.12):

$$\rho_{ex} = \left(\frac{m_1}{m_2 - m_3}\right) g/cc \tag{2.12}$$

where m_1 is the mass of the pellet, m_2 is the mass of the pellet suspended in air, and m_3 is the mass of the pellet immersed in distilled water. The porosity of the ceramic is calculated using Eq. (2.13):

$$P\ (\%) = \left(\frac{\rho_{th} - \rho_{ex}}{\rho_{th}}\right) \times 100 \tag{2.13}$$

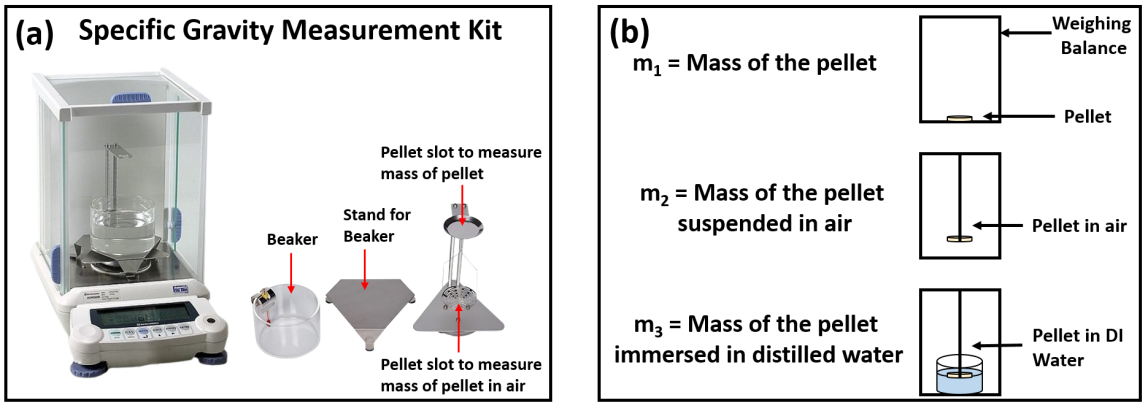

Figure 2.5: (a) Specific gravity kit for density measurement (b) Procedure for density measurement.

2.2 CHARACTERIZATION DETAILS

To investigate the physical properties and internal structure of materials using external methods in material science, characterization is a crucial part of the testing and analysis process. Various characterization methods were utilized to analyze the structural, electrical, and luminescent characteristics of the samples generated in this investigation, briefly discussed in the subsequent section.

2.2.1 X-ray Diffraction

X-ray diffraction (XRD) is a powerful analytical technique used to study the crystallographic structure of materials. It relies on the principle of X-ray diffraction, where X-rays are scattered by the periodic arrangement of atoms in a crystal lattice. This scattering pattern provides valuable information about the atomic arrangement, crystal orientation, and other structural characteristics of the material under investigation. The foundation of X-ray diffraction is Bragg's law, which describes the relation between the angles of incidence and the resulting constructive interference of X-rays scattered by crystal lattice planes, as depicted in **Figure 2.6(a)**. This law is expressed in Eq. (2.14) [5]:

$$2d \sin\theta = n\lambda \tag{2.14}$$

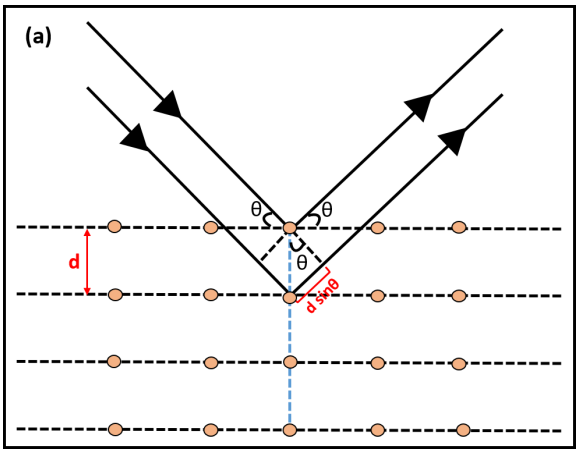

Figure 2.6: (a) Bragg's law reflection.

where d is the spacing between crystal lattice planes, θ is the angle of incidence, n is an integer representing the order of diffraction, and λ is the wavelength of the X-rays. **Figure 2.6(b)** shows the schematic diagram for generating X-rays in an X-ray tube consisting of anode and cathode. The X-rays are produced using a vacuum tube. The X-rays fall under the category of electromagnetic waves, and their wavelengths vary between 0.1 Å and 100 Å. Since all crystals are the same size, electromagnetic waves with wavelengths between half an inch and two and a half inches are used while diffracting from them. X-ray production involves accelerating electrons and directing them towards a target material. The tungsten filament releases high-energy electrons that rapidly move toward the anode with a strong accelerating force ranging from 30 kV to 60 kV. These highly energetic electrons dislodge electrons from the inner shell upon collision with copper metal. Consequently, electrons from the L and M shells transition to the K shell to occupy the unoccupied electron sites. The process produces CuKα and CuKβ radiations, which have wavelengths of 1.54 Å (from L to K) and 1.39 Å (from M to K) correspondingly. A nickel filter gets monochromatic radiation with a wavelength of 1.54 Å. This filter efficiently removes the CuKβ radiation, which has a 1.39 Å wavelength [6].

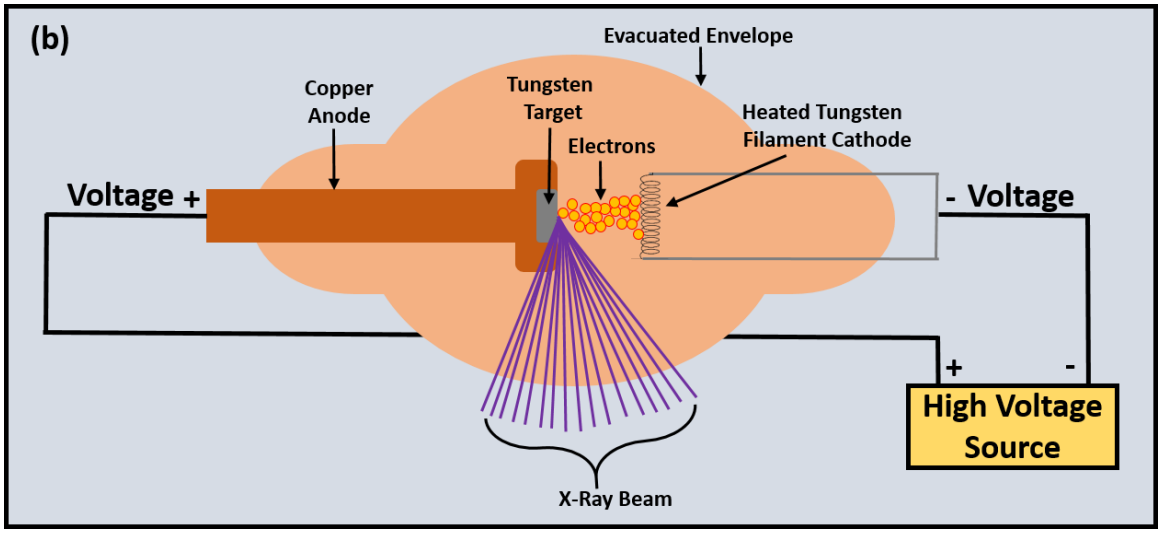

Figure 2.6: (b) Setup for the generation of X-rays.

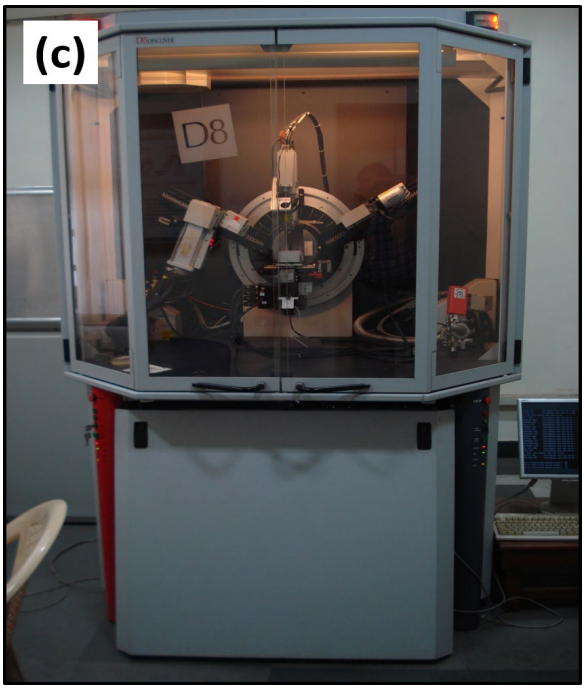

Figure 2.6: (c) Bruker D-8 advance X-ray diffractometer.

In the present study, the XRD analysis of all the undoped and doped $BaBi_2Nb_2O_9$ ceramics is performed using a Bruker D-8 Advance diffractometer with CuKα radiation (λ = 1.5405 Å). The XRD measurements were conducted within the 10° to 70° angular range, with a step size of 0.02°. This facility is available in the Department of Applied Physics, Delhi Technological University, New Delhi, India, as shown in **Figure 2.6(c)**.

2.2.1.1 Rietveld Refinement

Rietveld refinement is a powerful method in X-ray and neutron diffraction analysis for determining the crystal structure of a material with high precision. Named after its creator, Hugo Rietveld, this technique allows researchers to refine crystal structures by fitting calculated diffraction patterns to experimental data [7]. Rietveld refinement may be used to quantitatively analyze the structural modifications in the material caused by thermal treatment, doping, compression, and strain using the observed experimental data. This approach is a refining technique based on the least-square fitting principle for the whole

profile structure. The XRD data is subjected to a calculated profile fit and then compared to the empirically acquired data to determine the optimal alignment between the calculated and experimental patterns. The assessment of proper fitting is often determined by the weighted profile R-value (R_{wp}) given in Eq. (2.15):

$$R_{wp} = \left(\frac{\sum_i W_i\,[y_i(\text{observed}) - y_i(\text{calculated})]^2}{\sum_i W_i\,[y_i(\text{observed})]^2}\right)^{\frac{1}{2}} \tag{2.15}$$

where y_i is the intensity, and W_i is the weighted factor. R_{wp} should be lower during the refinement process. To get the most accurate fit, the value of R_{wp} should approach the expected profile R-value (R_{exp}) using Eq. (2.16):

$$R_{exp} = \left(\frac{(N - P)^2}{\sum_i^N W_i\,[y_i(\text{observed})]^2}\right)^{\frac{1}{2}} \tag{2.16}$$

where N is total observation, and P is total parameters. The goodness of fit (χ^2) is calculated by Eq. (2.17):

$$\chi^2 = \frac{R_{wp}}{R_{exp}} \tag{2.17}$$

$$R_{Bragg} = \frac{\sum_{hkl} |I_{hkl}\,(\text{observed}) - I_{hkl}\,(\text{calculated})|}{\sum_{hkl} |I_{hkl}\,(\text{observed})|} \tag{2.18}$$

Another important R factor is Bragg's factor (R_{Bragg}), defined in Eq. (2.18), where I_{hkl} is the intensity of spectra. A lower value of the R_{Bragg} indicates a more accurate match between the experimental and observed data. TOPAZ software is used for Rietveld refinement in which a comprehensive input file is created, including all relevant details about the instrument, including the computed model peak locations, peak intensities, and background information. The necessary parameters are given either fixed or refined throughout the refining process. Each output file generated throughout the refining process serves as the input file for the subsequent refinement step. The technique is iterated several times to get the most optimal refined values of structural parameters and R factors.

2.2.2 Scanning Electron Microscopy

Scanning electron microscopy (SEM) is a technique used to visualize the surface morphology and topography of a wide range of materials at high magnification. SEM provides detailed, three-dimensional images by scanning a focused beam of electrons across the sample surface and detecting the secondary electrons emitted from the sample. Electrons are primarily released from the cathode ray by thermionic emission, with an energy range of 0.1 - 30 keV. This emission may be achieved using thorium oxide-coated tungsten filaments, lanthanum hexa-boride (LaB_6), or a field emission gun (FEG). The electrons accelerate towards the condensing lens and then converge onto the specimen via the objective lens, forming a highly concentrated beam with a small focal spot size. A scanning coil is used to move the focused beam over the surface of the object. Upon the collision of the electron beam with the sample's surface, many signals of different kinds are produced. The signals mainly consist of secondary and backscattered electrons, which are used to recreate the surface shape of the examined material [8, 9]. The detector

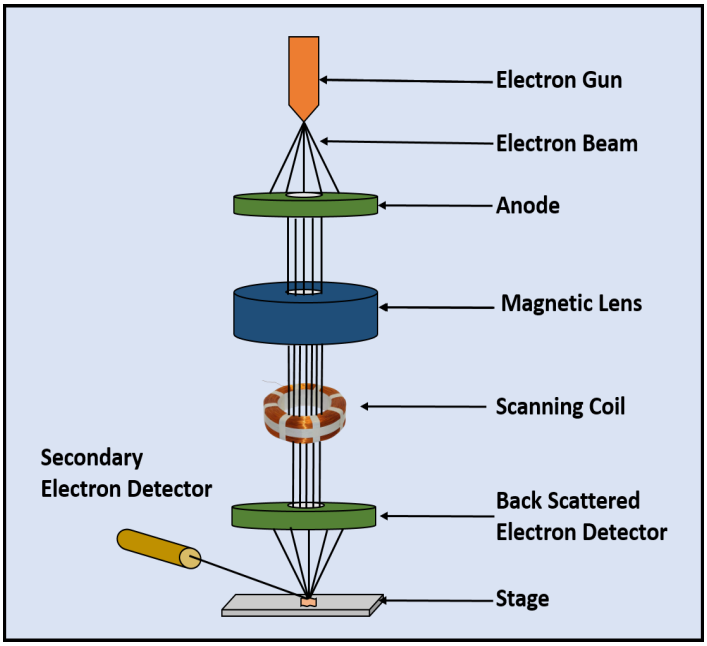

Figure 2.7: Schematic diagram of scanning electron microscope.

quantifies the produced electrons and transforms them into a two-dimensional representation by amplifying the signal. **Figure 2.7** displays a schematic representation of a SEM.

2.2.3 Fourier Transform Infrared Spectroscopy

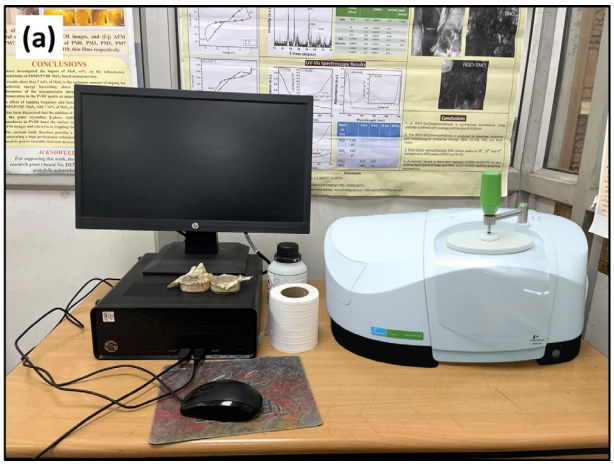

Figure 2.8: (a) FTIR setup facility present at CFMRL, Department of Applied Physics, Delhi Technological University, Delhi.

Fourier transform infrared spectroscopy (FTIR) may be used to examine the vibrational characteristics of functional groups in organic and semi-organic compounds [10]. The compounds are subjected to electromagnetic radiation in the 400 cm^{-1} to 4000 cm^{-1} range. The FTIR instrument used is available in the Department of Applied Physics, Delhi Technological University, from a brand named Elmer Perkins, as seen in **Figure 2.8(a)**. The vibrational energy levels of the molecules undergo alteration upon absorption of infrared light. The vibrations appear in two separate modes: stretching and bending. The assimilated energy enables modifications in various energy states. This approach is essential for detecting organic compounds with strong dipoles and polar chemical interactions, such as NH, OH, CH, etc [11, 12]. The FTIR spectroscopy method has several advantages, such as its superior scanning speed compared to various dispersive techniques

and its versatility in analyzing solids, liquids, and gases. This approach relies on the intermolecular linkages among the constituents of the sample. The molecular bonds are determined by the component atoms. When the sample is subjected to infrared (IR) light, its molecules absorb energy and transition to higher energy levels. Upon reverting to their original (de-excited) states, these molecules release radiation corresponding to the energy gap between the excited and de-excited states. The incoming light consists of several wavelengths, and each substance can absorb a certain infrared (IR) wavelength, contributing to its unique spectral signature [13]. Infrared spectroscopy is a technique used to detect and analyze molecules that exhibit specific vibrations or rotations at distinct frequencies, which correspond to various energy levels. The resonant frequencies are affected by several characteristics, including atomic masses, molecular potential energy surfaces, and vibronic coupling. Consequently, a correlation between different types of binding and vibration frequencies emerges. Diatomic molecules possess a solitary bond capable of stretching, whereas complex compounds have several bonds that may stretch and undergo conjugate vibrations. This interaction produces chemically related infrared absorption frequencies. IR spectroscopy is like a fingerprint because each functional group

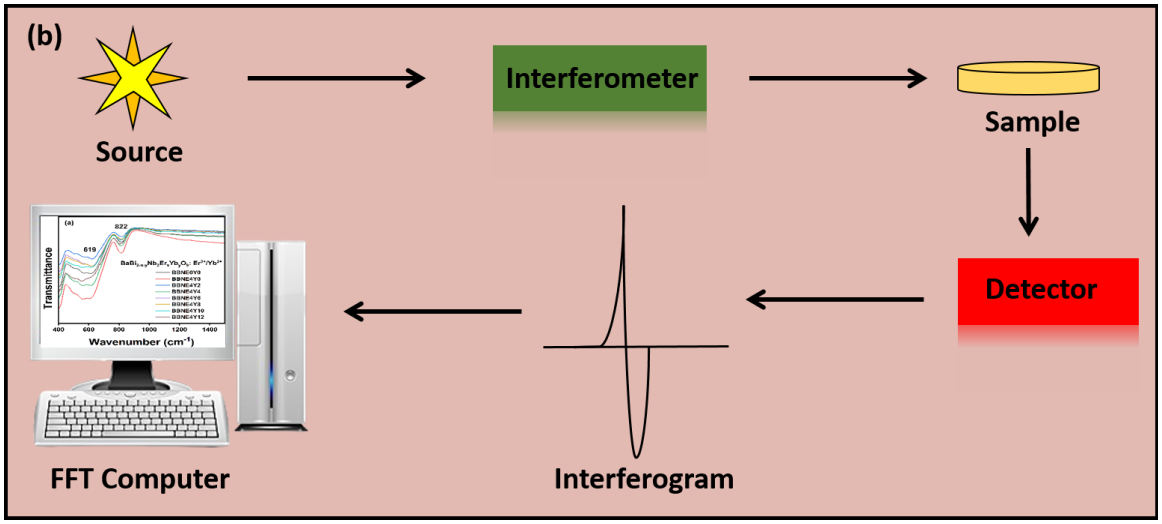

Figure 2.8: (b) Steps involved in FTIR spectroscopy.

has a unique vibrational energy. These absorbed wavelengths may be quantified using FTIR spectroscopy to identify and bind materials. The graph may display infrared light transmittance or absorption on the y-axis and wavenumber on the x-axis. The graph may have numerous peaks depending on the substance. Thorough analysis and comparison of these peaks with IR signatures for different materials and bonds help identify functional groups in the sample. **Figure 2.8(b)** is a schematic showing the several processes involved in FTIR spectroscopy. The interferometer setup involves directing the source's infrared radiation toward the beam splitter using a collimator. The beam splitter then divides the incoming beam into two distinct ones. The mirrors of the interferometer receive both beams; one of these mirrors is always in motion. Because of the route discrepancy that this motion creates, the incident beam's wavelengths are modulated at various frequencies. After passing through the mirrors, the rays merge to create an intricate interferogram.

2.2.4 Raman Spectroscopy

Raman spectroscopy is a highly precise and reliable method for determining phase purity and material composition based on vibrational, rotational, and low-frequency modes. In contrast to the elastic Rayleigh scattering, the Raman effect in solids occurs due to the medium's bond vibrations (phonons) interacting with the incoming light, leading to an inelastic scattering process. Raman scattering involves the creation of electron-hole pairs via electron-radiation interaction between the lattice and the incoming optical photon with a frequency ω_i and a wave vector k_i. A phonon is created or destroyed when an electron and a hole recombine via electron lattice contact. The energy of the dispersed light is reduced when phonons are formed and increased when they are destroyed. The wave vector conservation will be represented by Eq. (2.19) [14]:

$$\omega_i = \omega_s \pm \omega,\ k_i = k_s \pm k \quad (2.19)$$

where ω_s and k_s are the scattered photon frequency and energy. If $\omega_s < \omega_i$, then Stokes scattering occurs, whereas for anti-Stoke, $\omega_s > \omega_i$. The Raman spectrum is acquired by quantifying the difference in energy between the scattered light and the incoming laser light ($\omega_i - \omega_s$), known as the Raman shift. To investigate the Raman shifts, the sample is exposed to a laser beam source that emits light in the ultraviolet (UV), visible, or near-infrared range of wavelengths. The sample's molecular vibrations induce light scattering, which is then captured using a lens and filtered by a spectrophotometer to isolate the Raman signals. This is necessary since the strength of the Raman signal is lower than that of the Rayleigh signal. A detector is used to capture and interpret these emissions, as depicted in **Figure 2.9(a)**.

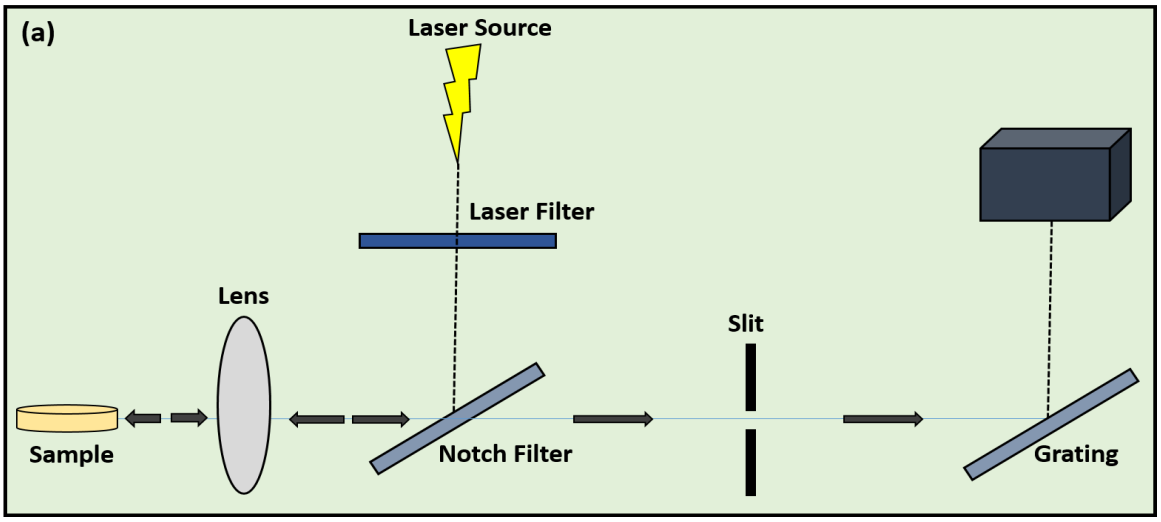

Figure 2.9: (a) Schematic showing Raman spectroscopy.

The current investigation included the acquisition of Raman spectra using a Renishaw Invia-type Raman microscope, which was accessible at the central facility (USIC) located at the University of Delhi, as seen in **Figure 2.9(b)**. The Renishaw Raman spectrometer is equipped with an argon ion laser with a wavelength of 785 nm. The laser had a spot size of 1 μm^2 and a power of 1.0 mW.

Figure 2.9: (b) Invia Raman spectrometer available at USIC, Delhi University, Delhi.

2.2.5 Upconversion Luminescence Spectroscopy

Upconversion luminescence refers to a process in which a material absorbs two or more lower-energy photons (typically in the infrared range) and emits a single higher-energy photon (usually in the visible or ultraviolet spectrum) [15]. A laser light source having a maximum power of 2 W under the wavelength of 980 nm is used to analyze the UCL emission spectra of Er^{3+}, Er^{3+}/Yb^{3+}, and $Er^{3+}/Yb^{3+}/W^{6+}$ doped $BaBi_2Nb_2O_9$ ceramics. A

Figure 2.10: (a) Upconversion luminescence spectroscopy using 980 nm laser present at USIC, Delhi University, Delhi.

monochromator from Acton, the SP2300, with a resolution of 1 nm and triple turret grating, was used to record the UC emission spectra, as shown in **Figure 2.10(a)**. The emission spectrum was recorded using a photomultiplier tube. **Figure 2.10(b)** shows a schematic of the methodical setup for capturing the UC emission spectra. The basic idea is that the light beam arrives at a converging lens after reflecting off a front-coated mirror and continuing along a route perpendicular to its original path. The sample is then focused by the laser beam, which is held at an adjustable height on a converging lens to reduce light dispersion caused by reflections in the mirror. The emitted light from the sample reaches the detector directly since the detector (PMT) is parallel to the sample. The necessary spectrum was captured once a computer received the PMT output.

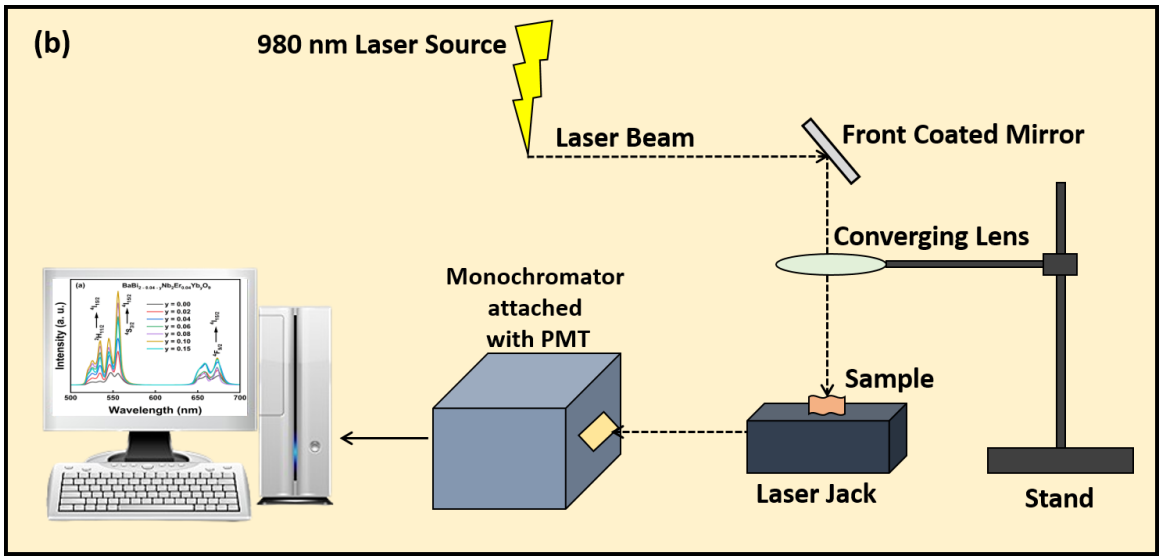

Figure 2.10: (b) Methodical setup for upconversion luminescence spectroscopy.

2.2.5.1 Time-Resolved Spectroscopy

Time-resolved spectroscopy is characterized by its ability to capture events that unfold in extremely short intervals, ranging from femtoseconds (10^{-15} seconds) to milliseconds (10^{-3} seconds) or longer [16]. The choice of technique depends on the timescale of the phenomenon under investigation. Pulsed or modulated stimulation is used to excite the

sample of interest in a typical time-resolved spectroscopy experiment, and the total luminescence evolution is tracked as a function of time after the pulse emission. The decay profiles may be captured by connecting the PMT's output channel to a digital storage oscilloscope (DSO). For various emission levels, the decay profiles provide vital information. The collected data is fitted using different exponential functions to determine the decay durations for various emission levels.

2.2.5.2 Optical Temperature Sensing

The study examines the sensing capability of the synthesized ceramics at different temperatures by analyzing the fluorescence intensity ratio (FIR) between two thermally linked energy levels of the rare earth ion incorporated into the host material. **Figure 2.10(c)** displays the setup for conducting temperature-dependent UCL measurements. The sensitivity (S) is determined by the FIR values of the thermally connected levels, as specified by the formula given in Eq. (2.20) [17]:

$$S = \frac{d(FIR)}{dT} \tag{2.20}$$

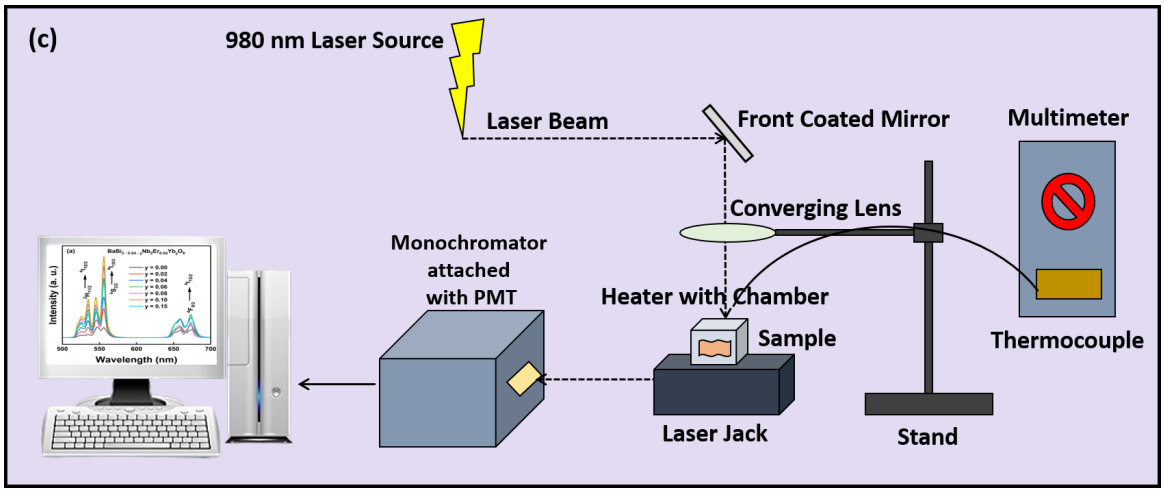

Figure 2.10: (c) Diagrammatic arrangement showing the steps for tracing temperature-dependent upconversion luminescence spectra.

2.2.6 Ferroelectric Measurements

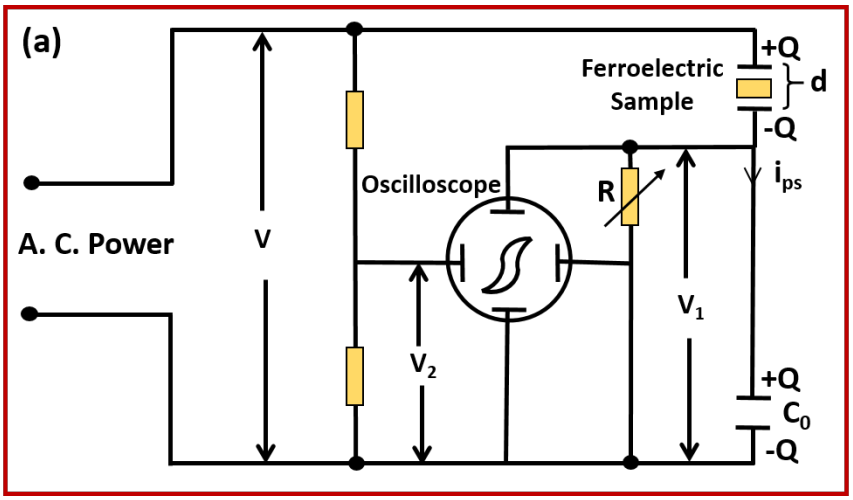

Figure 2.11: (a) Sawyer Tower circuit diagram.

A ferroelectric material has inherent electric polarization that may be altered or reoriented by introducing an electric field. The presence of hysteresis between the polarization and the applied field is regarded as a distinctive feature of ferroelectricity. If the dipoles inside the bulk material are originally randomly orientated, the observed polarization will be zero. However, the observed polarization increases when the electric field strength grows until all the dipoles are uniformly switched to the same state. At this point, the polarization becomes saturated and no longer depends on the strength of the electric field. Subsequently, as the electric field diminishes to zero, several dipoles persist in their altered condition, leading to residual polarization. Decreasing the field in the negative direction eventually reverses the dipoles, transitioning them from their initial position (either up or down) to the opposite state. The negative remnant polarization is the outcome of restoring the field to zero. The Sawyer Tower circuit is often used to test the P-E hysteresis loops, as demonstrated in **Figure 2.11(a)** [18].

A sine wave voltage applied between a ferroelectric sample and an integrating capacitor (C_0) is the standard procedure for measuring the P-E hysteresis loop. A big

integrating capacitance is necessary for the circuit. Thus, the polarization of the ferroelectric sample and the charge flow is proportional to the voltage across the integrating capacitor. This allows the C_0 to integrate the switching polarization current (i_{ps}) flowing through the sample. For each given sample, the voltage across the integrator capacitor will indicate the degree of polarization. Following the instructions in **Figure 2.11(a),** set the oscilloscope to x-y mode and connect the circuit to the X and Y inputs. C_0 is greater than C_F, and its value is selected so V_y can be measured precisely and with high precision. From the following relations, the values of the polarization and coercive fields can be computed using Eqs. (2.21) and (2.22):

$$P = \frac{C_0 V_y}{A} \tag{2.21}$$

$$E_c = \frac{V_x}{t} \tag{2.22}$$

where V_x and V_y are the voltages at the X and Y terminals of an oscilloscope, A is the area, and t is the thickness of the sample. The present study performed the ferroelectric measurement using a PE loop tracer by Marine India Pvt. Ltd., available at the Computational and Functional Material Research Lab (CFMRL) in the Department of Applied Physics, Delhi Technological University, as shown in **Figure 2.11(b)**.

Figure 2.11: (b) PE loop tracer from Marine India available at CFMRL, Department of Applied Physics, Delhi Technological University, Delhi.

2.2.7 Dielectric Measurements

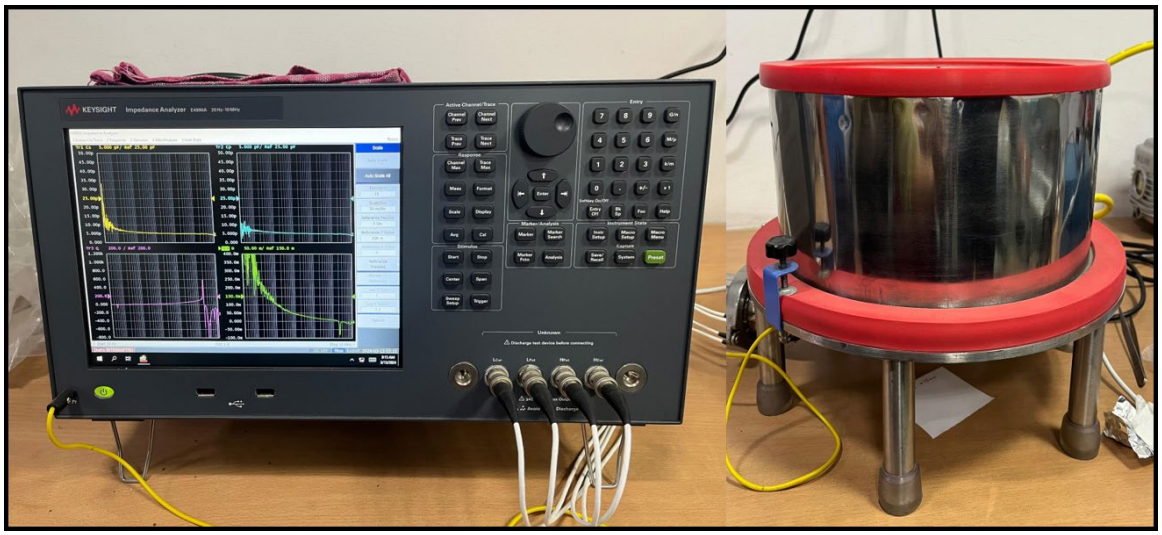

Figure 2.12: Impedance analyzer and furnace for dielectric measurements available at the Department of Applied Physics, Delhi Technological University, Delhi.

This method is used to evaluate variations in parameters like real and imaginary permittivity (ε' and ε'') and the loss factor (tanδ) with respect to changes in either frequency or temperature. The measurement is performed on sintered ceramic pellet electroded with silver paste on the parallel surface of the pellet. The distance between these electrodes is the thickness of the pellet (d). The geometric capacitance C_0 can be determined using the following Eq. (2.23):

$$C_0 = \frac{\varepsilon_0 A}{d} \tag{2.23}$$

where ε_0 is the permittivity of free space (8.854×10^{-12} F/m) and A is the area of electrodes. When a ceramic pellet is placed in the measuring cell, the capacitance of the capacitor increases by a factor ε' called the dielectric constant of the material. The formula for the modified capacitance (C) of a parallel plate capacitor with a dielectric material inserted between the plates is given in Eq. (2.24):

$$C = \frac{\varepsilon' \varepsilon_0 A}{d} = \varepsilon' C_0 \tag{2.24}$$

The measurements of the imaginary component of dielectric (ε") of the samples are performed using Eq. (2.25):

$$\varepsilon'' = \varepsilon' \tan\delta \quad (2.25)$$

In this thesis, the dielectric measurement was performed using Keysight Impedance Analyzer E4990A, as shown in **Figure 2.12**. The dielectric constant is measured under various temperatures ranging from 1 kHz to 1 MHz.

2.3 SUMMARY

The forthcoming chapters will utilize these diverse strategies to characterize and evaluate the results.

2.4 REFERENCES

[1] V. V. Gusarov, "Fast solid-phase chemical reactions," *Russian Journal of General Chemistry*, vol. 67, pp. 1846-1851, 1997.

[2] L. Lv, J. P. Zhou, Q. Liu, G. Zhu, X. Z. Chen, X. B. Bian, and P. Liu, "Grain size effect on the dielectric and magnetic properties of $NiFe_2O_4$ ceramics," *Physica E: Low-dimensional Systems and Nanostructures*, vol. 43, no. 10, pp. 1798-1803, 2011.

[3] H. Tanaka, A. Yamamoto, J. I. Shimoyama, H. Ogino, and K. Kishio, "Strongly connected *ex situ* MgB_2 polycrystalline bulks fabricated by solid-state self-sintering," *Superconductor Science and Technology*, vol. 25, 115022, 2012.

[4] B. D. Cullity and S. R. Stock, "Elements of X-ray diffraction," *Prentice Hall Inc*, New Jersey, 2001.

[5] D. S. Sivia, "Elementary scattering theory for X-ray and neutron users," *Oxford University Press*, pp. 7-10, 2011.

[6] C. Kittel, "Introduction to solid state physics," *John Wiley & Sons*, 2005

[7] H. M. Rietveld, "A profile refinement method for nuclear and magnetic structures," *Journal of Applied Crystallography*, vol. 2, pp. 65-71, 1969.

[8] K. Akhtar, S. A. Khan, S. B. Khan, and A. M. Asiri, "Scanning electron microscopy: Principle and applications in nanomaterials characterization," *Handbook of Materials Characterization*, pp. 113-145, 2018.

[9] J. I. Goldstein, D. E. Newbury, J. R. Michael, N. W. M. Ritchie, J. H. J. Scott, and D. C. Joy, "Scanning electron microscopy and X-ray microanalysis," *Springer*, New York, pp. 209-234, 2018.

[10] W. M. Doyle, "Principles and applications of Fourier transform infrared (FTIR) process analysis," *Process Control and Quality*, vol. 2, pp. 11-41, 1992.

[11] E. Knözinger, *Wiley Online Library*, 1986.

[12] G. C. Schatz, R. P. Van Duyne, J. M. Chalmers, P. R. Griffiths, "Handbook of vibrational spectroscopy," *New York: Wiley*, vol. 1, pp. 759, 2002.

[13] D. Titus, E. J. J. Samuel, and S. M. Roopan, "Chapter 12 - Nanoparticle characterization techniques," *Green Synthesis, Characterization and Applications of Nanoparticles: Micro and Nano Technologies*, pp. 303-319, 2019.

[14] R. Bokolia, "Upconversion luminescence and temperature sensing of $Er^{3+}/Yb^{3+}/W^{6+}$ doped $Bi_4Ti_3O_{12}$ ferroelectric ceramics," *Department of Physics and Astrophysics,* University of Delhi, India, 2017.

[15] G. Blasse and B. C. Grabmaier, "A general introduction to luminescent materials," *Luminescent Materials*, Springer Verlag, Berlin, HeidelBerg, 1994.

[16] F. Auzel, "Upconversion and anti-stokes processes with f and d ions in solids," *Chemical Reviews*, vol. 104, pp. 139-174, 2004.

[17] A. Banwal and R. Bokolia, "Efficient tunable temperature sensitivity in thermally coupled levels of Er^{3+}/Yb^{3+} co-doped $BaBi_2Nb_2O_9$ ferroelectric ceramic," *Journal of Luminescence*, vol. 263, 120071, 2023.

[18] N. Perera, G. Kampitsis, R. V. Erp, J. Ancay, A. Jafari, M. S. Nikoo, and E. Matioli, "Analysis of large-signal output capacitance of transistors using Sawyer - Tower circuit," *IEEE Journal of Emerging and Selected Topics in Power Electronics*, vol. 19, no. 5, pp. 448-456, 2008.

3

CHAPTER

Upconversion Luminescence and Optical Temperature Sensing Properties of Er^{3+} Doped $BaBi_2Nb_2O_9$ Ferroelectric Ceramic

- *This chapter discusses the structural, optical, ferroelectrical, and sensing analysis of a series of $BaBi_{2-x}Nb_2Er_xO_9$ ceramic compositions with different Er^{3+} concentrations (x = 0-8 mol %) by a conventional solid-state reaction method.*
- *The upconversion (UC) light emission under 980 nm excitation with different pump powers and luminescence-based temperature sensing ability of $BaBi_{2-x}Nb_2Er_xO_9$ composition have been examined.*
- *For an optimum content of x = 0.04, two strong UC green emission bands were observed at 549 nm via $^4S_{3/2} \rightarrow {}^4I_{15/2}$ transition and 527 nm via $^2H_{11/2} \rightarrow {}^4I_{15/2}$ transitions, and a weak red emission appears at 657 nm attributed to the $^4F_{9/2} \rightarrow {}^4I_{15/2}$ transition.*
- *The maximum value for remnant polarization and coercive field of doped $BaBi_{2-x}Nb_2Er_xO_9$ ceramic for (x = 0.08) Er^{3+} concentration comes out to be 2.9524 $\mu C/cm^2$ and 49.8980 kV/cm.*
- *Temperature sensing evaluated by the change in the fluorescence intensity ratio (I_H/I_S) indicates the highest sensitivity to be 0.99% K^{-1} at 483 K for an optimum concentration of Er^{3+} at x = 0.04 in $BaBi_{2-x}Nb_2Er_xO_9$ composition and is useful for non-contact optical thermometry.*

3.1 INTRODUCTION

Trivalent rare-earth (RE^{3+}) ions doped with different host materials excited by cheap laser sources exhibit upconversion (UC) photoluminescence, which can change lower energy near-infrared radiation (NIR) into higher energy visible radiation [1-10]. Current research focuses on the fluorescence intensity ratio (FIR) technique as a non-contact probe for temperature sensing as it is insensitive to electromagnetic interference and spatial recording of temperature fluctuations at a sub-micron scale with high sensitivity and accuracy. For optical temperature sensing, a large number of oxide host materials have exhibited a reasonably high sensitivity over an extensive temperature range with decent thermal stability and a quick response speed. Recently, good linearity and high sensitivity (0.0139 K^{-1}) have been attained in Er^{3+}/Yb^{3+} co-doped $SrMoO_4$ ceramic composition [11]. Enhanced luminescence thermometry in Y_2O_3 is achieved by Lojpur et al. when co-doped with Er^{3+} and Yb^{3+} [1]. Similarly, $La_2Ti_2O_7$ ferroelectric ceramic doped with Er^{3+} exhibits increased temperature sensitivity for optical thermometry, and Li^{3+}/Er^{3+} doped $BaTiO_3$ ceramics indicates the possibility for non-contact localized probing of ferroelectric transition temperature [3, 12]. Furthermore, in $Sr_{2-x}SnO_4:Sm^{3+}$ multifunctional ceramic, thermoluminescence, photochromism reaction, photoluminescence, and photo-stimulated luminescence are testified for potential applications in optical storage technology and high-sensitivity optical switches [10].

From the last two decades, ferroelectric materials have been widely used as luminescent host materials with extensively wide applications in luminescent thermometry, biological imaging systems, white light-emitting diodes, solid-state lasers, infrared detectors, various medical diagnoses, etc. [13-16]. The ferroelectric materials meet the need

for good host material for luminescence, including decent thermal stability, significant radiative transition, lower values of leakage current, and high sensitivity over an extensive temperature range [17-19]. In the group of ferroelectrics, bismuth layered structure ferroelectric (BLSF) are better candidates for upconversion luminescence as they are lead-free ferroelectric materials, which make them more advantageous due to their non-toxicity [20, 21] and also minimize the degradation of P-E hysteresis characteristics associated with lead base ferroelectrics because BLSFs show good fatigue endurance even after 10^{11} - 10^{12} cycles [22-25]. Their environmental and health concerns and multiple properties, such as pyroelectric, piezoelectric, and integrated electro-optic behavior combined with functional luminescence properties, make them smart materials.

Recent literature has found that doping ferroelectric materials with suitable dopants enhance and improve their multifunctional properties [26-29]. The PL properties of the ferroelectric materials doped with RE^{3+} ions are intently due to the crystal field revealed by the phase structure (crystal symmetry) and point defects in the lattice. The ferroelectric has an ABO_3 structure with vacancies that frequently affect the ferroelectric and luminescence properties [30]. Er^{3+} and Yb^{3+} were established to be the most effective dopants for improving ferroelectric, piezoelectric, and upconversion emission [31, 32]. For instance, Bokolia et al. revealed enhancement in the dielectric, ferroelectric, and PL properties of $Bi_3Ti_4O_{12}$ when doped with Er^{3+} [13]. Bayart et al. investigated $LaTiO_7$ doped with Er^{3+} for temperature sensing applications [3], $NaBi_4Ti_4O_{15}$ doped with Er^{3+} showed improved dielectric, luminescent, and piezoelectric properties in Hui et al. study [33]. Recently, Li et al. developed a new Er^{3+} doped $Na_{0.5}Bi_{0.5}TiO_3{-}xK_{0.5}Na_{0.5}NbO_3$ photochromic (PC) ceramic and investigated PC reaction and tunable luminescence contrast with electric poling field and related with the ergodicity of ceramics [8].

In recent years, barium bismuth niobium oxide (BBN), which is a relaxor ferroelectric (RF) and member of BLSF, has fascinated researchers due to its possible uses in high-temperature piezo sensor devices and non-volatile random access memory (NVRAM). BBN is also a good host for UC because it is chemically and thermally stable, has lower phonon energy (860 cm^{-1}), and allows modifications in its crystal structure with additional dopants [4]. Being an aurivillius family member, the BLSFs have the established formula $(A_{m-1}B_mO_{3m+1})^{2-}(Bi_2O_2)^{2+}$, where m denotes the number of octahedral layers present in perovskites block $(A_{m-1}B_mO_{3m+1})^{2-}$ piled between rigid $(Bi_2O_2)^{2+}$ layers. A symbolizes trivalent, divalent, monovalent cations or a combination like Bi^{3+}, Na^{+}, Pb^{2+}, Ba^{2+}, etc., while B indicates hexavalent, pentavalent, or tetravalent ions such as W^{6+}, Ta^{5+}, Nb^{5+}, Ti^{4+} [4, 6, 34-36]. Some of the BLSF examples with different values of m are (i) Bi_2WO_6 (m = 1) [33], (ii) $BaBi_2Nb_2O_9$ (m = 2) [4, 22, 25, 37], (iii) $Bi_4Ti_3O_{12}$ (m = 3) [2, 14], (iv) $BaBi_4Ti_4O_{15}$ (m = 4) [38, 39] etc. Studies on strong upconversion luminescence in Er^{3+}/Yb^{3+} doped $BaBi_2Nb_2O_9$ powders are reported by Façanha et al. [4]. Recently, novel white light emission has been reported by modulating Li^{+} and Tm^{3+} ions content in $BaBi_2Nb_2O_9$: $Li^{+}/Tm^{3+}/Yb^{3+}/Er^{3+}$ phosphors for its possible use in solid-state lighting technology [7]. Moreover, recent developments on strong upconversion luminescence, good thermal and chemical durability, lower phonon energy, and tuning of the optical properties reported in BBN host material motivate us to examine the usefulness of Er^{3+} doped $BaBi_2Nb_2O_9$ ceramics for thermometric application and understand its influence on structural and electrical properties.

Hence, in this chapter, Er^{3+} is chosen as a dopant because it is the most useful dopant for upconversion emission, and in addition to this, its metastable energy levels ($^4I_{9/2}$ and $^4I_{11/2}$) can be easily occupied by using cheap and low power laser operating at 980 nm [40,

41]. $BaBi_{2-x}Nb_2Er_xO_9$ is systematically doped with Er^{3+} ions, and the effect of substituting smaller Er^{3+} ions for Bi^{3+} ions has been investigated using X-ray diffraction (XRD) and Raman spectroscopy. A substantial enhancement in the UC emission is seen for an optimum Er^{3+} concentration, and the effect of increasing Er^{3+} substitution on electrical and ferroelectric properties has been explored. The FIR technique has been utilized for exploring the thermally coupled electronic states ($^2H_{11/2}$ and $^4S_{3/2}$) of Er^{3+} ions, and the usefulness of the optimized configuration for temperature sensing is investigated over a wide temperature range (300-623 K).

3.2 SYNTHESIS AND CHARACTERIZATION DETAILS

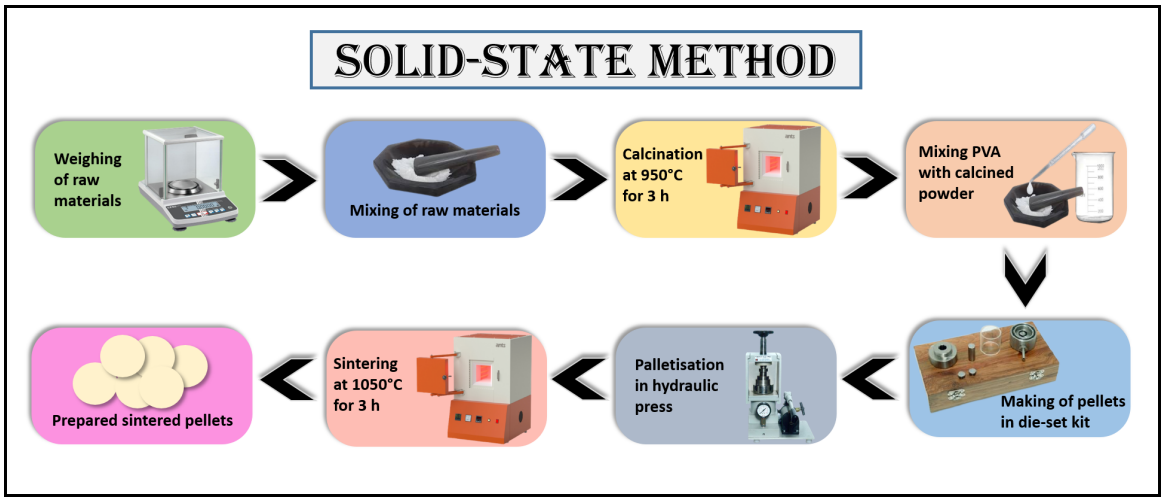

Figure 3.1: Schematic representation of the synthesis process (solid-state method).

The ceramic composition $BaBi_{2-x}Er_xNb_2O_9$ with different concentrations of Er^{3+} as x = 0.00, 0.02, 0.04, 0.06, 0.08 is processed by conventional solid-state reaction method. The schematic representation of the synthesis process is given in **Figure 3.1**. Raw high-purity powders were purchased from Sigma Aldrich, i.e., Nb_2O_5, $BaCO_3$, Bi_2O_3, and Er_2O_3, weighed in stoichiometric amounts, and mixed in a mortar pestle with ethanol for 8 hours. The mixed raw powders were kept at a temperature of 950°C for 3 hours for calcination.

The calcined powder samples were then given a circular disc shape of 10 mm diameter after rigorously mixing with 5 wt% polyvinyl alcohol (PVA). The circular discs were sintered in a high-temperature furnace at 1050℃ in two steps, first with intermittent heat treatment at 500℃ for 1 hour for removal of the PVA binder, and then the temperature was raised to 1050℃ for a dwell time of 3 hours. Eq. (3.1) and Eq. (3.2) represent the synthesis reaction for [22]:

Undoped BBN –

$$BaCO_3 + Bi_2O_3 + Nb_2O_5 \rightarrow BaBi_2Nb_2O_9 + CO_2 \uparrow \quad (3.1)$$

Er^{3+} doped BBN –

$$BaCO_3 + \frac{2-x}{2}Bi_2O_3 + Nb_2O_5 + \frac{x}{2}Er_2O_3 \rightarrow BaBi_{2-x}Nb_2Er_xO_9 + CO_2 \uparrow \quad (3.2)$$

The phase formation of synthesized samples was analyzed using XRD spectra collected using Bruker D-8 advance X-ray diffractometer with Cu-Kα radiation in the 2θ range 10° to 80°. The sintered pellet density is calculated using Archimedes' Principle. Using the Invia Raman spectrometer model having an argon-ion laser, Raman spectra were recorded at 785 nm. The prepared pellets were electroded by applying the silver paste on the faces of pellets and were baked in the furnace for 10 minutes at 500℃ so that the silver paste sticks entirely to the pellets. The Marine India Electricals Ltd. automated loop tracer is used to measure the P-E hysteresis loop on an electroded ceramic surface at 50 Hz frequency. The UCL spectra were recorded using HORIBA PTI Quanta-master (8450-11) under 980 nm excitation wavelength. For lifetime decay measurement, the pulsed laser was operated in modulation mode at its maximum power capability of $2W/cm^2$ for 30 min. A manually constructed heater equipped with a thermocouple, multiplier, and variable-voltage control were utilized to conduct the sensing, resolution, and stability analyses.

3.3 RESULTS AND DISCUSSION

3.3.1 Structural Analysis

The X-ray diffraction (XRD) spectra of ceramic composition $BaBi_{2-x}Er_xNb_2O_9$ with different Er^{3+} concentrations (x = 0-8 mol %) sintered at 1050°C for 3 hours are displayed in **Figure 3.2(a)**. The observed XRD peaks depict good accord, as reported in the JCPDF file no. 00-012-0403 with no secondary peaks, implying good solubility of Er^{3+} ions in the host lattice with no structural changes. The observed Bragg's reflection confirmed the formation of single-phase BBN corresponding to orthorhombic geometry with the Fmmm space group. The refinement index and lattice parameters obtained from profile fit between observed and calculated XRD patterns using TOPAS software for composition $BaBi_{2-x}Er_xNb_2O_9$ are reported in Table 3.1. All the experimental data is best fitted with calculated data with the goodness of fit (GoF) ≈ 1. The highest peak intensity associated with the (115) plane of $BaBi_{2-x}Er_xNb_2O_9$ represents the BLSF with m = 2, and the result agrees with

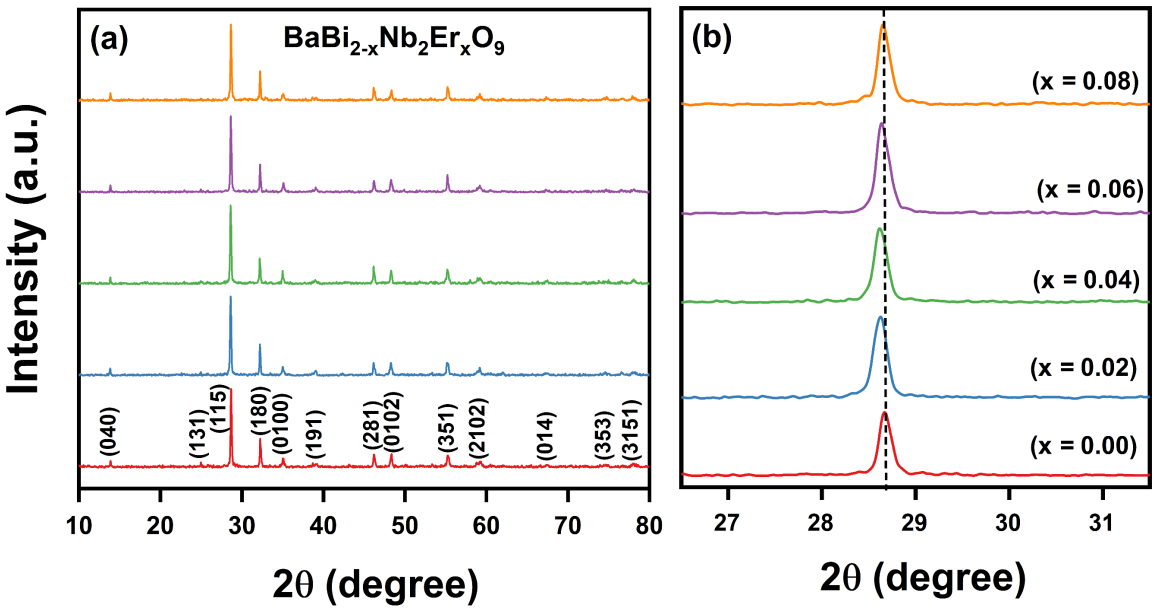

Figure 3.2: (a) XRD pattern of $BaBi_{2-x}Nb_2Er_xO_9$ with varying Er^{3+} concentration (x = 0.00, 0.02, 0.04, 0.06, 0.08) (b) Shifting of strongest XRD peak (115 planes) of $BaBi_{2-x}Nb_2Er_xO_9$ ceramic [22].

Table 3.1: Refinement index and lattice parameters for $BaBi_{2-x}Nb_2Er_xO_9$ compositions with varying Er^{3+} content (x = 0.0, 0.02, 0.04, 0.06, 0.08) [22].

$BaBi_{2-x}Nb_2Er_xO_9$	Refinement Index				Lattice Parameters					
	R_{exp}	R_{wp} (%)	GoF	R Bragg	a (Å)	b (Å)	c (Å)	V ($Å^3$)	ρ (g/cm^3)	c/a
x = 0.00	10.76	11.00	1.02	13.606	5.5394	25.5751	5.5571	787.2782	7.2277	1.003
x = 0.02	11.97	12.69	1.06	8.499	5.5540	25.5769	5.5580	789.5367	7.1012	1.001
x = 0.04	11.57	12.18	1.05	9.931	5.5526	25.6098	5.5623	790.9644	7.0718	1.001
x = 0.06	12.38	13.56	1.10	9.450	5.5482	25.5732	5.5599	788.8676	6.8776	1.002
x = 0.08	13.19	13.89	1.12	10.713	5.5485	25.5642	5.5579	788.3490	6.8080	1.002

the former explanations that the strong intensity diffraction peak corresponds to the (112m + 1) plane for BLSF materials in the Aurivillius phase [42, 43]. By using Archimedes' principle, the sintered pellet density (ρ) is found to be 7.22 g/cm^3, which has more than 98% accuracy. The density of the Er^{3+} doped $BaBi_{2-x}Er_xNb_2O_9$ composition decreases with increasing Er^{3+} concentration (Table 3.1). This decrement in density is due to the larger ionic radius of Bi^{3+} (≈ 1.17 Å) compared to the ionic radius of Er^{3+} (≈ 0.100 Å) [4]. The shift in the diffraction peak of the {115} family is displaced towards the lower values of 2θ, as shown in **Figure 3.2(b)**. Eq. (3.3) explains the tension within the lattice as [22]:

$$\sigma = \frac{E}{2\upsilon}\left[\frac{\mathrm{Sin}\theta_n}{\mathrm{Sin}\theta_i} - 1\right] \quad (3.3)$$

where E is the modulus of elasticity, υ denotes Poison's coefficient, θ_n is the shifted 2θ value over the reference angle, and θ_i is the reference angle. According to Eq. (3.3), the positive value of σ represents compression among the lattice, and a negative value means the stretching within the lattice after substituting the dopant. Since E and υ are constants, it may be concluded that after substituting the value of $\theta_i = 28.69$ and $\theta_n = 28.60$, the value of $\sigma < 0$, which is due to the stretching in the crystalline lattice, generated by the introduction of dopants. This is confirmed by the increase in cell volume with increasing Er^{3+}

concentration, causing stretching in the cell (Table 3.1). It can also be explained by the constrained character of the $6s^2$ lone-pair of Bi^{3+} ions in the host lattice, which causes the expansion of unit cell volume and shifting of the peaks towards lower 2θ [25]. Although there is a variation in the ionic radius of Er^{3+} and Bi^{3+}, the cell volume and lattice parameters (a, b, c) do not change much from undoped $BaBi_2Nb_2O_9$. This could be attributed to the creation of cationic vacancies, which preserve the electroneutrality of the lattice and minimize the deformation of the crystal [13, 28].

3.3.2 Raman Spectroscopy

The Raman spectra observed for undoped and Er^{3+}-substituted $BaBi_{2-x}Er_xNb_2O_9$ ceramic composition in the 100-1000 cm^{-1} frequency range are given in **Figure 3.3(a)**. The spectra were recorded under the excitation of laser source 785 nm at room temperature. Of all the theoretically predicted 12 Raman modes, only four strong and sharp modes at 164, 225, 560, and 860 cm^{-1} are identified for undoped $BaBi_2Nb_2O_9$, per the reported literature [4, 44, 45]. This is because of the possible overlapping of identical symmetrical vibrations and broadening of the bands or low intensity of vibration mode, whereas 10 distinct modes are detected in Er^{3+} doped $BaBi_2Nb_2O_9$ ceramics. The modes suppressed in undoped $BaBi_2Nb_2O_9$ ceramics can be easily observed in Er^{3+} doped compositions. However, in Er^{3+} doped $BaBi_{2-x}Er_xNb_2O_9$ composition, some less intense modes near 370, 389, 419, 437, 691, 730, and 771 cm^{-1} have been observed that might be associated with the degree of the structural disorder which has been described in materials belonging to the same family [13]. So, there is a good accord in the theoretically predicted and experimentally observed Raman modes. **Figure 3.3(b)** depicts the Raman shift as the function of Er^{3+} concentration, and the observed frequency shifts with their band assignments are tabulated in Table 3.2.

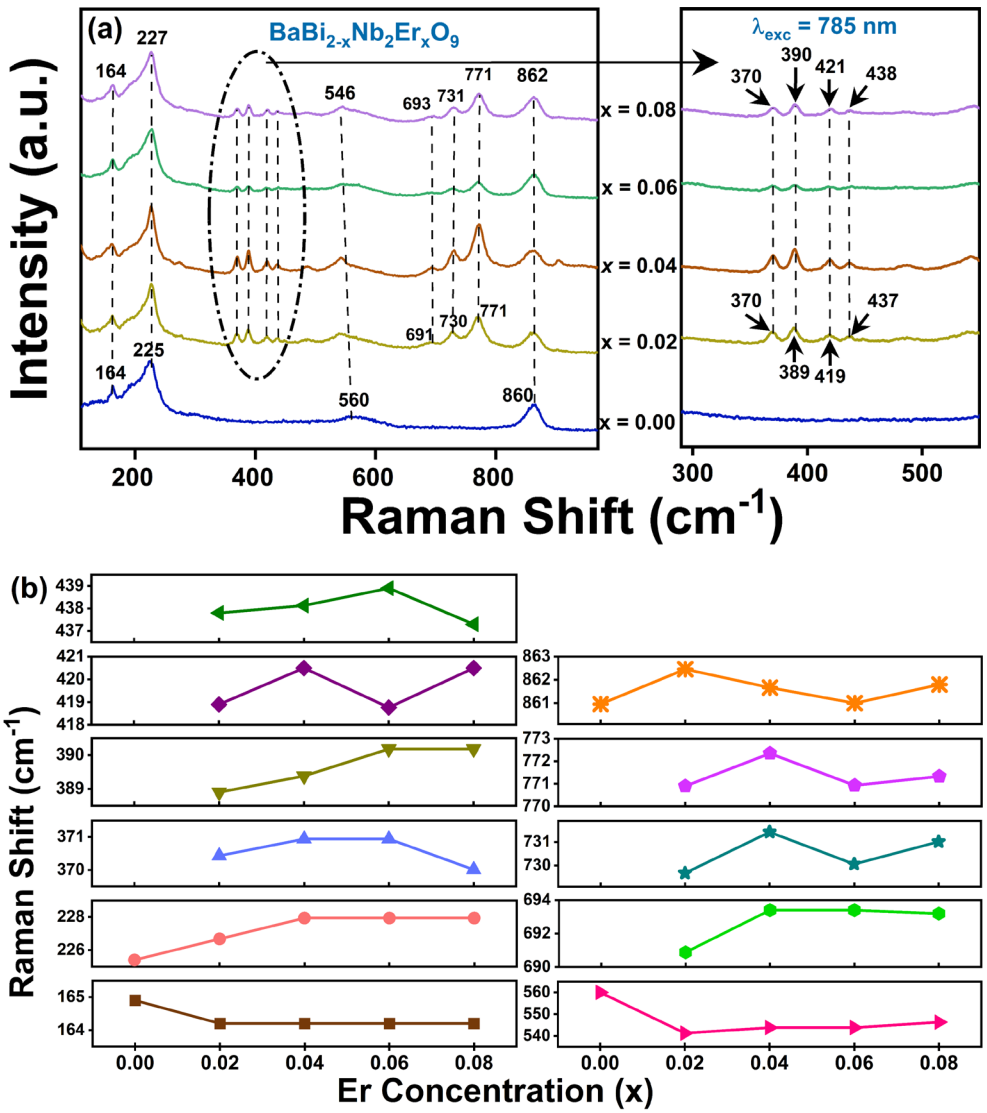

Figure 3.3: (a) Raman spectra of $BaBi_{2-x}Nb_2Er_xO_9$ with different Er^{3+} concentrations under the excitation of 785 nm (b) Compositional dependence of Raman modes [22].

The Raman spectra show the distinct modes corresponding to 164, 225, 560, and 860 cm^{-1}. The low-frequency Raman modes below 200 cm^{-1} correspond to Ba^{2+} ions vibrations at the A-site in the perovskite layer, whereas the high-frequency Raman modes above 200 cm^{-1} are correlated with the internal vibrational modes of the NbO_6 octahedron. The mode positioned at 164 cm^{-1} is attributed to displacements of Bi^{3+} ions of the pseudo-perovskite structure at the A-site. The presence of mode at 164 cm^{-1} with significant broadening with increasing Er^{3+} substitution suggests changes in the orthorhombical

distortion. The A_{1g} mode at 225 cm^{-1} is because of the torsion bending in the O-Nb-O arrangement of the NbO_6 group, and a slight shift to 227 cm^{-1} is observed with rising Er^{3+} substitution. The high-frequency mode observed at 560 cm^{-1} arising from B_{2g} mode is related to the opposite excursion of the apical oxygen atoms in NbO_6 octahedral, whereas the strong vibration mode near 860 cm^{-1} could be assigned A_{1g} character and is owing to symmetrical stretching of Nb-O of the NbO_6 group along the stacking z-axis [4, 43, 46]. The mode at 560 cm^{-1} depicts a gradual downshift to frequency 546 cm^{-1} and is found to be weakened and broadened with increasing Er^{3+} content, implying a decrease in the compressive stress due to substitution of Er^{3+} at Bi-sites and thereby suggesting relaxation in structural distortion. In contrast, the 860 cm^{-1} mode relates to the symmetrical stretch of Nb-O vibrations of the NbO_6 octahedron, shows an upshift to 862 cm^{-1}, and suggests a reduction of the interaction of Bi^{3+} with NbO_6 octahedron and hence leading to relaxation of structural deformation.

Table 3.2: Raman band assignment for $BaBi_2Nb_2O_9$ [22].

Raman Shift (cm^{-1})	**Band Assignments**	**References**
164	Vibration of Bi^{2+} ion	[4]
225	Torsion bending of O-Nb-O bond	[4, 44]
370	Vibration due to Bi-O_3 force constant	[43, 44]
389	Vibration due to Bi-O_3 force constant	[43]
419	Vibration due to Bi-O_3 force constant	[43]
437	Vibration due to Bi-O_3 force constant	[43]
560	Opposite excursion of apical oxygen atom	[4, 44, 45]
691	Symmetric bending vibration of NbO_6 octahedron	[43]
730	Symmetric bending vibration of NbO_6 octahedron	[43]
771	Symmetric bending vibration of NbO_6 octahedron	[43]
860	Symmetrical stretching of Nb-O_6 group	[42, 45]

The modes positioned at 389 and 419 cm^{-1} are assigned to B_1 mode, whereas 370 and 437 cm^{-1} bands from B_2 mode are completely dominated by the Bi-O_3 force constant, suggesting an insignificant contribution from Ba and Nb atoms [44]. The 691-771 cm^{-1} arise from T_{2g} symmetry and reflect symmetric bending vibrations of the NbO_6 octahedron. The modes observed at 730 and 771 cm^{-1} for x = 0.02 evolve prominently with increasing Er^{3+} content, although with lower intensity and significant broadening and clearly suggest changes in the structural distortion in the system and corroborate well with the XRD investigation and are observed to influence ferroelectric properties.

3.3.3 Ferroelectric Properties

The polarizations vs electric field (PE) loops of $BaBi_{2-x}Er_xNb_2O_9$ ceramic compositions (x = 0-8 mol %) measured at 50 Hz at an applied electric field ± 80 kV/cm is shown in **Figure 3.4**. The measured coercive field ($2E_c$) and remnant polarization ($2P_r$) with different Er^{3+} concentrations are recorded in Table 3.3. The values of $2P_r$ and $2E_c$ range from 2.49-3.39

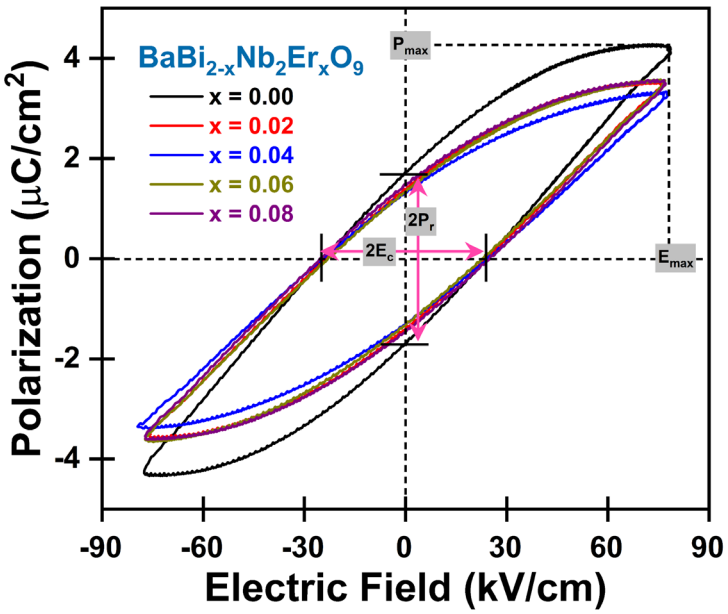

Figure 3.4: Polarization vs electric field curve of $BaBi_{2-x}Nb_2Er_xO_9$ ceramics with different Er^{3+} concentrations at room temperature at 50 Hz frequency [22].

$\mu C/cm^2$ and 45.5-49.8 kV/cm, respectively, and agree with reported results on polycrystalline $BaBi_2Nb_2O_9$ ceramics [47]. The P_r of $BaBi_{2-x}Er_xNb_2O_9$ ceramic decreases, and E_c increases with increasing Er^{3+} concentration. It is reported that the measurement of good-quality hysteresis loops and remnant polarization is affected by the presence of lattice strain, defects, density, and grain size in the lattice [48]. Compared with undoped $BaBi_2Nb_2O_9$, the observed decrease in P_r in Er^{3+} substituted composition could be attributed to structural distortion in the lattice owing to the incorporation of RE^{3+} ion with smaller ionic radius and also low density of ceramics as confirmed by XRD analysis and agrees with earlier reports on other BLSF materials [13].

Table 3.3: Variation of electrical conductivity and P-E loop parameters for different Er^{3+} concentrations in $BaBi_{2-x}Nb_2Er_xO_9$ ceramic composition (x = 0.00, 0.02, 0.04, 0.06, 0.08) [22].

$BaBi_{2-x}Nb_2Er_xO_9$	σ_{dc} ($\Omega^{-1}cm^{-1}$)	$2P_r$ ($\mu C/cm^2$)	$2E_c$ (kV/cm)
x = 0.00	3.92×10^{-12}	3.4944	48.7756
x = 0.02	1.04×10^{-12}	2.7668	48.0788
x = 0.04	8.62×10^{-13}	2.6384	48.9556
x = 0.06	5.02×10^{-13}	2.2677	45.8468
x = 0.08	2.75×10^{-14}	2.9524	49.8980

However, in comparison to previously reported unsaturated hysteresis loops in $BaBi_2Nb_2O_9$ ceramics [49, 50], it is noted that an improved hysteresis loop with a tendency to show saturation is observed at the applied electric field. However, complete P-E loop saturation was not achieved even at such a high applied field due to the least attainable sample thickness and the instrument's limitations in applying a higher electric field. Besides, the observed increase in E_c values with increasing Er^{3+} content is because of changing oxygen vacancies produced due to inherent bismuth loss. These oxygen vacancies tend to migrate and accumulate at the electrode interface and low energy domain

boundaries at high electric fields, thus hindering polarization switching due to domain pinning and increasing the coercive field [13, 28]. Moreover, with increasing Er^{3+} substitution, the oxygen vacancies owing to bismuth loss are seen to be reduced, which can be corroborated by the observed decrease in the room temperature dc conductivity (σ_{dc}) values (from 3.92×10^{-12} to 2.75×10^{-14} Ω^{-1} cm^{-1}) obtained for varying Er^{3+} content (x = 0-8 mol %) as shown in Table 3.3. The maximum value for P_r and E_c of doped $BaBi_{2-x}Er_xNb_2O_9$ ceramic is 2.9524 μC/cm^2 and 49.8980 kV/cm for the ceramic composition at x = 0.08. The upconversion luminescence properties of the ferroelectric materials doped with RE^{3+} ions are intently due to the change in crystal field, which is revealed by the phase structure (crystal symmetry) and point defects in the lattice and also possibly sensitive to external stimulus such as electric field polarization [8, 30]. In this chapter, the observed decrease in P_r in Er^{3+} substituted composition could be attributed to structural distortion in the lattice, suggesting alterations in the ligand field environment of luminescent ions in the crystal lattice. As a result, significant modification of the green and red emission luminescence intensity is observed with a change in ferroelectric properties, which is discussed in the next section.

3.3.4 Upconversion Luminescence Spectroscopy

Figure 3.5(a) shows strong upconverted light emission spectra of $BaBi_{2-x}Er_xNb_2O_9$ ceramics composition under 980 nm excitation at a pump power of 50mW with excitation source density 3.25 W/cm^2. Two green upconverted emissions are observed at 527 nm and 549 nm, allocated to the $^2H_{11/2} \rightarrow {}^4I_{15/2}$ and $^4S_{3/2} \rightarrow {}^4I_{15/2}$ transitions, respectively. Another weak band corresponds to the red emission band, which is visible to the naked eye at 657 nm and is attributed to the $^4F_{9/2} \rightarrow {}^4I_{15/2}$ transition. The obtained UC spectra align well with

previous studies on Er^{3+} doped host materials [51, 52]. It has been observed that with increasing Er^{3+} content, the intensity of red and green emission rises and attains a maximum at x = 0.04, and after that, the intensity starts decreasing with increasing Er^{3+} concentration, as presented in **Figure 3.5(b)**. It is caused by the quenching effect, which becomes appreciable when the concentration of dopant reaches a particular value where the distance between the nearest Er^{3+} ions is insignificant that they can quickly transfer energy from one ion to another and contribute to non-radiative emission [53, 54]. This results in radiative emission quenching and decreases the light emission intensity. The critical concentration for quenching is obtained at x = 0.04. Eq. (3.4) represents the Blasse formula used for evaluating the critical distance between the Er^{3+} ions [22, 55]:

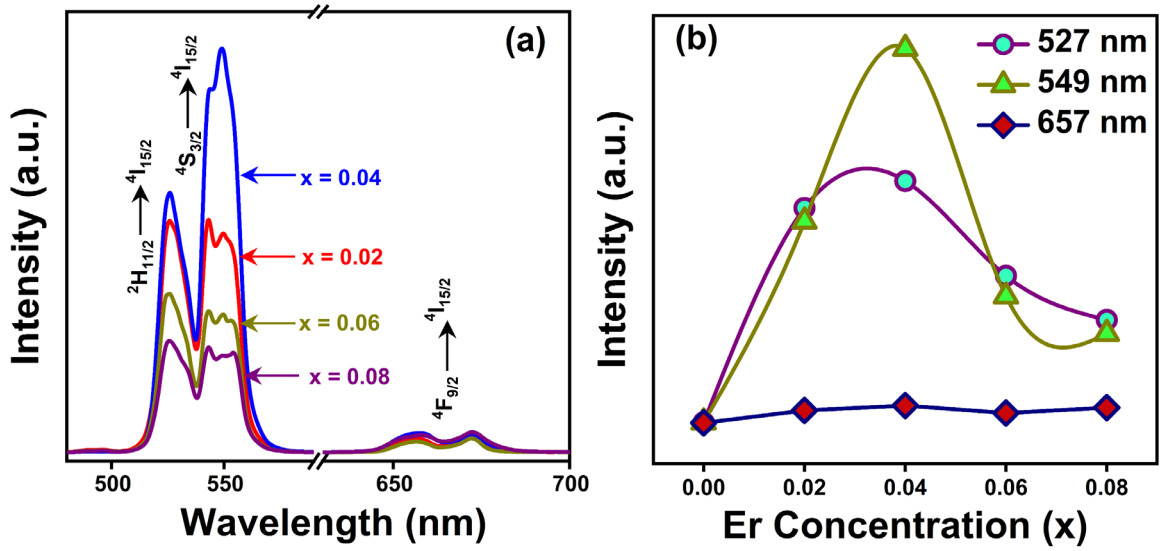

Figure 3.5: (a) Upconversion emission spectra of $BaBi_{2-x}Nb_2Er_xO_9$ with varying Er^{3+} concentrations under 980 nm excitation wavelength (b) Deviation of red and green emission intensity with varying Er^{3+} content [22].

$$R_c \approx 2\left[\frac{3V}{4\pi X_c Z}\right]^{\frac{1}{3}} \qquad (3.4)$$

where V denotes the volume of the unit cell and is equal to 790.96 cm^3, X_c is critical concentration, Z is the no. of host cation, and its value is 4 for $BaBi_2Nb_2O_9$, substituting all

these values in the above equation, R_c is valued to be 21.12 Å. The mechanism of upconversion luminescence is described by different mechanisms, which include cross-relaxation (CR), excited-state absorption (ESA), energy transfer (ET), ground-state absorption (GSA), and multi-phonon relaxation (MPR) [56]. When a laser of wavelength 980 nm illuminated on Er^{3+} doped $BaBi_{2-x}Er_xNb_2O_9$ ceramic compositions, the ground level ($^4I_{15/2}$) Er^{3+} ions absorb the energy and excited to higher energy level ($^4I_{11/2}$) by GSA as shown in **Figure 3.5(c)**. The Er^{3+} may absorb one or two photons via the ESA and ET mechanism at the $^4I_{11/2}$ metastable level of Er^{3+} ions, followed by further excitation to a higher $^4F_{7/2}$ level. Hence, the population at the $^4F_{7/2}$ level is maintained by two mechanisms, i.e., ESA and ET, which are followed by non-radiative decay transitions to lower energy levels $^2I_{11/2}$, $^4S_{3/2}$, and $^4F_{9/2}$ through MPR. The Er^{3+} ions at levels $^2H_{11/2}$ and $^4S_{3/2}$ produce green emission of wavelength 527 nm and 549 nm, respectively, and ions at levels $^4F_{9/2}$ produce red emission of wavelength 657 nm. The green emission intensity is stronger than the red emission intensity because the energy difference between $^2H_{11/2}$ and $^4S_{3/2}$ levels is smaller (approximately 800 cm^{-1}) as compared to the energy gap between $^4S_{3/2}$ and $^4F_{9/2}$

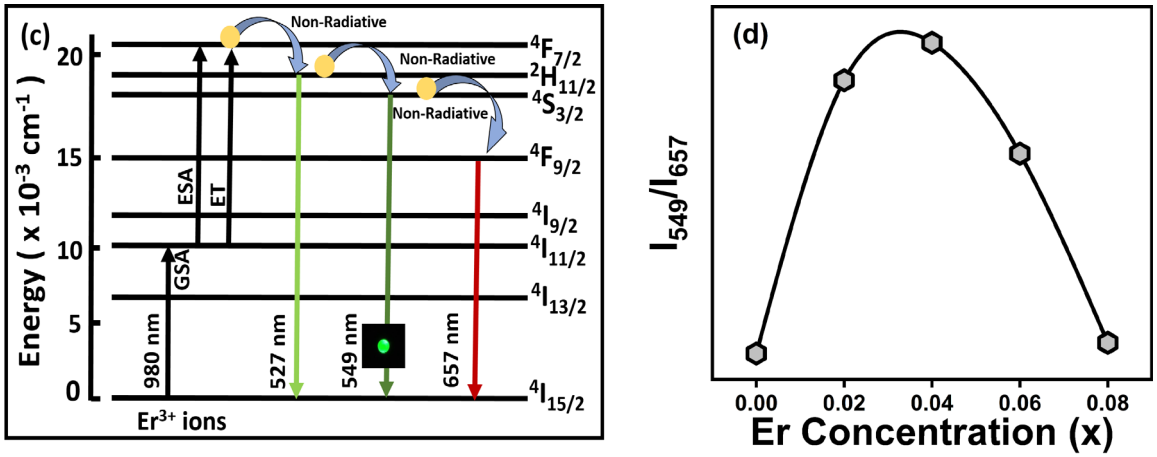

Figure 3.5: (c) Energy level diagram of Er^{3+} for UC mechanism (d) Intensity ratio of green and red emission (I_{549}/I_{657}) against Er^{3+} concentration in $BaBi_{2-x}Nb_2Er_xO_9$ ceramic [22].

levels (approximately 3000 cm^{-1}) [56]. Thereby, the MPR transition rate from the level $^2H_{11/2} \rightarrow {}^4S_{3/2}$ is faster than the transition $^4S_{3/2} \rightarrow {}^4F_{9/2}$ and results in the largest Er^{3+} population, which leads to strong green upconversion luminescence intensity [13, 56]. The intensity ratio of the green emission band to the red emission band (I_{549}/I_{657}) is decreasing at $x \geq 0.04$ and is described by the CR process [56], as shown in **Figure 3.5(d)**.

3.3.5 Pump Power Dependence on UCL

To examine the nature of photons included in the UC mechanism, the optimum amount of Er^{3+} ion in $BaBi_{2-x}Er_xNb_2O_9$ composition at x = 0.04 is examined at different pump powers ranging from 450 mW to 950 mW with excitation source density 29.3 W/cm^2 to 61.8 W/cm^2, as depicted in **Figure 3.6(a)**. It is observed that the upconverted light intensities obtained through the transitions $^2H_{11/2} \rightarrow {}^4I_{15/2}$, $^4S_{3/2} \rightarrow {}^4I_{15/2}$, and $^4F_{9/2} \rightarrow {}^4I_{15/2}$ increased by increasing the excitation power (P). Eq. (3.5) estimates the no. of photons included in the UC mechanism [22]:

$$I_{UP} \propto P^n \tag{3.5}$$

where n denotes the no. of photons needed for the upconversion operation, P signifies the excitation power, and I_{UP} stands for the upconversion luminescence intensity. The linear fit of logarithmic plots of intensity versus excitation power (Ln (I) vs. Ln (P)) is given in **Figure 3.6(b)**. From the linear fit of experimental data for UC emission bands at 527, 549, and 657 nm, the slope (n) value is found to be ~ 1.73, 2.34, and 1.53. Thus, a two-photon mechanism is confirmed for transitions corresponding to red and green emission in the UC process. The deviation in the n values corresponding to green and red UC emission bands rounded to the theoretical value of 2 due to the involvement of several mechanisms, such as ESA, ET, non-radiative relaxations, etc. [29].

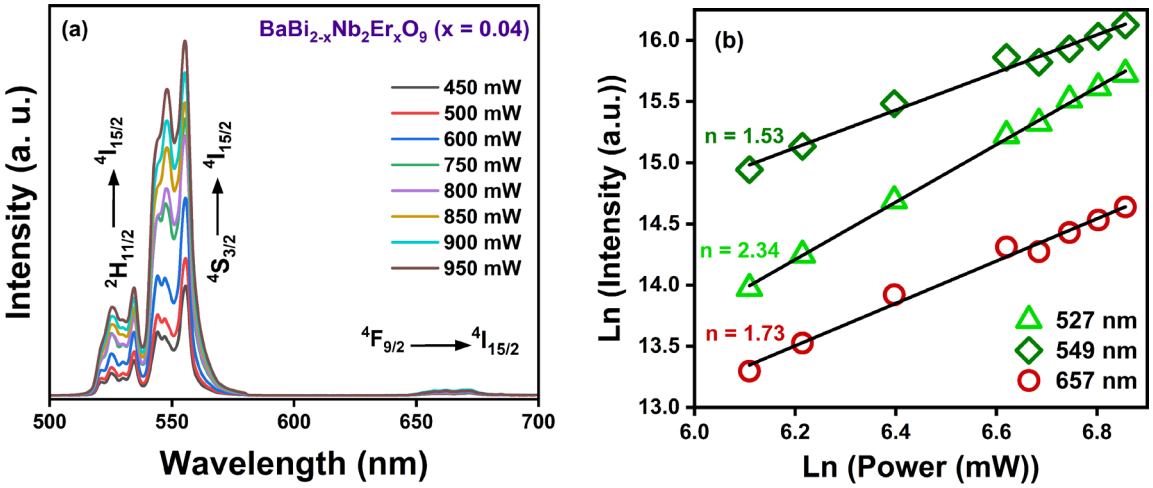

Figure 3.6: (a) UCL spectra with different pump powers ranging from 450 to 950 mW (b) Log-log plot of power and UC intensity [22].

3.3.6 Time-Resolved Spectroscopy

The time-resolved measurements were performed and examined for green emission transition ($^4S_{3/2} \rightarrow {}^4I_{15/2}$) at 549 nm under the excitation of 980 nm using a pulsed laser. In **Figure 3.7(a-c)**, the detectable time decay profiles of $BaBi_{2-x}Er_xNb_2O_9$ (x = 0.02, 0.04, 0.06) ceramic has been reported. The curve is fitted by tri exponential function expressed as Eq. (3.6) [22, 57]:

$$I(t) = I_0 + A_1 \exp\left(-\frac{t}{\tau_1}\right) + A_2 \exp\left(-\frac{t}{\tau_2}\right) + A_3 \exp\left(-\frac{t}{\tau_3}\right) \quad (3.6)$$

where I_0 is the intensity at t = 0, A_1, A_2, A_3, and τ_1, τ_2, τ_3 are the fitting parameters. The average lifetime is calculated by Eq. (3.7) [22]:

$$< \tau > = \frac{A_1\tau_1^2 + A_2\tau_2^2 + A_3\tau_3^2}{A_1\tau_1 + A_2\tau_2 + A_3\tau_3} \quad (3.7)$$

The estimated lifetime of the green emission (549 nm) for the various concentrations of Er^{3+} is represented in **Figure 3.7(d)**. The estimated fluorescence lifetime of green emission transition ($^4S_{3/2} \rightarrow {}^4I_{15/2}$) in $BaBi_{2-x}Er_xNb_2O_9$ ceramic increases from 15.33 µs to 20.90 µs for Er^{3+} content x = 0.02 to 0.04. This increase in lifetime confirms

the energy transfer mechanism between Er^{3+} ions and confirms the involvement of the ET process in the upconversion process depicted in **Figure 3.5(c)**. Subsequently, on further increasing Er^{3+} content (x = 0.06), the lifetime decreases to 15.05 µs, indicating increased probability for non-radiative transitions along with cross-relaxation processes within Er^{3+} [11, 55].

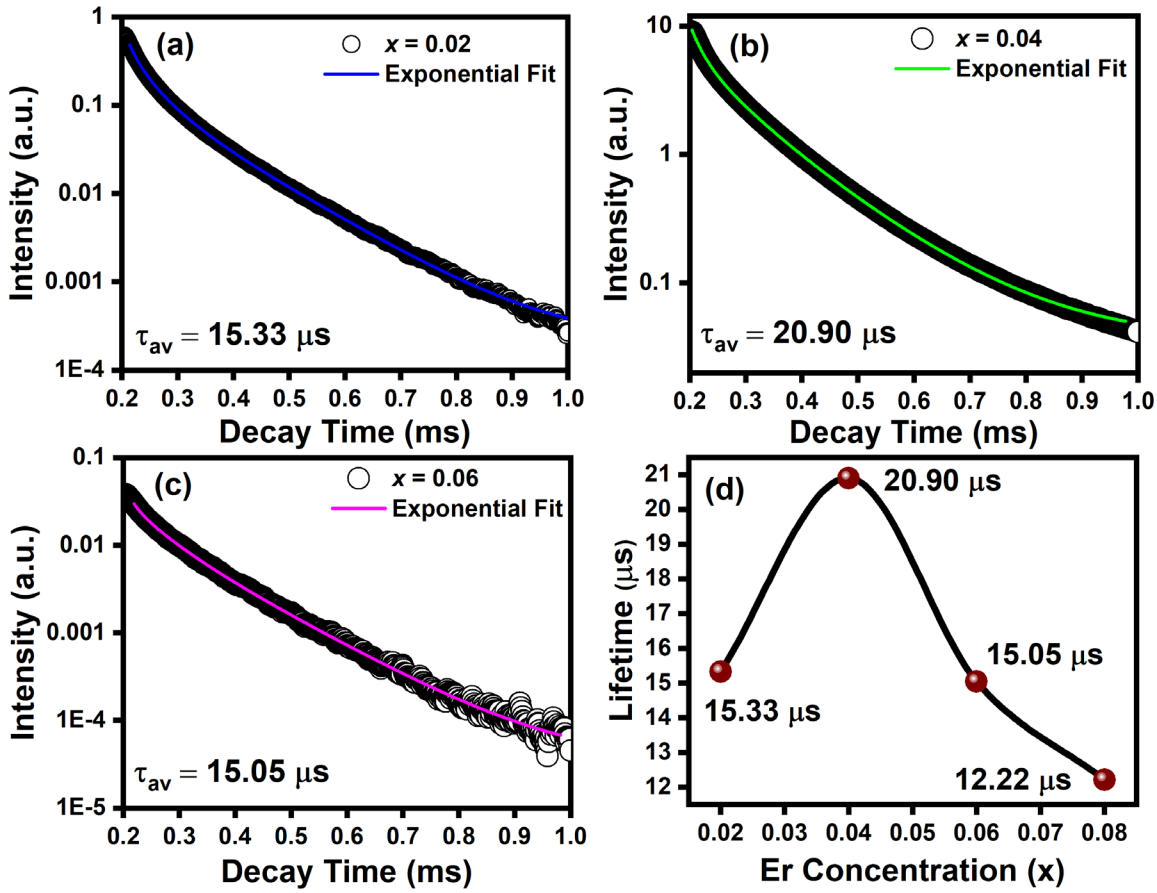

Figure 3.7: Time-resolved photoluminescence decay profile of $BaBi_{2-x}Nb_2Er_xO_9$ ceramic with Er^{3+} content at (a) x = 0.02 (b) x = 0.04 (c) x = 0.06 (d) Variation of a lifetime with different Er^{3+} concentration [22].

3.3.7 Optical Temperature Sensing

The fluorescence intensity ratio (FIR) technique is utilized for non-contact temperature measurement because it is a simple technique, easy to access, and independent of excitation

intensity fluctuations [42]. To show the optical temperature sensing application in optimized Er^{3+} doped $BaBi_{2-x}Er_xNb_2O_9$ composition, the FIR analysis is carried out by comparing the emission intensities of two green UC emission bands (I_H and I_S) arise due to thermally interacting levels $^2H_{11/2}$ and $^4S_{3/2}$ of Er^{3+} ions. This procedure examines the intensity ratio of two thermally coupled levels (TCLs) with external temperature. This approach extensively investigates temperature sensing in RE^{3+} doped materials [32, 42, 58]. **Figure 3.8(a)** depicts the variation in UC spectra for optimized Er^{3+} doped $BaBi_{2-x}Er_xNb_2O_9$ (x = 0.04) ceramic composition for temperatures ranging from 303-623 K. The

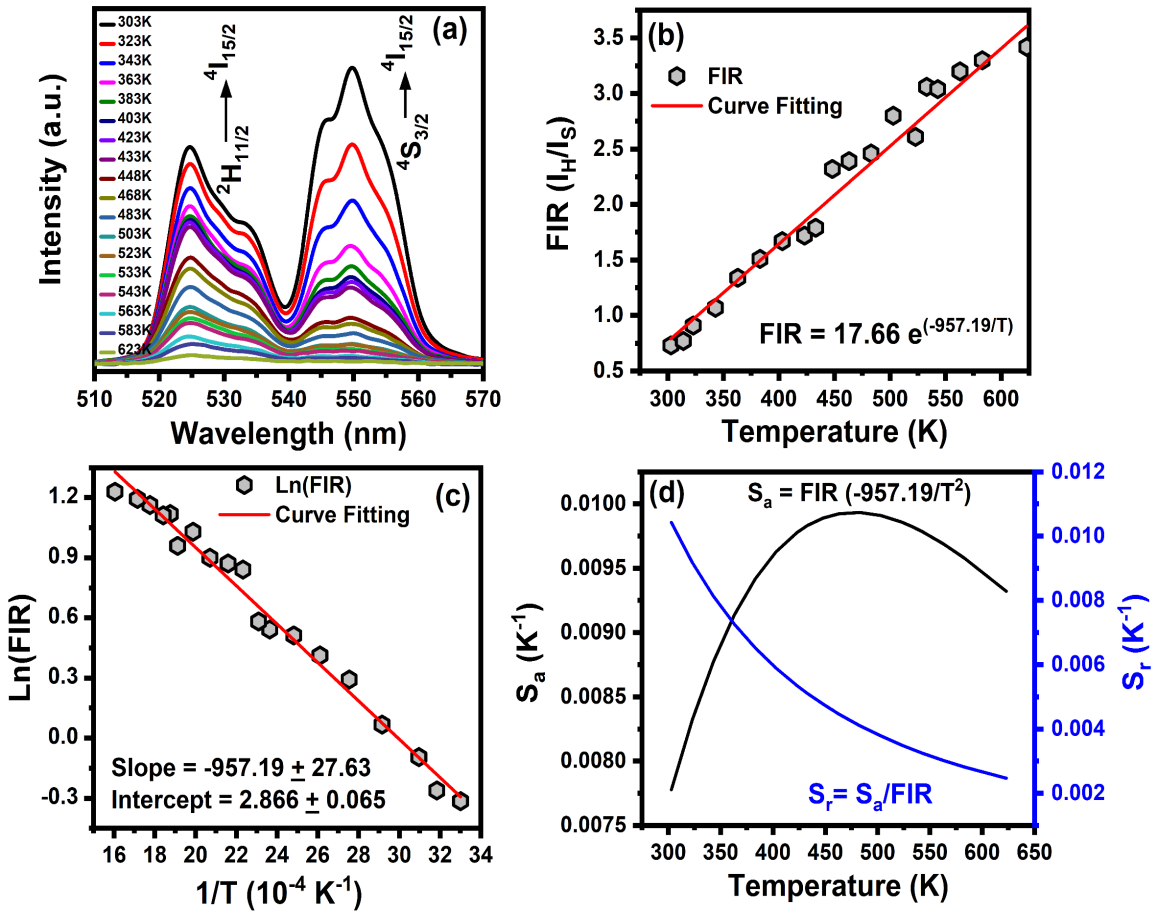

Figure 3.8: (a) UC emission spectra recorded at various temperatures (303-623 K) for optimum composition $BaBi_{2-x}Nb_2Er_xO_9$ (x = 0.04) (b) Temperature dependence of FIR for $BaBi_{2-x}Nb_2Er_xO_9$ ceramic (c) Ln(FIR) vs inverse of temperature (d) Variation of absolute sensitivity and relative sensitivity with temperature [22].

electrons follow Boltzmann's distribution law in electronic levels $^2H_{11/2}$ and $^4S_{3/2}$ because these levels occur in thermal equilibrium; therefore, the fluorescence intensity ratio (I_H/I_S) of $^2H_{11/2} \rightarrow {}^4I_{15/2}$ and $^4S_{3/2} \rightarrow {}^4I_{15/2}$ transition can be expressed by Eq. (3.8) [22]:

$$FIR = \frac{I_H}{I_S} = C \exp\left(-\frac{\Delta E}{K_B T}\right) \tag{3.8}$$

where K_B is the Boltzmann's constant, T denotes absolute temperature, ΔE represents the energy difference between $^2H_{11/2}$ and $^4S_{3/2}$ levels, C is a pre-exponential coefficient that depends on the degeneracy factor of coupled levels and the comparative transition probability, I_S and I_H are integrated intensity for $^4S_{3/2} \rightarrow {}^4I_{15/2}$ and $^2H_{11/2} \rightarrow {}^4I_{15/2}$ transition. The calculated value of FIR changes from 0.73 to 3.3 in the 303-623 K temperature range, as displayed in **Figure 3.8(b)**. The increasing temperature reduces the intensity ratio of the upconversion spectra [42]. In the linear form, Eq. (3.9) can be written as [22]:

$$Ln(FIR) = -\left(\frac{\Delta E}{K_B}\right)\left(\frac{1}{T}\right) + LnC \tag{3.9}$$

Figure 3.8(c) represents the linear fit of Ln(FIR) against absolute temperature inverse (1/T), which gives the intercept Ln(C) and slope $\Delta E/K_B$. From experimentally fitted data, the slope and intercept values are -951.2173 ± 16.327 and 2.8627 ± 0.0411, respectively, for Er^{3+} doped $BaBi_{2-x}Er_xNb_2O_9$ composition at x = 0.04. The values of ΔE and C from experimentally fitting the data using Eq. (3.9) are evaluated to be 661.129 cm^{-1} and 17.5, respectively. The absolute sensitivity (S_a) is calculated using the FIR parameters for optical temperature sensing. S_a is the degree to which the FIR deviates with a temperature variation, as represented by Eq. (3.10) [22, 59]:

$$S_a = \frac{d(FIR)}{dT} = \frac{d\left(C \exp\left(-\frac{\Delta E}{K_B T}\right)\right)}{dT} = C \exp\left(-\frac{\Delta E}{K_B T}\right)\left(\frac{\Delta E}{K_B T^2}\right) \tag{3.10}$$

$$S_r = \frac{1}{FIR} \times S_a = \left(\frac{\Delta E}{K_B T^2}\right) \tag{3.11}$$

Another important factor for optical thermometry is relative sensitivity (S_r), which is the ratio of absolute sensitivity to the FIR value and is given in Eq. (3.11) [22]. **Figure 3.8(d)** exhibits the absolute and relative sensor sensitivity. It is noticed that the material sensitivity rises with a temperature rise, achieves the highest value, and then reduces marginally. The sensitivity surges from 0.78% K^{-1} to 0.95% K^{-1} with a temperature rise from 300 to 623 K in optimized Er^{3+} doped $BaBi_{2-x}Er_xNb_2O_9$ (x = 0.04) ceramic composition. The maximum values of S_a and S_r obtained are 0.99% K^{-1} and 0.40% K^{-1} at 483 K and 300 K, respectively. Table 3.4 compares the thermometric parameters to determine the sensitivity of various optical sensor materials. The resolution (δT) and repeatability (R) are the important parameters in temperature sensing and can be deduced using Eq. (3.12) and Eq. (3.13) [22, 60]:

$$\delta T = \frac{1}{S_r} \times \frac{\delta\Delta}{\Delta} \tag{3.12}$$

$$R = 1 - \mathrm{Max}\frac{(\Delta_{Av} - \Delta_{Sp})}{\Delta_{Av}} \tag{3.13}$$

where Δ_{Av} and Δ_{Sp} are the average and specific values of FIR in the 16 cycles between 303 and 623 K, and $\delta\Delta/\Delta$ is the instrumental accuracy parameter. The plots associated with

Table 3.4: Sensitivity of various Er^{3+} doped host materials in different temperature ranges [22].

Host Material	C	ΔE (cm^{-1})	Temp. Range (K)	T_{max} (K)	S_a (K^{-1})	S_r (K^{-1})	References
$SrMoO_4$: Er^{3+}/Yb^{3+}	20.36	704	93 - 773	473	0.0139	0.0042	[11]
$Bi_4Ti_3O_{12}$: Er^{3+}	12.49	591	293 - 523	415	0.0082	0.0054	[29]
$BaMoO_4$: Er^{3+}	-	655	303 - 463	463	0.0227	0.0044	[30]
$Na_{0.5}Bi_{0.5}TO_3$: Er^{3+}/Yb^{3+}	4.71	574	163 - 613	400	0.0031	0.0055	[59]
$La_2Ti_2O_7$: Er^{3+}/Yb^{3+}	-	760	333 - 553	483	0.0057	0.0063	[61]
$BaBi_2Nb_2O_9$: Er^{3+}	17.5	661	300 - 623	483	0.00996	0.0040	**This work**

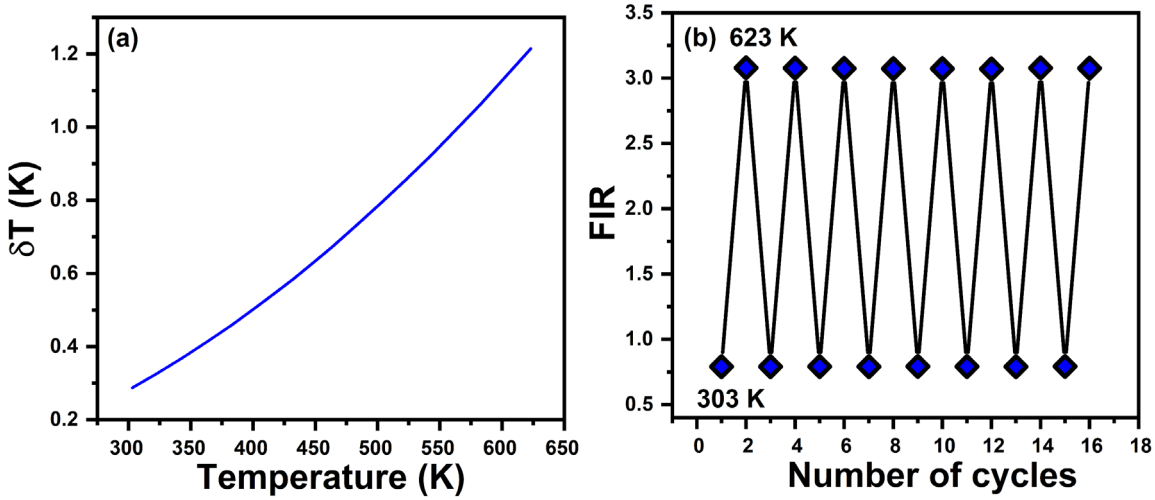

Figure 3.9: (a) Temperature resolution (b) Repeatability test for temperature sensing between 303-623 K temperature range [22].

resolution and repeatability are represented in **Figure 3.9(a, b)**, respectively. The resolution varies from 0.3 to 1.2 K in the 303-623 K temperature range. The repeatability test shows a negligible change in FIR values during the heating and cooling cycle. Thus, $BaBi_{2-x}Er_xNb_2O_9$ composition at x = 0.04 has good sensitivity, repeatability, and decent resolution for temperature sensor applications from 300-623 K.

3.4 SUMMARY

Er^{3+} substituted $BaBi_{2-x}Er_xNb_2O_9$ ceramic composition is effectively synthesized by the solid-state reaction method. The evolution of a single-phase $BaBi_2Nb_2O_9$ unit cell having orthorhombic geometry is confirmed by X-ray diffraction. Structural deformation with Er^{3+} doping has been detected by Raman spectroscopy and XRD. Shifts in the Raman modes indicate reduced interaction of Bi^{3+} ions with NbO_6 octahedrons, leading to relaxation of structural distortion with increasing Er^{3+} content. Raman and XRD analysis demonstrate that ferroelectric properties degrade with increasing Er^{3+} substitution due to relaxation in a structural deformation. However, increasing Er^{3+} substitution exhibits significant

improvement in DC electrical conductivity owing to suppression of oxygen vacancy concentration. Strong upconversion luminescence is obtained for green emission at 549 and 527 nm through $^4S_{3/2} \rightarrow {}^4I_{15/2}$, $^2H_{11/2} \rightarrow {}^4I_{15/2}$ transitions, and less intense red emission spectra appear at 657 nm via $^4F_{9/2} \rightarrow {}^4I_{15/2}$ transition under the excitation of 980 nm for an optimal Er^{3+} concentration. The luminescence quenching is effective beyond a certain Er^{3+} concentration of x = 0.04. The estimated fluorescence lifetime of green emission of Er^{3+} ion increases from 15.33 to 20.90 μs for Er^{3+} content x = 0.02 to 0.04, suggesting radiative emission due to energy transfer within Er^{3+} ions. The pump power dependence of upconversion luminescence intensity of emission bands confirms that upconversion is a two-photon mechanism. The FIR of the two green spectra was calculated and linearly increased with temperature ranging from 300-623 K. This is due to the thermal excitation and quasi-thermal equilibrium processes between $^2H_{11/2}$ and $^4S_{3/2}$. The FIR technique shows a maximum sensitivity of 0.99% K^{-1} at 483 K for an optimized Er^{3+} substituted $BaBi_{2-x}Nb_2Er_xO_9$ ceramic composition (x = 0.04) for optical temperature sensing applications with good repeatability and temperature resolution.

Following a comprehensive analysis of the single Er^{3+} doped $BaBi_{2-x}Er_xNb_2O_9$ ferroelectric ceramic, it is imperative to address the concerns associated with this system. Incorporating Er^{3+} doping enhanced upconversion luminescence and sensing capabilities, but the ferroelectric characteristics degraded. Therefore, it is crucial to explore the effect of Yb^{3+} ions along with Er^{3+} ions in $BaBi_2Nb_2O_9$ ferroelectric ceramic, which will be the primary focus area of the next chapter.

3.5 REFERENCES

[1] V. Lojpur, G. Nikolic, and M. D. Dramićanin, "Luminescence thermometry below room temperature via up-conversion emission of Y_2O_3:Yb^{3+}, Er^{3+} nanophosphors," *Journal of Applied Physics*, vol. 115, 203106, 2014.

[2] R. Bokolia, O. P. Thakur, V. K. Rai, S. K. Sharma, and K. Sreenivas, "Electrical properties and light upconversion effects in $Bi_{3.79}Er_{0.03}Yb_{0.18}Ti_{3-x}W_xO_{12}$ ferroelectric ceramics," *Ceramics International*, vol. 42, no. 5, pp. 5718-5730, 2016.

[3] A. Bayart, F. Szczepanski, J. F. Blach, J. Rousseau, A. Katelnikovas, and S. Saitzek, "Upconversion luminescence properties and thermal quenching mechanisms in the layered perovskite $La_{1.9}Er_{0.1}Ti_2O_7$ towards an application as optical temperature sensor," *Journal of Alloys and Compounds*, vol. 744, pp. 516-527, 2018.

[4] M. X. Façanha, J. P. C. do Nascimento, M. S. Silva, M. Filho, A. L. B. Marques, A. G. Pinheiro, and A. S. B. Sombra, "Up-conversion emission of Er^{3+}/Yb^{3+} co-doped $BaBi_2Nb_2O_9$ (BBN) phosphors," *Journal of Luminescence*, vol. 183, pp. 102-107, 2017.

[5] Q. Cao, D. Peng, H. Zou, J. Li, X. Wang, and X. Yao, "Up-conversion luminescence of Er^{3+} and Yb^{3+} co-doped $CaBi_2Ta_2O_9$ multifunctional ferroelectrics," *Journal of advanced dielectrics*, vol. 4, no. 3, 1450018, 2014.

[6] T. Wei, C. Z. Zhao, Q. J. Zhou, Z. P. Li, Y. Q. Wang, and L. S. Zhang, "Bright green upconversion emission and enhanced ferroelectric polarization in $Sr_{1-1.5x}Er_xBi_2Nb_2O_9$," *Optical Materials*, vol. 36, pp. 1209-1212, 2014.

[7] M. X. Façanha, F. F. do Carmo, J. P. C. do Nascimento, T. O. Sales, W. Q. Santos, A. S. G. Neto, C. J. da Silva, and A. S. B. Sombra, "A novel white-light emitting $BaBi_2Nb_2O_9$: Li^+/Tm^{3+}/Er^{3+}/Yb^{3+} upconversion phosphor," *Journal of Luminescence*, vol. 204, pp. 539-547, 2018.

[8] K. Li, L. Luo, Y. Zhang, W. Li, and Y. Hou, "Tunable luminescence contrast in photochromic ceramics $(1-x)Na_{0.5}Bi_{0.5}TiO_3-xNa_{0.5}K_{0.5}NbO_3$:0.002 Er by an electric field poling," *ACS Applied Material and Interfaces*, vol. 10, pp. 41525-41534, 2018.

[9] R. Sahu and P. Kumar, "Microstructural, dielectric and ferroelectric properties of $Sr_{0.8}Bi_{2.15}Ta_2O_9$ ceramics synthesized by microwave processing technique," *Phase Transitions*, vol. 93, no. 1, pp. 91-99, 2020.

[10] J. Tang, P. Du, W. Li, G. Yuan, Z. Liu, and L. Luo, "The integration of diverse fluorescence performances of $Sr_{2-x}SnO_4$:xSm^{3+} ceramics with an infinite luminescence modulation ratio," *Chemical Engineering Journal*, vol. 410, 128287, 2021.

[11] A. Shandilya, R. S. Yadav, A. K. Gupta, and K. Sreenivas, "Temperature-dependent light upconversion and thermometric properties of Er^{3+}/Yb^{3+} co-doped $SrMoO_4$ sintered ceramics," *Journal of Materials Science*, vol. 56, pp. 12716-12731, 2021.

[12] J. Li, E. Sun, L. Tang, Y. Zhou, L. Li, J. Miao, Z. Zhang, and W. Cao, "Non-contact localized probing of ferroelectric phase transitions in Li^{+}/ Er^{3+}: $BaTiO_3$ ceramics using fluorescence abnormalities," *Applied Physics Letters*, vol. 116, no. 4, 2020.

[13] R. Bokolia, O. P. Thakur, V. K. Rai, S. K. Sharma, and K. Sreenivas, "Dielectric, ferroelectric and photoluminescence properties of Er^{3+} doped $Bi_4Ti_3O_{12}$ ferroelectric ceramics," *Ceramics International*, vol. 41, no. 4, pp. 6055-6066, 2015.

[14] Z. Peng, Q. Chen, Y. Chen, D. Xiao, and J. Zhu, "Microstructure and electrical properties in W/Nb co-doped Aurivillius phase $Bi_4Ti_3O_{12}$ piezoelectric ceramics," *Materials Research Bulletin*, vol. 59, pp. 125-130, 2014.

[15] P. Banerjee and A. Franco, "Role of higher valent substituent on the dielectric and optical properties of $Sr_{0.8}Bi_{2.2}Nb_2O_9$ ceramics," *Materials Chemistry and Physics*, vol. 225, pp. 213-218, 2019.

[16] C. Ma, W. Zhou, Z. Gan, X. Wang, W. Tan, Z. Zhang, and Z. Zhai, "Upconversion photoluminescence modulation by electric field poling in Er^{3+} doped $(Ba_{0.85}Ca_{0.15})(Zr_{0.1}Ti_{0.9})O_3$ piezoelectric ceramics," *Journal of Alloys and Compounds*, vol. 794, pp. 325-332, 2019.

[17] D. Dhak, P. Dhak, T. Ghorai, S. K. Biswas, and P. Pramanik, "Preparation of nano-sized $ABi_2Nb_2O_9$ (A = Ca^{2+}, Sr^{2+}, Ba^{2+}) ferroelectric ceramics by soluble Nb(V) tartarate precursor and their dielectric characteristics after sintering," *Journal of Materials Science: Materials in Electronics*, vol. 19, no. 5, pp. 448-456, 2008.

[18] C. Karthik and K. B. R. Varma, "Dielectric and AC conductivity behavior of $BaBi_2Nb_2O_9$ ceramics," *Journal of Physics and Chemistry of Solids*, vol. 67, no. 12, pp. 2437-2441, 2006.

[19] M. P. Dasaria, K. S. Rao, P. M. Krishna, and G. G. Krishna, "Barium strontium bismuth niobate layered perovskites: Dielectric, impedance and electrical modulus characteristics," *Acta Physica Polonica A*, vol. 119, no. 3, pp. 387-394, 2011.

[20] Z. Yao, R. Chu, Z. Xu, J. Hao, W. Li, and G. Li, "Processing and enhanced electrical properties of $Sr_{1-x}(K_{0.5}Bi_{0.5})xBi_2Nb_2O_9$ lead-free piezoelectric ceramics," *Ceramics International*, vol. 42, no. 9, pp. 10619-10623, 2016.

[21] Z. Yao, R. Chu, Z. Xu, J. Hao, and G. Li, "Enhanced electrical properties of (Li, Ce) co-doped $Sr(Na_{0.5}Bi_{0.5})Bi_4Ti_5O_{18}$ high temperature piezoceramics," *RSC Advances*, vol. 6, no. 40, pp. 33387-33392, 2016.

[22] A. Banwal and R. Bokolia, "Enhanced upconversion luminescence and optical temperature sensing performance in Er^{3+} doped $BaBi_2Nb_2O_9$ ferroelectric ceramic," *Ceramics International*, vol. 48, no. 2, pp. 2230-2240, 2022.

[23] T. Mazon, M. A. Zaghete, M. Cilense, and J. A. Varela, "Effect of the excess of bismuth on the morphology and properties of the $BaBi_2Nb_2O_9$ thin films," *Ceramics International*, vol. 35, no. 8, pp. 3143-3146, 2009.

[24] Z. Zhou, Y. Li, S. Hui, and X. Dongand, "Effect of tungsten doping in bismuth-layered $Na_{0.5}Bi_{2.5}Nb_2O_9$ high temperature piezoceramics," *Applied Physics Letters*, vol. 104, no. 1, 012904, 2014.

[25] A. Banwal and R. Bokolia, "Efficient tunable temperature sensitivity in thermally coupled levels of Er^{3+}/Yb^{3+} co-doped $BaBi_2Nb_2O_9$ ferroelectric ceramic," *Journal of Luminescence*, vol. 263, 120071, 2023.

[26] X. Wu, K. W. Kwok, and F. Li, "Upconversion fluorescence studies of sol-gel-derived Er-doped KNN ceramics," *Journal of Alloys and Compounds*, vol. 580, pp. 88-92, 2013.

[27] Y. Zhang, X. Wang, H. Ye, Y. Li, and X. Yao, "$xLiNbO_3$-(1-x)(K, Na)NbO_3 ceramics: A new class of phosphors with tunable upconversion luminescence by external electric field and excellent optical temperature sensing property," *Journal of Alloys and Compounds*, vol. 770, pp. 214-221, 2019.

[28] L. Sun, C. Feng, L. Chen, and S. Huang, "Dielectric and piezoelectric properties of $SrBi_{2-x}Sm_xNb_2O_9$ (x = 0, 0.05, 0.1, 0.2, 0.3, and 0.4) ceramics," *Journal of the American Ceramic Society*, vol. 90, no. 12, pp. 3875-3881, 2007.

[29] R. Bokolia, M. Mondal, V. K. Rai, and K. Sreenivas, "Enhanced infrared-to-visible up-conversion emission and temperature sensitivity in (Er^{3+}, Yb^{3+}, and W^{6+}) tri-doped $Bi_4Ti_3O_{12}$ ferroelectric oxide," *Journal of Applied Physics*, vol. 121, no. 8, 2017.

[30] C. Liu, Q. Wang, X. Wu, B. Sa, H. Sun, L. Luo, C. Lin, X. Zheng, T. Lin, and Z. Sun, "Boosting upconversion photoluminescence and multielectrical properties via Er-doping-modulated vacancy control in $Ba_{0.85}Ca_{0.15}Ti_{0.9}Zr_{0.1}O_3$," *ACS Omega*, vol. 4, pp. 11004-11013, 2019.

[31] A. K. Soni, A. Kumari, and V. K. Rai, "Optical investigation in shuttle like $BaMoO_4$:Er^{3+}-Yb^{3+} phosphor in display and temperature sensing," *Sensors and Actuators B Chemical*, vol. 216, pp. 64-71, 2015.

[32] X. Li, X. Wang, H. Zhong, L. Cheng, S. Xu, J. Sun, J. Zhang, X. Li, L. Tong, and B. Chen, "Effects of Er^{3+} concentration on down-/up-conversion luminescence and temperature sensing properties in $NaGdTiO_4$: Er^{3+}/Yb^{3+} phosphors," *Ceramics International*, vol. 42, no. 13, pp. 14710-14715, 2016.

[33] X. Hui, D. Peng, H. Zou, J. Li, Q. Cao, Y. Li, X. Wang, and X. Yao, "A new multifunctional Aurivillius oxide $Na_{0.5}Er_{0.5}Bi_4Ti_4O_{15}$: Up-conversion luminescent, dielectric, and piezoelectric properties," *Ceramics International*, vol. 40, no. 8, Part A, pp. 12477-12483, 2014.

[34] A. Banwal and R. Bokolia, "Preparation and characterisations of Yb^{3+} substituted $BaBi_{2-y}Nb_2Yb_yO_9$ ferroelectric ceramic," *Materials Today: Proceedings*, vol. 62, part 6, pp. 3782-3785, 2022.

[35] Z. Chen, L. Sheng, X. Li, P. Zheng, W. F. Bai, L. Li, F. Wen, W. Wu, L. Zheng, and J. Cui, "Enhanced piezoelectric properties and electrical resistivity in W/Cr co-

doped $CaBi_2Nb_2O_9$ high-temperature piezoelectric ceramics," *Ceramics International*, vol. 45, no. 5, pp. 6004-6011, 2019.

[36] H. Zou, Y. Yu, J. Li, Q. Cao, X. Wang, and J. Hou, "Photoluminescence, enhanced ferroelectric, and dielectric properties of Pr^{3+}-doped $SrBi_2Nb_2O_9$ multifunctional ceramics," *Materials Research Bulletin*, vol. 69, pp. 112-115, 2015.

[37] A. Banwal and R. Bokolia, "Effect of Er^{3+} ion doping on structural, ferroelectric and up/down conversion luminescence in $BaBi_2Nb_2O_9$ ceramic," *Materials Today: Proceedings*, vol. 47, part 14, pp. 4692-4695, 2021.

[38] S. Kojima, R. Imaizumi, S. Hamazaki, and M. Takashige, "Raman scattering study of bismuth layer-structure ferroelectrics," *Japanese Journal of Applied Physics*, vol. 33, no. 9, pp. 5559-5564, 1994.

[39] J. D. Bobić, M. M. V. Petrović, and B. D. Stojanović, "Aurivillius $BaBi_4Ti_4O_{15}$ based compounds: Structure, synthesis and properties," *Processing and Application of Ceramics*, vol. 7, no. 3, pp. 97-110, 2013.

[40] S. F. L. Luis, U. R. R. Mendoza, E. Lalla, and V. Lavín, "Chemical temperature sensor based on the Er^{3+} green upconverted emission in a fluorotellurite glass," *Sensors and Actuators B*, vol. 158, no. 1, pp. 208-213, 2011.

[41] M. K. Mahata, T. Koppe, T. Mondal, C. B. Sewitz, K. Kumar, V. K. Rai, H. Hofsass, and U. Vetter, "Incorporation of Zn^{2+} ions into $BaTiO_3$:Er^{3+}/Yb^{3+} nanophosphor: An effective way to enhance upconversion, defect luminescence and temperature sensing," *Physical Chemistry Chemical Physics*, vol. 17, no. 32, pp. 20741-20753, 2015.

[42] L. Mukhopadhyay, V. K. Rai, R. Bokolia, and K. Sreenivas, "980 nm excited Er^{3+}/Yb^{3+}/Li^{+}/Ba^{2+}: $NaZnPO_4$ upconverting phosphors in optical thermometry," *Journal of Luminescence*, vol. 187, pp. 368-377, 2017.

[43] R. Ramaraghavulu and S. Buddhudu, "Structural and dielectric properties of $BaBi_2Nb_2O_9$ ferroelectric ceramic powders by a solid state reaction method," *Ferroelectrics*, vol. 460, no. 1, pp. 57-67, 2014.

[44] H. C. Gupta, Archana, and V. Luthra, "Lattice vibrations of $ABi_2Nb_2O_9$ crystals (A = Ca, Sr, Ba)," *Vibrational Spectroscopy*, vol. 56, pp. 235-240, 2011.

[45] Y. G. Abreu, A. P. Barranco, Y. Gagou, J. Belhadi, and P. S. Grégoire, "Vibrational analysis on two-layer Aurivillius phase $Sr_{1-x}Ba_xBi_2Nb_2O_9$ using Raman spectroscopy," *Vibrational Spectroscopy*, vol. 77, pp. 1-4, 2015.

[46] M. A. Basheer, G. Prasad, G. S. Kumar, and N. V. Prasad, "Dielectric studies on Sm-modified two-layered BLSF ceramics," *Bulletin of Materials Science*, vol. 42, no. 3, pp. 1-11, 2019.

[47] W. Qi, Y. Wang, J. Wu, Z. Hu, C. Jia, G. Viola, H. Zhang, and H. Yan, "Relaxor behavior and photocatalytic properties of $BaBi_2Nb_2O_9$", *Journal of the American Ceramic Society*, vol. 103, no. 1, pp. 28-34, 2020.

[48] Y. Zhang, J. Roscow, R. Lewis, H. Khanbareh, V. Y. Topolov, M. Xie, and C. R. Bowen, "Understanding the effect of porosity on the polarisation-field response of ferroelectric materials," *Acta Materialia*, vol. 154, pp. 100-112, 2018.

[49] H. Zhang, H. Yan, and M. J. Reece, "Microstructure and electrical properties of Aurivillius phase ($CaBi_2Nb_2O_9$)1-x($BaBi_2Nb_2O_9$)x solid solution," *Journal of Applied Physics*, vol. 108, no. 1, 014109, 2010.

[50] B. S. Babu, S. N. Babu, G. Prasad, G. S. Kumar, and N. V. Prasad, "Structural, electrical and photoluminescence properties of Er^{3+}-doped $Bi_4Ti_3O_{12}$-$SrBi_4Ti_4O_{15}$ inter-growth ceramics," *Frontiers of Materials Science*, vol. 13, no. 1, pp. 99-106, 2019.

[51] N. A. Lomanova, "Synthesis and thermal properties of nano-and macro-crystalline ceramic materials based on $Bi_5FeTi_3O_{15}$," *Refractories and Industrial Ceramics*, vol. 59, no. 3, pp. 301-305, 2018.

[52] L. Yu, J. Hao, Z. Xu, W. Li, R. Chu, and G. Li, "Strong photoluminescence and good electrical properties in Eu-modified $SrBi_2Nb_2O_9$ multifunctional ceramics," *Ceramics International*, vol. 42, no. 13, pp. 14849-14854, 2016.

[53] M. Chen, "Study on the structure and luminescence quenching of Pr doped $Na_{0.5}Bi_{4.5}Ti_4O_{15}$ multifunctional ceramics," *Journal of Materials Science: Materials in Electronics*, vol. 30, no. 23, pp. 20393-20399, 2019.

[54] Z. Zhang, J. Li, L. Liu, J. Sun, J. Hao, and W. Li, "Upconversion luminescence and electrical properties of (K, Er) co-modified $Na_{0.5}Bi_{4.5}Ti_4O_{15}$ high-temperature piezoceramics," *Physica B: Condensed Matter*, vol. 580, 411920, 2020.

[55] W. Lv, Y. Jia, Q. Zhao, W. Lü, M. Jiao, B. Shao, and H. You, "Synthesis, structure, and luminescence properties of $K_2Ba_7Si_{16}O_{40}$:Eu^{2+} for white light emitting diodes," *The Journal of Physical Chemistry C*, vol. 118, pp. 4649-4655, 2014.

[56] F. Liu, X. Jiang, C. Chen, X. Nie, X. Huang, Y. Chen, H. Hu, and C. Su, "Structural, electrical and photoluminescence properties of Er^{3+}-doped $SrBi_4Ti_4O_{15}$-$Bi_4Ti_3O_{12}$ inter-growth ceramics," *Journal of Materials Science*, vol. 13, no. 1, pp. 99-106, 2019.

[57] A. Shandilya, R. S. Yadav, A. K. Gupta, and K. Sreenivas, "Effects of Yb^{3+} ion doping on lattice distortion, optical absorption and light upconversion in Er^{3+}/Yb^{3+} co-doped $SrMoO_4$ ceramics," *Materials Chemistry and Physics*, vol. 264, no. 2, 124441, 2021.

[58] J. Li, J. Sun, J. Liu, X. Li, J. Zhang, Y. Tian, S. Fu, L. Cheng, H. Zhong, H. Xia, and B. Chen, "Pumping-route-dependent concentration quenching and temperature effect of green up- and down-conversion luminescence in Er^{3+}/Yb^{3+} co-doped $Gd_2(WO_4)_3$ phosphors," *Materials Research Bulletin*, vol. 48, no. 6, pp. 2159-2165, 2013.

[59] P. Du, L. Luo, W. Li, and Q. Yue, "Upconversion emission in Er-doped and Er/Yb-codoped ferroelectric $Na_{0.5}Bi_{0.5}TiO_3$ and its temperature sensing application," *Journal of Applied Physics*, vol. 116, no. 1, pp. 1-7, 2014.

[60] L. J. Li, Y. Tong, J. Chen, Y. H. Chen, G. A. Ashraf, L. P. Chen, T. Pang, and H. Guo, "Up-conversion and temperature sensing properties of $Na_2GdMg_2(VO_4)_3$: Yb^{3+}, Er^{3+} phosphors," *Journal of the American Ceramic Society*, vol. 105, pp. 384-391, 2021.

[61] Y. Liu, G. Bai, E. Pan, Y. Hua, L. Chen, and S. Xu, "Upconversion fluorescence property of Er^{3+}/Yb^{3+} co-doped lanthanum titanate microcrystals for optical thermometry," *Journal of Alloys and Compounds*, vol. 822, 153449, 2020.

4

CHAPTER

Upconversion Luminescence and Optical Temperature Sensing Properties of Er^{3+}/Yb^{3+} Co-Doped $BaBi_2Nb_2O_9$ Ferroelectric Ceramic

- *This chapter discusses the upconversion luminescence and temperature sensing behavior of Er^{3+}/Yb^{3+} co-doped ferroelectric ceramic $BaBi_{2-0.04-y}Nb_2Er_{0.04}Yb_yO_9$ prepared by the solid-state method.*
- *The optimized Er^{3+} content (x = 0.04) is doped with varying Yb^{3+} content (y = 0.00, 0.02, 0.04, 0.06, 0.08, 0.10, and 0.12) at the A-site of $BaBi_2Nb_2O_9$ ferroelectric ceramic.*
- *Upconversion luminescence (UCL) spectra revealed two prominent green emission bands near 535 nm and 557 nm and a notable red band at 672 nm, corresponding to a 980 nm excitation wavelength.*
- *Decay time measurements support the effective energy transfer from Yb^{3+} to Er^{3+} ions. The average lifetime increases with increasing Er^{3+}/Yb^{3+} doping concentration up to the optimal concentration (y = 0.10).*
- *The absolute sensitivity, S_a (0.69% K^{-1} and 0.58% K^{-1}) and relative sensitivity, S_r (1.1% K^{-1} and 1.01% K^{-1}) have been recorded for Er^{3+}/Yb^{3+} co-doped $BaBi_{2-0.04-y}Nb_2Er_{0.04}Yb_yO_9$ ceramic at y = 0.06 and 0.10, respectively, suggesting it is a viable non-contact sensor ceramic whose sensitivity can be tuned by varying dopant concentrations.*

4.1 INTRODUCTION

Chapter 3 describes the substitution of Er^{3+} ions with Bi^{3+} ions in the A-site of perovskite structure that has affected the luminescence and sensing properties of $BaBi_2Nb_2O_9$ ceramic. The upconversion luminescence improved with Er^{3+} doping up to an optimum Er^{3+} content (x = 0.04); after that, the PL emission intensity degrades. This happens due to the critical distance between the dopant ions, resulting in non-radiative transitions [1-5]. Also, the luminescence efficiency is limited in Er^{3+} due to the lower cross-sectional absorption of the $^4I_{11/2}$ level. Keeping these observations in mind, the $BaBi_{2-x-y}Nb_2Er_xYb_yO_9$ system is co-doped with Yb^{3+} ions at the A-site along with optimized Er^{3+} content (x = 0.04) for the efficient transfer of energy between them. Yb^{3+} is selected as the co-dopant because it functions as a sensitizer to increase the absorption cross-section and thereby enhance the efficacy of the upconversion [6-10]. Some of the examples of Er^{3+} and Yb^{3+} co-doped systems are given as follows: Luo et al. studied Er^{3+}/Yb^{3+} co-doped $Ba_2NaNb_5O_{15}$ glass ceramics for UC luminescence, thermal sensing, and energy storage performance [11]. Er^{3+}/Yb^{3+} co-doped tungsten tellurite glass was used to make a temperature sensor with an absolute sensibility of around 28.72×10^{-4} K^{-1} at 690 K and decent green emission luminescence [12]. Swami et al. studied the luminescence intensity ratio of Yb^{3+}/Er^{3+} co-doped La_2TiO_7 ceramics and reported an absolute sensitivity value of around 0.0029 K^{-1} at 498 K [13]. In addition, Peng et al. fabricated Yb^{3+}/Er^{3+} co-doped BNT across a wide temperature range and determined a sensitivity of approximately 0.0049 K^{-1} at 363 K [14]. Therefore, in this chapter, bismuth ions in the A-site in $BaBi_2Nb_2O_9$ ceramic are replaced with the optimized Er^{3+} concentration and varying Yb^{3+} content to study the effect of Yb^{3+} ions on the optical and sensing properties of the prepared ceramic.

This chapter is organized as follows: Section 4.2 offers information about the synthesis and characterization details of the prepared sample. The results of various characterizations are discussed in section 4.3. In subsection 4.3.1, the structural and microstructural studies were performed using XRD spectra and SEM micrographs. Subsection 4.3.2 discusses the upconversion luminescence spectra under the 980 nm laser wavelength excitation. The optimized ceramic is excited at various pump powers to examine the number of photons involved in the UC process (subsection 4.3.3). The time-resolved spectroscopy is given in subsection 4.3.4 for all the dopant concentrations. In subsection 4.3.5, the optical temperature sensitivity of ceramic is analyzed over a wide temperature range in thermally coupled levels ($^2H_{11/2}$ and $^4S_{3/2}$) using the fluorescence intensity ratio (FIR) approach. The findings and implications of this analysis are summarized in section 4.4.

4.2 SYNTHESIS AND CHARACTERIZATION DETAILS

The solid-state approach synthesized the ceramics with the configuration $BaBi_{2-0.04-y}Nb_2Er_{0.04}Yb_yO_9$ (y = 0.02, 0.04, 0.06, 0.08, 0.10, and 0.12). The initial precursors ($BaCO_3$, Bi_2O_3, Nb_2O_5, Er_2O_3, and Yb_2O_3) were obtained from Sigma Aldrich and had the greatest possible purity level (99.99%). The precursors were measured and weighed according to their stoichiometric proportions. The raw powders were manually crushed using a pestle and mortar in ethanol for 8 hours before being sent to a regulated high-temperature furnace that operated at 950°C for 3 hours. After being calcined, the granules were combined with polyvinyl alcohol (PVA), which was used to form the pellets in a circular shape. The round pellets of 10 mm in diameter were constructed by applying a pressure of approximately 5 MPa for 1 minute in a manual hydraulic press. After the pellets were made, they were

sintered in two stages: firstly, they rose to 500°C/h to eliminate the PVA, then reached about 1050°C and were held there for 2 hours. Cu-Kα radiations are used in conjunction with a sophisticated X-ray diffractometer manufactured by Bruker to investigate the phase structure of the sample. The upconversion luminescence (UCL) spectra were acquired with the help of the HORIBA PTI Quanta-master under the wavelength of 980 nm laser. The SEM micrographs from the cracked pallet sample were obtained using a ZEISS scanning electron microscope. The thermally dependent UCL emitting spectra were studied by positioning the synthesized material on the heaters while using a thermocouple to measure the temperature. The handcrafted heater that was controlled by variable voltage and coupled with a thermocouple and multimeter was used for the thermal sensing, resolution, and stability studies that were carried out.

4.3 RESULTS AND DISCUSSION

4.3.1 Structural and Microstructural Analysis

The XRD pattern of the prepared composition $BaBi_{2-0.04-y}Nb_2Er_{0.04}Yb_yO_9$ (y = 0.00, 0.02, 0.04, 0.06, 0.08, 0.10, and 0.12) was exhibited in **Figure 4.1(a)** after being sintered at a temperature of 1050℃ for 3 hours. The detected XRD peaks show a good correlation, as stated in the JCPDF file no. 00-012-0403, and the lack of secondary peaks imply that the dopants are fully soluble in the host lattice without causing structural modifications or other drastic changes. The detected Bragg reflections showed that the prepared ceramic had a single phase with an orthorhombic geometry and belonged to the phase group Fmmm. Also, the maximum peak intensity of the (115) plane in $BaBi_{2-0.04-y}Nb_2Er_{0.04}Yb_yO_9$ ceramic reflects the BLSF with m = 2, according to previous reports, the (112m + 1) plane relates to the high-intensity diffraction pattern for BLSF materials in the Aurivillius phase [15-

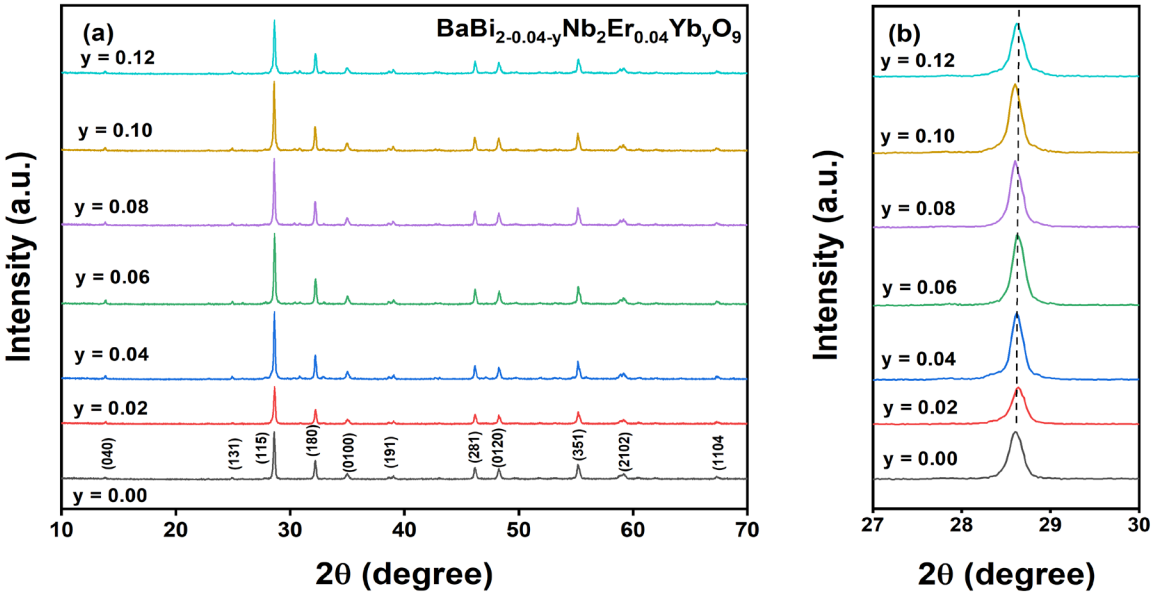

Figure 4.1: (a) XRD spectra of $BaBi_{2-0.04-y}Nb_2Er_{0.04}Yb_yO_9$ (y = 0.00, 0.02, 0.04, 0.06, 0.08, 0.10, and 0.12) ceramic (b) Peak displacement of (115) plane for various dopant concentrations [20].

18]. The ionic radii of Er^{3+} and Yb^{3+} are similar to one another such that the ions Yb^{3+} (1.22 Å) and Er^{3+} (1.25 Å) may favor occupying A-sites (Bi^{3+}) rather than B-sites (Nb^{5+}). This is because their effective ionic radii are the same as A site ions [19]. The density of sintered pellets was calculated using Archimedes' principle and recorded in Table 4.1. It was found that the density of the sintered pellets decreases with increasing dopant concentration. The tension within the host lattice due to the insertion of dopants causes the shifting of diffraction peaks slightly from their mean position and is given by Eq. (4.1) [20]:

$$\sigma = \frac{E}{2\upsilon}\left[\frac{\mathrm{Sin}\theta_n}{\mathrm{Sin}\theta_i} - 1\right] \qquad (4.1)$$

where υ represents Poison's coefficient, E is the modulus of elasticity, θ_n is the displaced value of 2θ, and θ_i is the reference angle. Eq. (4.1) states that a positive σ indicates lattice compression, whereas a negative σ suggests lattice expansion after dopant substitution. **Figure 4.1(b)** represents the shifting of peaks to slightly lower 2θ angles. Here, $\theta_n < \theta_i$ (E and υ are constants), therefore, σ comes out to be negative. This implies the expansion within the crystal lattice, which can also be verified from the increased cell volume

Table 4.1: Refinement and lattice parameters for $BaBi_{2-0.04-y}Nb_2Er_{0.04}Yb_yO_9$ compositions with constant Er^{3+} content and varying Yb^{3+} content [20].

Parameters	$BaBi_{2-0.04-y}Nb_2Er_{0.04}Yb_yO_9$						
	y = 0.00	y = 0.02	y = 0.04	y = 0.06	y = 0.08	y = 0.10	y = 0.12
R_{exp}	10.76	10.39	10.13	10.01	7.07	7.27	10.21
R_p	12.84	14.93	13.53	14.46	8.64	9.19	14.87
GoF	1.02	1.46	1.35	1.44	1.07	1.08	1.45
a (Å)	5.5439	5.5448	5.5450	5.5454	5.5479	5.5488	5.5497
b (Å)	5.5536	5.5551	5.5552	5.5561	5.5601	5.5612	5.5600
c (Å)	25.5975	25.5980	25.5989	25.5991	25.6178	25.6200	25.6219
V ($Å^3$)	788.111	788.467	788.537	788.728	790.229	790.581	790.597
Orthorhombic Distortion (b/a)	1.00174	1.00185	1.00183	1.00192	1.00219	1.00223	1.00185
Experimental Density, ρ (g/cm^3)	7.00919	6.83796	6.72015	6.77289	6.47426	6.76007	6.0106
Theoretical Density, ρ_0 (g/cm^3)	5.82447	5.88589	5.81015	5.9373	5.79818	5.94532	5.24095
Porosity $(1-\rho_0/\rho) \times 100\%$	16.90	13.92	13.54	12.33	10.44	12.05	12.80
Average Grain Size (μm)	1.39 ± 0.0278	1.54 ± 0.0125	1.67 ± 0.1365	1.78 ± 0.0889	1.89 ± 0.1129	1.92 ± 0.1761	1.45 ± 0.0295

parameters of the doped $BaBi_2Nb_2O_9$ ceramic, as shown in Table 4.1. This can also be explained by the constrained character of the $6s^2$ lone-pair of Bi^{3+} ions in the host lattice, which causes the expansion of unit cell volume and shifting of the peaks towards lower 2θ [10, 19]. The increased cell volume parameters (a, b, c) suggest the increased interplanar spacing, which decreases the 2θ values. Although the ionic radius of Er^{3+}, Yb^{3+}, and Bi^{3+} varies, the cell volume and lattice parameters of undoped $BaBi_2Nb_2O_9$ do not vary significantly. This could be ascribed to the formation of cationic vacancies, which maintain the lattice's electroneutrality and minimize crystal deformation [5].

The scanning electron microscopy images (SEIs) of the $BaBi_{2-0.04-y}Nb_2Er_{0.04}Yb_yO_9$ ceramics are shown in **Figure 4.2(a-g)**. These sintered ceramics possess a compact

microstructure. These plate-like structures are composed of irregularly aligned non-uniform grains. This is consistent with the standard properties of BLSFs. In Table 4.1, the reduction in porosity suggests that as the dopant concentration rises, the ceramic becomes denser. ImageJ software performs the necessary calculations to estimate the average particle size. In **Figure 4.2(h)**, the average grain size increases up to the optimum dopant concentration (y = 0.10), and then there is a subsequent reduction in the average grain size. This grain size variation may result from a rise in the electron charge distribution on the interface of Er^{3+}/Yb^{3+}. This increase in electron charge density slows grain boundary diffusion and inhibits grain development, resulting in smaller grain sizes [21, 22].

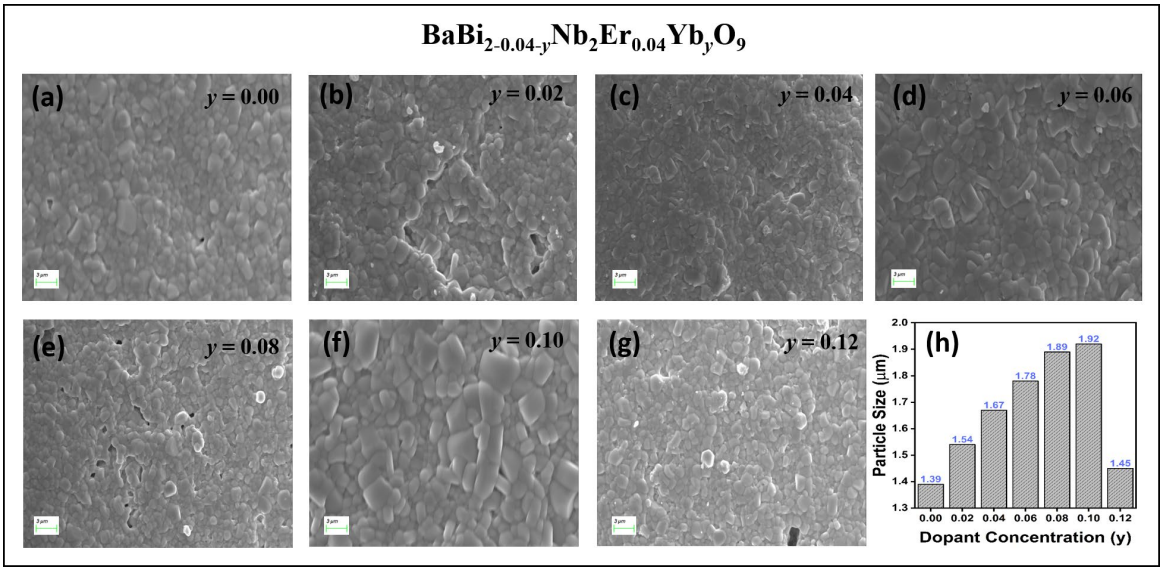

Figure 4.2: (a-g) SEM micrographs of $BaBi_{2-0.04-y}Nb_2Er_{0.04}Yb_yO_9$ with y = 0.00 to 0.12 sintered at 1050°C (h) Variation of particle size with all dopant concentrations [20].

4.3.2 Upconversion Luminescence Spectroscopy

To evaluate the effect of Yb^{3+} on the upconversion luminescence, the UC spectra for the ceramic $BaBi_{2-0.04-y}Nb_2Er_{0.04}Yb_yO_9$ with constant Er^{3+} content and variable Yb^{3+} content (y = 0.02, 0.04, 0.06, 0.08, 0.10, and 0.12) were measured. The UCL measurements were done under the illumination of 980 nm excitation, with a pumping power of 50 mW and an

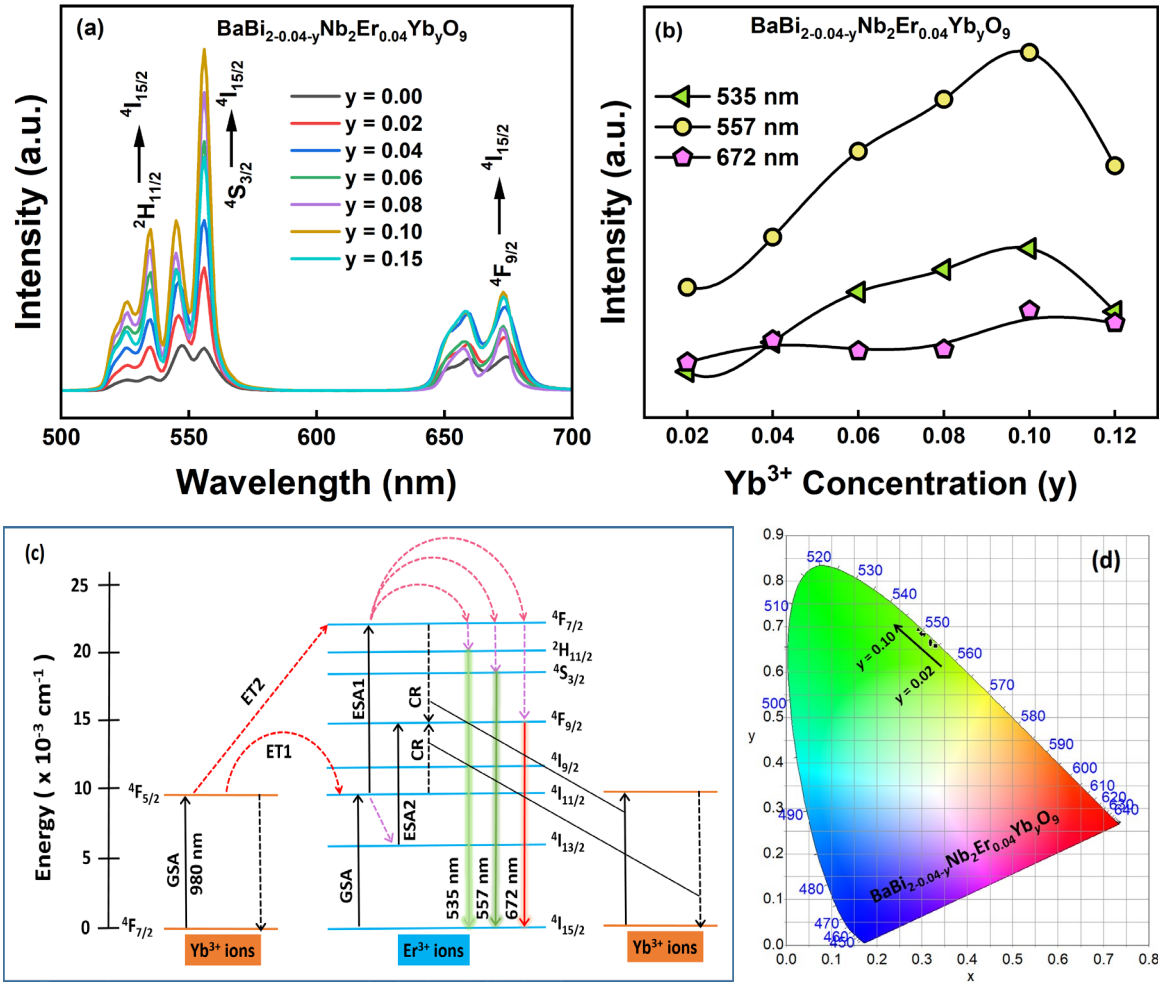

Figure 4.3: (a) UC emission spectra of $BaBi_{2-0.04-y}Nb_2Er_{0.04}Yb_yO_9$ for various Yb^{3+} concentrations under 980 nm excitation (b) Variation of intensity vs different concentrations of Yb^{3+} (c) Schematic depiction of the energy pathways of Er^{3+}/Yb^{3+} ions (d) CIE plot [20].

excitation source density of 3.25 W/cm^2, and are shown in **Figure 4.3(a)**. The transitions from $^2H_{11/2}$ to $^4I_{15/2}$ and $^4S_{3/2}$ to $^4I_{15/2}$ are responsible for the two strong green emission bands at 535 nm and 557 nm. Also, there is a notable red emission peak at 672 nm when the ions migrate from level $^4F_{9/2}$ to level $^4I_{15/2}$. The two partial bands near 672 nm are related to the split of the $^4F_{9/2}$ energy level by the crystal field that occurs due to the action of upconversion luminescence. Considering this, the collected UCL spectra of the prepared ceramic show a fair degree of consistency with previously published results [7, 8]. The changing UCL intensity as a function of dopants is illustrated in **Figure 4.3(b)**. Initially,

there is a rise in UCL intensity, and after reaching critical intensity at y = 0.10, it degrades with further insertion of dopants. This results from the concentration quenching effect, which occurs when dopant ions are so near to one another that energy transfer becomes easier, resulting in non-radiative emissions [1, 16]. Furthermore, the distances between dopant ions may be calculated using the Blasse formula, as shown in Eq. (4.2) [20].

$$R_c \approx 2\left[\frac{3V}{4\pi X_c Z}\right]^{\frac{1}{3}} \quad (4.2)$$

Here, the amount for quenching is X_c (0.04 + y), where V = 790.58 cm^3 is the volume of a unit cell in $BaBi_2Nb_2O_9$ ferroelectric ceramic, and Z = 4 shows the number of host cations. The R_c was calculated to be 13.92 Å. It was observed that in the absence of Yb^{3+} ions, the R_c value is 21.12 Å, whereas the R_c value is reduced in the presence of Yb^{3+} ions. This implies that the energy is efficiently transferring from Yb^{3+} to Er^{3+} ions. Notably, the upconversion emission process is often characterized by three processes, including ET (energy transfer), ESA (excited state absorption), and GSA (ground state absorption), along with CR and MPR (cross-relaxation processes and multi-phonon relaxation) [23, 24]. In **Figure 4.3(c)**, the schematic diagram of upconversion luminescence is portrayed using these processes. The 980 nm laser is illuminated on Yb^{3+} ions, and it absorbs energy via GSA and transfers it to a higher level at $^4I_{11/2}$ via ET1 and $^4F_{7/2}$ through ET2. The Er^{3+} ions may also absorb photons through GSA. Thus, level $^4I_{11/2}$ is prepared for the ESA to reach a higher energy level, i.e., $^4F_{7/2}$. Therefore, level $^4F_{7/2}$ is overpopulated by two processes, namely ET and ESA. The ions fall non-radiatively to levels $^2I_{11/2}$, $^4S_{3/2}$, and $^4F_{9/2}$ via MPR. From these levels, the ions transit to the lower level $^4F_{15/2}$, resulting in two green emission bands and one red emission band at 535 nm, 557 nm, and 672 nm, respectively. Another decay channel created by the cross-relaxation tracks (CR1 and CR2) is responsible for the

increased red emission when the Yb^{3+} content increases. Besides, emission spectrum data from prepared ceramics were used to get the CIE chromaticity coordinates (x, y) for dopant concentrations. The predicted CIE points, which are sited in the green region and then become bright green as dopant concentrations rise, are shown in **Figure 4.3(d)**.

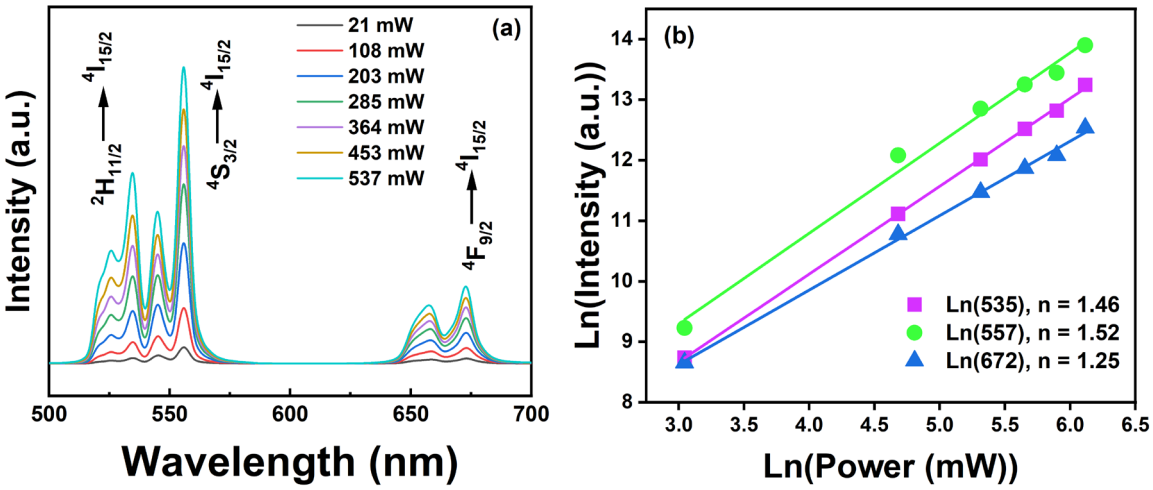

Figure 4.4: (a) UCL emission spectra with different pump power ranging from 21 to 537 mW (b) Plot of Ln(power) vs Ln(UC intensity) [20].

4.3.3 Pump Power Dependence on UCL

To learn more about how UCL works, transitions of levels $^2H_{11/2}$, $^4S_{3/2}$, and $^4F_{9/2}$ to level $^4I_{15/2}$ in $BaBi_{2-0.04-y}Nb_2Er_{0.04}Yb_yO_9$ (y = 0.10) ceramic at distinct pump powers range from 21 mW to 453 mW with an excitation source density of 1.37 W/cm^2 to 29.51 W/cm^2, as depicted in **Figure 4.4(a)**. It has been found that the UCL gets stronger as the pump power goes up. The relation between pump power and intensity is given in Eq. (4.3) [20, 25, 26]:

$$I_{UP} \propto P^n \tag{4.3}$$

where n is the number of low-energy photons required for the UCL to proceed, P is the pump power, and I_{UP} refers to the intensity of UC luminescence. **Figure 4.4(b)** depicts the log-log curve of the intensity versus the excitation pump power. The magnitude of n for the green band near 535 and 557 nm and the red emissions band at 672 nm is determined by

the slope of the logarithmic plot, and it comes out to be 1.46, 1.52, and 1.25, respectively. Therefore, the red and green UC bands are produced by the emission of two low-energy photons. The n values of both colors have been rounded to 2 because various upconversion processes are involved [11, 13].

4.3.4 Time-Resolved Spectroscopy

A pulsed laser source was used to analyze the lifetime decay of $BaBi_{2-0.04-y}Nb_2Er_{0.04}Yb_yO_9$ (y = 0.04, 0.08, 0.10, and 0.12) ceramic for 557 nm transition from $^2S_{3/2}$ to $^4I_{15/2}$ energy level under 980 nm excitation wavelength. **Figure 4.5(a-d)** depicts the decay overview of $BaBi_{2-0.04-y}Nb_2Er_{0.04}Yb_yO_9$ ceramics. The curves were fitted using Eq. (4.4) (tri exponential decay fit) [20]:

$$I(t) = I_0 + A_1 \exp\left(-\frac{t}{\tau_1}\right) + A_2 \exp\left(-\frac{t}{\tau_2}\right) + A_3 \exp\left(-\frac{t}{\tau_3}\right) \quad (4.4)$$

where I_0 corresponds to the intensity at the time t = 0, A_1, A_2, A_3 are the fitting factors, and τ_1, τ_2, and τ_3 are luminescence decay times. The average lifetime is evaluated using Eq. (4.5) [20]:

$$<\tau> = \frac{A_1\tau_1^2 + A_2\tau_2^2 + A_3\tau_3^2}{A_1\tau_1 + A_2\tau_2 + A_3\tau_3} \quad (4.5)$$

Figure 4.5(e) depicts the predicted lifespan of Er^{3+} doped and Er^{3+}/Yb^{3+} doped $BaBi_{2-0.04-y}Nb_2Er_{0.04}Yb_yO_9$ ceramics. The calculated lifetime of $BaBi_{2-0.04-y}Nb_2Er_{0.04}Yb_yO_9$ ceramic varies from 28.74 μs to 40.11 μs for the co-doped system. An increase in lifespan suggests effective energy transmission in dopant ions, leading to non-radiative transition at a higher doping content [20]. However, the time decay in Er^{3+} doped ceramic is 41.29 μs greater than co-doped ceramic. Thus, the efficiency of energy transfer (ET) in co-doped $BaBi_{2-0.04-y}Nb_2Er_{0.04}Yb_yO_9$ ceramic can be calculated by Eq. (4.6) [20]:

$$\eta = 1 - \frac{\tau_a}{\tau_b} \quad (4.6)$$

where τ_a is the mean lifetime for Er^{3+}/Yb^{3+} co-doped ceramic and τ_b is the average lifetime for Er^{3+} doped ceramic [20]. The efficiency of the energy transfer process is influenced by 32% by adding Yb^{3+} to the host lattice at a minimum Yb^{3+} concentration.

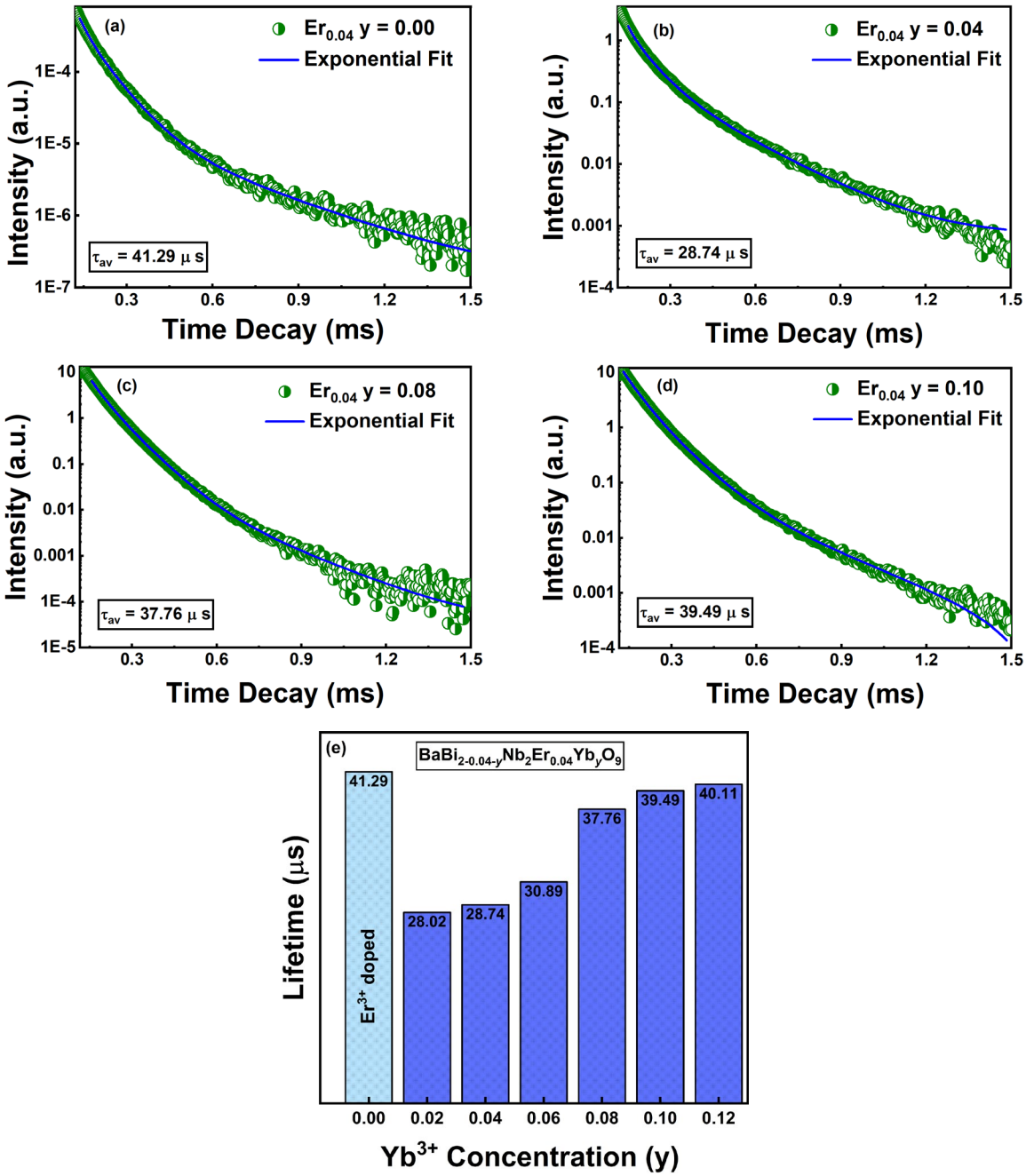

Figure 4.5: (a-d) Time decay profile of $BaBi_{2-0.04-y}Nb_2Er_{0.04}Yb_yO_9$ composition with an exponential fit (e) Variation of lifetime of $BaBi_{2-0.04-y}Nb_2Er_{0.04}Yb_yO_9$ ceramic with Yb^{3+} concentrations [20].

4.3.5 Optical Temperature Sensing

In order to evaluate the possibility of using the present synthesized ceramic in optical temperature measurements, the Fluorescence Intensity Ratio (FIR) approach is applied. For non-contact temperature measurements, the FIR is a basic approach that does not depend on variations in excitation intensity. This method was employed widely for temperature sensing in several host materials treated with RE^{3+} [27-29]. The sensing behavior in $BaBi_{2-0.04-y}Nb_2Er_{0.04}Yb_yO_9$ system is investigated by varying Yb^{3+} concentrations (y = 0.06 and 0.10). This FIR technique compares the UC intensity of two thermocouple energy levels (green emission bands) during transitions $^2H_{11/2}$ to $^4I_{15/2}$ and $^4S_{3/2}$ to $^4I_{15/2}$. **Figure 4.6(a, b)** represents the temperature-dependent UCL spectra for the $BaBi_{2-0.04-y}Nb_2Er_{0.04}Yb_yO_9$ (y = 0.06 and 0.10) at temperatures ranging from 303 to 573 K. It can be seen that in both the co-doped systems (y = 0.06 and 0.10), the UC emission intensity decreases with increasing temperatures. However, the FIR values follow the increasing trend, as demonstrated in **Figure 4.6(c)**. The mathematical expression of FIR is given by Eq. (4.7) [20]:

$$\mathrm{FIR} = \frac{I_H}{I_S} = C \exp\left(-\frac{\Delta E}{K_B T}\right) \tag{4.7}$$

where I_H and I_S represent the integrated intensity of the green band at 535 nm and 557 nm, respectively, ΔE denotes the energy gap of levels $^4S_{3/2}$ and $^2H_{11/2}$, and C is the constant depending upon the transitions and degeneracy factor of thermally coupled levels (TCLs). To calculate constant (C) and energy gap (ΔE), Eq. (4.7) can be put in linear form, as shown in Eq. (4.8):

$$\mathrm{Ln(FIR)} = -\left(\frac{\Delta E}{K_B}\right)\left(\frac{1}{T}\right) + \mathrm{LnC} \tag{4.8}$$

The curve of ln(FIR) and the negative of temperature are illustrated in **Figure 4.6(d)**. The slope of this graph analyzes the value of $\Delta E/K_B$ and the ln C intercept. For y =

0.06 and 0.10, $\Delta E/K_B$ is -1015.67 and -925.38, while C is 2.545 and 2.260, respectively. These FIR characteristics define the optical thermometric sensitivity of the fabricated ceramic $BaBi_{2-0.04-y}Nb_2Er_{0.04}Yb_yO_9$. The external temperature influences the population redistribution ability (PRA) of thermally coupled levels $^4S_{3/2}$ and $^2H_{11/2}$ and can be expressed by Eq. (4.9) [20]:

$$\text{PRA} = \frac{C}{C + \exp\left(\frac{\Delta E}{K_B T}\right)} \tag{4.9}$$

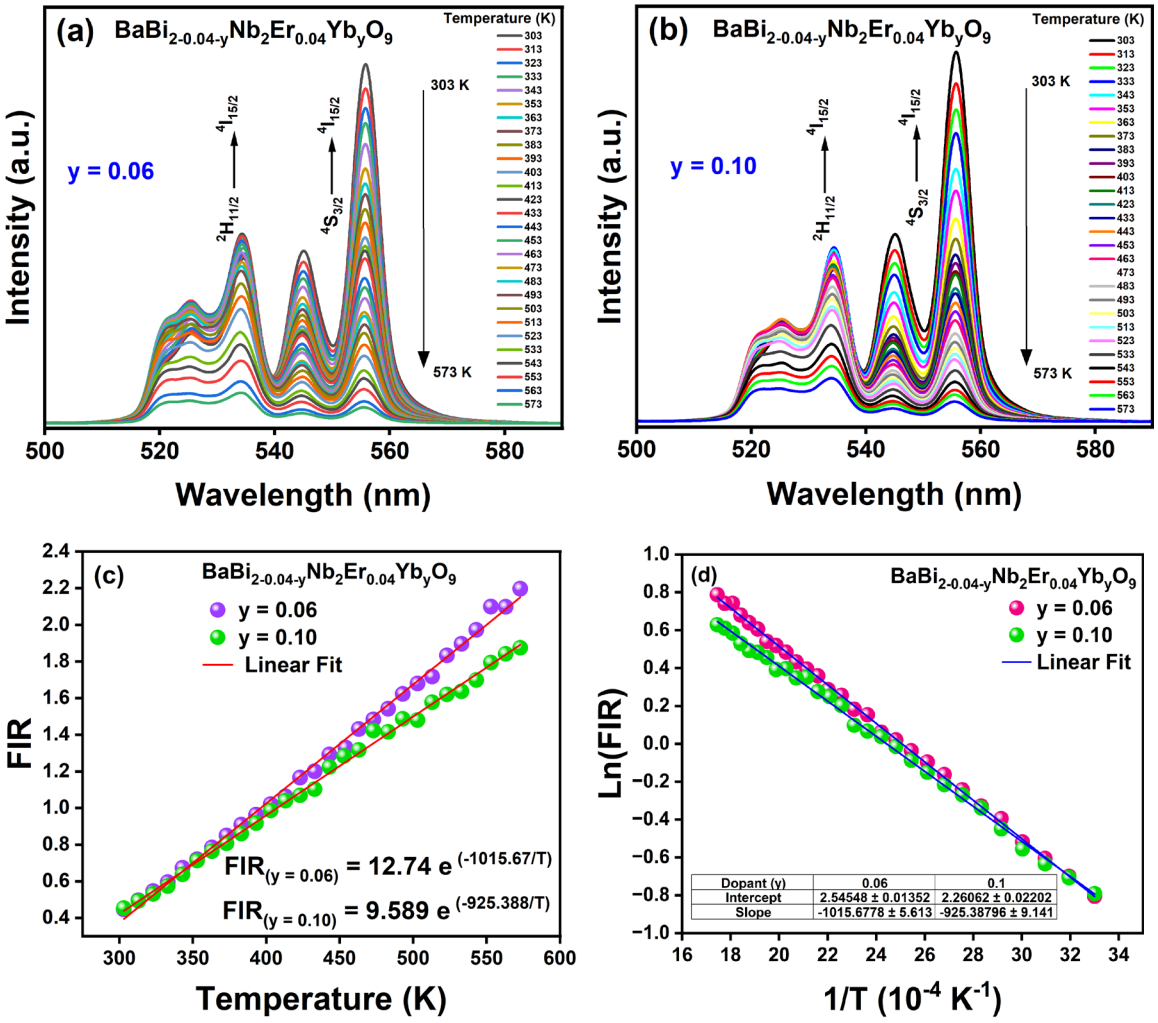

Figure 4.6: (a-b) Temperature-dependent UC emission pattern of $BaBi_{2-0.04-y}Nb_2Er_{0.04}Yb_yO_9$ at y = 0.06 and 0.10 (c) Variation of FIR vs temperature at y = 0.06 and 0.10 (d) Plot of Ln(FIR) vs negative temperature [20].

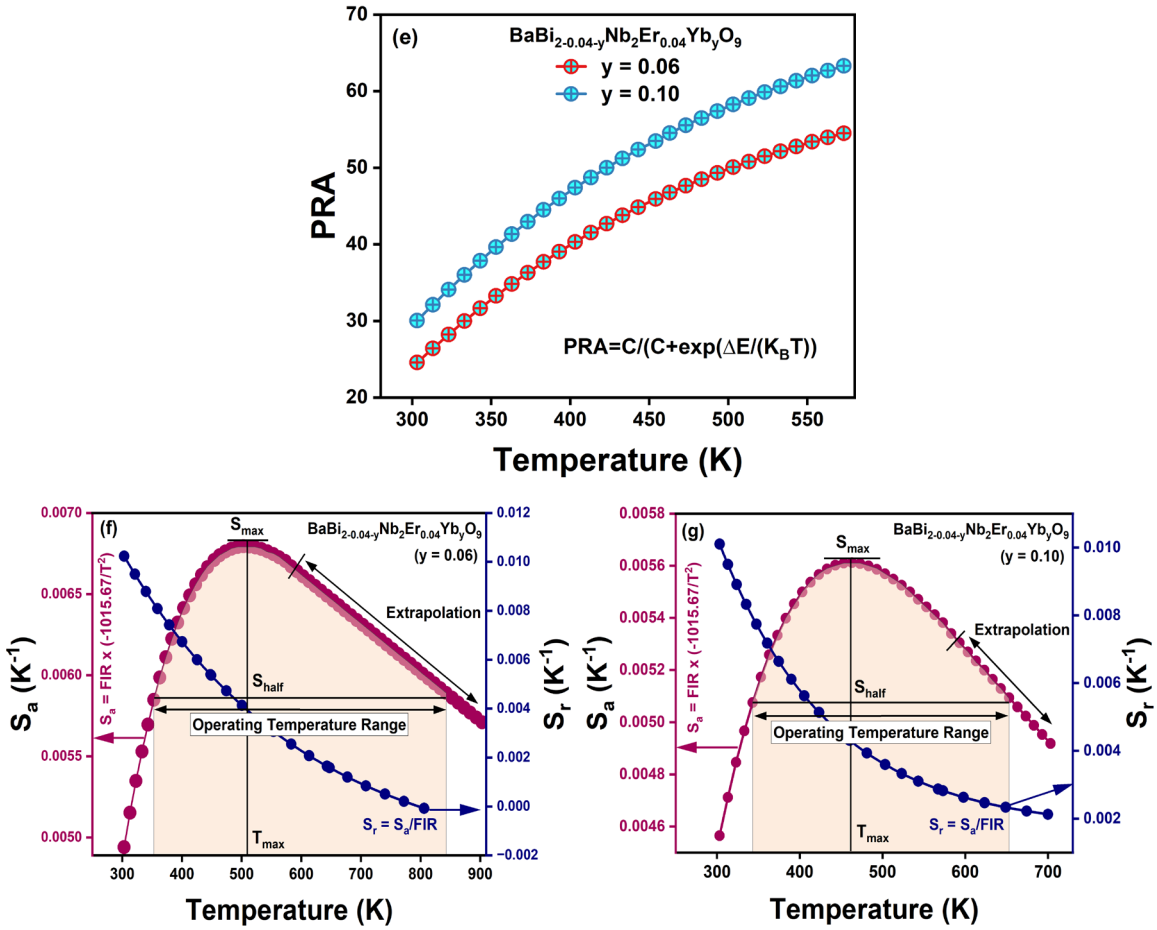

Figure 4.6: (e) PRA values of thermally coupled levels ($^2H_{11/2}$ and $^4S_{3/2}$) at y = 0.06 and 0.10 (f-g) S_a and S_r as a function of temperature for $BaBi_{2-0.04-y}Nb_2Er_{0.04}Yb_yO_9$ ceramic at y = 0.06 and 0.10 with operating temperature range (shaded region) [20].

The PRA values for $BaBi_{2-0.04-y}Nb_2Er_{0.04}Yb_yO_9$ (y = 0.06 and 0.10) ceramics are given in **Figure 4.6(e)**. It seems that the population of these thermally coupled levels increases with temperature. The absolute sensitivity (S_a) of a material is defined by Eq. (4.10) as the variation rate of FIR with temperature [20].

$$S_a = \frac{d(FIR)}{dT} = \frac{d\left(C\exp\left(-\frac{\Delta E}{K_B T}\right)\right)}{dT} = C\exp\left(-\frac{\Delta E}{K_B T}\right)\left(\frac{\Delta E}{K_B T^2}\right) \quad (4.10)$$

By multiplying the absolute sensitivity with the negative FIR, the relative sensitivity (S_r) can be calculated, as employed in Eq. (4.11) [20, 30, 31]:

$$S_r = \frac{1}{FIR} \times S_a = \left(\frac{\Delta E}{K_B T^2}\right) \quad (4.11)$$

The S_a and S_r for $BaBi_{2-0.04-y}Nb_2Er_{0.04}Yb_yO_9$ (y = 0.06 and 0.10) are displayed in **Figure 4.6(f, g)**. In both cases, the absolute sensitivity increases with temperature up to the maximum T_a. For y = 0.06 and 0.10, S_a is 0.69% K^{-1} and 0.58% K^{-1} at T_a 523 K and 463 K, respectively. To check the operating temperature range for sensing application (denoted by the shaded region in **Figure 4.6(f, g)**), the S_a values are extrapolated using Eq. (4.9), where the S_a is higher than half of its maximum value (S_{half}). It has been found that the sensitivity of lower dopant concentrations (y = 0.06) shows higher sensitivity than the optimal dopant concentrations (y = 0.10), and the extrapolated data reveals the gradual decrease in the case of y = 0.06 whereas, in y = 0.10 the absolute sensitivity decreases exponentially. The operational temperature region is extended to a wider temperature range in y = 0.06 compared to y = 0.10, as shown in **Figure 4.6(f, g)**. These observations suggest that the sensing characteristics of the $BaBi_{2-0.04-y}Nb_2Er_{0.04}Yb_yO_9$ ceramic can be tuned by altering the dopant concentration. The material sensitivity is suitable if the theoretically calculated ΔE_{th} and the experimentally matched ΔE_{ex} are substantially comparable. The experimental value for ΔE_{ex} may be derived from **Figure 4.6(d)**, and the deconvolution of UC spectra using the Viogt fit yields the theoretical value for ΔE_{th}, shown in **Figure 4.7(a, b)**. According to Eq. (4.12), the inaccuracy (δ) in $BaBi_{2-0.04-y}Nb_2Er_{0.04}Yb_yO_9$ ceramic at y = 0.06 and 0.10 equals 2.89% and 4.01%, respectively [20].

$$\delta = \frac{|\Delta E_{th} - \Delta E_{ex}|}{\Delta E_{th}} * 100\% \quad (4.12)$$

A sensor's repeatability (R) and resolution (δT) are essential to determine its efficacy. The mathematical expression of these parameters is stated in Eqs. (4.13 and 4.14) [20, 32]:

$$R = 1 - \text{Max}\frac{(\Delta_{Av} - \Delta_{Sp})}{\Delta_{Av}} \quad (4.13)$$

$$\delta T = \frac{1}{S_r} \times \frac{\delta\Delta}{\Delta} \tag{4.14}$$

where δ_Δ/Δ is the device's precision, Δ_{Av} and Δ_{Sp} are the mean and specific parameters of FIR with 17 cycles within temperature 303-573 K. The repeatability and resolution of the produced ceramic are shown in **Figure 4.8(a, b)**, respectively. **Figure 4.8(a)** displays no discernible shift in the FIR values of both concentrations anywhere in the temperature range from 303 K to 573 K. In **Figure 4.8(b)**, the resolution improves from 2.74 to 9.72

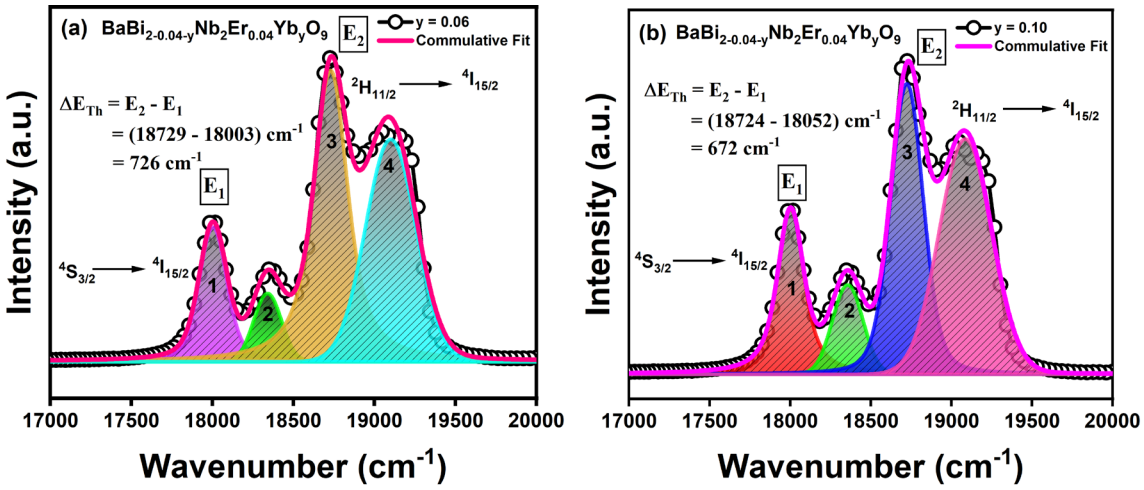

Figure 4.7: (a-b) Deconvolution of temperature-dependent UC spectra by Voigt fit for $BaBi_{2-0.04-y}Nb_2Er_{0.04}Yb_yO_9$ at y = 0.06 and 0.10 [20].

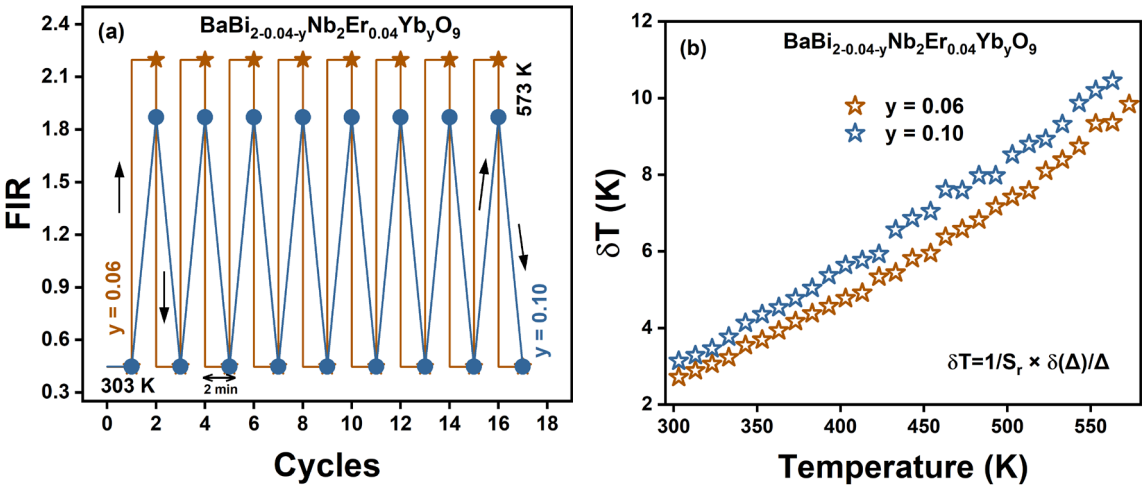

Figure 4.8: (a) Reliability test of $BaBi_{2-0.04-y}Nb_2Er_{0.04}Yb_yO_9$ ceramic in the temperature range 303-573 K with a stabilization period of 2 min (b) Resolution of temperature between 303 K and 573 K [20].

and 3.13 to 10.45 for y = 0.06 and 0.10, respectively. Table 4.2 compares the sensitivity of prepared $BaBi_{2-0.04-y}Nb_2Er_{0.04}Yb_yO_9$ ceramic to that of currently published Er^{3+}/Yb^{3+} co-doped host materials. This chapter demonstrates the ability of non-contact temperature sensors to function throughout a broad and high-temperature range, with a maximum temperature of 523 K, while maintaining excellent sensitivity. Consequently, it may concluded that the ceramic $BaBi_{2-0.04-y}Nb_2Er_{0.04}Yb_yO_9$ is a competent sensor material that has the potential to be further investigated for use in the applications area of optical temperature sensors.

Table 4.2: Temperature sensing parameters of various Er^{3+}/Yb^{3+} co-doped host materials in the different temperature ranges [20].

Host Material	ΔE (cm^{-1})	Temp. Range (K)	T_a (K)	S_a (K^{-1})	S_r (K^{-1})	T_r (K)	References
$BaTiO_3$: Er/Yb	600	125-430	410	0.19%	-	-	[2]
$CaBi_2Ta_2O_9$: Er/Yb	1181	153-603	590	0.39%	-	-	[3]
$Na_{0.5}Bi_{0.5}TiO_3$: Er/Yb	706.68	173-553	493	0.35%	-	-	[8]
La_2O_3: Er/Yb	566	303-600	303	0.91%	-	-	[9]
$Ba_2NaNb_5O_{15}$: Er/Yb	735.5	298-573	373	0.68%	0.90%	298	[11]
$La_2Ti_2O_7$: Er/Yb	683	93-773	493	0.29%	0.41%	300	[13]
BNT-SBT: Er/Yb	-	303-573	363	0.49%	-	-	[14]
$Na_{0.5}Bi_{2.5}Ta_2O_9$: Er/Yb	-	153-483	483	0.78%	5.99%	153	[26]
$La_2Ti_2O_7$: Er/Yb	760	333-553	525	0.57%	0.63%	333	[27]
$BaGd_2O_4$: Er/Yb	873.94	298-573	573	0.42%	-	-	[28]
$Na_{0.5}Er_{0.5}Bi_4Ti_4O_{15}$	500.1	175-500	380	0.17%	-	-	[31]
$Sr_{0.75}Ba_{0.25}Nb_2O_6$: Er/Yb	-	310-470	410	0.54%	0.85%	310	[33]
$(Bi_{0.5}Er_{0.1}Yb_{0.4})Ta_7O_{19}$	660.65	303-693	475	0.162%	1.04%	303	[34]
$BaBi_{2-0.04-y}Nb_2Er_{0.04}Yb_yO_9$ (y=0.06)	705	303-573	523	0.69%	1.10%	303	**This work**
$BaBi_{2-0.04-y}Nb_2Er_{0.04}Yb_yO_9$ (y=0.10)	645	303-573	463	0.58%	1.01%	303	**This work**

4.4 SUMMARY

The co-doped Er^{3+}/Yb^{3+} ferroelectric ceramic $BaBi_{2-0.04-y}Nb_2Er_{0.04}Yb_yO_9$ (y = 0.00, 0.02, 0.04, 0.06, 0.08, 0.10, and 0.12) produced by the solid-state reaction technique at 1050°C have been studied for upconversion luminescence and temperature sensing applications. The XRD investigation confirmed the ceramic's orthorhombic geometry. The microstructure seen by SEM resembles plate-like formations and comprises non-uniform grains with irregular orientation. An increase in grain size with Yb^{3+} content up to y = 0.10 was found to promote upconversion luminescence. Two bright green bands at 535 and 557 nm and a detectable red spectrum near 672 nm were observed in upconversion luminescence (UCL) spectra, corresponding to an excitation wavelength of 980 nm. The effective energy transfer process from Yb^{3+} to Er^{3+} ions is supported by decay time measurements, which increase with increasing Er^{3+}/Yb^{3+} content because of the non-radiative transition at higher doping concentrations. The pump power dependence upon the UC luminescence intensity for an optimum Yb^{3+} content y = 0.10 reveals that green and red UC emissions involve two photons. Er^{3+}/Yb^{3+} co-doped $BaBi_{2-0.04-y}Nb_2Er_{0.04}Yb_yO_9$ ceramic system with y = 0.06 and 0.10 exhibit a maximum absolute sensitivity (S_a) of 0.69% K^{-1} and 0.58% K^{-1} at T_a = 523 K and 463 K, respectively, and maximum relative sensitivity (S_r) of 1.10% and 1.01% at T_r = 303 K, suggesting a viable contactless temperature sensor with tunable sensitivity.

After a thorough analysis of upconversion luminescence and optical temperature sensing properties of Er^{3+}/Yb^{3+} co-doped $BaBi_2Nb_2O_9$ ferroelectric system, it was found that the produced ceramic is significantly affected by the presence of Yb^{3+} ions. Therefore, to delve further into the impact of co-doping on dielectric and ferroelectric behavior, the

next chapter thoroughly investigates the ferroelectric relaxor properties of the co-doped system, which has not been addressed in the current chapter.

4.5 REFERENCES

[1] Z. Tianmin, Z. Yanqiu, W. Zhongli, and C. Baojiu, "Concentration effect and temperature quenching of upconversion luminescence in $BaGd_2ZnO_5$: Er^{3+}/Yb^{3+} phosphor," *Journal of Rare Earths*, vol. 33, no. 7, pp. 686-692, 2015.

[2] M. K. Mahata, T. Koppe, T. Mondal, C. B. Sewitz, K. Kumar, V. K. Rai, H. Hofsass, and U. Vetter, "Incorporation of Zn^{2+} ions into $BaTiO_3$: Er^{3+}/Yb^{3+} nanophosphor: An effective way to enhance upconversion, defect luminescence, and temperature sensing," *Physical Chemistry Chemical Physics*, vol. 17, pp. 20741-20753, 2015.

[3] Q. Cao, D. Peng, H. Zou, J. Li, X. Wang, and X. Yao, "Up-conversion luminescence of Er^{3+} and Yb^{3+} co-doped $CaBi_2Ta_2O_9$ multifunctional ferroelectrics," *Journal of Advanced Dielectrics*, vol. 4, no. 03, 1450018, 2014.

[4] V. Lojpur, G. Nikoli, and M. D. Dramianin, "Luminescence thermometry below room temperature via up-conversion emission of Y_2O_3: Yb^{3+}, Er^{3+} nanophosphors," *Journal of Applied Physics*, vol. 115, 203106, 2014.

[5] R. Bokolia, O. P. Thakur, V. K. Rai, S. K. Sharma, and K. Sreenivas, "Electrical properties and light up conversion effects in $Bi_{3.79}Er_{0.03}Yb_{0.18}Ti_{3x}W_xO_{12}$ ferroelectric ceramic," *Ceramics International*, vol. 42, pp. 5718-5730, 2016.

[6] L. Mukhopadhyay, V. K. Rai, R. Bokolia, and K. Sreenivas, "980 nm excited $Er^{3+}/Yb^{3+}/Li^{+}/Ba^{2+}$: $NaZnPO_4$ upconverting phosphors in optical thermometry" *Journal of Luminescence*, vol. 187, pp. 368-377, 2017.

[7] P. Du, L. Luo, W. Li, and Q. Yue, "Upconversion emission in Er-doped and Er/Yb-codoped ferroelectric $Na_{0.5}Bi_{0.5}TiO_3$ and its temperature sensing application," *Journal of Applied Physics*, vol. 116, 014102, 2014.

[8] P. Du and J. S. Yun, "Effect of molybdenum on upconversion emission and temperature sensing properties in $Na_{0.5}Bi_{0.5}TiO_3$: Er/Yb ceramics," *Ceramics International*, vol. 41, pp. 6710-6714, 2015.

[9] R. Dey and V. K. Rai, "Yb^{3+} sensitized Er^{3+} doped La_2O_3 phosphor in temperature sensors and display devices," *Dalton Transactions*, vol. 43, pp. 111-118, 2014.

[10] M. X. Façanha, J. P. C. do Nascimento, M. A. S. Silva, M. C. C. Filho, A. N. L Marques, A. G. Pinheiro, and A. S. B. Sombra, "Up-conversion emission of Er^{3+}/Yb^{3+} co-doped $BaBi_2Nb_2O_9$ (BBN) phosphors," *Journal of Luminescence*, vol. 183, pp. 102-107, 2017.

[11] F. Luo, J. Xing, Y. Qin, Y. Zhong, F. Shang, and G. Chen, "Up-conversion luminescence, temperature sensitive and energy storage performance of lead-free

transparent Yb^{3+}/Er^{3+} co-doped $Ba_2NaNb_5O_{15}$ glass-ceramics," *Journal of Alloys and Compounds*, vol. 910, 164859, 2022.

[12] A. Pandey, S. Som, V. Kumar, V. Kumar, K. Kumar, V. K. Rai, and H. C. Swart, "Enhanced upconversion and temperature sensing study of Er^{3+}-Yb^{3+} co-doped tungsten-tellurite glass," *Sensors and Actuators B: Chemical*, vol. 202, pp. 1305-1312, 2014.

[13] R. Swami, A. Shandilya, A. K. Shukla, P. S. Kumar, and K. Sreenivas, "Luminescence intensity ratio based wide range contactless temperature sensing properties of Er^{3+}/Yb^{3+} ions co-doped $La_2Ti_2O_7$ ceramics," *Journal of Alloys and Compounds*, vol. 948, 169610, 2023.

[14] P. Wang, X. Wang, G. Li, Y. Li, X. Yao, and Z. Pan, "Energy density capability and upconversion luminescence in Er^{3+}/Yb^{3+}-codoping BNT-based ferroelectric thin films," *Ceramics International*, vol. 48, no. 19, pp. 28606-28613, 2022.

[15] A. Banwal, and R. Bokolia, "Enhanced upconversion luminescence and optical temperature sensing performance in Er^{3+} doped $BaBi_2Nb_2O_9$ ferroelectric ceramic," *Ceramics International*, vol. 48, no. 2, pp. 2230-2240, 2022.

[16] R. Bokolia, O. P. Thakur, V. K. Rai, S. K. Sharma, and K. Sreenivas, "Dielectric, ferroelectric and photoluminescence properties of Er^{3+} doped $Bi_4Ti_3O_{12}$ ferroelectric ceramics," *Ceramics International*, vol. 41, no. 4, pp. 6055-6066, 2015.

[17] A. Banwal and R. Bokolia, "Effect of Er^{3+} ion doping on structural, ferroelectric and up/down conversion luminescence in $BaBi_2Nb_2O_9$ ceramic," *Materials Today: Proceedings*, vol. 47, part 14, pp. 4692-4695, 2021.

[18] A. Banwal, and R. Bokolia, "Phase evolution and microstructure of $BaBi_2Nb_2O_9$ ferroelectric ceramics," *Materials Today: Proceedings*, vol. 46, part 20, pp. 10121-10124, 2020.

[19] R. D. Shannon, "Revised effective ionic radii and systematic studies of interatomic distances in halides and chalcogenides," *Acta Crystallographica*, vol. A32, pp. 751-767, 2016.

[20] A. Banwal and R. Bokolia, "Efficient tunable temperature sensitivity in thermally coupled levels of Er^{3+}/Yb^{3+} co-doped $BaBi_2Nb_2O_9$ ferroelectric ceramic," *Journal of Luminescence*, vol. 263, 120071, 2023.

[21] A. Banwal and R. Bokolia, "Thermometric sensing performance in Erbium modified $SrBi_{2-x}Nb_2Er_xO_9$ ferroelectric ceramic for optoelectronic devices," *Ceramics International*, vol. 48 part 23A, pp. 34405-34414, 2022.

[22] F. Wang, Y. Han, C. S. Lim, Y. Lu, J. Wang, J. Xu, H. Chen, C. Zhang, M. Hong, and X. Liu, "Simultaneous phase and size control of upconversion nanocrystals through lanthanide doping," *Nature*, vol. 463, pp. 1061-1065, 2010.

[23] P. Du, L. Luo, W. Li, and Q. Yue, "Upconversion emission in Er-doped and Er/Yb-codoped ferroelectric $Na_{0.5}Bi_{0.5}TiO_3$ and its temperature sensing application," *Journal of Applied Physics*, vol. 116, 014102, 2014.

[24] J. Shi, J. Suna, B. Fanga, Q. Dua, S. Zhanga, and J. Ding, "Photoluminescence performance of Er/Yb co-doped NBT ceramics prepared via hydrothermal method," *Journal of Physics and Chemistry of Solids*, vol. 121, pp. 228-235, 2018.

[25] R. Bokolia, M. Mondal, V. K. Rai, and K. Sreenivas, "Enhanced infrared-to-visible up-conversion emission and temperature sensitivity in (Er^{3+}, Yb^{3+}, and W^{6+}) tri-doped $Bi_4Ti_3O_{12}$ ferroelectric oxide," *Journal of Applied Physics*, vol. 121, 084101, 2017.

[26] P. Li, Z. Zhang, Z. Xu, H. Sun, Q. Zhang, and X. Hao, "Photomodulated cryogenic temperature sensing through a photochromic reaction in $Na_{0.5}Bi_{2.5}Ta_2O_9$: Er/Yb multicolour upconversion," *Optics Express*, vol. 31, no. 5, pp. 7047-7059, 2023.

[27] Y. Liu, G. Bai, E. Pan, Y. Hua, L. Chen, and S. Xu, "Upconversion fluorescence property of Er^{3+}/Yb^{3+} co-doped lanthanum titanate microcrystals for optical thermometry," *Journal of Alloys and Compounds*, vol. 822, 153449, 2014.

[28] Z. Guan, X. Li, R. Shen, Z. Tian, H. Yu, Y. Cao, Y. Wang, J. Zhang, S. Xu, and B. Chen, "Intense red up-conversion luminescence and temperature sensing property of Yb^{3+}/Er^{3+} co-doped $BaGd_2O_4$ phosphors," *Spectrochimica Acta, Part A: Molecular and Biomolecular Spectroscopy*, vol. 284, 121805, 2023.

[29] P. Du, L. Luo, W. Li, and Q. Yue, "Upconversion emission in Er-doped and Er/Yb-codoped ferroelectric $Na_{0.5}Bi_{0.5}TiO_3$ and its temperature sensing application," *Journal of Applied Physics*, vol. 116, 014102, 2014.

[30] J. Xing, F. Shang, and G. Chen, "Upconversion luminescence of Yb^{3+}/Er^{3+} co-doped $NaSrPO_4$ glass ceramic for optical thermometry," *Ceramics International*, vol. 147, pp. 8330-8337, 2021.

[31] X. Hui, D. Peng, H. Zou, J. Li, Q. Cao, Y. Li, X. Wang, and X. Yao, "A new multifunctional Aurivillius oxide $Na_{0.5}Er_{0.5}Bi_4Ti_4O_{15}$: Up-conversion luminescent, dielectric, and piezoelectric properties," *Ceramics International*, vol. 40, part 4A, pp. 12477-12483, 2014.

[32] M. D. Dramićanin, "Trends in luminescence thermometry," *Journal of Applied Physics*, vol. 128, 040902, 2020.

[33] J. Song, F. Luo, and G. Chen, "A new photoelectric niobate glass ceramic material: Up-conversion optical thermometry and dielectric energy storage," *Ceramics International*, vol. 49, no. 16, pp. 27266-27276, 2023.

[34] H. Cui, Y. Cao, Y. Zhang, L. Cao, S. Ran, X. Wang, D. Wu, X. Li, X. Zhang, and Baojiu Chen, "Extremely intense green up-conversion luminescent and ultra-high temperature sensitivity in Er^{3+}/Yb^{3+} co-doped $BiTa_7O_{19}$ phosphors," *Journal of Luminescence*, vol. 241, 118484, 2022.

5

CHAPTER

Structural, Dielectric, Ferroelectric, and Energy Storage Density Properties of Undoped, Er^{3+} Doped, and Er^{3+}/Yb^{3+} Co-Doped $BaBi_2Nb_2O_9$ Ferroelectric Ceramic

- *This chapter gives detailed insight into the structural, dielectric, ferroelectric, and energy storage density performance of undoped, Er^{3+} doped, and Er^{3+}/Yb^{3+} co-doped $BaBi_2Nb_2O_9$ ferroelectric ceramic.*
- *FTIR and Raman spectroscopy provide details of various vibrational modes of the prepared BBN compositions.*
- *Temperature-dependent dielectric studies show considerable dispersion below and above maximum temperature (T_m), and the dielectric constant (ε') decreases with an increase in frequency. The dielectric loss (ε") curves are quite diffused, and shifts in the maxima with frequency have been observed, thus validating the relaxor behavior of all the prepared BBN compositions.*
- *The slimmer PE curves were obtained under moderate electric fields ranging from 75 kV/cm to 100 kV/cm. The energy storage efficiency (η) obtained for undoped, Er^{3+} doped, and Er^{3+}/Yb^{3+} co-doped BBN ceramics are 78.25%, 83.39%, and 90.87%, respectively.*
- *W, W_{rec}, and η showed decent temperature stability in the temperature range varying from 303 K to 415 K, suggesting that the prepared material may help develop advanced electronic equipment for energy storage applications.*

5.1 INTRODUCTION

Chapter 4 explores the impact of Er^{3+} and Yb^{3+} ions on the upconversion luminescence and optical temperature sensing properties of $BaBi_2Nb_2O_9$ ceramic. The co-doping of Yb^{3+} ions with the optimum Er^{3+} concentration (x = 0.04) enhanced the upconversion luminescence. Additionally, the temperature-dependent upconversion luminescence spectra were used to calculate the optical temperature sensing of the prepared material using the fluorescence intensity ratio (FIR) method. The effect of altering the Yb^{3+} ions on sensing characteristics was investigated. It was observed that S_a is 0.69% and 0.58% K^{-1} for Er^{3+}/Yb^{3+} co-doped $BaBi_{2-0.04-y}Nb_2Er_{0.04}Yb_yO_9$ ceramic at y = 0.06 and 0.10, respectively. However, the previous chapter did not cover the dielectric and ferroelectric behavior of Yb^{3+} ions with Er^{3+} ions on the A-site of $BaBi_2Nb_2O_9$ ceramic. Therefore, this chapter comprehensively analyzes the dielectric and ferroelectric properties of the undoped and doped $BaBi_2Nb_2O_9$ system. It also gives information on the energy storage density performance of undoped, Er^{3+} doped, and Er^{3+}/Yb^{3+} co-doped $BaBi_2Nb_2O_9$ systems.

Ferroelectric ceramics based on lead, such as lead zirconate titanate and lead titanate, are well recognized for their piezoelectric properties and find widespread application in the fields of sensing, actuator, detector, and energy storage applications [1-10]. Peng et al. obtained a noticeable energy storage density in the $Pb_{0.8}Ba_{0.2}ZrO_3$ thin film. Even though lead-based materials are good at storing energy, they also cause a lot of damage to the planet when they disintegrate [11]. To achieve good energy storage in ferroelectrics, the following things should be checked: larger maximum polarization (P_m), lesser remnant polarization (P_r), and higher breakdown strength (BDS). Investigations are being conducted on alternative lead-free formulations, including barium titanate, bismuth

perovskites, alkaline niobates, bismuth layered structured ferroelectrics (BLSFs), etc. [12-15]. The basic ferroelectric materials have larger P_m and P_r [16]. However, a relaxor ferroelectric has larger P_m and lesser P_r; consequently, $BaBi_2Nb_2O_9$ relaxor ferroelectric (BLSF) is chosen. Literature studies revealed that due to the overconsumption of fossil fuels, there is a demand for developing green and sustainable energy like hydropower, wind or solar power, and many more. However, storing these kinds of energy is also challenging [17-21]. In the last decade, ferroelectric-based capacitors have been used in energy storage applications because they have a rapid charge rate (less than a microsecond) and more extended charge-discharge periods than conventional cells to produce intense power pulses [22, 23]. In addition, these capacitors exhibit improved energy storage capabilities at higher temperatures. Few investigations have been conducted on using ferroelectric-based materials as energy storage devices. In one study, Huang et al. discussed the consequences of different RE ions on $BaTiO_3$ ceramic to examine its performance in energy storage applications [24]. The energy storage properties of $Ba_{0.5}Na_{0.5}TiO_3$ ceramic doped with $NaNbO_3$ were explored by Wan et al. [25]. Also, in other reports, a relaxor ceramic $Bi_{0.5}Na_{0.5}TiO_3$-$Sr_{0.7}Bi_{0.2}TiO_3$ and $Bi_{0.5}Na_{0.5}TiO_3$-$BaTiO_3$-$SrTi_{0.875}Nb_{0.1}O_3$ were investigated for their potential application in energy storage devices [1, 21]. **Figure 5.1** depicts the schematic representation to enhance the energy storage parameters.

This chapter is arranged in the following way: Methods for synthesis and characterization are detailed in Section 5.2. Section 5.3 contains the results and discussions, which are further subdivided. Subsection 5.3.1 gives information about the typical FTIR bands and their shifting using FTIR spectra. Subsection 5.3.2 provides information about the Raman bands utilizing a laser source under the excitation of 785 nm. The temperature-dependent dielectric studies are discussed in subsection 5.3.3 at frequencies ranging from

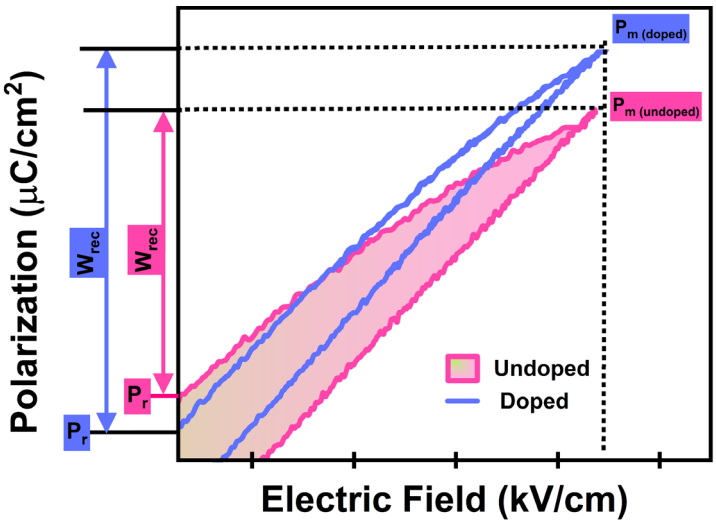

Figure 5.1: Diagrammatic illustration of the basic strategy for improving energy storage density parameters.

1 kHz to 1 MHz. Subsection 5.3.4 describes the polarization versus electric field loops of undoped, Er^{3+} doped, and Er^{3+}/Yb^{3+} co-doped BBN systems under various applied electric fields. The energy storage density properties were discussed using the PE loop parameters for various applied fields ranging from 75 kV/cm to 100 kV/cm. The summary of the chapter is provided in section 5.4.

5.2 SYNTHESIS AND CHARACTERIZATION DETAILS

The solid-state procedure is utilized to prepare the ceramics with the configuration of $BaBi_{2-x-y}Nb_2Er_xYb_yO_9$ (BBN) doped with Er^{3+} and Yb^{3+}. The initial precursors ($BaCO_3$, Bi_2O_3, Nb_2O_5, Er_2O_3, and Yb_2O_3) were bought from Sigma Aldrich and Alfa Aesar. The raw powders were measured stoichiometrically, followed by mixing in ethanol for 5 hours in a mortar pestle before heat treating at 950°C for 3 hours. The high-temperature cured calcined powder was added to the solution of PVA (polyvinyl alcohol) prepared in distilled water. After thoroughly mixing PVA, the powder is pressed in circular discs in a manual pelletizer. These pressed pellets (diameter = 10 mm, thickness = 1 mm) were heated at

1050°C in a high-temperature furnace for 3 hours. For the electrical measurements, these pellets were polished by rubbing with sandpaper to ensure good adhesion of the silver paste. The air-drying silver paste is used to prevent breaking while handling delicate pellets. The temperature-dependent dielectric studies were performed by an impedance analyzer from Keysight Impedance Analyzer E4990A for frequencies ranging from 1 kHz to 1 MHz. A high-end automated loop tracer measured the polarization against the applied electric field at room temperature under 20 Hz. The Perkin Elmer spectrum-II was used to acquire the FTIR spectra. The Raman spectra were attained with the Invia Raman spectrometer equipped with a laser source emitting light at a wavelength of 785 nm. The sample coding for all the Er^{3+}/Yb^{3+} co-doped BBN ceramics is recorded in Table 5.1.

Table 5.1: Coding of the prepared compositions of $BaBi_{2-x-y}Nb_2Er_xYb_yO_9$ ceramic.

Compositions	Sample Code	Er^{3+} (x)	Yb^{3+} (y)
$BaBi_{2-x-y}Nb_2Er_xYb_yO_9$	BBNE0Y0	0.00	0.00
$BaBi_{1.96}Nb_2Er_{0.04}Yb_{0.00}O_9$	BBNE4Y0	0.04	0.00
$BaBi_{1.94}Nb_2Er_{0.04}Yb_{0.02}O_9$	BBNE4Y2	0.04	0.02
$BaBi_{1.92}Nb_2Er_{0.04}Yb_{0.04}O_9$	BBNE4Y4	0.04	0.04
$BaBi_{1.90}Nb_2Er_{0.04}Yb_{0.06}O_9$	BBNE4Y6	0.04	0.06
$BaBi_{1.88}Nb_2Er_{0.04}Yb_{0.08}O_9$	BBNE4Y8	0.04	0.08
$BaBi_{1.86}Nb_2Er_{0.04}Yb_{0.10}O_9$	BBNE4Y10	0.04	0.10
$BaBi_{1.84}Nb_2Er_{0.04}Yb_{0.12}O_9$	BBNE4Y12	0.04	0.12

5.3 RESULTS AND DISCUSSION

The structural and microstructural analysis of undoped and doped BBN composition has already been explained in Section 4.3.1 of **Chapter 4**. It has been observed that the XRD pattern matches well with JCPDF (00-012-0403), having orthorhombic geometry with the Fmmm phase group.

5.3.1 Fourier Transform Infrared Spectroscopy

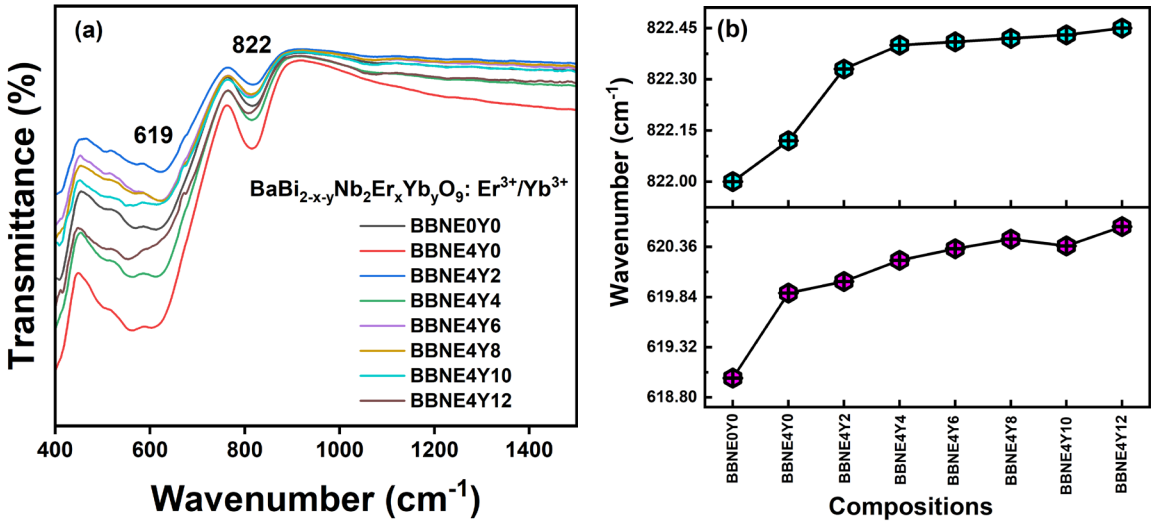

Figure 5.2: (a) FTIR spectra obtained for all the compositions of prepared BBN ceramic (b) Shifting of FTIR modes (619 cm^{-1} and 822 cm^{-1}).

The Fourier transform infrared spectra of all the Er^{3+} and Yb^{3+} doped and undoped BBN are depicted in **Figure 5.2(a)**. A broad and intense band can be seen at 619 and 822 cm^{-1}, the distinctive peaks of the Aurivillius phase [26, 27]. The stretching of the NbO_6 bond causes the frequency band at positions 619 and 822 cm^{-1}, and the degree to which this stretching occurs is extremely dependent on dopant concentration. The compositional dependency of dopants on the band positions is shown in **Figure 5.2(b)**, and curves seem to be shifted towards higher values. The observed frequency shift may be ascribed to changing conditions near the NbO_6 bond. It means that the dopant ions affect the lattice structure, and this distortion causes the shifting of the FTIR bands. Therefore, it may be assumed that the FTIR spectra exhibit significant vulnerability to changes in the host material's local structure by dopants [26].

5.3.2 Raman Spectroscopy

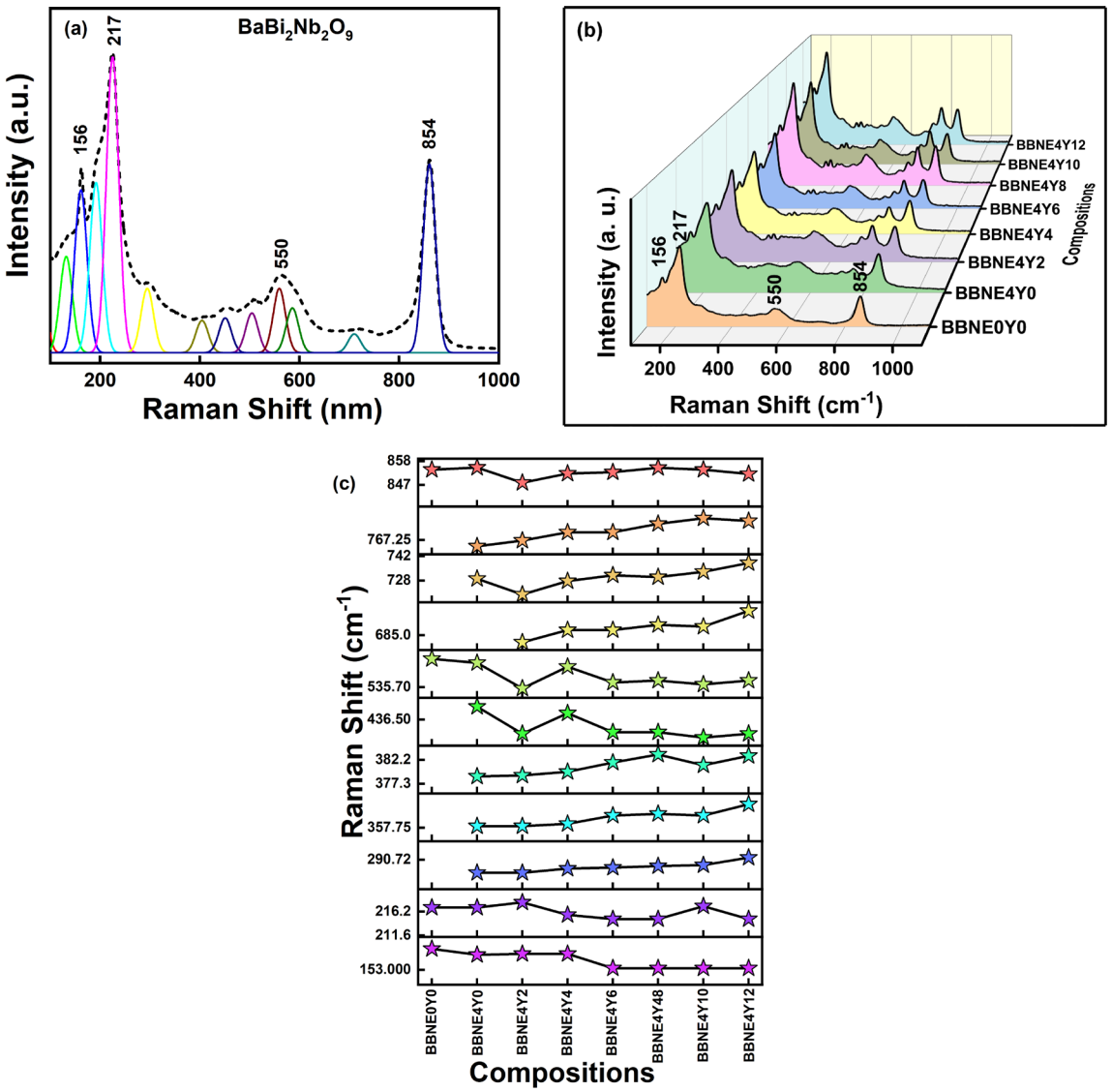

Figure 5.3: (a) Deconvoluted Raman spectra of $BaBi_{2-x-y}Nb_2Er_xYb_yO_9$ (x = 0.00, y = 0.00) ceramic under the excitation of 785 nm laser source (b) Raman spectra of all the compositions of BBN (c) Dependency of dopant concentrations on various Raman modes.

The Raman spectra of all the compositions of BBN were acquired using a laser source with a wavelength of 785 nm in the frequency range of 100-1000 cm^{-1}. The deconvoluted Raman plot of undoped BBN composition is provided in **Figure 5.3(a)**. The four significant peaks were obtained and positioned at 156, 215, 550, and 854 cm^{-1}. The spectra detected for all the prepared compositions are reported in **Figure 5.3(b)**. According to the literature survey,

there are 12 Raman modes, out of which only four Raman bands (156, 215, 550, and 854 cm^{-1}) are detectable in the case of undoped BBN ferroelectric ceramic [27-29]. The occurrence of these bands might be due to the coinciding of the same symmetrical vibrations or expansions of the vibration modes or the weakening of the vibrational mode's intensity. However, in Er^{3+}/Yb^{3+} BBN compositions, almost 12 experimental modes can be observed, verified from deconvoluted Raman spectra (**Figure 5.3(a)**). These modes are effectively reduced in undoped BBN ceramic, but they may be rapidly noticed in the case of Er^{3+}/Yb^{3+} doped BBN compositions. These suppressed modes are positioned at 289, 358, 379, 443, 681, 720, and 765 cm^{-1}. These modes might potentially be linked to the level of structural disorder present in materials belonging to the same family [17, 27, 30]. As a result, the theoretically expected and experimentally observed Raman modes have a decent correlation. **Figure 5.3(c)** displays the Raman shift as a dependent variable of the dopant concentration, while Table 5.2 presents a comprehensive compilation of the observed frequency shifts with their corresponding band allocations.

Table 5.2: Assignment of various observed Raman bands in synthesized $BaBi_2Nb_2O_9$ compositions.

Raman Bands Position (cm^{-1})	Band Assignments	References
156	Vibration of Bi^{2+} ion	[17]
215	Torsion Bending of O-Nb-O bond	[17]
289	Vibration due to Bi-O_3 force constant	[27]
358	Vibration due to Bi-O_3 force constant	[27]
379	Vibration due to Bi-O_3 force constant	[27]
443	Vibration due to Bi-O_3 force constant	[27]
550	Opposite excursion of apical oxygen atom	[27]
681	Symmetric bending vibration of NbO_6 octahedron	[28]
720	Symmetric bending vibration of NbO_6 octahedron	[27]
765	Symmetric bending vibration of NbO_6 octahedron	[27]
854	Symmetrical stretching of Nb-O_6 group	[17]

The Raman spectra show four modes at 156, 215, 550, and 854 cm^{-1} frequencies. The Raman mode seen at a lower frequency (beneath 200 cm^{-1}) is related to the vibrational motions of Ba^{2+} ions present at the A-site. The higher frequency bands (beyond 200 cm^{-1}) result from the inner vibration of the NbO_6 octahedron. The observed mode with a frequency of 155 cm^{-1} has been ascribed to the vibrations of Bi^{3+} ions located on the A-site within the pseudo-perovskite structure. The A_{1g} mode at a frequency of 215 cm^{-1} in the NbO_6 group is due to the torsional bending of the O-Nb-O configuration. With the replacement of Bi^{3+} ions by dopant ions (Er^{3+}/Yb^{3+}), a little shift within the range of 215 to 217 cm^{-1} is recorded. The intense vibration mode at around 854 cm^{-1} may be attributed to the A_{1g} symmetry because of the symmetrical elongation of the Nb-O bonds in the NbO_6 in the z-axis of the crystal lattice [17, 27, 31]. The counter-directional movement in the apical oxygen atoms inside the NbO_6 octahedral structure, which arises from the B_{2g} mode, results in the Raman mode centered at 550 cm^{-1}. This mode exhibits a progressive decrease from 550 cm^{-1} to 539 cm^{-1}, and it has been determined that introducing dopants results in its attenuation. This observation implies that introducing Er^{3+}/Yb^{3+} at Bi-sites decreases compressive stress, indicating a relaxation in structural deformation. The band at 854 cm^{-1} is due to the symmetrical stretching of Nb-O vibrations inside the NbO_6 octahedron, exhibiting a slight decrease in frequency to 852 cm^{-1}.

The bond length analysis of Nb-O at 854 cm^{-1} Raman band is crucial for investigating the impact of dopants on it. Badger's rule is the widely used expression that connects bond lengths to force constants in diatomic and polyatomic compounds [32]. The general form of this rule is expressed in Eq. (5.1) [33]:

$$k^{-\frac{1}{3}} = \left(a_{ij} - d_{ij}\right)^{-1} (R - d_{ij}) \tag{5.1}$$

Here, k stands for the force constant, R for the bond length, and a_{ij} and d_{ij} are constants for certain bonds between atoms in rows i and j of the periodic table. However, Badger's rule does not effectively account for the correlation between the Nb-O bond and force constants in niobate reference compounds. This is because $k^{-1/3}$ does not follow a linear relation with R but shows a minor curvature [32, 33]. Herschbach had a similar issue while attempting to fit cubic and quartic anharmonic force constants to internuclear distances for diatomic molecules [34]. Herschbach utilized an exponential fit to address the slight curvature in the data accurately. Thus, following Herschbach's treatment, the current work utilizes a comparable method to correlate Nb-O stretching frequencies with their corresponding bond lengths. The exponential function used is represented in Eq. (5.2) [35]:

$$\nu = A \exp(BR) \tag{5.2}$$

where ν is the Nb-O stretching frequency, R is the Nb-O bond length in Angstroms, and A and B are fitting parameters. The fitting parameters are determined from an exponential least squares fit of the crystallographic and the obtained Raman data from several niobium oxide reference compounds (Table 1 [32]). Then, Eq. (5.2) takes the form of Eq. (5.3) [32]:

$$\nu = 25922 \exp(-1.9168\ R) \tag{5.3}$$

Table 5.3: Bond length of Nb-O at 854 cm^{-1} Raman band for all the composition of $BaBi_2Nb_2O_9$.

Sample	Band Position (cm^{-1})	Bond Length (Å)
BBNE0Y0	854.00	1.7805
BBNE4Y0	855.00	1.7799
BBNE4Y2	848.00	1.7842
BBNE4Y4	854.25	1.7803
BBNE4Y6	852.80	1.7812
BBNE4Y8	854.90	1.7799
BBNE4Y10	854.00	1.705
BBBNE4Y12	852.00	1.7817

Using Eq. (5.3), the bond length of all the compositions of BBN is evaluated for the Raman band positioned near 854 cm^{-1} and is tabulated in Table 5.3. The variation in bond length shows structural relaxation due to dopant introduction, which can also be corroborated by XRD and FTIR spectra.

5.3.3 Dielectric Measurements

The dielectric constant (ε') and dielectric loss (ε") at various frequencies (1 kHz - 1 MHz) for different BBN compositions are represented in **Figure 5.4(a-d)** and **Figure 5.5(a-d)**, respectively. The dielectric constant exhibits a wide anomaly around a temperature (T_m) associated with a diffuse ferroelectric phase transition, followed by a relaxation of the permittivity, consistent with previous findings [36-38]. There is a significant dielectric dispersion below and above the temperature T_m, displacement of T_m with increasing frequency, and a decrease in the value of ε' with increasing frequency. The ε" curves are quite diffused, and shifts in the maxima with frequency have been observed. These observations validate the relaxor behavior of all the prepared BBN compositions. Additionally, in contrast to the Curie-Weiss law, which governs the dielectric permittivity of a typical ferroelectric material, a modified Curie-Weiss law is applied to relaxor ferroelectrics to define the variation in the reciprocal of the dielectric constant at high temperature and the diffuseness of the phase transition. It is given by Eq. (5.4) [38, 39]:

$$\frac{1}{\varepsilon'} - \frac{1}{\varepsilon'_m} = \frac{1}{C}\,(T - T_m)^{\gamma} \qquad (5.4)$$

where ε'_m is the highest value of the dielectric constant, C is the Curie-like constant, and γ is the degree of diffuseness. The value of γ lies between 1 and 2. For normal ferroelectrics, the value is 1; for relaxors, it is 2 [40]. **Figure 5.6(a-d)** shows a linear relationship between the plot of $\ln(1/\varepsilon' - 1/\varepsilon'_m)$ and $\ln(T - T_m)$ at 500 kHz for all prepared BBN compositions.

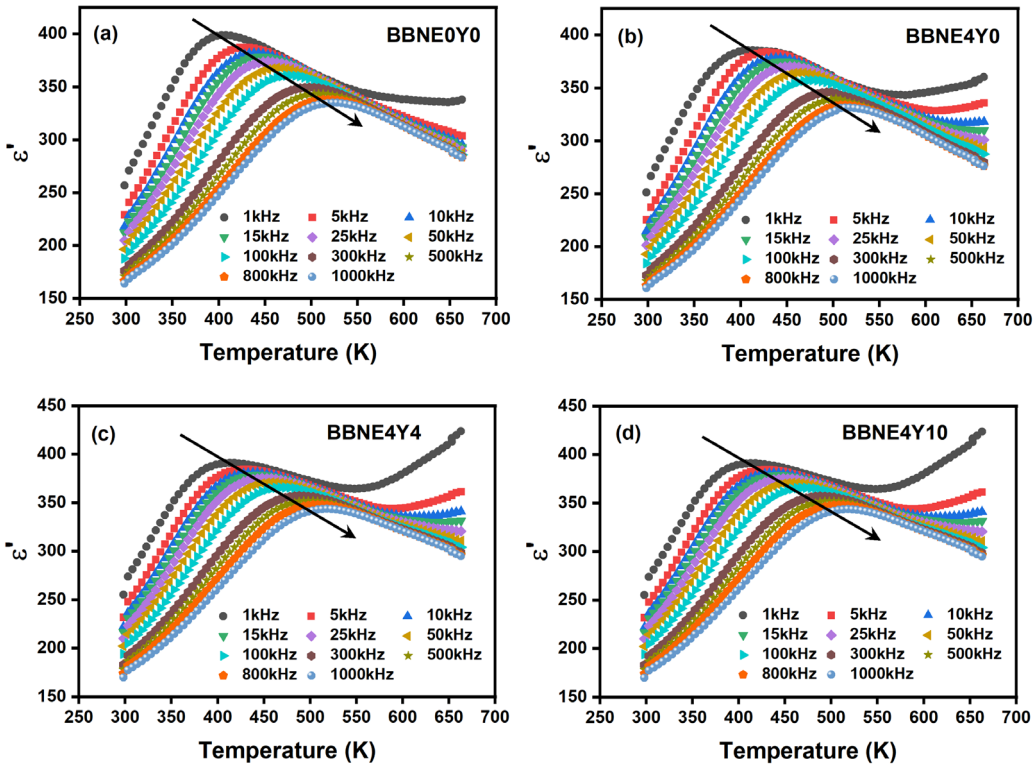

Figure 5.4: Dielectric constant (ε') at various frequencies (1 kHz - 1 MHz) between the temperature range 303K to 673K for (a) BBNE0Y0 (b) BBNE4Y0 (c) BBNE4Y4 (d) BBNE4Y10 compositions.

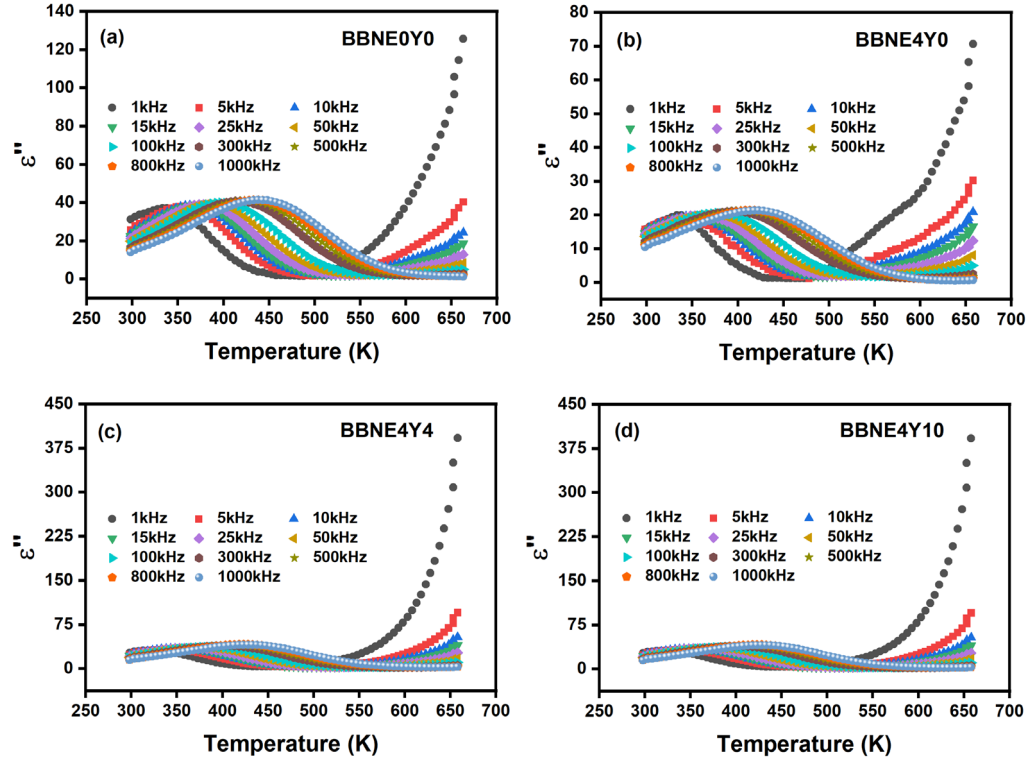

Figure 5.5: Dielectric loss (ε'') at various frequencies (1 kHz - 1 MHz) between the temperature range 303K to 673K for (a) BBNE0Y0 (b) BBNE4Y0 (c) BBNE4Y4 (d) BBNE4Y10 compositions.

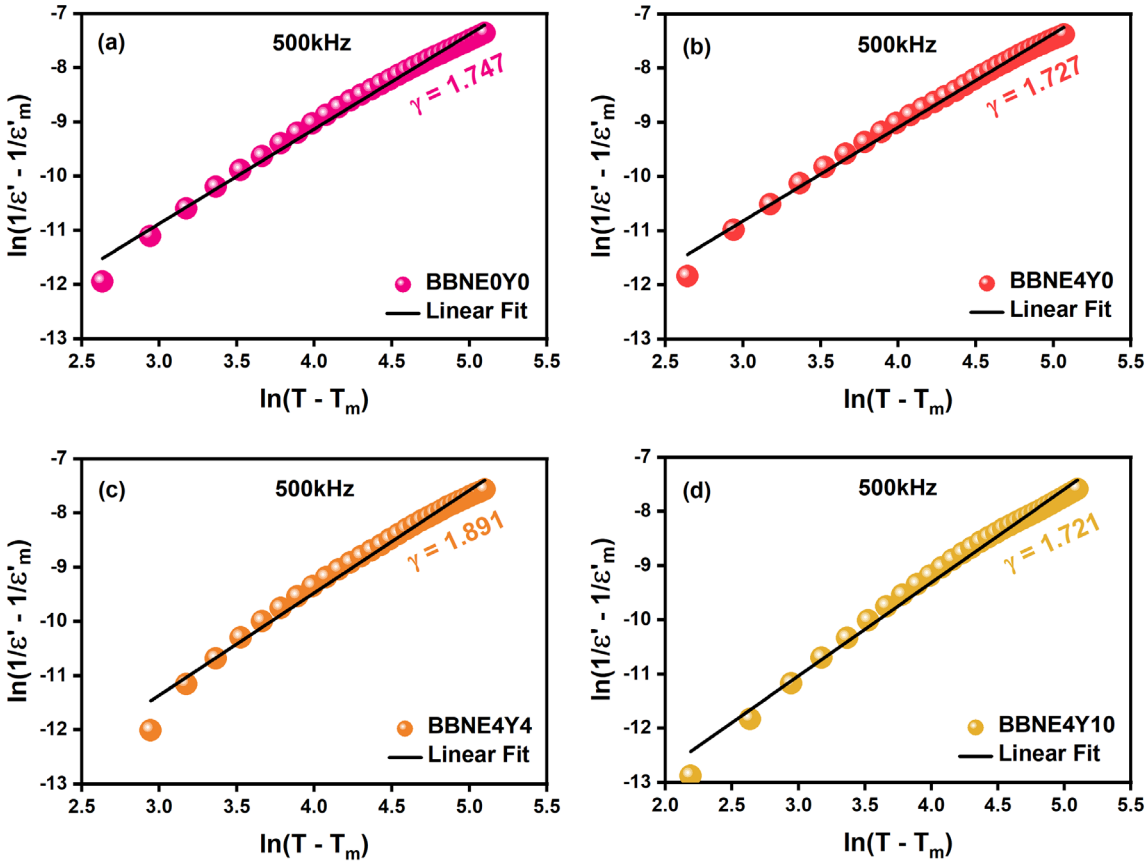

Figure 5.6: Plot of ln(1/ε' - 1/ε'$_m$) and ln(T - T_m) at 500kHz for (a) BBNE0Y0 (b) BBNE4Y0 (c) BBNE4Y4 (d) BBNE4Y10 compositions.

The slope (γ) comes out to be 1.747, 1.727, 1.891, and 1.721 for BBNE0Y0, BBNE4Y0, BBNE4Y4, and BBNE4Y10, respectively. Thus proving the relaxor-type behavior of BBN ceramic. The dielectric measurement parameters at 500 kHz of all BBN compositions are tabulated in Table 5.4.

Table 5.4: Variation in dielectric measurement parameters at 500 kHz of all BBN compositions.

Sample	ε'$_{303K}$	ε'$_m$	T_m (K)	γ
BBNE0Y0	175.94	343.26	503	1.747
BBNE4Y0	172.42	341.21	500	1.727
BBNE4Y4	196.94	353.22	489	1.891
BBNE4Y10	186.67	347.84	484	1.721

5.3.4 PE Loops and Energy Storage Analysis

The polarization versus electric field curves (PE loops) of undoped and doped compositions of BBN ceramic are represented in **Figure 5.7(a-h)** for various applied electric fields ranging from 75 kV/cm to 100 kV/cm. The PE loops are traced at room temperature at a 20 Hz frequency. The slimmer PE loops result in low remnant polarization of $BaBi_2Nb_2O_9$ ceramic. In Table 5.5, it is seen that the PE loop parameters decrease with increasing dopant concentration. The P_m and P_r values obtained for undoped BBN are 5.162 $\mu C/cm^2$ to 6.831 $\mu C/cm^2$ and 1.158 $\mu C/cm^2$ to 1.485 $\mu C/cm^2$ between the electric field range 75 kV/cm to 100 kV/cm, respectively. In doped BBN compositions, the obtained P_m and P_r values increase with increasing electric field but are smaller than the undoped BBN. The decrease in P_m and P_r values may be elucidated by incorporating external ions into the host lattice, replacing bismuth ions, and forming oxygen vacancies. When subjected to a strong electric field, the oxygen vacancies migrate toward the domain wall, impeding the domain-flipping process. Nevertheless, the estimation of high-quality PE loops is subjected to several factors, including lattice strain, defects, grain size, density, and minimum sample thickness.

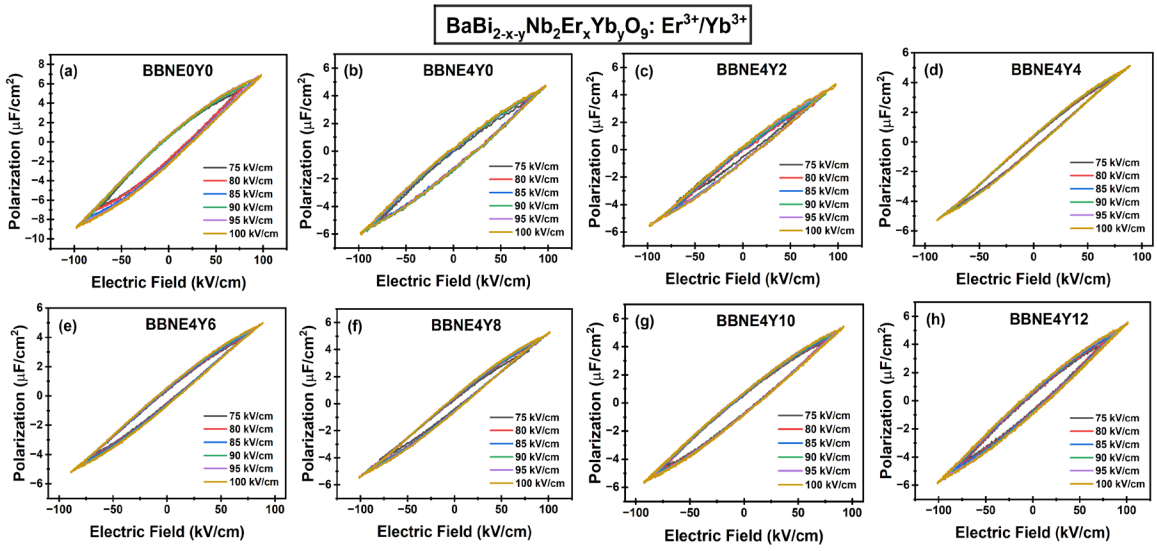

Figure 5.7: (a-h) PE hysteresis loops of all the compositions with varying applied electric fields ranging from 75 kV/cm to 100 kV/cm.

Table 5.5: Energy storage parameters of all BBN ceramic compositions.

E_{Max} (kV/cm)	Parameters	Compositions							
		BBNE0Y0	BBNE4Y0	BBNE4Y2	BBNE4Y4	BBNE4Y6	BBNE4Y8	BBNE4Y10	BBNE4Y12
75	P_r (μC/cm^2)	1.158	0.711	0.324	0.380	0.425	0.365	0.654	0.624
	P_m (μC/cm^2)	5.162	3.780	3.278	4.315	4.060	3.955	4.424	4.038
	W (J/cm^3)	0.387	0.283	0.245	0.323	0.304	0.296	0.331	0.302
	W_{rec} (J/cm^3)	0.300	0.230	0.221	0.295	0.273	0.269	0.282	0.256
	η (%)	77.59	81.18	90.09	91.19	89.51	90.77	85.21	84.54
80	P_r (μC/cm^2)	1.172	0.738	0.464	0.395	0.490	0.465	0.713	0.680
	P_m (μC/cm^2)	5.786	4.059	3.532	4.539	4.209	4.598	4.689	4.458
	W (J/cm^3)	0.463	0.324	0.282	0.363	0.337	0.368	0.375	0.356
	W_{rec} (J/cm^3)	0.369	0.265	0.245	0.331	0.297	0.331	0.318	0.302
	η (%)	79.76	81.80	86.86	91.28	88.35	89.88	84.79	84.72
85	P_r (μC/cm^2)	1.314	0.684	0.438	0.434	0.511	0.497	0.728	0.670
	P_m (μC/cm^2)	6.308	4.296	3.782	4.689	4.410	4.719	4.811	4.767
	W (J/cm^3)	0.536	0.365	0.321	0.398	0.374	0.401	0.409	0.405
	W_{rec} (J/cm^3)	0.424	0.307	0.284	0.361	0.331	0.358	0.347	0.348
	η (%)	79.16	84.07	88.39	90.73	88.41	89.46	84.86	85.93
90	P_r (μC/cm^2)	1.403	0.754	0.507	0.448	0.602	0.492	0.744	0.782
	P_m (μC/cm^2)	6.426	4.348	4.094	4.900	4.682	4.882	5.014	5.110
	W (J/cm^3)	0.578	0.391	0.368	0.441	0.421	0.439	0.451	0.459
	W_{rec} (J/cm^3)	0.452	0.323	0.323	0.401	0.367	0.395	0.384	0.389
	η (%)	78.16	82.65	87.60	90.85	87.13	89.97	85.14	84.68
95	P_r (μC/cm^2)	1.395	0.743	0.540	0.459	0.640	0.560	0.790	0.792
	P_m (μC/cm^2)	6.768	4.535	4.477	5.102	4.818	5.080	5.221	5.348
	W (J/cm^3)	0.643	43.09	0.425	0.485	0.457	0.483	0.496	0.508
	W_{rec} (J/cm^3)	0.510	0.360	0.374	0.441	0.397	0.429	0.421	0.432
	η (%)	79.38	0.836	87.99	90.99	86.71	88.95	84.86	85.18
100	P_r (μC/cm^2)	1.485	0.781	0.638	0.463	0.636	0.566	0.780	0.802
	P_m (μC/cm^2)	6.831	4.708	4.712	5.080	4.949	5.288	5.359	5.474
	W (J/cm^3)	0.683	0.471	0.471	0.508	0.495	0.529	0.536	0.547
	W_{rec} (J/cm^3)	0.534	0.392	0.407	0.461	0.431	0.472	0.457	0.467
	η (%)	78.25	83.39	86.45	90.87	87.14	89.28	85.44	85.34

The P_r, P_m, and applied electric field values were used to calculate the energy storage parameters: energy density (W), recoverable energy density (W_{rec}), and efficiency (η). Eqs. (5.5 - 5.7) give the mathematical expression for the energy storage parameters [41, 42]:

$$W = \int_0^{P_m} EdP \tag{5.5}$$

$$W_{rec} = \int_{P_r}^{P_m} EdP \tag{5.6}$$

$$\eta = \frac{W_{rec}}{W} \times 100\% \tag{5.7}$$

Based on these expressions, it can be said that ceramic materials with a high energy density and efficiency should have a high maximum polarization, a low remnant polarization, and high BDS simultaneously. Table 5.5 tabulates the W, W_{rec}, and η values for all the applied electric fields. The energy storage parameters improved with increasing electric field for all the compositions, as shown in **Figure 5.8(a-c)**. The η varies from 77.59% to 79.76% for undoped BBN ceramic within the electric field range. However, η increases with the rise in the applied electric field for doped BBN compositions. The highest value for η is obtained for BBNE4Y4 prepared composition and equals 91.28% at

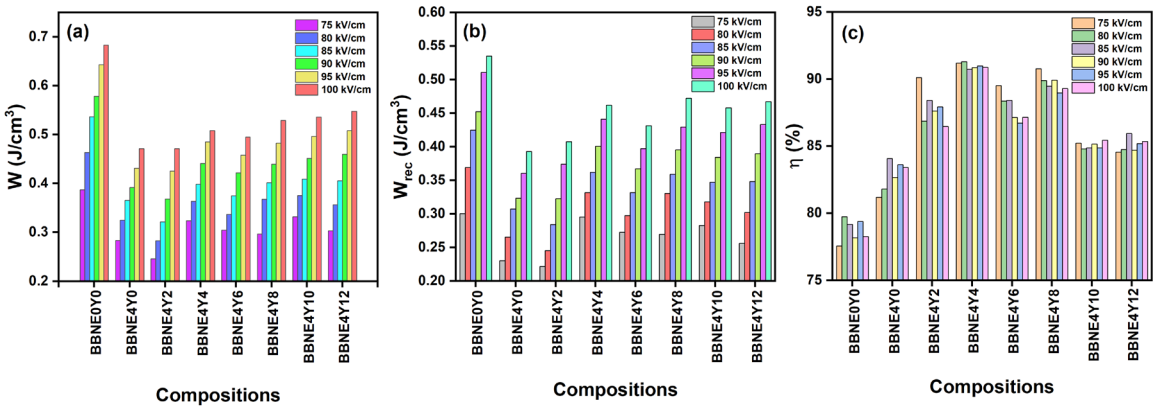

Figure 5.8: (a-c) Energy storage parameters of all the prepared compositions of BBN with varying applied electric fields ranging from 75 kV/cm to 100 kV/cm.

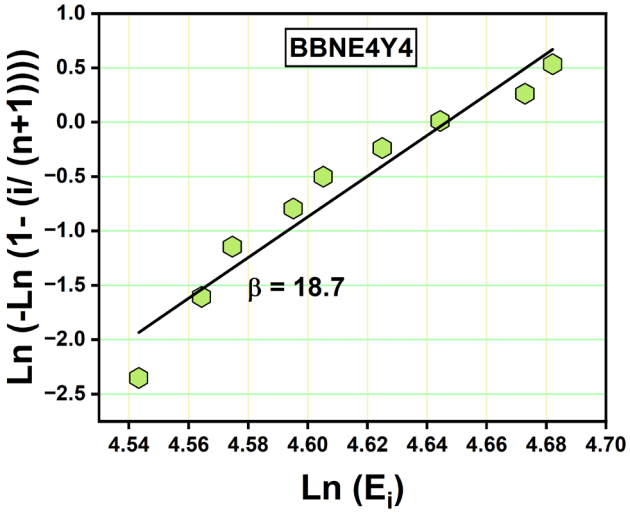

Figure 5.9: Weibull distribution function for BBNE4Y4 prepared composition.

80 kV/cm. The Weibull distribution function for BBNE4Y4 prepared composition is shown in **Figure 5.9**. Determining the maximum electric fields and energy storage capabilities for the practical application of energy storage ceramics relies on the vital parameter known as the breakdown strength (BDS). BDS can be expressed by the Weibull distribution function given in Eq. (5.8) and (5.9) [20, 22]:

$$X_i = \mathrm{Ln}(E_i) \tag{5.8}$$

$$Y_i = \mathrm{Ln}\left(-\mathrm{Ln}\left(1-\left(\frac{i}{1+n}\right)\right)\right) \tag{5.9}$$

where E_i is the BDS of the sample, i is the sequence of the sample, and n is the number of samples. To validate the experimental data, the Weibull shape parameter (β) is an essential factor that can be calculated from the linearly fitted X_i and Y_i slope. The Weibull distribution model is appropriate for analyzing breakdown outcomes when the value of β exceeds 1 [24].

The temperature stability of prepared ceramic (BBNE4Y4) is studied between a wide temperature range (303 K - 415 K), as shown in **Figure 5.10(a)**. It has been observed that the W, W_{rec}, and η of synthesized composition do not vary much with increasing

temperature under 80 kV/cm applied electric field, as depicted in **Figure 5.10(b)**. This is because of the transition of extensive diffusive phases in nonergodic and ergodic states of relaxor materials [22]. The W, W_{rec} increases with increasing temperature, and η remains constant. The change in W, W_{rec}, and η is 0.03%. A comparison of energy storage parameters of different host materials is given in Table 5.6.

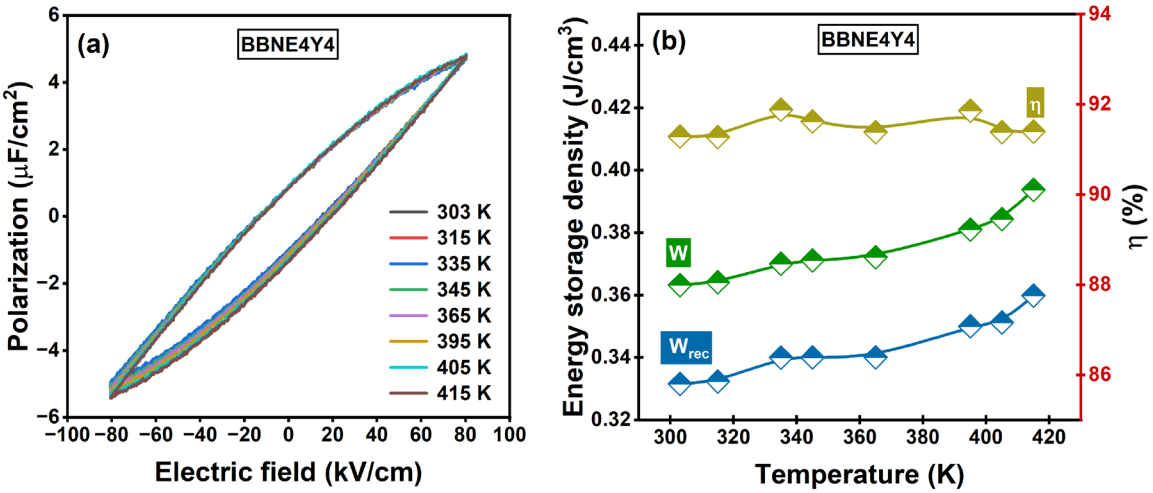

Figure 5.10: (a) Temperature stability analysis of BBNE4Y4 (Er^{3+} = 0.04 and Yb^{3+} = 0.04) at various temperature ranges (303 K - 415 K) (b) Variation of energy storage density parameters of the BBNE4Y4.

Table 5.6: Comparison of energy storage parameters of various ferroelectric ceramics.

Host Material	**E_{max} (kV/cm)**	**W_{rec} (J/cm³)**	**η (%)**	**Reference**
$Bi_{0.5}Na_{0.5}TiO_3$-$BaTiO_3$-$SrTi_{0.875}Nb_{0.1}O_3$	105	1.17	91	[1]
$0.98(0.94Bi_{0.5}Na_{0.5}TiO_3$-$0.06BaTiO_3)$-$0.02BiAlO_3$	95	0.69	-	[2]
$(Na_{0.38}K_{0.12}Bi_{0.38}La_{0.12})TiO_3$	90	0.72	93	[5]
$BaBi_2Nb_2O_9$:ZrO_2	-	0.014	-	[32]
$Na_{0.5}Bi_{0.5}TiO_3$:Ho^{3+}	114	0.68	-	[33]
$BaBi_2Nb_2O_9$ (Er^{3+} = 0.00, Yb^{3+} = 0.00)	100	0.534	78.25	**This work**
$BaBi_2Nb_2O_9$ (Er^{3+} = 0.04, Yb^{3+} = 0.00)	100	0.392	83.39	**This work**
$BaBi_2Nb_2O_9$ (Er^{3+} = 0.04, Yb^{3+} = 0.04)	100	0.461	90.87	**This work**

5.4 SUMMARY

The structural, dielectric, ferroelectric, and energy storage properties of undoped $BaBi_{2-x-y}Nb_2Er_xYb_yO_9$ (BBN), Er^{3+} doped BBN, and Er^{3+}/Yb^{3+} co-doped BBN ferroelectric ceramics have been investigated using the solid-state method. FTIR spectra showed characteristic peaks of the Aurivillius phase at 619 cm^{-1} and 822 cm^{-1}. Four Raman modes are visible in undoped BBN, whereas 12 modes have been observed in doped BBN compositions. Herschbach's exponential function approach is utilized to calculate the bond length of Nb-O at 840 cm^{-1} Raman band to establish a correlation between the stretching frequencies of Nb-O and the corresponding bond lengths. Temperature-dependent dielectric tests reveal significant dispersion below and above the maximum temperature (T_m), and the dielectric constant (ε') decreases with increasing frequency. The dielectric loss (ε'') curves are diffused, and variations in the maxima with frequency have been detected, demonstrating the relaxor behavior of all produced BBN compositions. The thinner PE loops were achieved under applied electric fields between 75 kV/cm and 100 kV/cm. The remnant polarization (P_r) and maximum polarization (P_m) were used to calculate the energy storage parameters (W, W_{rec}, η) of each ceramic composition. The energy storage parameters improve as the applied electric field increases. The energy density (W), recoverable energy storage density (W_{rec}), and energy storage efficiency (η) for undoped, Er^{3+} doped, and Er^{3+}/Yb^{3+} co-doped BBN ceramics were approximately (0.683 J/cm^3, 0.534 J/cm^3, and 78.25%), (0.471 J/cm^3, 0.392 J/cm^3, and 83.39%) and (0.508 J/cm^3, 0.461 J/cm^3, and 90.87%), respectively. The W, W_{rec}, η showed decent temperature stability between 303 K and 415 K. The change in energy storage density parameters is only 0.03%. It can be concluded that the η of undoped, Er^{3+} doped, and Er^{3+}/Yb^{3+} co-doped

$BaBi_{2-x-y}Nb_2Er_xYb_yO_9$ ceramics increased with doping concentrations. In contrast, the W and W_{rec} of Er^{3+} doped and Er^{3+}/Yb^{3+} co-doped BBN ceramic are comparable with undoped BBN. The dielectric constant at room temperature (ε'_{303K}), degree of diffuseness (γ), and energy storage efficiency (η) are superior in BBNE4Y4 compared to other BBN compositions, making this concentration the best among others. Therefore, all the above observations suggest that the prepared material may be helpful in the development of sophisticated electronic apparatus for applications involving energy storage.

Following an extensive examination of the dielectric and ferroelectric characteristics of the $BaBi_2Nb_2O_9$ system doped with Er^{3+} and Yb^{3+} ions, it was determined that the resulting ceramic exhibited relaxor characteristics, thinner PE loops, and improved energy storage efficiency. The next chapter explores the impact of transition metal ions (W^{6+}) to enhance the overall properties of the prepared BBN compositions.

5.5 REFERENCES

[1] J. Shi, X. Liu, and W. Tian, "High energy-storage properties of $Bi_{0.5}Na_{0.5}TiO_3$-$BaTiO_3$-$SrTi_{0.875}Nb_{0.1}O_3$ lead-free relaxor ferroelectrics," *Journal of Materials Science & Technology*, vol. 34, no. 12, pp. 2371-2374, 2018.

[2] A. Manan, S. Khan, A. Ullah, A. S. Ahmad, Y. Iqbal, I. Qazi, A. Ullah, Z. Yao, H. Liu, H. Hao, M. A. Khan, and M. U. Rehman, "Improved energy storage characteristic of Yb doped $0.98(0.94Bi_{0.5}Na_{0.5}TiO_3$-$0.06BaTiO_3)$-$0.02BiAlO_3$ ceramics," *Materials Research Bulletin*, vol. 137, 111175, 2021.

[3] Z. Peng, L. Chen, Y. Xiang, and F. Cao, "Microstructure and electrical properties of lanthanides-doped $CaBi_2Nb_2O_9$ ceramics," *Materials Research Bulletin*, vol. 148, 111670, 2022.

[4] K. Wu, H. Wang, Z. Miao, S. Ding, Y. Qi, Y. Ming, W. Ding, H. Yuan, Q. Zheng, and D. Lin, "Improved energy storage properties of $Sr(Zr_{0.8}Nb_{0.16})O_3$-doped $Bi_{0.47}Na_{0.47}Ba_{0.06}TiO_3$ ceramics with excellent temperature/frequency stability," *Ceramics International*, vol. 46, no. 9, pp. 13159-13169, 2020.

[5] A. Verma, A. K. Yadav, S. Kumar, V. Srihari, R. Jangir, H. K. Poswal, S. Biring, and S. Sen, "Enhanced energy storage properties in A-site substituted

$Na_{0.5}Bi_{0.5}TiO_3$ ceramics," *Journal of Alloys and Compounds*, vol. 792, pp. 95-107, 2019.

[6] F. Yan, X. Zhou, X. He, H. Bai, S. Wu, B. Shen, and J. Zhai, "Superior energy storage properties and excellent stability achieved in environment-friendly ferroelectrics via composition design strategy," *Nano Energy*, vol. 75, 105012, 2020.

[7] F. Luo, J. Xing, Y. Qin, Y. Zhong, F. Shang, and G. Chen, "Up-conversion luminescence, temperature sensitive and energy storage performance of lead-free transparent Yb^{3+}/Er^{3+} co-doped $Ba_2NaNb_5O_{15}$ glass-ceramics," *Journal of Alloys and Compounds*, vol. 910, 164859, 2022.

[8] P. Wang, X. Wang, G. Li, Y. Li, X. Yao, and Z. Pan, "Energy density capability and upconversion luminescence in Er^{3+}/Yb^{3+}-co-doping BNT-based ferroelectric thin films," *Ceramics International*, vol. 48, no. 19, pp. 28606-28613, 2022.

[9] A. Banwal and R. Bokolia, "Enhanced upconversion luminescence and optical temperature sensing performance in Er^{3+} doped $BaBi_2Nb_2O_9$ ferroelectric ceramic," *Ceramics International*, vol. 48, no. 2, pp. 2230-2240, 2022.

[10] A. Banwal and R. Bokolia, "Effect of Er^{3+} ion doping on structural, ferroelectric and up/down conversion luminescence in $BaBi_2Nb_2O_9$ ceramic," *Materials Today: Proceedings*, vol. 47, part 14, pp. 4692-4695, 2021.

[11] Z. Liu, P. Ren, C. Long, X. Wang, Y. Wan, and G. Zhao, "Enhanced energy storage properties of $NaNbO_3$ and $SrZrO_3$ modified $Bi_{0.5}Na_{0.5}TiO_3$ based ceramics," *Journal of Alloys and Compounds*, vol. 721, pp. 538-544, 2017.

[12] T. Zhou, Y. Zhang, Z. Wu, and B. Chen, "Concentration effect and temperature quenching of upconversion luminescence in $BaGd_2ZnO_5$: Er^{3+}/Yb^{3+} phosphor," *Journal of Rare Earths*, vol. 33, no. 7, pp. 686-692, 2015.

[13] R. D. Shannon, "Revised effective ionic radii and systematic studies of interatomic distances in halides and chalcogenides," *Acta Crystallographica Section A.*, vol. 32, no. 5, pp. 751-767, 1976.

[14] J. Zhang, Y. Lin, L. Wang, Y. Yang, H. Yang, and Q. Yuan, "Significantly enhanced energy storage density in sodium bismuth titanate-based ferroelectrics under low electric fields," *Journal of the European Ceramic Society*, vol. 40, no. 15, pp. 5458-5465, 2020.

[15] Z. Chen, L. Sheng, X. Li, P. Zheng, W. Bai, L. Li, F. Wen, W. Wu, L. Zheng, and J. Cui, "Enhanced piezoelectric properties and electrical resistivity in W/Cr co-doped $CaBi_2Nb_2O_9$ high-temperature piezoelectric ceramics," *Ceramics International*, vol. 45, no. 5, pp. 6004-6011, 2019.

[16] P. Ren, Z. Liu, X. Wang, Z. Duan, Y. Wan, F. Yan, and G. Zhao, "Dielectric and energy storage properties of $SrTiO_3$ and $SrZrO_3$ modified $Bi_{0.5}Na_{0.5}TiO_3$-$Sr_{0.8}Bi_{0.1}\square_{0.1}TiO_3$ based ceramics," *Journal of Alloys and Compounds*, vol. 742, pp. 683-689, 2018.

[17] M. X. Façanha, J. P. C. doNascimento, M. A. S. Silva, M. C. C. Filho, A. N. L Marques, A. G. Pinheiro, and A. S. B. Sombra, "Up-conversion emission of Er^{3+}/Yb^{3+} co-doped $BaBi_2Nb_2O_9$ (BBN) phosphors," *Journal of Luminescence*, vol. 183, pp. 102-107, 2017.

[18] R. Bokolia, O. P. Thakur, V. K. Rai, S. K. Sharma, and K. Sreenivas, "Electrical properties and light upconversion effects in $Bi_{3.79}Er_{0.03}Yb_{0.18}Ti_{3-x}W_xO_{12}$ ferroelectric ceramics," *Ceramics International*, vol. 42, no. 5, pp. 5718-5730, 2016.

[19] A. Banwal and R. Bokolia, "Phase evolution and microstructure of $BaBi_2Nb_2O_9$ ferroelectric ceramics," *Materials Today: Proceedings*, vol. 46, part 20, pp. 10121-10124, 2021.

[20] D. Hu, Z. Pan, Z. He, F. Yang, X. Zhang, P. Li, and J. Liu, "Significantly improved recoverable energy density and ultrafast discharge rate of $Na_{0.5}Bi_{0.5}TiO_3$-based ceramics," *Ceramics International*, vol. 46, no. 10, pp. 15364-15371, 2020.

[21] X. Qiao, D. Wu, F. Zhang, M. Niu, B. Chen, X. Zhao, P. Liang, L. Wei, X. Chao, and Z. Yang, "Enhanced energy density and thermal stability in relaxor ferroelectric $Bi_{0.5}Na_{0.5}TiO_3$-$Sr_{0.7}Bi_{0.2}TiO_3$ ceramics," *Journal of the European Ceramic Society*, vol. 39, no. 15, pp. 4778-4784, 2019.

[22] W. Ma, Y. Zhu, M. A. Marwat, P. Fan, B. Xie, D. Salamon, Z. G. Ye, and H. Zhang, "Enhanced energy-storage performance with excellent stability under low electric fields in BNT-ST relaxor ferroelectric ceramics," *Journal of Materials Chemistry C*, vol. 7, no. 2, pp. 281-288, 2019.

[23] C. Kornphom, K. Saenkam, and T. Bongkarn, "Enhanced energy storage properties of BNT-ST-AN relaxor ferroelectric ceramics fabrication by the solid-state combustion technique," *Physica Status Solidi (A): Applications and Materials Science*, vol. 220, no. 10, 2023.

[24] Q. Huang, F. Si, and B. Tang, "The effect of rare-earth oxides on the energy storage performances in $BaTiO_3$ based ceramics," *Ceramics International*, vol. 48, no. 12, pp. 17359-17368, 2022.

[25] Y. Wan, N. Hou, P. Ren, M. Ma, K. Song, F. Yan, X. Lu, and G. Zhao, "High-temperature energy storage properties of $Bi_{0.5}Na_{0.5}TiO_3$ based ceramics modified by $NaNbO_3$," *Journal of Alloys and Compounds*, vol. 888, 161591, 2021.

[26] A. Banwal and R. Bokolia, "Thermometric sensing performance in Erbium modified $SrBi_{2-x}Nb_2Er_xO_9$ ferroelectric ceramic for optoelectronic devices," *Ceramics International*, vol. 48, part 23A, pp. 34405-34414, 2022.

[27] R. Ramaraghavulu and S. Buddhudu, "Structural and dielectric properties of $BaBi_2Nb_2O_9$ ferroelectric ceramic powders by a solid state reaction method," *Ferroelectrics*, vol. 460, no. 1, pp. 57-67, 2014.

[28] H. C. Gupta, Archana, and V. Luthra, "Lattice vibrations of $ABi_2Nb_2O_9$ crystals (A = Ca, Sr, Ba)," *Vibrational Spectroscopy*, vol. 56, no. 2, pp. 235-240, 2011.

[29] Y. González-Abreu, A. Pelaíz-Barranco, Y. Gagou, J. Belhadi, and P. Saint-Grégoire, "Vibrational analysis on two-layer Aurivillius phase $Sr_{1-x}Ba_xBi_2Nb_2O_9$ using Raman spectroscopy," *Vibrational Spectroscopy*, vol. 77, pp. 1-4, 2015.

[30] R. Bokolia, O. P. Thakur, V. K. Rai, S. K. Sharma, and K. Sreenivas, "Dielectric, ferroelectric and photoluminescence properties of Er^{3+} doped $Bi_4Ti_3O_{12}$ ferroelectric ceramics," *Ceramics International*, vol. 41, no. 4, pp. 6055-6066, 2015.

[31] A. Basheer, G. Prasad, G. S. Kumar, and N. V. Prasad, "Dielectric studies on Sm-modified two-layered BLSF ceramics," *Bulletin of Materials Science*, vol. 42, no. 3, pp. 1-11, 2019.

[32] F. D. Hardcastle and I. E. Wachs, "Determination of niobium-oxygen bond distances and bond orders by Raman spectroscopy," *Solid State Ionics*, vol. 45, pp. 201-213, 1991.

[33] F. D. Hardcastle and I. E. Wachs, "Determination of vanadium-oxygen bond distances and bond orders by Raman spectroscopy," *The Journal of Physical Chemistry*, vol. 95, pp. 5031-5041, 1991.

[34] G. D. Chryssikos, "Bond length-Raman frequency correlations in borate crystals," *Journal of Raman Spectroscopy*, vol. 22, pp. 645-650, 1991.

[35] F. D. Hardcastle and I. E. Wachs, "Determination of molybdenum-oxygen bond distances and bond orders by Raman spectroscopy," *Journal of Raman Spectroscopy*, vol. 21, pp. 683-691, 1991.

[36] P. Keburis, J. Banys, A. Brilingas, J. Prapuolenis, A. Kholkin, and M. E. V. Costa, "Dielectric properties of relaxor ceramics BBN," *Ferroelectrics*, vol. 353, pp. 149-153, 2007.

[37] J. D. Bobic, M. M. V. Petrovic, and B. D. Stojanovic, "Review of the most common relaxor ferroelectrics and their applications," *Magnetic, Ferroelectric, and Multiferroic Metal Oxides*, pp. 233-249, 2018.

[38] P. Sun, H. Wang, X. Bu, Z. Chen, J. Du, L. Li, F. Wen, W. Bai, P. Zheng, W. Wu, L. Zheng, and Y. Zhang, "Enhanced energy storage performance in bismuth layer-structured $BaBi_2Me_2O_9$ (Me = Nb and Ta) relaxor ferroelectric ceramics," *Ceramics International*, vol. 46, pp. 15907-15914, 2020.

[39] A. Khokhar, M. L. V. Mahesh, A. R. James, P. K. Goyal, and K. Sreenivas, "Sintering characteristics and electrical properties of $BaBi_4Ti_4O_{15}$ ferroelectric ceramics," *Journal of Alloys and Compounds*, vol. 581, pp. 150-159, 2013.

[40] A. Khokhar, P. K. Goyal, O. P. Thakur, and K. Sreenivas, "Effect of excess of bismuth doping on dielectric and ferroelectric properties of $BaBi_4Ti_4O_{15}$ ceramics," *Ceramics International*, vol. 41, pp. 4189-4198, 2015.

[41] A. Kumar and S. Asthana, "Investigation on energy storage properties and thermally stable dielectric constant for high temperature electronic device applications in the holmium substituted $Na_{0.5}Bi_{0.5}TiO_3$," *Journal of Materials Science: Materials in Electronics*, vol. 32, pp. 20225-20239, 2021.

[42] A. Chakrabarti and A. R. Molla, "Zirconia assisted crystallization of ferroelectric $BaBi_2Nb_2O_9$ based glass-ceramics: Kinetics, optical and dielectrical properties," *Journal of Alloys and Compounds*, vol. 844, 156181, 2020.

6

CHAPTER

Upconversion Luminescence, Optical Temperature Sensing, Ferroelectric, and Energy Storage Properties of $Er^{3+}/Yb^{3+}/W^{6+}$ Tri-Doped $BaBi_2Nb_2O_9$ Ferroelectric Ceramic

- *This chapter gives insight into the upconversion, sensing, and ferroelectric properties of $BaBi_{2-0.04-0.10}Nb_{2-z}Er_{0.04}Yb_{0.10}W_zO_9$ ceramic doped with transition metal ion, W^{6+}, and an optimized concentration of Er^{3+} and Yb^{3+}.*
- *The UCL intensity improves with W^{6+} concentration and reaches a maximum at (z = 0.02); the quenching effect occurs after this concentration.*
- *The time-resolved fluorescence analysis was done for green and red emissions, and it was observed that the decay time values increased for higher dopant concentrations, suggesting a non-radiative transition at higher dopant concentrations.*
- *The FIR technique measured the absolute sensitivity (S_a) with a value of 0.91% K^{-1} at 573 K.*
- *The PE loops improved with W^{6+} doping and attained the maximum polarization (P_m) value (9.719 $\mu C/cm^2$) for z = 0.02.*
- *The recorded energy density (W), recoverable energy storage density (W_{rec}), and energy storage efficiency (η) for undoped and tri-doped BBN ceramics were (0.662 J/cm^3, 0.518 J/cm^3, and 78.25%) and (0.874 J/cm^3, 0.792 J/cm^3, and 90.53%), respectively. Therefore, the prepared material has the potential to develop advanced electronic devices for a wide range of applications.*

6.1 INTRODUCTION

Chapter 5 explores the impact of Er^{3+} and Yb^{3+} ions on the dielectric, ferroelectric, and energy storage properties of $BaBi_2Nb_2O_9$ ceramic. The PE loops were traced under moderate applied electric fields ranging from 75 kV/cm to 100 kV/cm. The energy storage properties of the Er^{3+}/Yb^{3+} doped BBN system were also investigated for the aforementioned applied electric fields. It has been observed that the energy storage variables (W, W_{rec}, η) improve as the applied electric field increases. Although the efficiency is enhanced in the Er^{3+}/Yb^{3+} co-doped BBN system, the undoped system has greater recoverable energy storage than the doped system. Also, in **Chapter 4**, the UCL emission intensity has increased in the Er^{3+}/Yb^{3+} co-doped $BaBi_2Nb_2O_9$ system, but the optical temperature sensitivity has lowered in the co-doped system. Therefore, this chapter aims to enhance the optical, electrical, and sensing properties of the BBN compositions by systematically replacing the B-site ions (Nb^{5+}) with the transition metal ions (W^{6+}).

Previous studies have investigated host materials consisting of fluoride and ferroelectric oxide, focusing on three dopants [1-4]. Among these dopants, the addition of a transition metal such as tungsten, molybdenum, or manganese has been extensively studied [5, 6]. These dopants have been found to effectively modify the local environment around the rare earth (RE) ion. Implementing this approach was expected to induce a portion of the parity-prohibited intra-4f transitions of RE ions, leading to a modification of the local Coulombic field. This alteration could facilitate the mingling of f-states with higher electronic configurations [7]. For instance, Pandey et al. reported the frequency upconversion property of yellow light-emitting Ho^{3+}/Yb^{3+} embedded tungsten tellurite (TeO_2-WO_3) glass [1]. Babu et al. studied the blue-green cooperative upconverted

luminescence and radiative energy transfer in Yb-doped tungsten tellurite glass [2]. The enhanced piezoelectric properties have been explored in transition metal ion-doped KNN ceramic [3]. In $Bi_{0.9}Eu_{0.1}FeO_3$ thin films, the effect of transition metal ions on structural and electrical properties is discussed [4]. Bobic et al. investigated $BaBi_4Ti_{4-x}W_xO_{15}$ doped with W^{6+} and revealed that the remnant polarization increases with W^{6+} doping [5]. In tungsten-doped $SrBi_2Ta_2O_9$ ferroelectric ceramic, the dielectric constant of the samples increases with tungsten doping at their respective Curie temperatures [6]. In another study, the introduction of W^{6+} in $Bi_{2.93}Ce_{0.07}TiNb_{1-x}W_xO_9$ ceramic enhanced the octahedral tilt angle along the "a" axis, which resulted in an optimal piezoelectric property [7]. These studies indicate that adding a third dopant not only enhances the electrical characteristics but also improves the optical properties of the material. Consequently, this chapter presents a comprehensive analysis of the tri-doped BBN system to enhance its optical, electrical, and sensing properties.

This chapter is organized as follows: Section 6.2 presents a comprehensive discussion of the characterization and synthesis procedures. Section 6.3 details the results and discussions. In subsection 6.3.1, the focus is on structural analysis, elucidated through XRD spectra. Subsection 6.3.2 delves into the upconversion luminescence (UCL) spectra of the prepared sample, while subsection 6.3.3 provides insights into the variation of UCL spectra with different pump powers. Subsection 6.3.4 offers a detailed analysis of time-resolved photoluminescence. Non-invasive temperature sensing is addressed in subsection 6.3.5. Furthermore, subsection 6.3.6 provides information about the PE loops and energy storage properties of the prepared ceramic. The chapter concludes with a concise summary in section 6.4.

6.2 SYNTHESIS AND CHARACTERIZATION DETAILS

The ceramic $BaBi_{2-0.04-0.10}Nb_{2-z}Er_{0.04}Yb_{0.10}W_zO_9$ (BBN) is manufactured by a simple solid-state method. The Er^{3+} (x = 0.04) and Yb^{3+} (y = 0.10) were fixed at optimized concentrations, and W^{6+} was varied during the process (z = 0.01 to 0.04). The precursors used were $BaCO_3$, Bi_2O_3, Nb_2O_5, Er_2O_3, Yb_2O_3, and WO_3, having the highest purity (99.99%) from Sigma Aldrich and Alfa Aesar. These initial precursors were measured in stoichiometric proportions and homogenized with a mortar and pestle for 5 hours, using ethanol as the solvent. The automated high-temperature furnace is used for the calcination of the sample at 950°C with a hold time of 3 hours. Then, a binder of PVA is mixed with calcined powder to prepare the pellets. The pellets were fabricated using a hydraulic press at a pressure of 5 MPa with a diameter of 10 mm and a thickness of approximately 1 mm. These pellets were again put into the same furnace for sintering at 1050°C for 3 hours for the densification of the sample. Following the sintering process, some pellets remained unaltered, while others were reduced in thickness to 0.20 mm to facilitate PE measurements. These fragile pellets were coated with air-drying silver paste on both sides to avoid breaking.

The investigation of the phase of the material was conducted through the analysis of XRD spectra utilizing Cu-Kα radiations by the use of a Bruker high-quality X-ray diffractometer. The refinement and lattice parameters are calculated by TOPAZ software. The polarization measurement in response to the applied electric field is conducted using a sophisticated automated loop tracer. The experiment was conducted at ambient temperature with a frequency of 50 Hz. The HORIBA quanta master instrument was used to facilitate UCL spectra using laser source light at 980 nm. For the lifetime decay measurement, a

pulsed laser was operated in modulation mode at its maximum power capability of 2W/cm^2 for 30 minutes. The synthesized material was placed on the heaters to analyze the temperature-dependent UCL emission spectra while the temperature was measured with a thermocouple. A manually constructed heater equipped with a thermocouple, multimeter, and variable-voltage control was utilized to conduct the sensing, resolution, and stability analyses. The sample coding for various compositions of $BaBi_{2-x-y}Nb_{2-z}Er_xYb_yW_zO_9$ ceramic is recorded in Table 6.1.

Table 6.1: Abbreviation used for various compositions of $BaBi_{2-x-y}Nb_{2-z}Er_xYb_yW_zO_9$ ceramic.

Compositions	Sample Code	Er^{3+} (x)	Yb^{3+} (y)	W^{6+} (z)
$BaBi_{2-x-y}Nb_{2-z}Er_xYb_yW_zO_9$	BBNE0Y0W0	0.00	0.00	0.00
$BaBi_{1.96}Nb_{2-z}Er_{0.04}Yb_{0.00}W_{0.00}O_9$	BBNE4Y0W0	0.04	0.00	0.00
$BaBi_{1.86}Nb_{2-z}Er_{0.04}Yb_{0.10}W_{0.00}O_9$	BBNE4Y10W0	0.04	0.10	0.00
$BaBi_{1.86}Nb_{1.99}Er_{0.04}Yb_{0.10}W_{0.01}O_9$	BBNE4Y10W1	0.04	0.10	0.01
$BaBi_{1.86}Nb_{1.98}Er_{0.04}Yb_{0.10}W_{0.02}O_9$	BBNE4Y10W2	0.04	0.10	0.02
$BaBi_{1.86}Nb_{1.97}Er_{0.04}Yb_{0.10}W_{0.03}O_9$	BBNE4Y10W3	0.04	0.10	0.03
$BaBi_{1.86}Nb_{1.96}Er_{0.04}Yb_{0.10}W_{0.04}O_9$	BBNE4Y10W4	0.04	0.10	0.04

6.3 RESULTS AND DISCUSSION

6.3.1 Structural Analysis

The spectra of XRD for undoped, Er^{3+} doped, Er^{3+}/Yb^{3+} co-doped, and $Er^{3+}/Yb^{3+}/W^{6+}$ tri-doped BBN ceramic are represented in **Figure 6.1**. The XRD peaks resemble the JCPDS file number 00-012-0403, associated with an orthorhombic crystal structure and classified within the Fmmm phase group. The absence of secondary peaks in the XRD patterns provides evidence for extensive incorporation of the dopant within the host lattice. The prominent XRD peak corresponds to the (115) plane, attributed to the BLSFs having n = 2.

From the previous findings, it can be confirmed that the (112n+1) plane is associated with an intense XRD peak in the BLSF materials of the Aurivillus family. The density of the prepared sintered pellet is evaluated by the Archimedes method (Table 6.2). The measured density is comparable with the reported density in the JCPDS file with 95% accuracy. The A-site Bi^{3+} ions are replaced by Er^{3+} and Yb^{3+} ions at an optimized concentration, whereas W^{6+} ions systematically replace the B-site ion Nb^{5+}. The explanation for this replacement is based on the fact that they have equal charge valency and nearly comparable radii. The resulting change in lattice parameters is shown in Table 6.2, indicating a minor shift in the parameters, which implies the maintenance of electroneutrality inside the lattice, preventing lattice deformation. Also, the increment in lattice cell volume can be explained by the lone pair character of Bi^{3+} ions. In the $BaBi_2Nb_2O_9$ structure, this phenomenon might be attributed to the restricted nature of the $6s^2$ lone pair of Bi^{3+} inside the host. This restricted lone pair in Bi^{3+} induces a minor deformation in the surrounding lattice structure, which expands the unit cell volume [8-10].

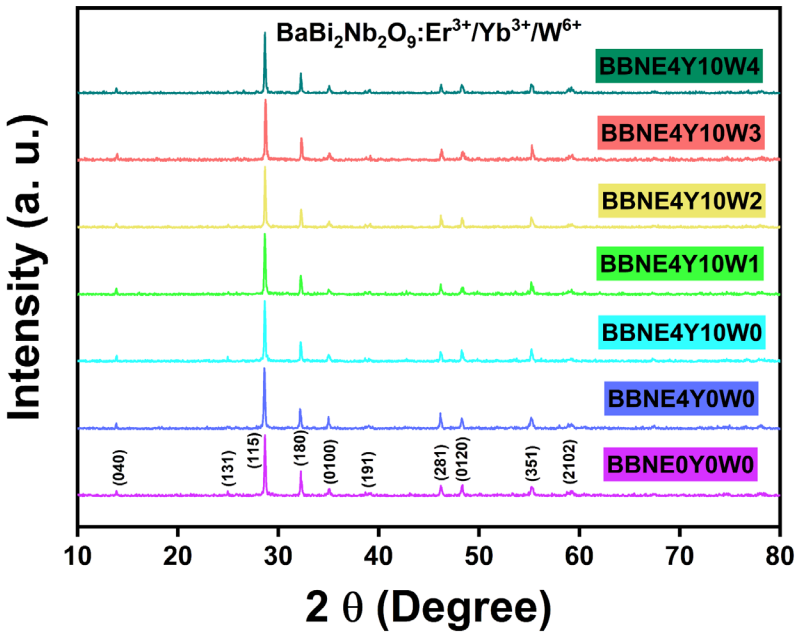

Figure 6.1: XRD spectra of all the doped and undoped BBN ceramics compositions.

Table 6.2: Refinement parameters, lattice parameters, and experimental density of all the BBN ceramic.

Compositions	Refinement Parameters				
	R_p	R_{wp}	R_{exp}	R Braggs	Gof (χ)
BBNE0Y0W0	12.84	11.00	10.76	13.606	1.02
BBNE4Y0W0	13.59	12.18	11.57	9.391	1.05
BBNE4Y10W0	11.76	12.98	10.22	9.651	1.06
BBNE4Y10W1	10.56	9.22	8.52	9.971	1.08
BBNE4Y10W2	10.93	9.38	8.66	11.566	1.08
BBNE4Y10W3	10.37	8.74	8.32	12.757	1.05
BBNE4Y10W4	11.02	9.57	8.82	8.886	1.08
	Lattice Parameters and Experimental Density				
	a (Å)	**b (Å)**	**c (Å)**	**V (Å^3)**	**Density (g/cm^3)**
BBNE0Y0W0	5.5394	25.5751	5.5571	787.294	7.0091
BBNE4Y0W0	5.5526	25.609	5.5623	790.982	6.8724
BBNE4Y10W0	5.5488	25.620	5.5612	790.581	6.7600
BBNE4Y10W1	5.5675	25.6679	5.5637	795.095	6.1919
BBNE4Y10W2	5.5640	25.6734	5.5630	794.672	6.2246
BBNE4Y10W3	5.5631	25.6771	5.5658	795.063	6.3253
BBNE4Y10W4	5.5627	25.6625	5.5577	793.394	6.6633

6.3.2 Upconversion Luminescence Spectroscopy

The upconversion luminescence (UCL) spectra of W^{6+} doped BBN compositions for different W^{6+} concentrations (z = 0.01, 0.02, 0.03, and 0.04) are shown in **Figure 6.2(a)**. The spectra are acquired using an irradiation of 980 nm excitation wavelength with a source density of 3.25 W/cm^2. At 535 nm and 546 nm, two distinct green emission bands were detected due to the transitions from $^4H_{11/2}$ to $^4I_{15/2}$ and $^4S_{3/2}$ to $^4I_{15/2}$, respectively. The red band at 673 nm through the transition from $^4F_{9/2}$ to $^4I_{15/2}$ can be visible.

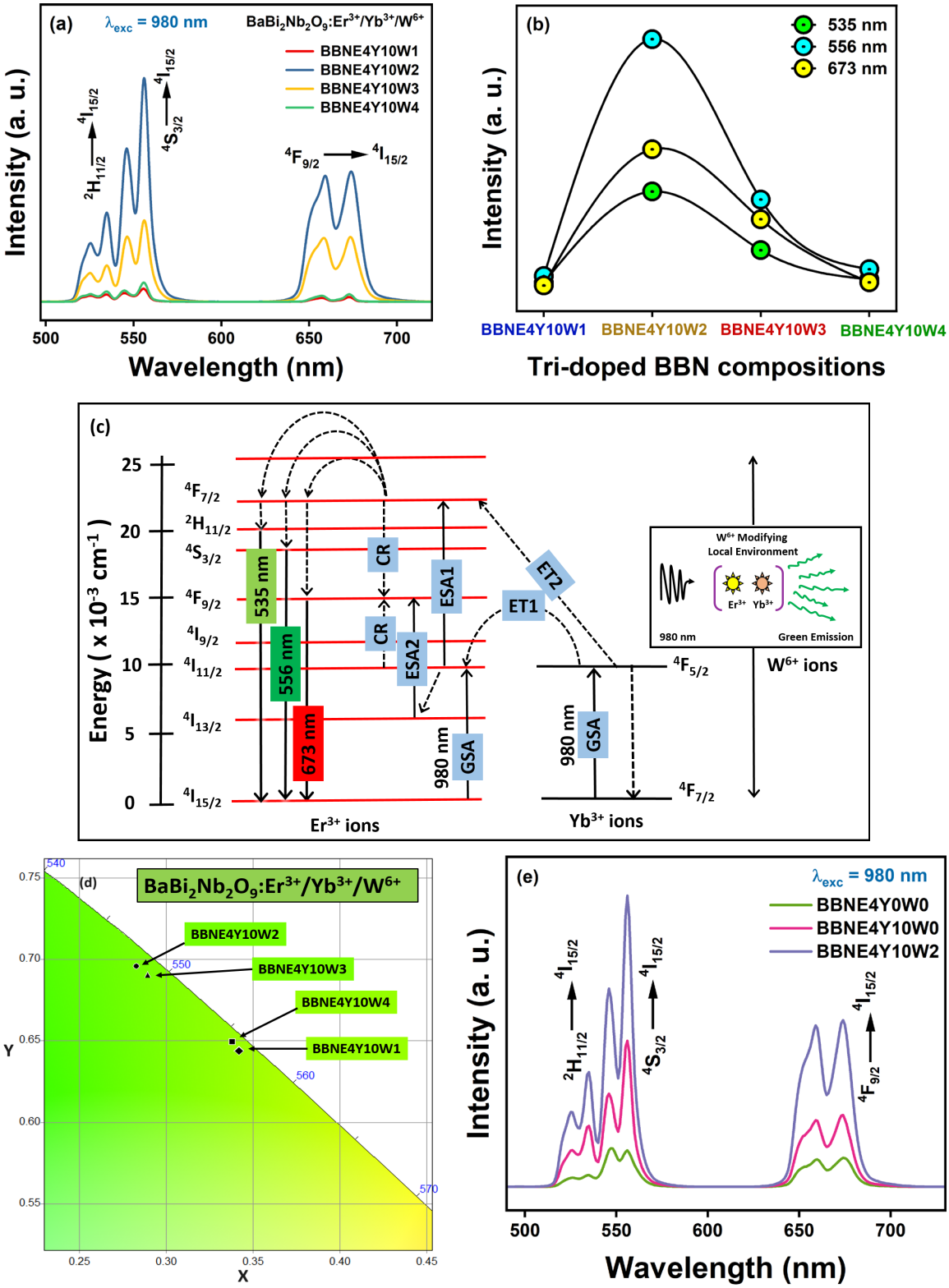

Figure 6.2: (a) UCL spectra of all the compositions of tri-doped BBN ceramics (b) Variation of UCL intensity in the tri-doped system (c) Schematic depiction of possible pathways for UCL (d) CIE (x, y) plot of tri-doped BBN ceramics (e) Comparison of UCL intensity of BBNE4Y0W0, BBNE4Y10W0, and BBNE4Y10W2 ceramic.

The crystal field causes the $^4F_{9/2}$ energy level of the Er^{3+} ion to be split into sublevels via upconversion luminescence [11]. **Figure 6.2(b)** demonstrates that the emission intensity reaches its maximum value at a concentration of z = 0.02. Subsequently, the emission intensity decreases due to the occurrence of the concentration quenching effect. In this effect, the proximity of the dopant ions becomes sufficiently close, leading to their involvement in non-radiative transitions, hence causing a deterioration in the intensity of photoluminescence. The calculation of the interionic distance between dopant ions can be accomplished by the Blasse equation represented in Eq. (6.1) [11, 12]:

$$R_c \approx 2\left[\frac{3V}{4\pi X_c Z}\right]^{\frac{1}{3}} \tag{6.1}$$

where V represents the volume of the unit cell, Z denotes the number of host cations, and X_c (x+y+z) refers to the optimal concentration at which quenching occurs. By substituting the given values into Eq. (6.1), the value of R_c comes out to be 13.34 Å. **Figure 6.2(c)** depicts the energy level diagram illustrating the potential pathways for the UCL. The Yb^{3+} ions are subjected to illumination from a 980 nm laser, which results in energy absorption by GSA. This energy is then transferred to a higher energy level at $^4I_{11/2}$ through ET1 and to $^4F_{7/2}$ level through ET2. Photons may potentially be absorbed by Er^{3+} ions via GSA. Therefore, the level $^4I_{11/2}$ is produced by the ESA process to transition to a higher energy level, namely the $^4F_{7/2}$ level. Consequently, the level $^4F_{7/2}$ experiences an excessive population due to distinct processes, ET1, ET2, and ESA. The ions undergo a non-radiative process known as multiphonon relaxation (MPR), resulting in their transition to energy levels $^2I_{11/2}$, $^4S_{3/2}$, and $^4F_{9/2}$. Ions emit a single red band at 672 nm and two green bands at 535 and 556 nm due to their transition to the lower energy level. The red emission band may be attributed to an additional decay path facilitated via cross-relaxation channels CR1

and CR2. The CIE chromaticity coordinates (x, y) for all tri-doped BBN compositions were also calculated from the emission spectra. It has been observed that at z = 0.01 and 0.04, the spectra exhibit in a brighter green region, whereas for z = 0.02 and 0.03, they manifest in a deeper green region, as depicted in **Figure 6.2(d)**. Furthermore, the enhancement in UCL emission intensity by the incorporation of W^{6+} ions in the host lattice is displayed in **Figure 6.2(e)**. The local electric field surrounding the Er^{3+} ions changes, increasing the chance of electronic-dipole (ED) transitions, which causes this intensity spike. Consistent with earlier observations, the results show that changes in the crystal field influence the UC emissions of Er^{3+} ions linked to the intra-4f electronic dipole transitions [13].

6.3.3 Pump Power Dependence on UCL

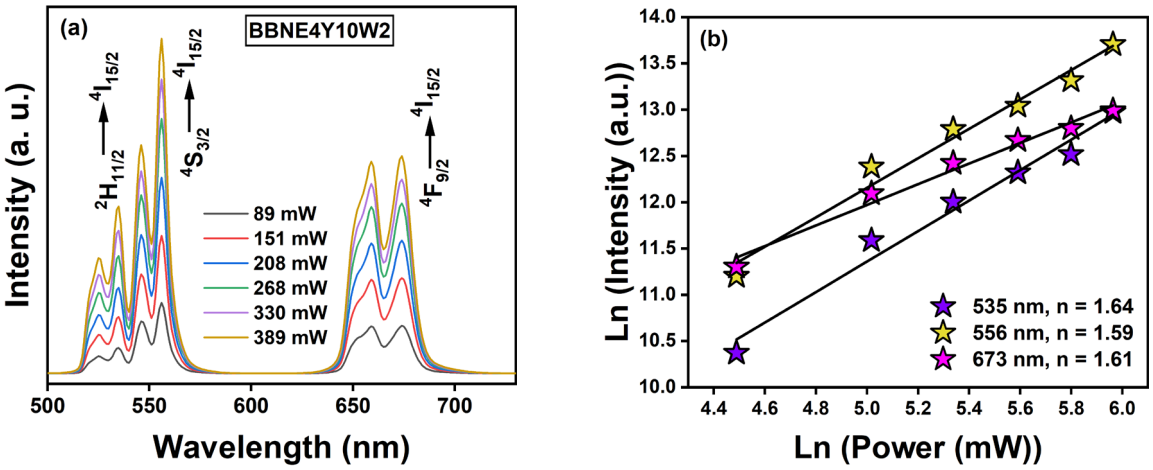

Figure 6.3: (a) Dependency of varying pump power on UCL spectra (b) Ln(Intensity) vs Ln(Power).

To get a deeper understanding of the mechanisms behind UCL, the transitions involving the levels $^2H_{11/2}$, $^4S_{3/2}$, and $^4F_{9/2}$ to level $^4I_{15/2}$ in the BBNE4Y10W2 composition were investigated. The distinct pump powers range from 89 mW to 389 mW with an excitation source density of 5.79 W/cm^2 to 25.34 W/cm^2, as depicted in **Figure 6.3(a)**. It has been observed that as the pump power increases, the UCL intensity also increases. Eq. (6.2) illustrates the correlation between pump power and UCL emission intensity [14, 15].

$$I_{UP} \propto P^{n} \quad (6.2)$$

where P represents the pump power, n signifies the low-energy photons necessary for the UCL, and I_{UP} denotes the luminescence intensity of the UCL. The curve of the Ln(Intensity) against the Ln(Power) is given in **Figure 6.3(b)**. The value of n can be obtained from the slope of the graph. The n equals 1.64, 1.59, and 1.61 for emission bands at 535 nm, 556 nm, and 673 nm, respectively. The fact that n is rounded to 2 means that two photons are involved in UCL. The disparity from n = 2 might be due to the impact of distinct UC mechanisms [12].

6.3.4 Time-Resolved Spectroscopy

The laser source in the modulation mode under the excitation of 980 nm wavelength is used to study the time-resolved photoluminescence spectra of green band and red band through transition $^4S_{3/2}$ to $^4I_{15/2}$ and $^4F_{9/2}$ to $^4I_{15/2}$ energy levels, respectively. The time decay profile of the green band at 556 nm for the tri-doped BBN system is given in **Figure 6.4(a-d)**. The curve is fitted using decay exponential fit given by Eq. (6.3):

$$I(t) = I_0 + \sum_i A_i \exp(-\frac{t}{\tau_i}) \ (i = 1, 2, 3) \quad (6.3)$$

where A_i (i = 1, 2, 3) is the fitting coefficient, τ_i (i = 1, 2, 3) is the decay time of luminescence, and I_0 is the intensity at the initial time. The mean lifetime is calculated using Eq. (6.4):

$$< \tau > = \sum_i \frac{A_i \tau_i^2}{A_i \tau_i} \ (i = 1, 2, 3) \quad (6.4)$$

The average lifetime for optimized BBNE4Y10W2 composition is 30 µs, which supports the high emission UCL intensity. After this, the average lifetime increases, possibly due to the non-radiative transitions at higher dopant concentrations. The

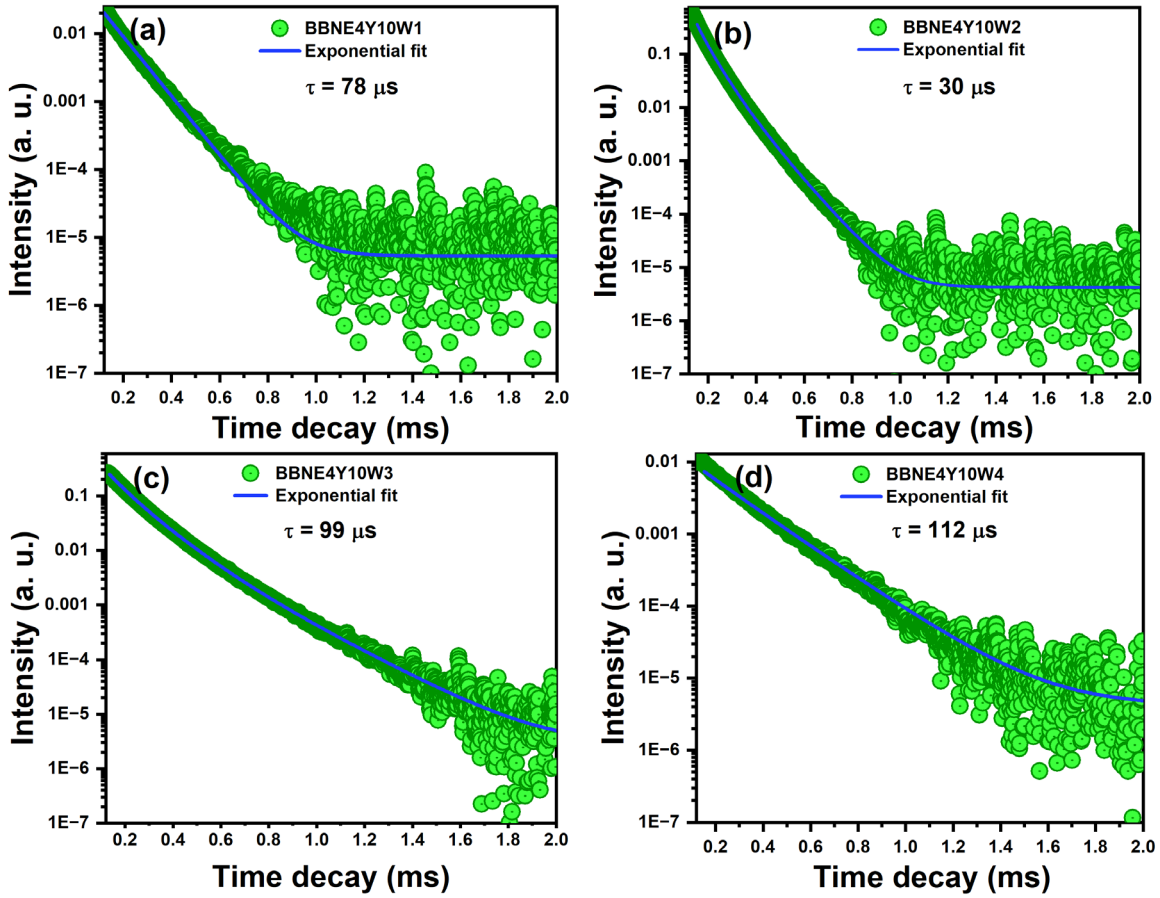

Figure 6.4: Time decay curve of tri-doped (a) BBNE4Y10W1 (b) BBNE4Y10W2 (c) BBNE4Y10W3 (d) BBNE4Y10W4 ceramics of green emission band at 556 nm.

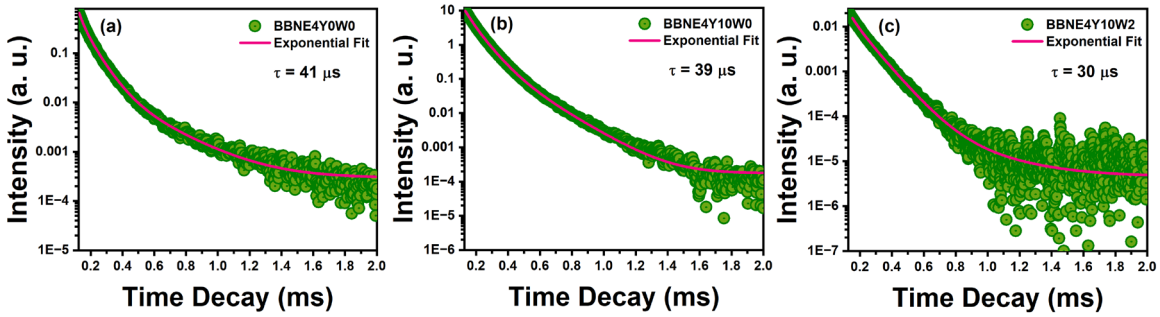

Figure 6.5: Comparison of decay process of green emission band of (a) BBNE4Y0W0 (b) BBNE4Y10W0 (c) BBNE4Y10W2 ceramic.

comparison of the time decay profile of Er^{3+} doped, Er^{3+}/Yb^{3+} co-doped, and $Er^{3+}/Yb^{3+}/W^{6+}$ tri-doped BBN for the green emission band is depicted in **Figure 6.5(a-c)**. It has been observed that the average lifetime of the green emission band at 556 nm is decreasing from single-doped BBN to tri-doped BBN, which prompts that the tri-doped system has a larger

radiative transition probability of the emitting level than the single-doped BBN system [16, 17]. Further, the time-resolved spectroscopy for the red emission band at 672 nm through the transition of ions from $^4F_{9/2}$ to $^4I_{15/2}$ is shown in **Figure 6.6(a-d)**. The average decay time for red emission is increasing with increasing W^{6+} concentration.

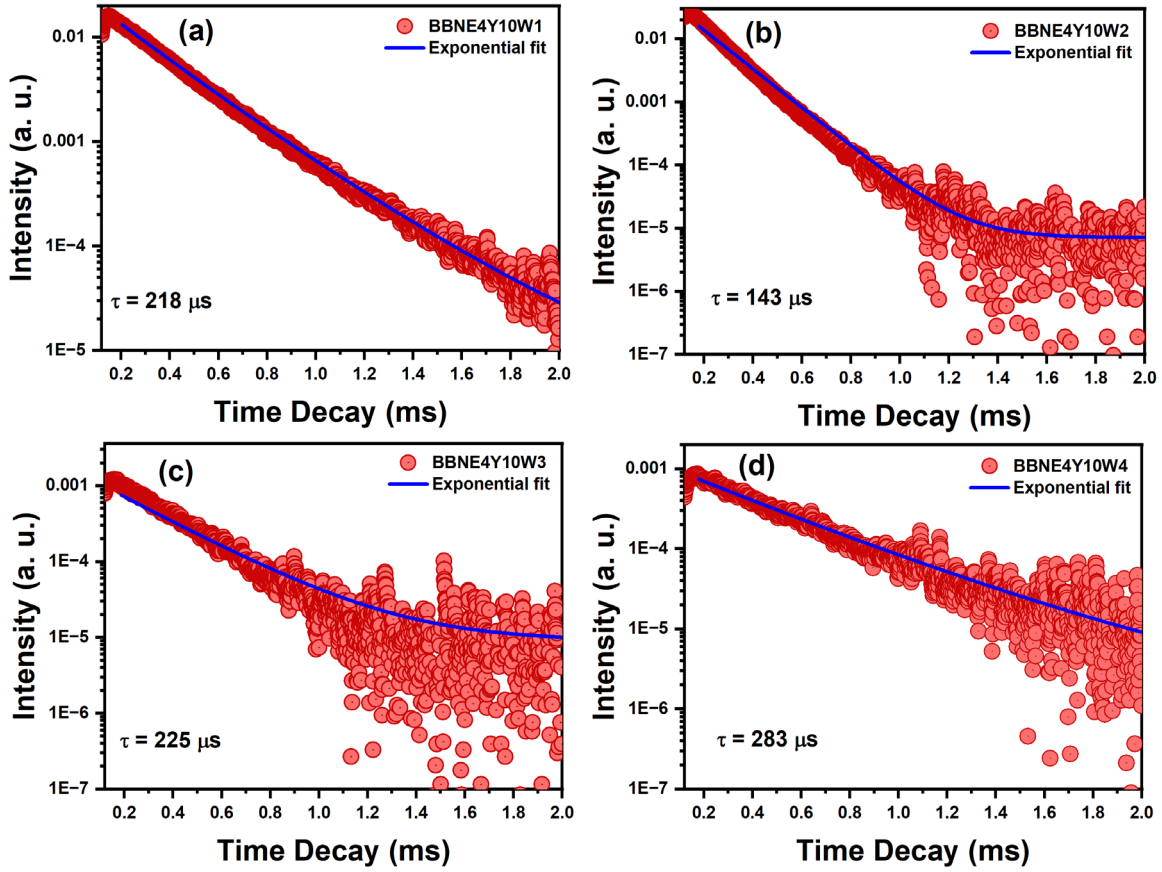

Figure 6.6: Time decay curve of tri-doped (a) BBNE4Y10W1 (b) BBNE4Y10W2 (c) BBNE4Y10W3 (d) BBNE4Y10W4 ceramics of red emission band at 673 nm.

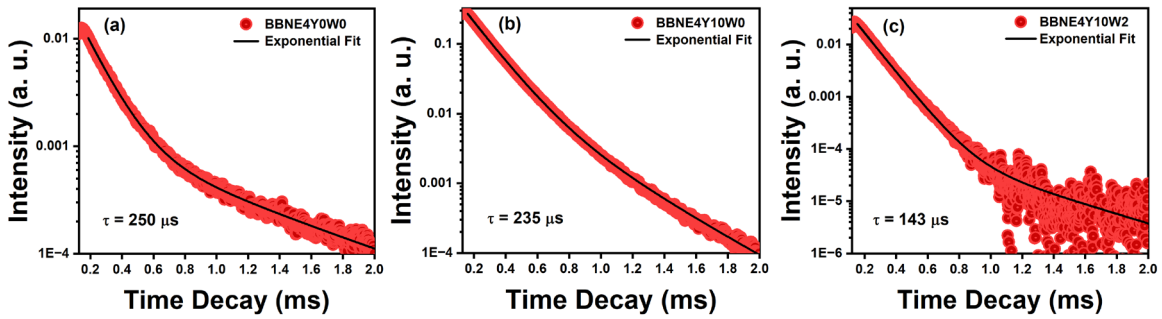

Figure 6.7: Comparison of decay process of red emission band of (a) BBNE4Y0W0 (b) BBNE4Y10W0 (c) BBNE4Y10W2 ceramic.

Figure 6.7(a-c) represents the average lifetime of the red emission band for Er^{3+} doped, Er^{3+}/Yb^{3+} co-doped, and $Er^{3+}/Yb^{3+}/W^{6+}$ tri-doped BBN ceramic. It can be seen that the lifetime is reduced in the co-doped and tri-doped systems, which is due to the effective radiative transition probabilities in these BBN compositions. Also, the presence of Yb^{3+} ions prevents the clustering of Er^{3+} ions, thereby increasing the optical properties [17].

6.3.5 Optical Temperature Sensing

The well-known method for contactless temperature sensitivity is the fluorescence intensity ratio (FIR) technique. This method is compatible with checking the capabilities of materials to be used as optical temperature sensors. The sensitivity of optimized BBNE4Y10W2 is calculated for the applicability of ceramic to be used as a potential sensor material. **Figure 6.8(a)** depicts the temperature-dependent UC spectra of BBNE4Y10W2. In this method, the ratio of the integral intensity of two green emission bands through transitions $^4H_{11/2}$ to $^4I_{15/2}$ and $^4S_{3/2}$ to $^4I_{15/2}$ is utilized **(Figure 6.8(b))**, as given in Eq. (6.5) [12]:

$$\mathrm{FIR} = \frac{I_H}{I_S} = C \exp\left(-\frac{\Delta E}{K_B T}\right) \tag{6.5}$$

where I_H and I_S are the symbolic representation for intensities via transitions $^4H_{11/2}$ to $^4I_{15/2}$ and $^4S_{3/2}$ to $^4I_{15/2}$, respectively, ΔE is the difference between thermally coupled energy levels, C is the coefficient of exponential, K_B is the Boltzmann constant, and T is the temperature at which spectra is traced. Eq. (6.5) can be re-written in linear form to ΔE and C and is given in Eq. (6.6) [12]:

$$\mathrm{Ln(FIR)} = -\left(\frac{\Delta E}{K_B}\right)\left(\frac{1}{T}\right) + \mathrm{LnC} \tag{6.6}$$

The Ln(FIR) slope against the temperature inverse gives us the value of $\Delta E/K_B$ and LnC to be 1158.53 and 2.97, respectively, provided in **Figure 6.8(c)**. These parameters

determine the optical temperature sensitivity of the produced ceramic BBNE4Y10W2. Eq. (6.7) may determine the absolute sensitivity of the material by plotting its changing FIR value against temperature [12]:

$$S_a = \frac{d(FIR)}{dT} = \frac{d\left(C \exp\left(-\frac{\Delta E}{K_B T}\right)\right)}{dT} = C \exp\left(-\frac{\Delta E}{K_B T}\right)\left(\frac{\Delta E}{K_B T^2}\right) \quad (6.7)$$

To acquire the relative sensitivity (S_r) of the material, the absolute sensitivity (S_a) is divided by FIR as employed in Eq. (6.8) [12]:

$$S_r = \frac{1}{FIR} \times S_a = \left(\frac{\Delta E}{K_B T^2}\right) \quad (6.8)$$

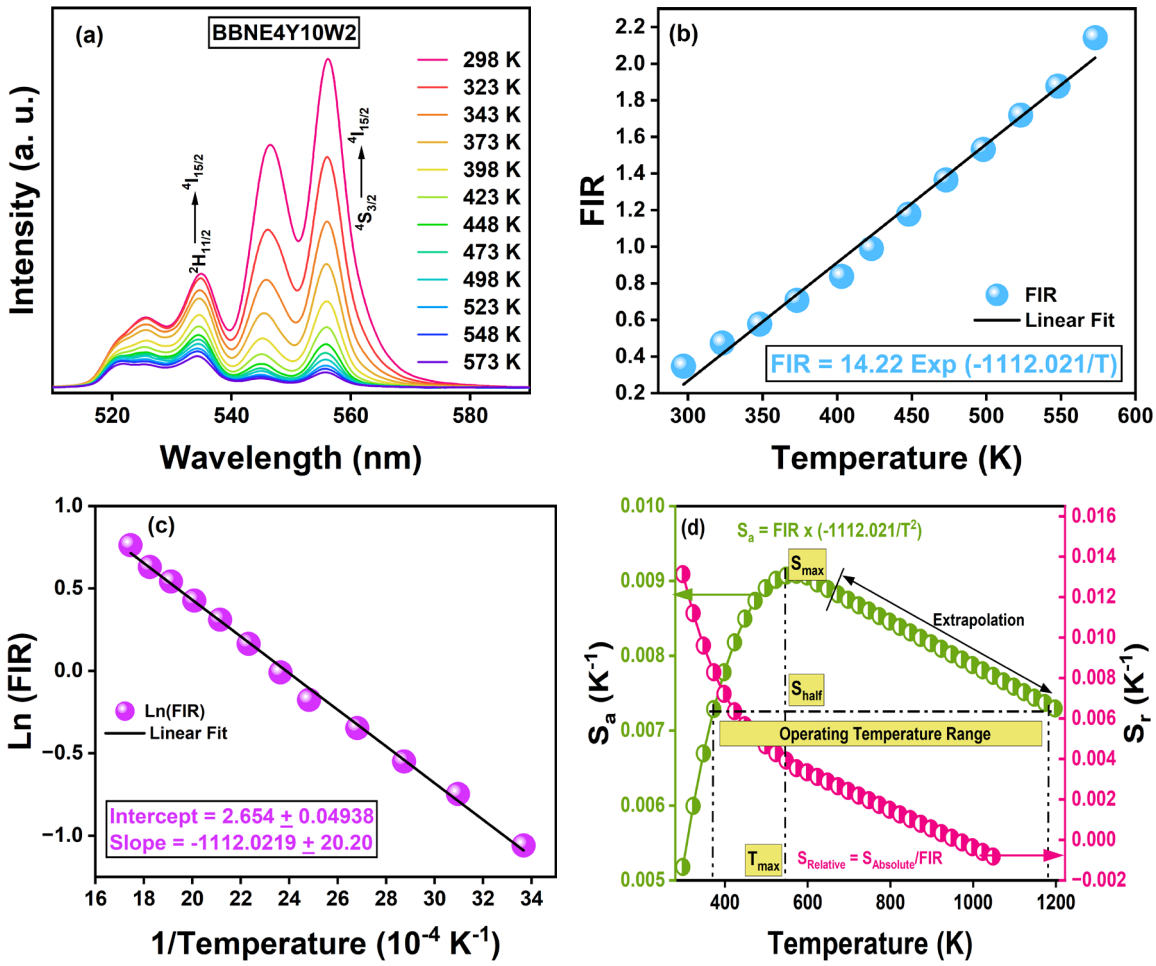

Figure 6.8: (a) Temperature-dependent UCL spectra of BBNE4Y10W2 ranging 303-573 K (b) FIR vs temperature (c) Ln(FIR) against the inverse of temperature (d) Variation of S_a and S_r with temperature.

The curve of S_r and S_a is shown in **Figure 6.8(d)**. The maximum S_a obtained at 573 K is 0.91% K^{-1} whereas S_r is 1.32% K^{-1} at 297 K. S_a values are extrapolated up to S_{half} (S_a is more than half of the highest value) using Eq. (6.7). When the experimentally observed ΔE_{ex} and the theoretically calculated ΔE_{th} are nearly the same; the material sensitivity is considered suitable. The ΔE_{ex} is calculated from the slope of **Figure 6.8(c)**, and the deconvoluted emission spectra give ΔE_{th} by the Viogt fit, as illustrated in **Figure 6.9**. The inaccuracy is approximately 3.0%, calculated using Eq. (6.9) [18]:

$$\delta = \frac{|\Delta E_{th} - \Delta E_{ex}|}{\Delta E_{th}} \times 100\% \qquad (6.9)$$

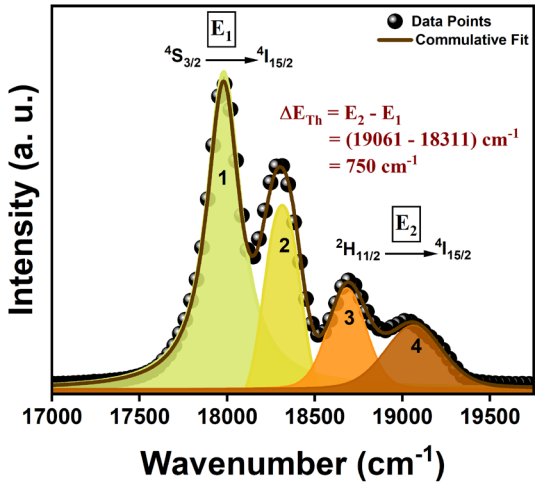

Figure 6.9: Deconvoluted curve of BBNE4Y10W2 sample using Voigt fit for ΔE_{th} calculation.

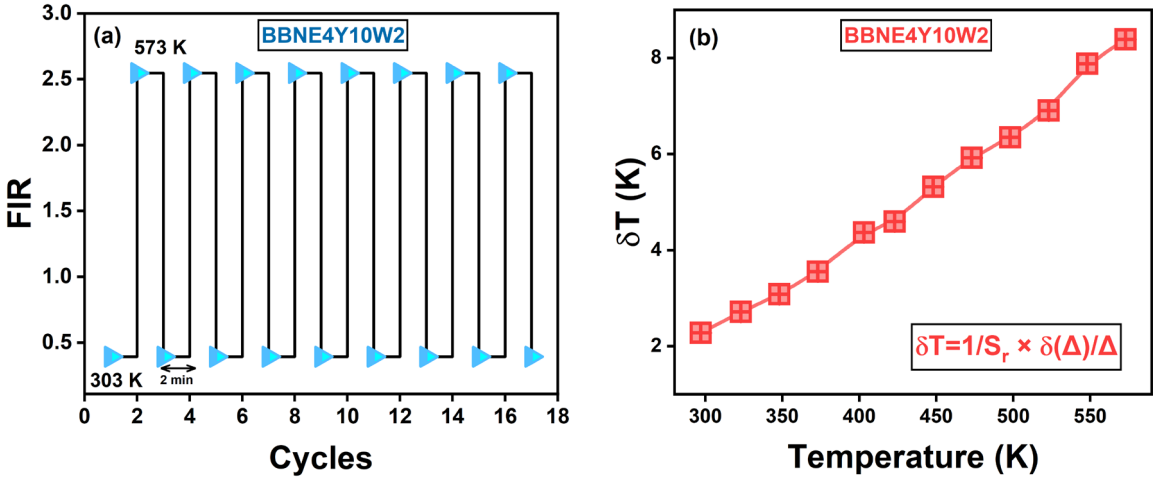

Figure 6.10: (a) Repeatability test of BBNE4Y10W2 for 17 cycles with stabilization time of 2 minutes (b) Resolution of temperature from 303 K to 573 K.

The repeatability (R) and resolution (δT) of a sensing material are critical in determining its effectiveness. These parameters can be presented by Eqs. (6.10 - 6.11) [18]:

$$R = 1 - \frac{\max(\Delta_{Av} - \Delta_{Sp})}{\Delta_{Av}} \quad (6.10)$$

$$\delta T = \frac{1}{S_r} \times \frac{\delta_\Delta}{\Delta} \quad (6.11)$$

where Δ_{Av} and Δ_{Sp} are FIR's mean and specific values in the temperature range 303-573 K for 17 cycles, and δ_Δ/Δ denotes the device's accuracy. **Figure 6.10(a)** shows negligible change in the FIR values across the entire temperature range. The temperature resolution has improved from 2.67 K to 8.78 K, as depicted in **Figure 6.10(b)**. Table 6.3 compares the sensitivity of the Er^{3+} doped, Er^{3+}/Yb^{3+} co-doped, and $Er^{3+}/Yb^{3+}/W^{6+}$ tri-doped BBN systems with other doped ferroelectric systems. Hence, it can be deduced that the prepared ceramic is a proficient material for sensing and has the potential to be extensively studied for its suitability in optical temperature sensor applications.

Table 6.3: Comparison of the sensitivity of various doped ferroelectric ceramics.

Host Material	**ΔE (cm^{-1})**	**Temp. Range (K)**	**T_a (K)**	**S_a (K^{-1})**	**S_r (K^{-1})**	**T_r (K)**	**Ref.**
$La_2Ti_2O_7$:Er/Yb	683	93-773	493	0.29%	0.41 %	300	[9]
$Na_{0.5}Bi_{0.5}TiO_3$:Er/Yb	706.6	173-553	493	0.35%	-	-	[10]
$BaBi_2Nb_2O_9$:Er/Yb (y = 0.06)	705	303-573	523	0.69%	1.10%	303	[12]
$BaBi_2Nb_2O_9$:Er/Yb (y = 0.10)	645	303-573	463	0.58%	1.01%	303	[12]
$Na_{0.5}Bi_{2.5}Ta_2O_9$: Er/Yb	-	153-483	483	0.78%	5.99%	153	[15]
$CaBi_2Ta_2O_9$:Er/Yb	1181	153-603	590	0.39%	-	-	[19]
$Na_{0.5}Er_{0.5}Bi_4Ti_4O_{15}$	500.1	175-500	380	0.17%	-	-	[20]
$BaTiO_3$:Er/Yb	600	125-430	410	0.19%	-	-	[21]
BNT-SBT:Er/Yb	-	303-573	363	0.49%	-	-	[22]
$Ba_2NaNb_5O_{15}$:Er/Yb	735.5	298-573	373	0.68%	0.90%	298	[23]
$BaBi_2Nb_2O_9$:Er	661	303-623	483	0.99%	0.40%	303	[24]
$BaBi_2Nb_2O_9$:Er/Yb/W	773	303-573	573	0.91%	1.32%	303	**This work**

6.3.6 PE Loops and Energy Storage Analysis

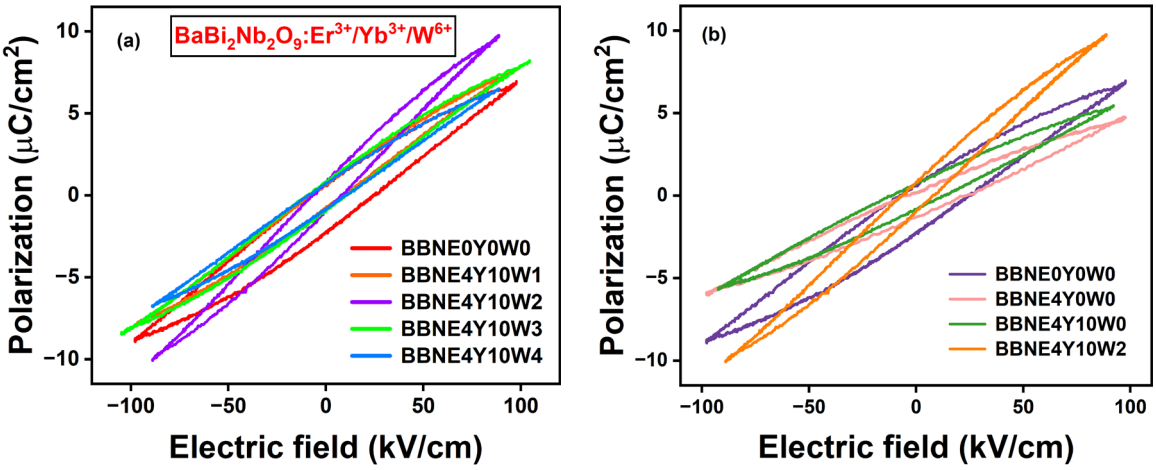

Figure 6.11: (a) PE loops of tri-doped BBN compositions at 50 Hz (b) Comparison of PE loops of BBNE0Y0W0, BBNE4Y0W0, BBNE4Y10W0, and BBNE4Y10W2 ceramic.

The polarization versus electric field (PE) curves of undoped and tri-doped compositions of BBN ceramic are represented in **Figure 6.11(a)** at an applied electric field of 100 kV/cm. The PE hysteresis loops are traced at room temperature at 50 Hz. It has been observed that after doping with W^{6+} ions, the PE loop acquires thinner shapes. The maximum polarization (P_m) obtained for undoped BBN is 6.831 μC/cm^2 and 9.719 μC/cm^2 for BBNE4Y10W2 composition at 100 kV/cm. In tri-doped BBN compositions, the P_m increases, whereas the remnant polarization ($2P_r$) decreases, as depicted in Table 6.4. These observations imply that with W^{6+} ions on the B-site of the perovskite structure, the slimming tendency of a BBN is increasing with an increase in P_m. The nano-polar regions align effectively due to the maintenance of the oxygen vacancies, which tend to migrate toward the domain wall when subjected to a strong electric field, helping the domain-flipping process. Nevertheless, the estimation of high-quality hysteresis loops is subjected to several factors, including lattice strain, defects, grain size, density, and minimum sample thickness. **Figure 6.11(b)** compares undoped, Er^{3+} doped, Er^{3+}/Yb^{3+} co-doped, and $Er^{3+}/Yb^{3+}/W^{6+}$ tri-doped BBN ceramic. It is concluded that the tri-doped BBN ceramic has higher P_m values,

whereas, in the case of singly-doped and co-doped BBN compositions, the P_m values are lesser than the undoped BBN ceramic. This indicates that the transition metal ions on the B-site play a crucial role in enhancing the polarization of the sample.

Moreover, the PE loops are beneficial for analyzing the energy storage density of the ceramic. The P_r, P_m, and applied electric field values were used to calculate the energy storage parameters: energy density (W), recoverable energy density (W_{rec}), and efficiency (η). The mathematical expression is given by Eqs. (6.12-6.14) [25, 26]:

$$W = \int_0^{P_m} EdP \tag{6.12}$$

$$W_{rec} = \int_{P_r}^{P_m} EdP \tag{6.13}$$

$$\eta = \frac{W_{rec}}{W} \times 100\% \tag{6.14}$$

Based on these expressions, it can be said that ceramic materials with a high energy density and efficiency should have a high maximum polarization, a low remnant polarization, and high BDS simultaneously [27, 28]. Table 6.4 tabulates the energy storage parameters W, W_{rec}, and η values for all the compositions of BBN. **Figure 6.12(a)** reveals the energy storage density parameters of undoped and tri-doped BBN compositions. It has been found that the W, W_{rec}, and η values of tri-doped BBN compositions are higher than those of undoped BBN. The efficiency lies between 85% and 90%, which is better for a

Table 6.4: PE and energy storage parameters of BBN ceramic composition.

Composition	$2P_r$ (μC/cm^2)	P_m (μC/cm^2)	W (J/cm^3)	W_{rec} (J/cm^3)	η (%)
BBNE0Y0W0	2.971	6.831	0.662	0.518	78.25
BBNE4Y0W0	1.562	4.708	0.471	0.392	83.39
BBNE4Y10W0	1.560	5.359	0.536	0.457	85.44
BBNE4Y10W1	1.397	7.650	0.742	0.674	90.86
BBNE4Y10W2	1.839	9.719	0.874	0.792	90.53
BBNE4Y10W3	1.765	8.087	0.808	0.720	89.08
BBNE4Y10W4	1.530	6.415	0.577	0.508	88.07

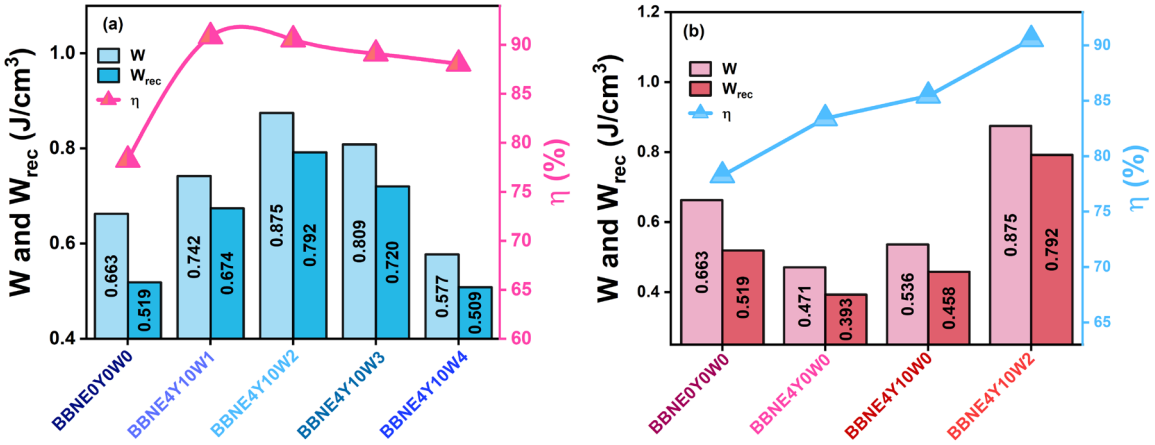

Figure 6.12: (a) Energy storage parameters of tri-doped BBN compositions (b) Comparison of energy storage parameters of BBNE0Y0W0, BBNE4Y0W0, BBNE4Y10W0, and BBNE4Y10W2 ceramic.

potential energy storage material. Also, a comparison of energy storage parameters for undoped, Er^{3+} doped, Er^{3+}/Yb^{3+} co-doped, and $Er^{3+}/Yb^{3+}/W^{6+}$ tri-doped BBN is given in **Figure 6.12(b)**. It is evident that the Er^{3+} doped and Er^{3+}/Yb^{3+} co-doped BBN systems exhibit lower W and W_{rec} values, but the η value is larger compared to the undoped BBN. In $Er^{3+}/Yb^{3+}/W^{6+}$ tri-doped BBN, the presence of W^{6+} ions significantly improve the W, W_{rec}, and η as compared to undoped BBN. However, in order to have a high-quality energy storage material, it is crucial to possess a higher W_{rec}. A detailed comparison of all the energy storage variables of doped ferroelectric ceramics is tabulated in Table 6.5.

Table 6.5: Comparison of energy storage parameters of various ferroelectric ceramics.

Host Material	E_{max} (kV/cm)	W_{rec} (J/cm^3)	η (%)	Ref.
$Na_{0.5}Bi_{0.5}TiO_3:Ho^{3+}$	114	0.68	-	[26]
$Bi_{0.5}Na_{0.5}TiO_3$-$BaTiO_3$-$SrTi_{0.875}Nb_{0.1}O_3$	105	1.17	91	[29]
$0.98(0.94Bi_{0.5}Na_{0.5}TiO_3$-$0.06BaTiO_3)$-$0.02BiAlO_3$	95	0.69	-	[30]
$(Na_{0.38}K_{0.12}Bi_{0.38}La_{0.12})TiO_3$	90	0.72	93	[31]
$BaBi_2Nb_2O_9:ZrO_2$	-	0.014	-	[32]
$BaBi_2Nb_2O_9$ (Er^{3+} = 0.00, Yb^{3+} = 0.00, W^{6+} = 0.00)	100	0.518	78.25	**This work**
$BaBi_2Nb_2O_9$ (Er^{3+} = 0.04, Yb^{3+} = 0.00, W^{6+} = 0.00)	100	0.392	83.39	**This work**
$BaBi_2Nb_2O_9$ (Er^{3+} = 0.04, Yb^{3+} = 0.10, W^{6+} = 0.00)	100	0.457	85.44	**This work**
$BaBi_2Nb_2O_9$ (Er^{3+} = 0.04, Yb^{3+} = 0.10, W^{6+} = 0.02)	100	0.792	90.53	**This work**

6.4 SUMMARY

The solid-state method is used to produce the relaxor ferroelectric ceramic $BaBi_{2-0.04-0.10}Nb_{2-z}Er_{0.04}Yb_{0.10}W_zO_9$ (BBN) which is doped with the transition metal ion, W^{6+}, at a constant concentration of Er^{3+} and Yb^{3+}. The X-ray diffraction (XRD) spectra revealed the presence of a perovskite phase in each ceramic sample, which exhibited an orthorhombic crystal structure. The UCL spectrum displayed two distinct green bands and one red band. The UCL intensity exhibits enhancement with an increasing concentration of W^{6+} ions, peaking at z = 0.02. Beyond this concentration, a quenching effect occurs. The presence of two photons was verified by observing the changes in UCL spectra caused by variations in pump power. The time-resolved fluorescence analysis was conducted to examine the emission of green and red light. The results indicated that the time decay increases as the dopant concentration increases, indicating the presence of non-radiative transitions at higher dopant concentrations. The FIR approach quantified the absolute sensitivity, yielding a result of 0.91% K^{-1} at a temperature of 573 K. The slim PE loops were achieved with an applied electric field of 100 kV/cm. It has been verified that by doping with W^{6+}, the PE loops are enhancing and reaching their maximum P_m value at 9.719 μC/cm^2 for z = 0.02. Furthermore, the energy storage characteristics (W, W_{rec}, η) have shown substantial enhancement compared to undoped BBN ceramic. The recorded energy density (W), recoverable energy storage density (W_{rec}), and energy storage efficiency (η) for undoped and tri-doped BBN ceramics were (0.662 J/cm^3, 0.518 J/cm^3, and 78.25%) and (0.874 J/cm^3, 0.792 J/cm^3 and 90.53%), respectively. These enhancements imply that the created material may be beneficial in developing sophisticated electronic devices for versatile applications.

Furthermore, the next chapter serves as the culmination of the research done in the thesis and provides an outlook on potential future developments.

6.5 REFERENCES

[1] A. Pandey, V. Kumar, R. E. Kroon, and H. C. Swart, "Photon upconversion in Ho^{3+}-Yb^{3+} embedded tungsten tellurite glass," *Journal of Luminescence*, vol. 192, pp. 757-760, 2017.

[2] P. Babu, I. R. Martín, G. Venkataiah, V. Venkatramu, V. Lavín, and C. K. Jayasankar, "Blue-green cooperative upconverted luminescence and radiative energy transfer in Yb^{3+} doped tungsten tellurite glass," *Journal of Luminescence*, vol. 169, pp. 233-237, 2016.

[3] F. Xu, J. Chen, Y. Lu, Q. Zhang, Q. Zhang, T. Zhou, and Y. He, "Exploration on the origin of enhanced piezoelectric properties in transition metal ion doped KNN based lead-free ceramics," *Ceramics International*, vol. 44, pp. 16745-16750, 2018.

[4] C. M. Raghavan, D. Do, J. W. Kim, W. J. Kim, and S. S. Kim, "Effects of transition metal ion doping on structure and electrical properties of $Bi_{0.9}Eu_{0.1}FeO_3$ thin films," *Journal of American Ceramics Society*, vol. 95, no. 6, pp. 1933-1938, 2012.

[5] J. D. Bobić, R. M. Katiliute, M. Ivanov, N. I. Ilić, A. S. Dzunuzović, M. M. Vijatović Petrović, J. Banys, and B. D. Stojanović, "Influence of tungsten doping on dielectric, electrical and ferroelectric behavior of $BaBi_4Ti_4O_{15}$ ceramics," *Journal of Alloys and Compounds*, vol. 702, pp. 619-625, 2017.

[6] I. Coondoo, A. K. Jha, and S. K. Agarwal, "Structural, dielectric and electrical studies in tungsten doped $SrBi_2Ta_2O_9$ ferroelectric ceramics," *Ceramics International*, vol. 33, pp. 41-47, 2007.

[7] J. Yuan, R. Nie, Q. Chen, J. Xing, and J. Zhu, "Evolution of structural distortion and electric properties of BTN-based high temperature piezoelectric ceramics with tungsten substitution," *Journal of Alloys and Compounds*, vol. 785, pp. 475-483, 2019.

[8] R. D. Shannon, "Revised effective ionic radii and systematic studies of interatomic distances in halides and chalcogenides," *Acta Crystallographica*, vol. A32, pp. 751-767, 2016.

[9] R. Swami, A. Shandilya, A. K. Shukla, P. S. Kumar, and K. Sreenivas, "Luminescence intensity ratio based wide range contactless temperature sensing properties of Er^{3+}/Yb^{3+} ions co-doped $La_2Ti_2O_7$ ceramics," *Journal of Alloys and Compounds*, vol. 948, 169610, 2023.

[10] P. Du and J. S. Yun, "Effect of molybdenum on upconversion emission and temperature sensing properties in $Na_{0.5}Bi_{0.5}TiO_3$: Er/Yb ceramics," *Ceramics International*, vol. 41, pp. 6710-6714, 2015.

[11] A. Banwal and R. Bokolia, "Thermometric sensing performance in erbium modified $SrBi_{2-x}Nb_2Er_xO_9$ ferroelectric ceramic for optoelectronic devices," *Ceramics International*, vol. 48 part 23A, pp. 34405-34414, 2022.

[12] A. Banwal and R. Bokolia, "Efficient tunable temperature sensitivity in thermally coupled levels of Er^{3+}/Yb^{3+} co-doped $BaBi_2Nb_2O_9$ ferroelectric ceramic," *Journal of Luminescence*, vol. 263, 120071, 2023.

[13] A. Banwal and R. Bokolia, "Phase evolution and microstructure of $BaBi_2Nb_2O_9$ ferroelectric ceramics," *Materials Today: Proceedings*, vol. 46, part 20, pp. 10121-10124, 2021.

[14] R. Bokolia, M. Mondal, V. K. Rai, and K. Sreenivas, "Enhanced infrared-to-visible up-conversion emission and temperature sensitivity in (Er^{3+}, Yb^{3+}, and W^{6+}) tri-doped $Bi_4Ti_3O_{12}$ ferroelectric oxide," *Journal of Applied Physics*, vol. 121, no. 8, 2017.

[15] P. Li, Z. Zhang, Z. Xu, H. Sun, Q. Zhang, and X. Hao, "Photo modulated cryogenic temperature sensing through a photochromic reaction in $Na_{0.5}Bi_{2.5}Ta_2O_9$: Er/Yb multicolour upconversion," *Optics Express*, vol. 31, no. 5, pp. 7047-7059, 2023.

[16] R. Bokolia, O. P. Thakur, V. K. Rai, S. K. Sharma, and K. Sreenivas, "Electrical properties and light up conversion effects in $Bi_{3.79}Er_{0.03}Yb_{0.18}Ti_{3-x}W_xO_{12}$ ferroelectric ceramics," *Ceramics International*, vol. 42, no. 5, pp. 5718-5730, 2016.

[17] A. Pandey, S. Som, V. Kumar, V. Kumar, K. Kumar, V. K. Rai, and H. C. Swart, "Enhanced upconversion and temperature sensing study of Er^{3+}-Yb^{3+} co-doped tungsten-tellurite glass," *Sensors and Actuators B*, vol. 202, pp. 1305-1312, 2014.

[18] M. Narwan, A. Banwal, R. Sharma, and R. Bokolia, "Non-invasive thermal sensing and improved recoverable energy storage density of $Bi_{0.5}Na_{0.5}TiO_3$: Er^{3+} doped multifunctional ferroelectric ceramic," *Journal of Luminescence*, vol. 265, 120236, 2024.

[19] Q. Cao, D. Peng, H. Zou, J. Li, X. Wang, and X. Yao, "Up-conversion luminescence of Er^{3+} and Yb^{3+} co-doped $CaBi_2Ta_2O_9$ multifunctional ferroelectrics," *Journal Advanced Dielectrics*, vol. 4, no. 03, 1450018, 2014.

[20] X. Hui, D. Peng, H. Zou, J. Li, Q. Cao, Y. Li, X. Wang, and X. Yao, "A new multifunctional aurivillius oxide $Na_{0.5}Er_{0.5}Bi_4Ti_4O_{15}$: Up-conversion luminescent, dielectric, and piezoelectric properties," *Ceramics International*, vol. 40, part 4A, pp. 12477-12483, 2014.

[21] M. K. Mahata, T. Koppe, T. Mondal, C. B. Sewitz, K. Kumar, V. K. Rai, H. Hofsass, and U. Vetter, "Incorporation of Zn^{2+} ions into $BaTiO_3$:Er^{3+}/Yb^{3+} nanophosphor: An effective way to enhance upconversion, defect luminescence, and temperature sensing," *Physical Chemistry Chemical Physics*, vol. 17, pp. 20741-20753, 2015.

[22] P. Wang, X. Wang, G. Li, Y. Li, X. Yao, and Z. Pan, "Energy density capability and upconversion luminescence in Er^{3+}/Yb^{3+}-codoping BNT-based ferroelectric thin films," *Ceramics International*, vol. 48, no. 19, pp. 28606-28613, 2022.

[23] F. Luo, J. Xing, Y. Qin, Y. Zhong, F. Shang, and G. Chen, "Up-conversion luminescence, temperature sensitive and energy storage performance of lead-free transparent Yb^{3+}/Er^{3+} co-doped $Ba_2NaNb_5O_{15}$ glass-ceramics," *Journal of Alloys and Compounds*, vol. 910, 164859, 2022.

[24] A. Banwal and R. Bokolia, "Enhanced upconversion luminescence and optical temperature sensing performance in Er^{3+} doped $BaBi_2Nb_2O_9$ ferroelectric ceramic," *Ceramics International*, vol. 48, no. 2, pp. 2230-2240, 2022.

[25] X. Qiao, D. Wu, F. Zhang, M. Niu, B. Chen, X. Zhao, P. Liang, L. Wei, X. Chao, and Z. Yang, "Enhanced energy density and thermal stability in relaxor ferroelectric $Bi_{0.5}Na_{0.5}TiO_3$-$Sr_{0.7}Bi_{0.2}TiO_3$ ceramics," *Journal of the European Ceramic Society*, vol. 39, no. 15, pp. 4778-4784, 2019.

[26] A. Kumar and S. Asthana, "Investigation on energy storage properties and thermally stable dielectric constant for high temperature electronic device applications in the holmium substituted $Na_{0.5}Bi_{0.5}TiO_3$," *Journal of Materials Science: Materials in Electronics*, vol. 32, pp. 20225-20239, 2021.

[27] C. Kornphom, K. Saenkam, and T. Bongkarn, "Enhanced energy storage properties of BNT-ST-AN relaxor ferroelectric ceramics fabrication by the solid-state combustion technique," *Physica Status Solidi (A)*, vol. 220, no. 10, 2023.

[28] Q. Huang, F. Si, and B. Tang, "The effect of rare-earth oxides on the energy storage performances in $BaTiO_3$ based ceramics," *Ceramics International*, vol. 48, no. 12, pp. 17359-17368, 2022.

[29] J. Shi, X. Liu, and W. Tian, "High energy-storage properties of $Bi_{0.5}Na_{0.5}TiO_3$-$BaTiO_3$-$SrTi_{0.875}Nb_{0.1}O_3$ lead-free relaxor ferroelectrics," *Journal of Materials Science and Technology*, vol. 34, no. 12, pp. 2371-2374, 2018.

[30] A. Manan, S. Khan, A. Ullah, A. S. Ahmad, Y. Iqbal, I. Qazi, A. Ullah, Z. Yao, H. Liu, H. Hao, M. A. Khan, and M. U. Rehman, "Improved energy storage characteristic of Yb doped $0.98(0.94Bi_{0.5}Na_{0.5}TiO_3$-$0.06BaTiO_3)$-$0.02BiAlO_3$ ceramics," *Materials Research Bulletin*, vol. 137, 111175, 2021.

[31] A. Verma, A. K. Yadav, S. Kumar, V. Srihari, R. Jangir, H. K. Poswal, S. Biring, and S. Sen, "Enhanced energy storage properties in A-site substituted $Na_{0.5}Bi_{0.5}TiO_3$ ceramics," *Journal of Alloys and Compounds*, vol. 792, pp. 95-107, 2019.

[32] A. Chakrabarti and A. R. Molla, "Zirconia assisted crystallization of ferroelectric $BaBi_2Nb_2O_9$ based glass-ceramics: Kinetics, optical and dielectrical properties," *Journal of Alloys and Compounds*, vol. 844, 156181, 2020.

7

CHAPTER

Conclusion and Future Scope

- *This chapter presents a concise overview of the research carried out in this thesis.*
- *Furthermore, the concrete conclusion derived from the presented results is also briefly discussed.*
- *Subsequently, this chapter outlines the possible future areas of research that might be explored to improve the current study.*

7.1 CONCLUSION

In summary, this thesis has meticulously examined the impact of doping with Er^{3+}, Er^{3+}/Yb^{3+}, and $Er^{3+}/Yb^{3+}/W^{6+}$ in $BaBi_2Nb_2O_9$ ceramic, shedding light on its structural, photoluminescence, sensing, and ferroelectric properties. The outcomes of this investigation offer significant contributions to understanding the influence of rare earth and transition metal ion doping on the material's characteristics. A systematic exploration of each doping scenario has been undertaken throughout the chapters, providing a nuanced perspective on the structural modifications and performance enhancements. As the research landscape evolves, these findings serve as a foundation for future studies exploring advanced functional materials and tailored properties. The outcomes of this work are not only relevant to the academic community but also hold potential implications for practical applications in areas such as advanced optoelectronic devices, security instruments, non-contact sensors, etc.

Chapter 1 provides a comprehensive overview of photoluminescence materials and ferroelectric materials. The examination delves into the fundamental characteristics and properties of these materials, offering insights into their unique features and potential applications. Furthermore, this chapter focuses on the critical role of rare earth ions in modulating host material properties through precise control of dopant concentrations. A brief discussion is given on the applications of upconversion luminescent materials in several domains. Furthermore, this chapter offers concise information on the objectives of the thesis and briefly details the thesis layout.

Chapter 2 addresses the synthesis process and several characterization approaches in depth. The solid-state technique is utilized to produce the $BaBi_2Nb_2O_9$ ceramic.

Furthermore, this chapter describes the characterization processes used to examine the properties of the synthesized ceramics. The structural analysis is carried out using XRD, SEM, FTIR, and Raman spectroscopy. Photoluminescence characteristics are investigated employing upconversion luminescence (UCL) spectra, pump power analysis, and time-resolved fluorescence spectroscopy. The fluorescence intensity ratio (FIR) approach investigates temperature-dependent UCL spectra. PE loops are used to investigate ferroelectric characteristics at room temperature. Temperature-dependent dielectric experiments disclose dielectric constants of the produced ceramics. This chapter provides a full explanation of the strategies mentioned above.

Chapter 3 investigates the synthesis and characterization of Er^{3+} substituted $BaBi_{2-x}Er_xNb_2O_9$ ceramic composition. The XRD spectra indicate the excellent solubility of Er^{3+} ions, as there are no extra peaks in the XRD spectra. Increasing Er^{3+} content caused the stretching in the unit cell of the host material, which is due to the constraint $6s^2$ lone pair character of the Bi^{3+} ions. Two green and one weak red band are observed via $^4S_{3/2} \rightarrow {}^4I_{15/2}$, $^2H_{11/2} \rightarrow {}^4I_{15/2}$, and $^4F_{9/2} \rightarrow {}^4I_{15/2}$ transitions, respectively. The highest emission intensity is obtained for Er^{3+} content x = 0.04. The fluorescence intensity ratio technique showed a maximum absolute sensitivity of 0.99% K^{-1} at 483 K for optimized Er^{3+} content. The PE loops are measured at room temperature for all the Er^{3+} doped $BaBi_{2-x}Er_xNb_2O_9$ ceramic composition, and it is observed that the remnant polarization degraded with Er^{3+} doping.

Chapter 4 discusses the structural, upconversion photoluminescence, and sensing properties of Er^{3+}/Yb^{3+} co-doped $BaBi_{2-0.04-y}Nb_2Er_{0.04}Yb_yO_9$ ceramic. The Er^{3+} content is fixed at an optimized concentration x = 0.04, and Yb^{3+} is varied during the synthesis process. The efficiency of UCL emission intensity increases with Yb^{3+} concentration, and the highest intensity is obtained for y = 0.10 dopant content. The presence of Yb^{3+} ions

results in a noticeable red emission band at 672 nm because of the efficient energy transfer from Yb^{3+} ions to Er^{3+} ions. The sensitivity of the material was determined for two different dopant concentrations (y = 0.06 and y = 0.10), and it was found that the sensitivity of the material can be tuned by altering dopant concentrations. The sensitivity of the material calculated for y = 0.06 is 0.69% K^{-1} at 523 K, and for y = 0.10 is 0.58% K^{-1} at 463 K.

Chapter 5 examines the structural, dielectric, ferroelectric, and energy storage properties of undoped, Er^{3+} doped, and Er^{3+}/Yb^{3+} co-doped $BaBi_{2-x-y}Nb_2Er_xYb_yO_9$ ceramics. FTIR spectra showed characteristic peaks of the Aurivillius phase at 619 cm^{-1} and 822 cm^{-1}. Four Raman modes are visible in undoped BBN, whereas 12 modes have been observed in doped BBN compositions. Temperature-dependent dielectric tests reveal significant dispersion below and above the maximum temperature (T_m), and the dielectric constant (ε') decreases with increasing frequency. The dielectric loss (ε'') curves are diffused, and variations in the maxima with frequency have been detected, demonstrating the relaxor behavior of all produced BBN compositions. The thinner PE loops are achieved under applied electric fields between 75 kV/cm and 100 kV/cm. The remnant polarization (P_r) and maximum polarization (P_m) are used to calculate the energy storage parameters (W, W_{rec}, η) of each ceramic composition. The energy storage parameters improve as the applied electric field increases. It can be concluded that the η of undoped, Er^{3+} doped, and Er^{3+}/Yb^{3+} co-doped $BaBi_{2-x-y}Nb_2Er_xYb_yO_9$ ceramics increased with doping concentrations. In contrast, the W and W_{rec} of Er^{3+} doped and Er^{3+}/Yb^{3+} co-doped BBN ceramic are comparable with undoped BBN.

Chapter 6 discusses the structural, upconversion photoluminescence, sensing, ferroelectric, and energy storage density characteristics of $BaBi_{2-0.04-0.10}Nb_{2-z}Er_{0.04}Yb_{0.10}W_zO_9$ (BBN), which is doped with the transition metal ion, W^{6+}, at a constant

concentration of Er^{3+} (x = 0.04) and Yb^{3+} (y = 0.10). The UCL emission intensity increases with the incorporation of W^{6+} ions and increases up to z = 0.02, and then concentration-quenching occurs. Time decay analysis is conducted for the green and red emission bands, corresponding to transitions from $^2H_{11/2}$ to $^4I_{15/2}$ and $^4S_{3/2}$ to $^4I_{15/2}$ energy levels, respectively. The absolute sensitivity (S_a) of the $Er^{3+}/Yb^{3+}/W^{6+}$ tri-doped BBN system yields a result of 0.91% K^{-1} at a temperature of 573 K, which is higher than the Er^{3+}/Yb^{3+} co-doped BBN system and comparable with the Er^{3+} doped BBN system. The PE loops have shown improvements and reached their maximum P_m value at 9.719 μC/cm^2 for z = 0.02. The W, W_{rec}, and η for undoped is 0.662 J/cm^3, 0.518 J/cm^3, and 78.25%, respectively, and 0.874 J/cm^3, 0.792 J/cm^3, and 90.53%, respectively, for the tri-doped BBN ceramics.

7.2 FUTURE SCOPE

The primary objective of this thesis is to investigate the structural, photoluminescence, sensing, and ferroelectric properties of Er^{3+} doped, Er^{3+}/Yb^{3+} co-doped, and $Er^{3+}/Yb^{3+}/W^{6+}$ tri-doped $BaBi_2Nb_2O_9$ ceramic. However, some objectives can be explored as potential future elements.

1. The dielectric measurements from below the room temperature to high temperature need to be investigated for undoped, Er^{3+} doped, Er^{3+}/Yb^{3+} co-doped, and $Er^{3+}/Yb^{3+}/W^{6+}$ tri-doped $BaBi_2Nb_2O_9$ ferroelectric ceramic because these measurements help in designing and optimizing electrical devices.
2. The absolute sensitivity of thermally coupled levels (TCL) of dopant ions has been measured in this thesis; however, more investigation is required to explore the sensitivity of non-TCL of dopant ions.

3. Studying the potential impact of electric field-induced piezoelectric strain on light upconversion luminescence will be intriguing.

4. Fabrication and characterization of $BaBi_2Nb_2O_9$-based thin films to explore the potential of the material to be used as energy harvesting devices.

5. A detailed comparative analysis of upconversion and ferroelectric properties of $BaBi_2Nb_2O_9$-based thin films and ceramics may be explored to check the versatility of the material.

Ceramics International 48 (2022) 2230–2240

Contents lists available at ScienceDirect

Ceramics International

journal homepage: www.elsevier.com/locate/ceramint

Enhanced upconversion luminescence and optical temperature sensing performance in Er^{3+} doped $BaBi_2Nb_2O_9$ ferroelectric ceramic

Ankita Banwal [a], Renuka Bokolia [a,*]

[a] Department of Applied Physics, Delhi Technological University, Delhi, India

ARTICLE INFO

Keywords:
Ceramics
Ferroelectrics
Upconversion
Raman spectra
Optical temperature sensor

ABSTRACT

A series of $BaBi_{2-x}Nb_2Er_xO_9$ ceramic compositions with different Er^{3+} concentration ($x = 0.0$–8 mol %) is synthesized by a conventional solid-state reaction method. The upconversion (UC) light emission under 980 nm excitation with different pump powers and luminescence-based temperature sensing ability of $BaBi_{2-x}Nb_2Er_xO_9$ composition have been examined. The formation of a Bi-layered perovskite phase of $BaBi_2Nb_2O_9$ is confirmed having an orthorhombic geometry and *Fmmm* space group. Shifts in the Raman modes indicate reduced interaction of Bi^{3+} ions with NbO_6 octahedron leading to relaxation of structural distortion with increasing Er^{3+} content. The maximum value for remnant polarization and coercive field of doped $BaBi_{2-x}Nb_2Er_xO_9$ ceramic for ($x = 0.08$) Erbium concentration comes out to be 2.9524 μC/cm^2 and 49.8980 kV/cm. For an optimum content of $x = 0.04$, two strong UC green emission bands were observed at 549 nm via $^4S_{3/2} \rightarrow {}^4I_{15/2}$ transition and 527 nm via $^2H_{11/2} \rightarrow {}^4I_{15/2}$ transitions, and a weak red emission appears at 657 nm attributed to the $^4F_{9/2} \rightarrow {}^4I_{15/2}$ transition. Pump power dependence suggests that UC emission is a two-photon mechanism for red and green emission bands. Temperature sensing evaluated by the change in the fluorescence intensity ratio (I_{527}/I_{549}) indicates the highest sensitivity to be 0.00996 K^{-1} at 483 K for an optimum concentration of Er^{3+} at $x = 0.04$ in $BaBi_{2-x}Nb_2Er_xO_9$ composition and is useful for non-contact optical thermometry.

1. Introduction

Trivalent rare-earth (RE^{3+}) ions doped different host materials excited by cheap laser sources exhibit upconversion (UC) photoluminescence which can change lower energy near-infrared radiation (NIR) into higher energy visible radiation [1–10]. Current research focuses on the fluorescence intensity ratio (FIR) technique as a non-contact probe for temperature sensing as it is insensitive to electromagnetic interference and spatial recording of temperature fluctuations at a sub-micron scale with high sensitivity and accuracy. For optical temperature sensing, a large number of oxide host materials have exhibited a reasonably high sensitivity over an extensive temperature range with decent thermal stability and a quick response speed. Recently, good linearity and high sensitivity (0.0139 K^{-1}) is attained in Er^{3+}/Yb^{3+} co-doped $SrMoO_4$ ceramic composition [11]. Also, when co-doped with Er^{3+}, Yb^{3+} enhanced luminescence thermometry in Y_2O_3 is achieved by Lojpur et al. [1]. Similarly, advances are reported for ferroelectric host materials, $La_2Ti_2O_7$ doped with Er^{3+} exhibits increased temperature sensitivity for optical thermometry and novel effects, indicating the possibility for non-contact localized probing of ferroelectric transition temperature in Li^{3+}/Er^{3+} doped $BaTiO_3$ ceramics has been demonstrated [3,12]. Furthermore, in $Sr_{2-x}SnO_4$:Sm^{3+} multifunctional ceramic, thermoluminescence, photochromism reaction, photoluminescence, and photo-stimulated luminescence are testified for potential applications in optical storage technology and high sensitivity optical switches [10].

From the last two decades, ferroelectric materials have been widely used as luminescent host materials with extensively wide applications in luminescent thermometry, biological imaging system, white light-emitting diodes, solid-state lasers, infrared detectors, various medical diagnoses, etc. [13–16]. The ferroelectric materials meet the need for good host material for luminescence, including decent thermal stability, significant radiative transition, lower values of leakage current, and high sensitivity over an extensive temperature range [17–19]. In the group of ferroelectrics, Bismuth Layered Structure Ferroelectric (BLSF) are better candidates for upconversion luminescence as they are lead-free ferroelectric materials, which make them more advantageous due to their non-toxicity [20,21] and also minimize the degradation of

* Corresponding author.
E-mail addresses: ankita_phd2k19@dtu.ac.in (A. Banwal), renukabokolia@dtu.ac.in (R. Bokolia).

https://doi.org/10.1016/j.ceramint.2021.09.314
Received 27 July 2021; Received in revised form 16 September 2021; Accepted 26 September 2021
Available online 6 October 2021

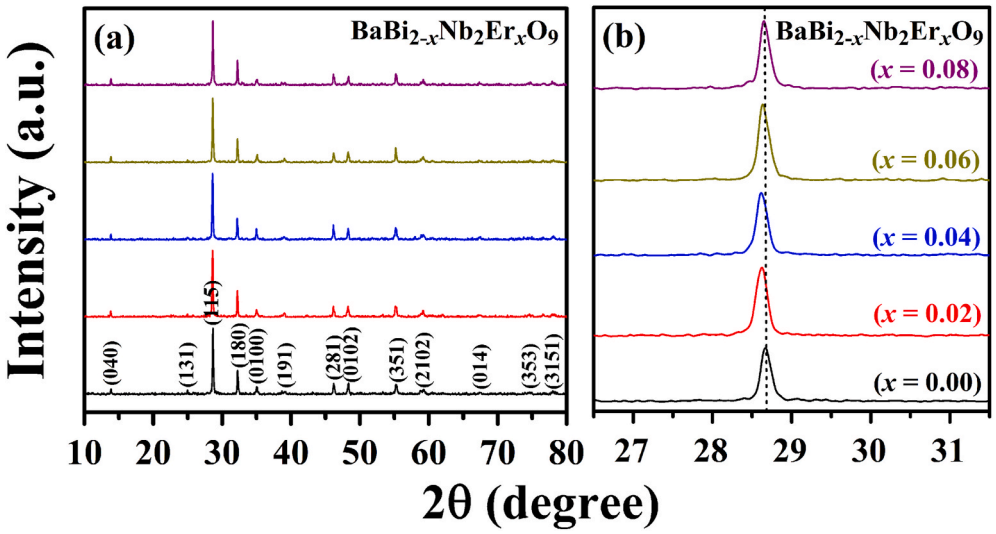

Fig. 1. (a) XRD spectra of the ceramic composition $BaBi_{2-x}Nb_2Er_xO_9$ with varying Er^{3+} concentration (x = 0, 0.02, 0.04, 0.06, 0.08). (b) Shifting of strongest XRD peak (115 planes) of $BaBi_{2-x}Nb_2Er_xO_9$ ceramics.

P-E hysteresis characteristics associated with lead base ferroelectrics because BLSFs show good fatigue endurance even after 10^{11} - 10^{12} cycles [22–25]. Their environmental and health concerns, along with multiple properties such as pyroelectric, piezoelectric, and integrated electro-optic behaviour combined with functional luminescence properties make them smart materials.

In recent literature, it has been found that doping ferroelectric materials with suitable dopants enhance and improve their multifunctional properties [25–29]. The luminescence properties of the ferroelectric materials doped with RE^{3+} ions are intently due to the crystal field, which is revealed by the phase structure (crystal symmetry) and point defects in the lattice. The ferroelectric has an ABO_3 structure, usually have vacancies that frequently affect the ferroelectric and luminescence properties [8,30]. Er^{3+} and Yb^{3+} were established to be the most effective dopants to improve ferroelectric, piezoelectric, and upconversion emission [31,32]. For instance, Bokolia et al. revealed enhancement in the dielectric, ferroelectric, and PL properties of $Bi_3Ti_4O_{12}$ when doped with Er^{3+} [13]. Bayart et al. investigated $LaTiO_7$ doped with Er^{3+} for temperature sensing applications [3], $NaBi_4Ti_4O_{15}$ doped with Er^{3+} showed improved dielectric, luminescent, and piezoelectric properties in Hui et al. study [33]. Recently, Kaixuan Li et al.; developed a new Er^{3+} doped $Na_{0.5}Bi_{0.5}TiO_{3-x}K_{0.5}Na_{0.5}NbO_3$ photochromic (PC) ceramic and investigated PC reaction and tunable luminescence contrast with electric poling field and related with the ergodicity of ceramics [8].

In current years, Barium Bismuth Niobium Oxide (BBN), which is a relaxor ferroelectric (RF) and member of BLSF, has fascinated researchers due to its possible uses in high-temperature piezo sensor devices and Non-Volatile Random Access Memory (NVRAM). BBN is also a good host for UC because it is chemically and thermally stable, has lower phonon energy (860 cm^{-1}), and allows modifications in its crystal structure with additional dopants [4]. Being an aurivillius family member, the BLSFs have the established formula $(A_{m-1}B_mO_{3m+1})^{2-}(Bi_2O_2)^{2+}$, where m denotes the number of octahedral layers present in perovskites block $(A_{m-1}B_mO_{3m+1})^{2-}$ piled between rigid $(Bi_2O_2)^{2+}$ layers. A symbolizes trivalent, divalent, monovalent cations or a combination like Bi^{3+}, Na^{+}, Pb^{2+}, Ba^{2+}, etc., while B indicates hexavalent, pentavalent, or tetravalent ions such as W^{6+}, Ta^{5+}, Nb^{5+}, Ti^{4+} [4,6,33–36]. Some of the BLSF examples with different values of m are, (i) Bi_2WO_6 (m = 1) [33], (ii) $BaBi_2Nb_2O_9$ (m = 2) [4,22,37], (iii) $Bi_4Ti_3O_{12}$ (m = 3) [2,14], (iv) $BaBi_4Ti_4O_{15}$ (m = 4) [38,39] etc. Studies on strong Upconversion Luminescence in Er^{3+}/Yb^{3+} doped $BaBi_2Nb_2O_9$ powders are reported by Façanha et al. [4]. Recently, novel white light emission has been reported by modulating Li^{+} and Tm^{3+} ions content in $BaBi_2Nb_2O_9$: $Li^{+}/Tm^{3+}/Yb^{3+}/Er^{3+}$ phosphors for its possible use in solid-state lighting technology [7]. Moreover, recent developments on strong upconversion luminescence, good thermal and chemical durability, lower phonon energy, and tuning of the optical properties reported in BBN host material motivate us to examine the usefulness of Er^{3+} doped $BaBi_2Nb_2O_9$ ceramics for thermometric application and understand its influence on structural and electrical properties.

Hence in our proposed research, we chose Er^{3+} as a dopant because it is the most useful dopant for upconversion emission, and in addition to this, its metastable energy levels ($^4I_{9/2}$ and $^4I_{11/2}$) can be easily occupied by using cheap and low power laser operating at 980 nm [12,40,41]. In the present work, we systematically doped Er^{3+} in BBN and see how the substitution of Bi^{3+} ions with smaller Er^{3+} ions in the $BaBi_2Nb_2O_9$ compound influences its structural properties and examining the results using X-ray Diffraction (XRD) and Raman spectroscopy. A substantial enhancement in the UC light emission is seen for an optimal Er^{3+} concentration, and the effect of increasing Er^{3+} substitution on electrical and ferroelectric properties has been explored. The FIR technique has been utilized for exploring the thermally coupled electronic states ($^2H_{11/2}$ and $^4S_{3/2}$) of Er^{3+} ions for non-contact optical thermometry and the usefulness of the optimized configuration for temperature sensing is investigated over a temperature range (300–623 K).

2. Experimental details

The ceramic composition $BaBi_{2-x}Er_xNb_2O_9$ with different concentration of Er^{3+} as x = 0.00, 0.02, 0.04, 0.06, 0.08 is processed by traditional solid-state diffusion method. Raw powders of high purity were purchased from Sigma Aldrich, i.e., Nb_2O_5, $BaCO_3$, Bi_2O_3, and Er_2O_3, weighed in stoichiometric amount, and finally mixed in a mortar pestle with ethanol for 8 h. The blended raw powders were kept at a temperature of 950 °C for 3 h for calcination. The calcined powder samples were then given a circular disc shape of 10 mm diameter after rigorously mixing with 5 wt% polyvinyl alcohol (PVA). The circular discs were sintered in a high-temperature furnace at 1050 °C in two steps, first with intermittent heat treatment at 500 °C for 1 h for removal of the PVA binder, and then the temperature was raised to 1050 °C for a dwell time of 3 h. Eq. (1) and Eq. (2) represents the synthesis reaction for:

Undoped BBN -

$$BaCO_3 + Bi_2O_3 + Nb_2O_5 \rightarrow BaBi_2Nb_2O_9 + CO_2\uparrow \quad (1)$$

Table 1
Refinement index and lattice parameters for $BaBi_{2-x}Nb_2Er_xO_9$ compositions with different varying Er^{3+} content (x = 0.0, 0.02, 0.04, 0.06, 0.08).

Sample	Refinement Index				Lattice Parameters					
	R_{exp}	R_{wp} (%)	GoF	R Bragg	a (Å)	b (Å)	c (Å)	V (Å^3)	Density (g/cm^3)	Orthorhombic distortion (c/a)
BBN: 0.0 Er^{3+}	10.76	11.00	1.02	13.606	5.5394	25.5751	5.5571	787.2782	7.2277	1.003
BBN: 0.02 Er^{3+}	11.97	12.69	1.06	8.499	5.5530	25.5769	5.5580	789.5367	7.1012	1.001
BBN: 0.04 Er^{3+}	11.57	12.18	1.05	9.931	5.5526	25.6098	5.5623	790.9644	7.0718	1.001
BBN: 0.06 Er^{3+}	12.38	13.56	1.10	9.450	5.5482	25.5732	5.5599	788.8676	6.8776	1.002
BBN: 0.08 Er^{3+}	13.19	13.89	1.12	10.713	5.5485	25.5642	5.5579	788.3490	6.8080	1.002

Er^{3+} Doped BBN -

$$BaCO_3 + \frac{2-x}{2}Bi_2O_3 + Nb_2O_5 + \frac{x}{2}Er_2O_3 \rightarrow BaBi_{2-x}Nb_2Er_xO_9 + CO_2\uparrow \quad (2)$$

The phase formation of synthesized samples was analysed using X-Ray Diffraction (XRD) spectra collected using Bruker D-8 Advance X-Ray diffractometer with Cu-Kα radiation in the 2θ range 10°–80°. The sintered pellets density is calculated by Archimedes' Principle. Using the Invia Raman spectrometer model having argon-ion laser, Raman spectra were recorded at 785 nm. The prepared pellets were electroded by applying the silver paste on the faces of pellets and were baked in the furnace for 10 min at 500 °C so that the silver paste stick entirely to the pellets. The Marine India Electricals Ltd. automated loop tracer is used to measure the P-E hysteresis loop on an electroded ceramic surface at 50 Hz frequency. The upconversion luminescence (UC) spectra were recorded using HORIBA PTI Quanta-master (8450–11) under 980 nm

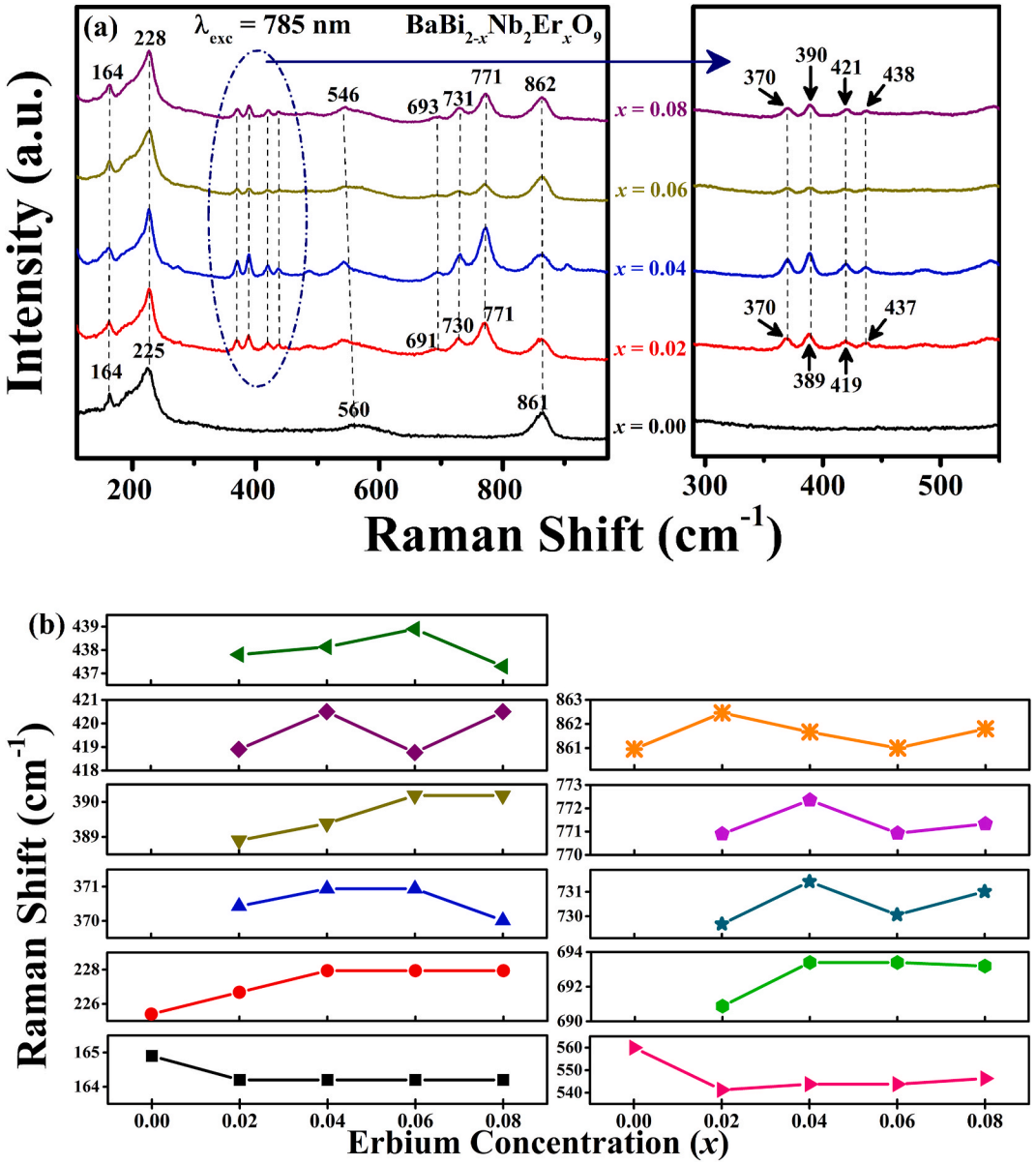

Fig. 2. (a) Raman spectra of $BaBi_{2-x}Nb_2Er_xO_9$ ceramics with different Erbium content under the excitation of 785 nm. (b) Compositional dependence of Raman modes.

excitation wavelength. Time decay measurements were recorded at room temperature using a pulsed 980 nm laser excitation source. In the 300–623 K temperature range, the temperature-dependent UC emission spectra were collected using a thermocouple by situating the sample on the heater.

3. Results and discussion

3.1. XRD analysis

The X-ray diffraction (XRD) spectra of ceramic composition $BaBi_{2-x}Er_xNb_2O_9$ with different Erbium concentrations (x = 0–8 mol %) sintered at 1050 °C for 3 h are displayed in Fig. 1(a). The observed XRD peaks depict good accord, as reported in the JCPDF file no. 00-012-0403 with no secondary peaks, implying good solubility of Erbium ions in the host lattice with no structural changes or minor changes. The observed Bragg's reflection confirmed the formation of single-phase BBN corresponding to orthorhombic geometry with the *Fmmm* space group.

The refinement index and lattice parameters obtained from profile fit between observed and calculated XRD patterns using TOPAS software for composition $BaBi_{2-x}Er_xNb_2O_9$ are reported in Table 1. All the experimental data is best fitted with calculated data with the goodness of fit (GoF) = 1 approximately. The highest peak intensity associated with the (115) plane of $BaBi_{2-x}Er_xNb_2O_9$ represents the BLSF with m = 2, and the result agrees with the former explanations that the strong intensity diffraction peak corresponds to the (112m + 1) plane for BLSF materials in the Aurivillius phase [2,13,42,43]. By using the Archimedes' Principle, the sintered pellet density (ρ) is found to be 7.22 g/cm^3, which has more than 98% accuracy. The density of the Er^{3+} doped $BaBi_{2-x}Er_xNb_2O_9$ composition decreases with increasing Er^{3+} concentration (Table 1). This decrement in density is due to the larger ionic radius of bismuth (≈ 1.17 Å) compared to the ionic radius of Erbium (≈ 0.100 Å) [4]. The shift in the diffraction peak of the {115} family is displaced towards the lower values of 2θ, as shown in Fig. 1(b). Eq. (3) explains the tension within the lattice as [4]:

$$\sigma = \frac{E}{2\vartheta}\left[\frac{\mathrm{Sin}\theta_n}{\mathrm{Sin}\theta_i} - 1\right] \quad (3)$$

where E is the modulus of elasticity, υ denotes Poison's coefficient, θ_n is shifted 2θ value over reference angle, and θ_i is the reference angle. According to Eq. (3), the positive value of σ represents compression among the lattice, and a negative value means the stretching within the lattice after substituting dopant. Since E and υ are constants, so it may be concluded that after substituting the value of $\theta_i = 28.69$ and $\theta_n = 28.60$, the value $\sigma < 0$ which is due to the stretching in the crystalline lattice, generated by the introduction of dopants. This is confirmed by the increase in cell volume with increasing Erbium concentration, causing stretching in the cell (Table 1). Although there is a variation in the ionic radius of Er^{3+} and Bi^{3+}, the cell volume and lattice parameters (a, b, c) do not change much from undoped $BaBi_2Nb_2O_9$. This could be attributed to the creation of cationic vacancies, which preserve the electroneutrality of lattice and minimize the deformation of the crystal [13,28].

3.2. Raman spectroscopy

The Raman spectra observed for pure and Erbium-substituted $BaBi_{2-x}Nb_2Er_xO_9$ ceramic composition in the 100-1000 cm^{-1} frequency range are given in Fig. 2(a). The spectra were recorded under the excitation of laser source 785 nm at room temperature. Of all the theoretically predicted 12 Raman modes, only four strong and sharp modes at 164, 225, 560, and 860 cm^{-1} were identified for undoped $BaBi_2Nb_2O_9$, as per the reported literature [4,44,45]. It is because of the possible overlapping of the identical symmetrical vibrations and broadening of the bands or low intensity of vibration mode, whereas 10 distinct modes are detected in Er^{3+} doped $BaBi_2Nb_2O_9$ ceramics. The modes which are suppressed in undoped $BaBi_2Nb_2O_9$ ceramics can be easily observed in Er^{3+} doped compositions. However, in doped Er^{3+} doped $BaBi_{2-x}Nb_2Er_xO_9$ composition, some less intense modes near 370, 389, 419, 437, 691, 730, 771 cm^{-1} have been observed that might be associated with the degree of the structural disorder which has been described in materials belonging to the same family [13]. So there is a good accord in the theoretical predicted and experimentally observed Raman modes. Fig. 2(b) depicts the Raman shift as the function of Erbium concentration, and the observed frequency shifts with their band assignments are tabulated in Table 2.

Table 2
Raman Band assignment for $BaBi_2Nb_2O_9$.

Raman shift (cm^{-1})	Band assignments	References
164	Vibration of Bi^{2+} ion at A-site of pseudo peroskite	[4]
225	Torsion Bending of O–Nb–O bond	[4,44]
370	Vibration due to Bi–O bond	[43,44]
389	Vibration due to Bi–O bond	[43]
419	Vibration due to Bi–O bond	[43]
437	Vibration due to Bi–O bond	[43]
560	Opposite excursion of apical oxygen atom of NbO_6 octahedron	[4,44,45]
691	Symmetric bending vibration of NbO_6 octahedron	[43]
730	Symmetric bending vibration of NbO_6 octahedron	[43]
771	Symmetric bending vibration of NbO_6 octahedron	[43]
861	Symmetrical stretching of Nb–O_6 group	[42,45]

The Raman spectra show the distinct modes corresponding to 164, 225, 560, 860 cm^{-1}. The low-frequency Raman modes below 200 cm^{-1} correspond to Ba^{2+} ions vibrations at the A-site in the perovskite layer, whereas the high-frequency Raman modes above 200 cm^{-1} are correlated with the internal vibrational modes of NbO_6 octahedron. The mode positioned at 164 cm^{-1} is attributed to displacements of Bismuth ions of the pseudo-perovskite structure at the A-site. The presence of mode at 164 cm^{-1} with significant broadening with increasing Er^{3+} substitution suggests changes in the orthorhombical distortion. The A_{1g} mode at 225 cm^{-1} is because of the torsion bending in the O–Nb–O arrangement of the NbO_6 group, and a slight shift to 227 cm^{-1} is observed with rising Er^{3+} substitution. The high-frequency mode observed at 560 cm^{-1} arising from B_{2g} mode is related to opposite excursion of the apical oxygen atoms in NbO_6 octahedral, whereas the strong vibration mode near 860 cm^{-1} could be assigned A_{1g} character and is owing to symmetrical stretching of Nb–O of the NbO_6 group along the stacking z-axis [4,43,46]. The mode at 560 cm^{-1} depicts a gradual downshift to frequency 546 cm^{-1} and is found to be weakened and broadened with increasing Er^{3+} content implying a decrease in the compressive stress due to substitution of Er^{3+} at Bi-sites and thereby suggesting relaxation in structural distortion. In contrast, 860 cm^{-1} mode relates to the symmetrical stretch of Nb–O vibrations of the NbO_6 octahedron shows an upshift to 862 cm^{-1} and suggests that NbO_6 octahedron linked to Bi layer shrinks due to substitution of Er^{3+} ions resulting in a reduction of the interaction of Bi^{3+} with NbO_6 octahedron and hence leading to relaxation of structural deformation.

The modes positioned at 389 and 419 cm^{-1} are assigned to B_1 mode, whereas 370 cm^{-1} and 437 cm^{-1} bands from B_2 mode are completely dominated by the Bi–O_3 force constant, suggesting an insignificant contribution from Ba and Nb atoms [44]. The 691-771 cm^{-1} arise from T_{2g} symmetry and reflect symmetric bending vibrations of NbO_6 octahedron. The modes observed at 730 and 771 cm^{-1} for x = 0.02 evolve prominently with increasing Er^{3+} content although with lower intensity and significant broadening and clearly suggests changes in the structural distortion in the system and corroborates well with the XRD investigation and are observed to influence ferroelectric properties.

3.3. Ferroelectric properties

The ferroelectric hysteresis (P-E) loops of $BaBi_{2-x}Nb_2Er_xO_9$ ceramic compositions (x = 0–8 mol %) measured at 50 Hz at an applied electric

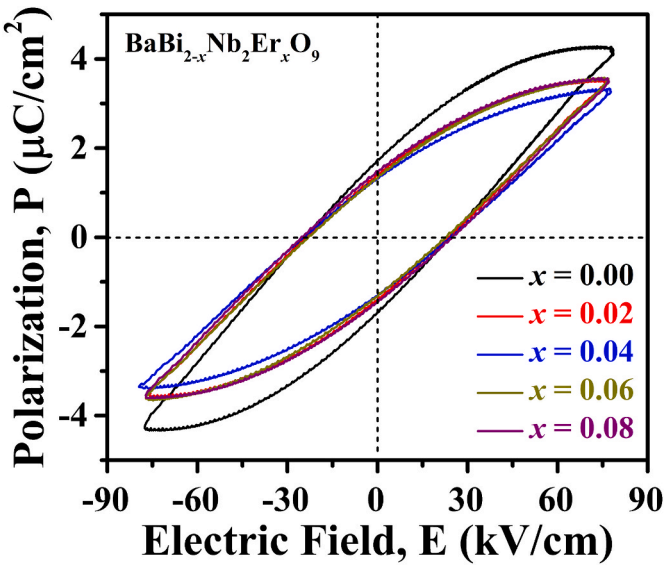

Fig. 3. Polarization vs. electric field curve of $BaBi_{2-x}Nb_2Er_xO_9$ ceramics with varying Erbium concentration at room temperature at 50 Hz frequency.

Table 3
Variation of electrical conductivity and P-E loop parameters for different Er^{3+} concentration in $BaBi_{2-x}Nb_2Er_xO_9$ ceramic composition (x = 0.00, 0.02, 0.04, 0.06, 0.08).

$BaBi_{2-x}Nb_2Er_xO_9$	σ_{dc} ($ohm^{-1}cm^{-1}$)	$2P_r$ ($\mu C/cm^2$)	$2E_c$ (kV/cm)
$x = 0.00$	3.92×10^{-12}	3.4944	48.7756
$x = 0.02$	1.04×10^{-12}	2.7668	48.0788
$x = 0.04$	8.62×10^{-13}	2.6384	48.9556
$x = 0.06$	5.02×10^{-13}	2.2677	45.8468
$x = 0.08$	2.75×10^{-14}	2.9524	49.8980

field ± 80 kV/cm is shown in Fig. 3. The measured coercive field ($2E_c$) and remnant polarization ($2P_r$) with different Er^{3+} concentrations are recorded in Table 3. The values of $2P_r$ and $2E_c$ range from 2.49 to 3.39 $\mu C/cm^2$ and 45.5–49.8 kV/cm respectively and agree with reported results on polycrystalline $BaBi_2Nb_2O_9$ ceramics [47]. The remnant polarization of $BaBi_{2-x}Nb_2Er_xO_9$ ceramic decreases with increasing Er^{3+} concentration, whereas the coercive field (E_c) is found to increase. It is reported that measurement of good quality hysteresis loops and remnant polarization is affected by the presence of lattice strain, defects, density, and grain size in the lattice [48]. Compared with undoped $BaBi_2Nb_2O_9$, the observed decrease in remnant polarization in Er^{3+} substituted composition could be attributed to structural distortion in the lattice owing to the incorporation of RE ion with smaller ionic radius and also low density of ceramics as confirmed by XRD analysis and agree with earlier reports on other BLSF materials [13]. However, in comparison to previously reported unsaturated hysteresis loops in $BaBi_2Nb_2O_9$ ceramics [43,47,49,50], it is noted that an improved hysteresis loop with a tendency to show saturation is observed at the applied electric field. However, complete P-E loop saturation was not achieved even at such a high applied field due to the least attainable sample thickness and the limitations of the instrument to apply a higher electric field. Besides, the observed increase in coercive field (E_c) values with increasing Er^{3+} content could be due to changing oxygen vacancies produced on account of inherent bismuth loss. These oxygen vacancies tend to migrate and accumulate at the electrode interface and low energy domain boundaries at high electric fields, thus hindering polarization switching due to domain pinning and resulting in an increase in the coercive field [13,28]. Moreover, with increasing Er^{3+} substitution, the oxygen vacancies owing to bismuth loss are seen to be reduced, which can be corroborated with the observed decrease in the room temperature dc conductivity (σ_{dc}) values (from 3.92×10^{-12} to 2.75×10^{-14} Ω^{-1} cm^{-1}) obtained for varying Er^{3+} content (x = 0–8 mol %) as shown in Table 3. The maximum value for remnant polarization and coercive field of doped $BaBi_{2-x}Nb_2Er_xO_9$ ceramic is 2.9524 $\mu C/cm^2$ and 49.8980 kV/cm for the ceramic composition at x = 0.08. The Up-conversion luminescence properties of the ferroelectric materials doped with RE^{3+} ions are intently due to the change in crystal field, which is revealed by the phase structure (crystal symmetry) and point defects in the lattice and also possibly sensitive to external stimulus such as electric field polarization [8,30]. In the present study, the observed decrease in ferroelctric properties in Er^{3+} substituted composition could be attributed to structural distortion in the lattice suggesting alterations in the ligand field environment of luminescent ions in the crystal lattice. As a result, significant modification of the green and red emission luminescence intensity is observed with change in Er content which is discussed in the next section.

3.4. Upconversion analysis

Fig. 4(a) shows strong upconverted light emission spectra of $BaBi_{2-x}Nb_2Er_xO_9$ ceramics composition under 980 nm excitation at a pump power of 50 mW with excitation source density 3.25 W/cm^2. Two green upconverted emissions are observed at 527 nm and 549 nm, which are allocated to the $^2H_{11/2} \rightarrow {}^4I_{15/2}$ and $^4S_{3/2} \rightarrow {}^4I_{15/2}$ transitions, respectively. Another weak band corresponds to the red emission band, visible to naked eyes at 657 nm, attributed to the $^4F_{9/2} \rightarrow {}^4I_{15/2}$ transition. The obtained UC spectra show good accord with previous studies on Erbium-doped host materials [4,13,51,52]. It has been observed that with increasing Er^{3+} content, the intensity of red and green emission rises and attains a maximum at x = 0.04, and after that, the intensity starts decreasing with increasing Erbium concentration, as presented in Fig. 4 (b). It is caused by the quenching effect, which becomes appreciable when the concentration of dopant reaches a particular value where the distance between nearest Erbium ions is insignificant that they can quickly transfer energy from one ion to another and contribute to non-radiative emission [53,54]. This results in radiative emission quenching and decreases the light emission intensity. The critical concentration for quenching is obtained at x = 0.04. Eq. (4) represents the Blasse formula used for evaluating the critical distance between the Er^{3+} ions [13,26,55]:

$$R_c \approx 2\left[\frac{3V}{4\pi X_c Z}\right]^{\frac{1}{3}} \quad (4)$$

where V denotes the volume of the unit cell and is equal to 790.96 cm^3, X_c is critical concentration, Z is the no. of host cation, and its value is 4 for $BaBi_2Nb_2O_9$, substituting all these values in the above equation, R_c is valued to be 21.12 Å. The mechanism of upconversion luminescence is described by different mechanisms, which include: cross-relaxation (CR), excited-state absorption (ESA), energy transfer (ET), ground-state absorption (GSA), and multi phonon relaxation (MPR) [4,54,56]. When laser of wavelength 980 nm illuminated on Er^{3+} doped $BaBi_{2-x}Nb_2Er_xO_9$ ceramic compositions, the ground level ($^4I_{15/2}$) Er^{3+} ions absorb the energy and excited to higher energy level ($^4I_{11/2}$) by GSA as shown in Fig. 4(c). The Er^{3+} may absorb one or two photons via ESA and ET mechanism at the $^4I_{11/2}$ metastable level of Er^{3+} ions, followed by further excitation to a higher $^4F_{7/2}$ level. Hence, the population at $^4F_{7/2}$ level is maintained by two mechanisms, i.e., ESA and ET, which is followed by non-radiative decay transitions to lower energy levels $^2I_{11/2}$, $^4S_{3/2}$, and $^4F_{9/2}$ through MPR. The Erbium ions at levels $^2H_{11/2}$ and $^4S_{3/2}$ produce green emission of wavelength 527 nm and 549 nm, respectively, and ions at level $^4F_{9/2}$ produce red emission of wavelength 657 nm. The green emission intensity is stronger than the red emission intensity owing to the fact that the energy difference between $^2H_{11/2}$ and $^4S_{3/2}$ levels is smaller (800 cm^{-1} approximately) as compared to the energy gap between $^4S_{3/2}$ and $^4F_{9/2}$ levels (3000 cm^{-1} approximately)

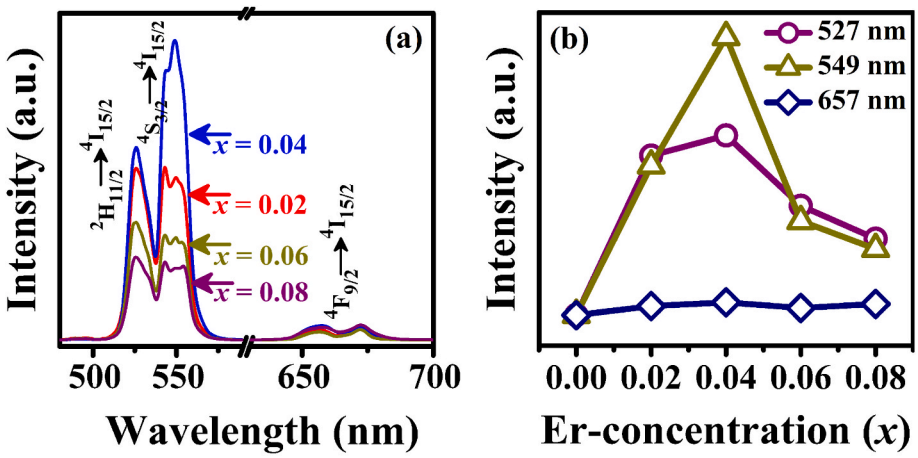

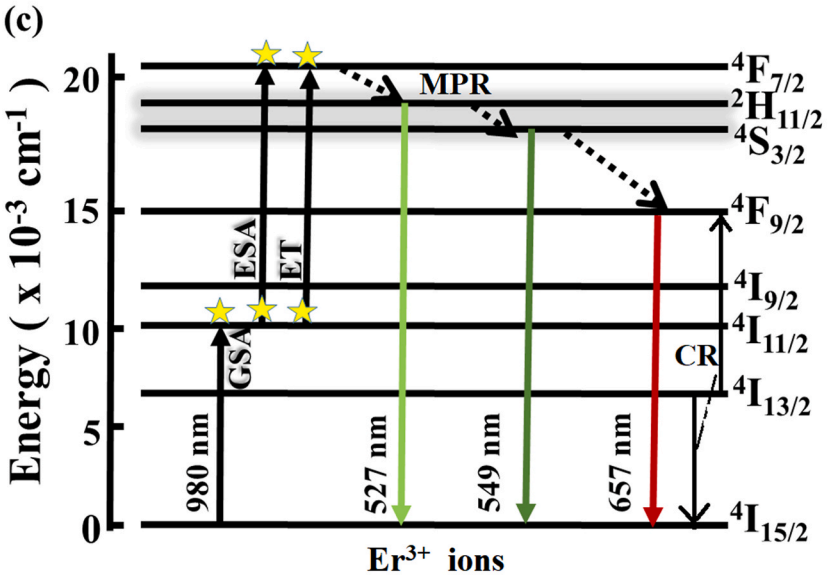

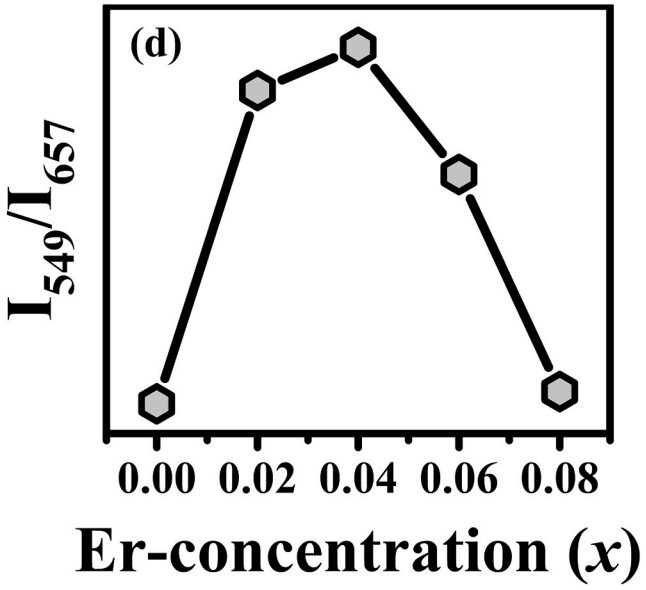

Fig. 4. (a) Upconversion emission spectra of $BaBi_{2-x}Nb_2Er_xO_9$ with varying Erbium concentration at 980 nm wavelength. (b) Deviation of red and green emission intensity with varying Erbium content. (c) Energy level diagram of Erbium ions for UC mechanism. (d) Intensity ratio of green and red emission (I_{549}/I_{657}) against Erbium concentration in $BaBi_{2-x}Nb_2Er_xO_9$ ceramics. (For interpretation of the references to colour in this figure legend, the reader is referred to the Web version of this article.)

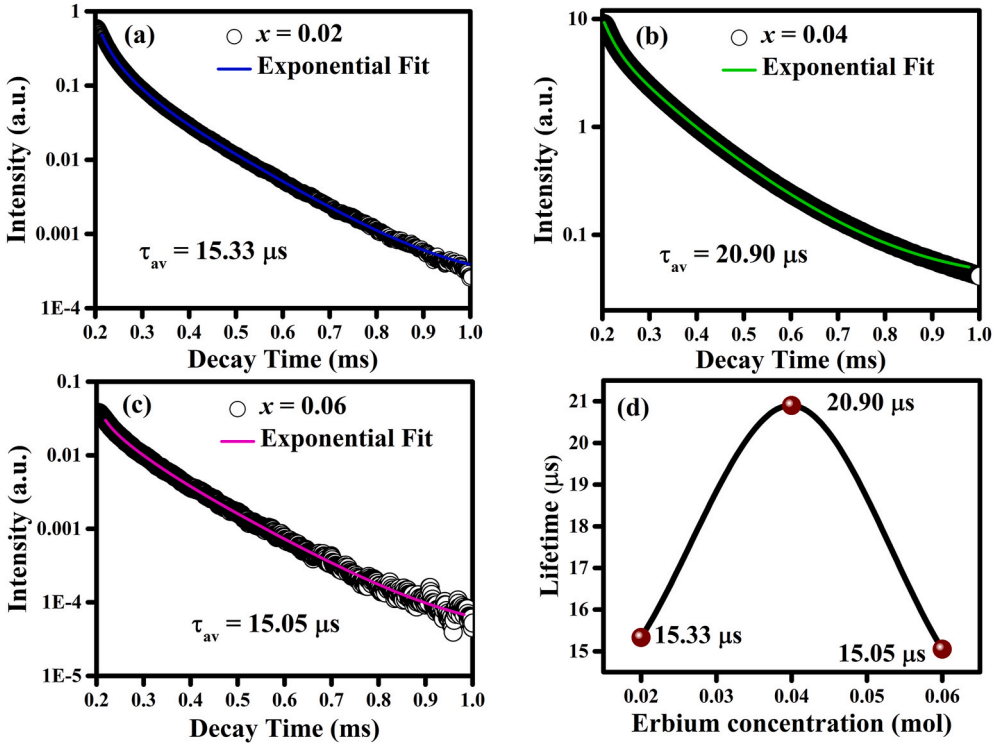

Fig. 5. Time resolved photoluminescence decay profile of $BaBi_{2-x}Nb_2Er_xO_9$ ceramics with Erbium content (a) $x = 0.02$, (b) $x = 0.04$, (c) $x = 0.06$ and (d) Variation of lifetime with the Erbium concentration.

[56]. Thereby, the MPR transition rate from the level $^2H_{11/2} \rightarrow {}^4S_{3/2}$ is faster than the transition $^4S_{3/2} \rightarrow {}^4F_{9/2}$ and results in the largest Er^{3+} population, which leads to strong green upconversion luminescence intensity [13,56]. The intensity ratio of the green emission band to the red emission band (I_{549}/I_{657}) is decreasing at $x \geq 0.04$ and is described by the CR process [56], as shown in Fig. 4(d).

3.4.1. Time decay measurements

The time resolved measurements were performed and examined for green emission transition ($^4S_{3/2} \rightarrow {}^4I_{15/2}$) at 549 nm under the excitation of 980 nm using a pulsed laser. In Fig. 5(a–c), the detectable time decay profiles of $BaBi_{2-x}Nb_2Er_xO_9$ ($x = 0.02, 0.04, 0.06$) ceramic has been reported. The curve is fitted by tri exponential function expressed as Eq. (5) [29,57]:

$$I(t) = I_0 + \ A_1 \exp\left(-\frac{t}{\tau_1}\right) + A_2 \exp\left(-\frac{t}{\tau_2}\right) + A_3 \exp\left(-\frac{t}{\tau_3}\right) \quad (5)$$

where I_0 is the intensity at $t = 0$, A_1, A_2, A_3, and τ_1, τ_2, τ_3 are the fitting parameters. The average lifetime is calculated by Eq. (6) [29]:

$$< \tau >= \frac{A_1\tau_1^2 + A_2\tau_2^2 + A_3\tau_3^2}{A_1\tau_1 + A_2\tau_2 + A_3\tau_3} \quad (6)$$

The estimated lifetime of the green emission (549 nm) for the various concentration of Erbium is represented in Fig. 5(d). The estimated fluorescence lifetime of green emission transition ($^4S_{3/2} \rightarrow {}^4I_{15/2}$) in $BaBi_{2-x}Nb_2Er_xO_9$ ceramic increases from 15.33 μs to 20.90 μs for Erbium content $x = 0.02$ to 0.04. This increase in lifetime confirms the energy transfer mechanism between Er^{3+} ions and confirms the involvement of the ET process in the upconversion process depicted in Fig. 4(c). Subsequently, on further increasing Erbium content ($x = 0.06$), the lifetime decreases to 15.05 μs indicating increased probability for non-radiative transitions and cross-relaxation processes within Er^{3+} [11,55].

3.4.2. Pump power dependence on upconversion luminescence

To examine the nature of photons included in the UC mechanism, the optimum amount of Er^{3+} ion in $BaBi_{2-x}Nb_2Er_xO_9$ composition at $x = 0.04$ is examined at different pump powers ranging from 450 mW to 950 mW with excitation source density 29.3 W/cm^2 to 61.8 W/cm^2. It is observed that the upconverted light intensities obtained through the transitions $^2H_{11/2} \rightarrow {}^4I_{15/2}$, $^4S_{3/2} \rightarrow {}^4I_{15/2}$, and $^4F_{9/2} \rightarrow {}^4I_{15/2}$ increased by increasing the excitation power (P). Eq. (7) estimates the no. of photons included in the UC mechanism:

$$I_{UP}(P) \propto P^n \quad (7)$$

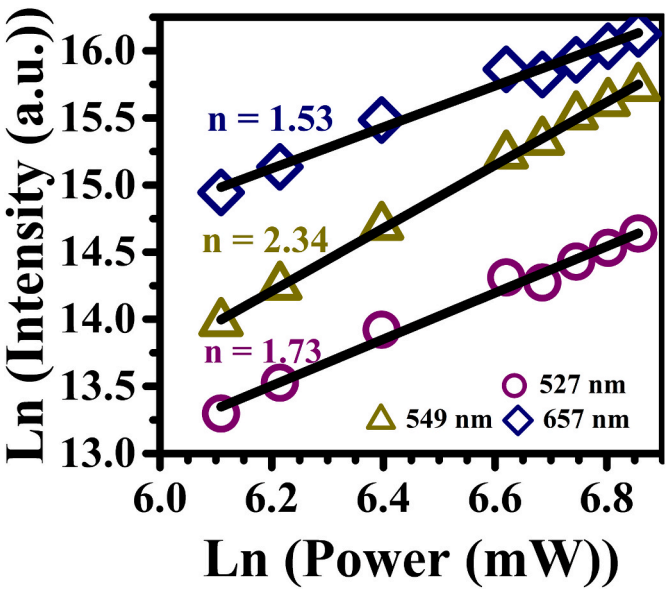

Fig. 6. Log plot of pump power dependence of UC intensity under 980 nm for $BaBi_{2-x}Nb_2Er_xO_9$ ($x = 0.04$).

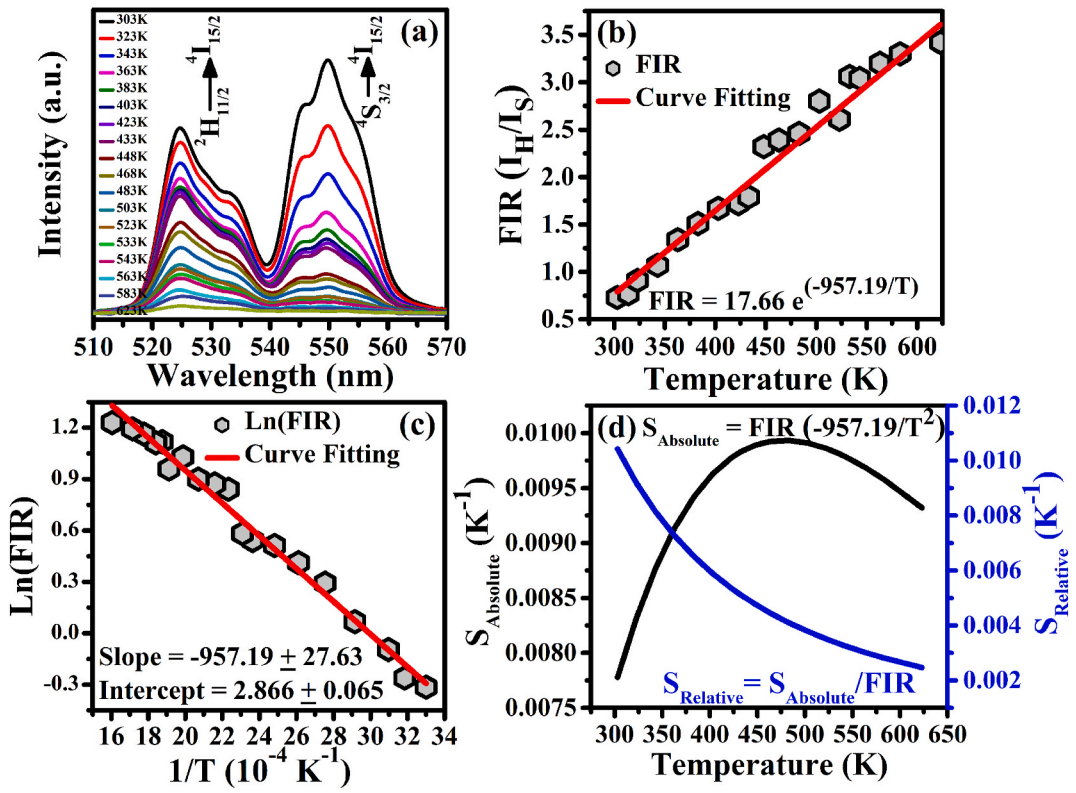

Fig. 7. (a) Upconversion emission spectra recorded at various temperature (303–623 K) for optimum composition $BaBi_{2-x}Nb_2Er_xO_9$ ($x = 0.04$). (b) Temperature dependence of Fluorescence Intensity ratio (I_{527}/I_{549}) for $BaBi_{2-x}Nb_2Er_xO_9$ ceramic composition. (c) Ln (FIR) vs. Temperature. (d) Variation of sensitivity and relative sensitivity with temperature for optimum composition $BaBi_{2-x}Nb_2Er_xO_9$.

where n denotes the no. of photons needed for the upconversion operation, P signifies the excitation power, and I_{UP} stands for the upconversion luminescence intensity. The linear fit of logarithmic plots of intensity versus excitation power (ln (I) versus ln (P)) is given in Fig. 6, and from the linear fit of experimental data for UC emission bands at 527, 549, and 657 nm, the value of slope (n) is found to be ~ 1.73, 2.34, and 1.53. Thus, a two-photon mechanism is confirmed for transitions corresponding to red and green emission in the UC process. The deviation in the slope (n) values corresponding to green and red UC emission bands rounded to the theoretical value of 2 is due to the involvement of several mechanisms such as excited state absorption (ESA), efficient energy transfer (ET), and non-radiative relaxations, etc. [29].

3.5. Noninvasive temperature sensing

The Fluorescence Intensity Ratio (FIR) technique is utilized for non-contact temperature measurement because it is a simple technique, easy to access, and independent from excitation intensity fluctuations [42]. To show the optical temperature sensing application in optimized Er^{3+} doped $BaBi_{2-x}Nb_2Er_xO_9$ composition, the FIR analysis is carried out by comparing the emission intensities of two green UC emission bands (I_{527} and I_{549}) arise due to thermally interacting levels $^2H_{11/2}$ and $^4S_{3/2}$ of Erbium ions. This procedure examines the intensity ratio of two thermally coupled levels (TCLs) with external temperature. This approach extensively investigates temperature sensing in rare-earth doped materials [32,42,58]. Fig. 7(a) depicts the variation in UC spectra for optimized Er^{3+} doped $BaBi_{2-x}Nb_2Er_xO_9$ ($x = 0.04$) ceramic composition for temperature ranging from 303 to 623 K. The electrons follow Boltzmann's distribution law in electronic levels $^2H_{11/2}$ and $^4S_{3/2}$ because these levels occur in thermal equilibrium, therefore, fluorescence intensity ratio (I_H/I_S) of $^2H_{11/2} \rightarrow {}^4I_{15/2}$ and $^4S_{3/2} \rightarrow {}^4I_{15/2}$ transition can be expressed by Eq. (8) [30,55–57]:

$$FIR = \frac{I_H}{I_S} = C \exp\left(-\frac{\Delta E}{K_B T}\right) \quad (8)$$

where K_B is the Boltzmann's constant, T denotes absolute temperature, ΔE represents the energy difference between $^2H_{11/2}$ and $^4S_{3/2}$ levels, C is a pre-exponential coefficient that depends on the degeneracy factor of coupled levels and the comparative transition probability, I_S and I_H are integrated intensity for $^4S_{3/2} \rightarrow {}^4I_{15/2}$ and $^2H_{11/2} \rightarrow {}^4I_{15/2}$ transition. The calculated value of FIR changes from 0.73 to 3.3 in the 303–623 K temperature range, as displayed in Fig. 7(b). The increasing temperature reduces the intensity ratio of the upconversion spectra [42]. In the linear form, Eq. (9) can be written as:

$$Ln(FIR) = -\left(\frac{\Delta E}{K_B}\right)\left(\frac{1}{T}\right) + LnC \quad (9)$$

Fig. 7(c) represents the linear fit of Ln (FIR) against absolute temperature inverse (1/T), which gives the intercept Ln(C) and slope $\Delta E/K_B$. From experimentally fitted data, the slope and intercept value is -951.2173 ± 16.327 and 2.8627 ± 0.0411, respectively, for Er^{3+} doped $BaBi_{2-x}Nb_2Er_xO_9$ composition at $x = 0.04$. The values of energy gap (ΔE) and pre-exponential coefficient (C) from experimentally fitting the data using Eq. (9) are evaluated to be 661.129 cm^{-1} and 17.5, respectively. For optical temperature sensing, the sensor sensitivity (S) is calculated using the FIR parameters. Sensor sensitivity is the degree to which the FIR deviates with a temperature variation, as represented by Eq. (10) [59]:

$$S = \frac{d(FIR)}{dT} = \frac{d\left(C\exp\left(-\frac{\Delta E}{K_B T}\right)\right)}{dT} = C\exp\left(-\frac{\Delta E}{K_B T}\right)\left(\frac{\Delta E}{K_B T^2}\right) \quad (10)$$

Table 4
Temperature sensing in different erbium-doped host materials in the different temperature ranges.

Host Material	ΔE	Temperature Range	T_{max}	Maximum Sensitivity (S_a)	Relative Sensitivity (S_r	References
$Bi_4Ti_3O_{12}$: Er^{3+}	591 cm^{-1}	293 K–523 K	415 K	0.0082 K^{-1}	0.0054 K^{-1}	[29]
$BaMoO_4$: Er^{3+}	655 cm^{-1}	303 K–463 K	463 K	0.0227 K^{-1}	0.0044 K^{-1}	[30]
$Na_{0.5}Bi_{0.5}TO_3$: Er^{3+}/Yb^{3+}	574 cm^{-1}	163 K–613 K	400 K	0.0031 K^{-1}	0.0055 K^{-1}	[59]
$SrMoO_4$: Er^{3+}/Yb^{3+}	704 cm^{-1}	93 K–773 K	473 K	0.0139 K^{-1}	0.0042 K^{-1}	[11]
$La_2Ti_2O_7$: Er^{3+}/Yb^{3+}	760 cm^{-1}	333 K–553 K	483 K	0.0057 K^{-1}	0.0063 K^{-1}	[61]
$BaBi_2Nb_2O_9$: Er^{3+}	661 cm^{-1}	300 K–623 K	483 K	0.00996 K^{-1}	0.0040 K^{-1}	Present work

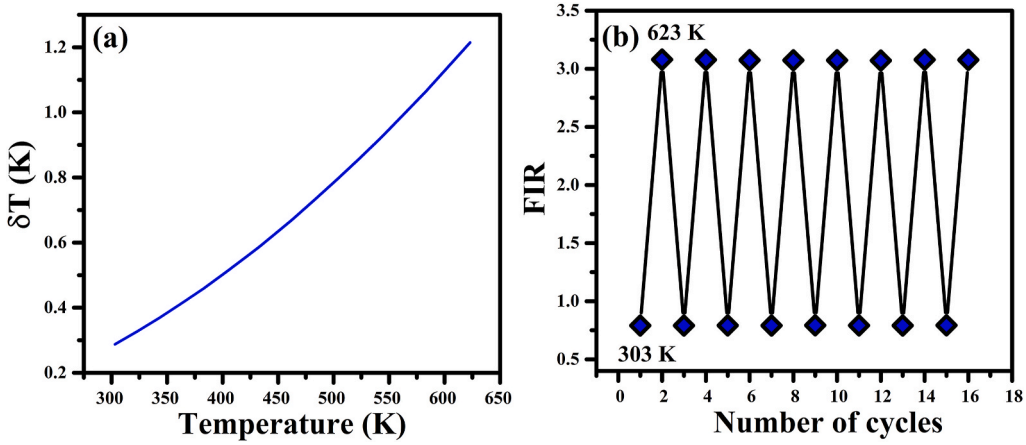

Fig. 8. (a) Temperature resolution and (b) Repeatability test for temperature sensing between 303 K and 623 K temperature range.

$$S_{Relative} = \frac{1}{FIR} * S_{Absolute} = \left(\frac{\Delta E}{K_B T^2}\right) \quad (11)$$

Another important factor for optical thermometry is relative sensitivity (S_r) which is the ratio of absolute sensitivity to the FIR value and is given in Eq. (11) [11]. Fig. 7(d) exhibits the absolute sensor sensitivity (S_a) and relative sensor sensitivity (S_r). It is noticed that the material sensitivity rises with a temperature rise and then achieves the highest value and then reduces marginally. The sensitivity surges from 0.00786 K^{-1} to 0.00959 K^{-1} with a temperature rise from 300 K to 623 K in optimized Er^{3+} doped $BaBi_{2-x}Nb_2Er_xO_9$ ($x = 0.04$) ceramic composition. The maximal sensitivity value $S_a = 0.00996\ K^{-1}$ is observed at 483 K, and the relative sensitivity value is as high as $S_r = 0.0040\ K^{-1}$ at 300 K. Table 4 represents the comparison of thermometric parameters to determine the sensitivity of various optical sensor materials. The resolution (δT) and repeatability (R) are the important parameters in the temperature sensing and can be deduced using Eq. (12) and Eq. (13) [60]:

$$\delta T = \frac{1}{S_{Relative}} * \frac{\delta \Delta}{\Delta} \quad (12)$$

$$R = 1 - Max \frac{(\Delta_{average} - \Delta_{specific})}{\Delta_{average}} \quad (13)$$

where $\Delta_{average}$ and $\Delta_{specific}$ is the average and specific value of FIR in the 16 cycles between 303 K and 623 K and $\frac{\delta\Delta}{\Delta}$ is the instrumental accuracy parameter. The associated plots for resolution and repeatability are represented in Fig. 8(a) and (b), respectively. The resolution varies from 0.3 K to 1.2 K in the temperature range 303 K–623 K. The repeatability test shows a negligible change in FIR values during the heating and cooling cycle. Thus, $BaBi_{2-x}Nb_2Er_xO_9$ composition at $x = 0.04$ has good sensitivity, repeatability, and decent resolution for temperature sensor applications in the temperature range 300 K–623 K.

4. Conclusion

Er^{3+} substituted $BaBi_{2-x}Nb_2Er_xO_9$ ceramic composition is effectively synthesized by the solid-state diffusion method. The evolution of a single-phase $BaBi_2Nb2O_9$ unit cell having orthorhombic geometry is confirmed by X-Ray diffraction. Structural deformation with Erbium doping has been detected by Raman spectroscopy and XRD. Shifts in the Raman modes indicate reduced interaction of Bi^{3+} ions with NbO_6 octahedron leading to relaxation of structural distortion with increasing Er^{3+} content. As demonstrated through Raman and XRD analysis, ferroelectric properties degrade with increasing Er substitution due to relaxation in a structural deformation. However, increasing Er^{3+} substitution exhibits significant improvement in dc electrical conductivity owing to suppression of oxygen vacancy concentration. Strong upconversion luminescence is obtained for green emission at 549 nm and 527 nm through $^4S_{3/2} \rightarrow {}^4I_{15/2}$, $^2H_{11/2} \rightarrow {}^4I_{15/2}$ transitions, and less intense red emission spectra appear at 657 nm via $^4F_{9/2} \rightarrow {}^4I_{15/2}$ transition under the excitation of 980 nm for an optimal Er^{3+} concentration ($x = 0.04$). The luminescence quenching is found to be effective beyond a certain Er^{3+} concentration of $x = 0.04$. The estimated fluorescence lifetime of green emission of Er^{3+} ion increases from 15.33 μs to 20.90 μs for Erbium content $x = 0.02$ to 0.04, suggests radiative emission due to energy transfer within Er3+ ions. The pump power dependence of upconversion luminescence intensity of emission bands confirms that upconversion is a two-photon mechanism. The FIR of the two green spectra was calculated and found linearly increasing with temperature ranging from 300 to 623 K. This is due to the thermal excitation and quasithermal equilibrium processes between $^2H_{11/2}$ and $^4S_{3/2}$. The FIR technique shows a maximum sensitivity of 0.00996 K^{-1} at 483 K for an optimized Er^{3+} substituted $BaBi_{2-x}Nb_2Er_xO_9$ ceramic composition ($x = 0.04$) for optical temperature sensing applications with good repeatability and temperature resolution.

Declaration of competing interest

The authors declare that they have no known competing financial

interests or personal relationships that could have appeared to influence the work reported in this paper.

Acknowledgement

The authors wish to thank the DTU Project Research Grant (F.NO. DTU/IRD/619/2019/2112) and the Advance Instrumentation Centre (AIC), Department of Applied Physics, DTU, for providing the research facility. Furthermore, the authors are thankful to Prof. K. Sreenivas and the University Science Instrumentation Centre, University of Delhi, for directing the up-conversion luminescence test.

References

[1] V. Lojpur, G. Nikoli, M.D. Dramianin, Luminescence thermometry below room temperature via up-conversion emission of Y_2O_3:Yb^{3+},Er^{3+} nanophosphors, J. Appl. Phys. 115 (2014) 20, https://doi.org/10.1063/1.4880158.

[2] R. Bokolia, O.P. Thakur, V.K. Rai, S.K. Sharma, K. Sreenivas, Electrical properties and light up conversion effects in $Bi_{3.79}Er_{0.03}Yb_{0.18}Ti_{3-x}W_xO_{12}$ ferroelectric ceramics, Ceram. Int. 42 (5) (2016) 5718–5730, https://doi.org/10.1016/j.ceramint.2015.12.103.

[3] A. Bayart, F. Szczepanski, J.F. Blach, J. Rousseau, A. Katelnikovas, S. Saitzek, Upconversion luminescence properties and thermal quenching mechanisms in the layered perovskite $La_{1.9}Er_{0.1}Ti_2O_7$ towards an application as optical temperature sensor, J. Alloys Compd. 744 (2018) 516–527, https://doi.org/10.1016/j.jallcom.2018.02.055.

[4] M.X. Façanha, J.P.C. doNascimento, M.A.S. Silva, M.C.C. Filho, A.N. LMarques, A. G. Pinheiro, A.S.B. Sombra, Up-conversion emission of Er^{3+}/Yb^{3+}co-doped $BaBi_2Nb_2O_9$ (BBN) phosphors, J. Lumin. 183 (2017) 102–107, https://doi.org/10.1016/j.jlumin.2016.08.011.

[5] Q. Cao, D. Peng, H. Zou, J. Li, X. Wang, X. Yao, Up-conversion luminescence of Er^{3+} and Yb^{3+} co-doped $CaBi_2Ta_2O_9$ multifunctional ferroelectrics, J. Adv. Dielectr. 4 (3) (2014), 1450018, https://doi.org/10.1142/s2010135x14500180.

[6] T. Wei, C.Z. Zhao, Q.J. Zhou, Z.P. Li, Y.Q. Wang, L.S. Zhang, Bright green upconversion emission and enhanced ferroelectric polarization in $Sr_{1-1.5x}Er_xBi_2Nb_2O_9$, Opt. Mater. 36 (7) (2014) 1209–1212, https://doi.org/10.1016/j.optmat.2014.03.001.

[7] M.X. Façanha, F.F. do Carmo, J.P.C. doNascimento, T.O. Sales, W.Q. Santos, A. S. Gouveia-Neto, C.J. da Silva, A.S.B. Sombra, A novel white-light emitting $BaBi_2Nb_2O_9$:Li^+/Tm^{3+}/Er^{3+}/Yb^{3+} upconversion phosphor, J. Lumin. 204 (August) (2018) 539–547, https://doi.org/10.1016/j.jlumin.2018.08.016.

[8] K. Li, L. Luo, Y. Zhang, W. Li, Y. Hou, Tunable luminescence contrast in photochromic ceramics (1 −Na0.5Bi0.5TiO3−xNa0.5K0.5NbO3:0.002Er by an electric field poling, ACS Appl. Mater. Interfaces 10 (2018) 41525–41534, https://doi.org/10.1021/acsami.8b15784.

[9] R. Sahu, P. Kumar, Microstructural, dielectric and ferroelectric properties of $Sr_{0.8}Bi_{2.15}Ta_2O_9$ ceramics synthesized by microwave processing technique, Phase Transitions 93 (1) (2020) 91–99, https://doi.org/10.1080/01411594.2019.1702190.

[10] J. Tang, P. Du, W. Li, G. Yuan, Z. Liu, L. Luo, "The integration of diverse fluorescence performances of $Sr_{2-x}SnO_4$:xSm^{3+} ceramics with an infinite luminescence modulation ratio, Chem. Eng. J. 410 (2021), 128287, https://doi.org/10.1016/j.cej.2020.128287.

[11] A. Shandilya, R.S. Yadav, A.K. Gupta, K. Sreenivas, Temperature-dependent light upconversion and thermometric properties of Er^{3+}/Yb^{3+}co-doped $SrMoO_4$ sintered ceramics, J. Mater. Sci. 56 (2021) 12716–12731, https://doi.org/10.1007/s10853-021-06078-8.

[12] J. Li, E. Sun, L. Tang, Y. Zhou, L. Li, J. Miao, Z. Zhang, W. Cao, Non-contact localized probing of ferroelectric phase transitions in Li^+/Er^{3+}:$BaTiO_3$ ceramics using fluorescence abnormalities, Appl. Phys. Lett. 116 (4) (2020), https://doi.org/10.1063/1.5129900.

[13] R. Bokolia, O.P. Thakur, V.K. Rai, S.K. Sharma, K. Sreenivas, Dielectric, ferroelectric and photoluminescence properties of Er^{3+} doped $Bi_4Ti_3O_{12}$ ferroelectric ceramics, Ceram. Int. 41 (4) (2015) 6055–6066, https://doi.org/10.1016/j.ceramint.2015.01.062.

[14] Z. Peng, Q. Chen, Y. Chen, D. Xiao, J. Zhu, Microstructure and electrical properties in W/Nb co-doped Aurivillius phase $Bi_4Ti_3O_{12}$ piezoelectric ceramics, Mater. Res. Bull. 59 (2014) 125–130, https://doi.org/10.1016/j.materresbull.2014.07.002.

[15] P. Banerjee, A. Franco Jr., Role of higher valent substituent on the dielectric and optical properties of $Sr_{0.8}Bi_{2.2}Nb_2O_9$ ceramics, Mater. Chem. Phys. 225 (2019) 213–218, https://doi.org/10.1016/j.matchemphys.2018.12.075. July 2018.

[16] C. Ma, W. Zhou, Z. Gan, X. Wang, W. Tan, Z. Zhang, Z. Zhai, Upconversion photoluminescence modulation by electric field poling in Er^{3+} doped $(Ba_{0.85}Ca_{0.15})(Zr_{0.1}Ti_{0.9})O_3$ piezoelectric ceramics, J. Alloys Compd. 794 (2019) 325–332, https://doi.org/10.1016/j.jallcom.2019.04.262.

[17] D. Dhak, P. Dhak, T. Ghorai, S.K. Biswas, P. Pramanik, Preparation of nano-sized $ABi_2Nb_2O_9$ (A = Ca^{2+}, Sr^{2+}, Ba^{2+}) ferroelectric ceramics by soluble Nb(V) tartarate precursor and their dielectric characteristics after sintering, J. Mater. Sci. Mater. Electron. 19 (5) (2008) 448–456, https://doi.org/10.1007/s10854-007-9361-y.

[18] C. Karthik, K.B.R. Varma, Dielectric and AC conductivity behavior of $BaBi_2Nb_2O_9$ ceramics, J. Phys. Chem. Solid. 67 (12) (2006) 2437–2441, https://doi.org/10.1016/j.jpcs.2006.06.012.

[19] M.P. Dasaria, K. Sambasiva Rao, P.M. Krishna, G.G. Krishna, Barium strontium bismuth niobate layered perovskites: dielectric, impedance and electrical modulus characteristics, Acta Phys. Pol. A 119 (3) (2011) 387–394, https://doi.org/10.12693/APhysPolA.119.387.

[20] Z. Yao, R. Chu, Z. Xu, J. Hao, W. Li, G. Li, Processing and enhanced electrical properties of $Sr_{1-x}(K_{0.5}Bi_{0.5})xBi_2Nb_2O_9$ lead-free piezoelectric ceramics, Ceram. Int. 42 (9) (2016) 10619–10623, https://doi.org/10.1016/j.ceramint.2016.03.156.

[21] Z. Yao, R. Chu, Z. Xu, J. Hao, G. Li, Enhanced electrical properties of (Li,Ce) co-doped $Sr(Na_{0.5}Bi_{0.5})Bi_4Ti_5O_{18}$ high temperature piezoceramics, RSC Adv. 6 (40) (2016) 33387–33392, https://doi.org/10.1039/c6ra02203k.

[22] Y. Wu, G. Cao, Ferroelectric and dielectric properties of strontium bismuth niobate vanadates, J. Mater. Res. 15 (7) (2000) 1583–1590, https://doi.org/10.1557/JMR.2000.0227.

[23] T. Mazon, M.A. Zaghete, M. Cilense, J.A. Varela, Effect of the excess of bismuth on the morphology and properties of the $BaBi_2Nb_2O_9$ thin films, Ceram. Int. 35 (8) (2009) 3143–3146, https://doi.org/10.1016/j.ceramint.2009.05.003.

[24] Z. Zhou, Y. Li, S. Hui, X. Dongand, Effect of tungsten doping in bismuth-layered $Na_{0.5}Bi_{2.5}Nb_2O_9$ high temperature piezoceramics, Appl. Phys. Lett. 104 (1) (2014), https://doi.org/10.1063/1.4861460, 0–4.

[25] P. Sharma, N. Berwal, N. Ahlawat, A.S. Maan, R. Punia, Study of structural, dielectric, ferroelectric and magnetic properties of vanadium doped BCT ceramics, Ceram. Int. 45 (16) (2019) 20368–20378, https://doi.org/10.1016/j.ceramint.2019.07.013.

[26] X. Wu, K.W. Kwok, F. Li, Upconversion fluorescence studies of sol-gel-derived Er-doped KNN ceramics, J. Alloys Compd. 580 (2013) 88–92, https://doi.org/10.1016/j.jallcom.2013.05.096.

[27] Y. Zhang, X. Wang, H. Ye, Y. Li, X. Yao, xLiNbO3-(1-x)(K,Na)NbO_3 ceramics: A new class of phosphors with tunable upconversion luminescence by external electric field and excellent optical temperature sensing property, J. Alloys Compd. 770 (2019) 214–221, https://doi.org/10.1016/j.jallcom.2018.08.019.

[28] L. Sun, C. Feng, L. Chen, S. Huang, Dielectric and piezoelectric properties of $SrBi_{2-x}Sm_xNb_2O_9$ (x=0, 0.05, 0.1, 0.2, 0.3, and 0.4) ceramics, J. Am. Ceram. Soc. 90 (12) (2007) 3875–3881, https://doi.org/10.1111/j.1551-2916.2007.02064.x.

[29] R. Bokolia, M. Mondal, V.K. Rai, K. Sreenivas, Enhanced infrared-to-visible up-conversion emission and temperature sensitivity in (Er^{3+}, Yb^{3+}, and W^{6+}) tri-doped $Bi_4Ti_3O_{12}$ ferroelectric oxide, J. Appl. Phys. 121 (8) (2017), https://doi.org/10.1063/1.4977006.

[30] C. Liu, Q. Wang, X. Wu, B. Sa, H. Sun, L. Luo, C. Lin, X. Zheng, T. Lin, Z. Sun, Boosting upconversion photoluminescence and multielectrical properties via Er-Doping-Modulated vacancy control in $Ba_{0.85}Ca_{0.15}Ti_{0.9}Zr_{0.1}O_3$, ACS Omega 4 (2019) 11004–11013, https://doi.org/10.1021/acsomega.9b01391.

[31] A.K. Soni, A. Kumari, V.K. Rai, Optical investigation in shuttle like $BaMoO_4$:Er^{3+}-Yb^{3+} phosphor in display and temperature sensing, Sensor. Actuator. B Chem. 216 (2015) 64–71, https://doi.org/10.1016/j.snb.2015.04.017.

[32] X. Li, X. Wang, H. Zhong, L. Cheng, S. Xu, J. Sun, J. Zhang, X. Li, L. Tong, B. Chen, Effects of Er^{3+} concentration on down-/up-conversion luminescence and temperature sensing properties in $NaGdTiO_4$: Er^{3+}/Yb^{3+} phosphors, Ceram. Int. 42 (13) (2016) 14710–14715, https://doi.org/10.1016/j.ceramint.2016.06.096.

[33] X. Hui, D. Peng, H. Zou, J. Li, Q. Cao, Y. Li, X. Wang, X. Yao, A new multifunctional Aurivillius oxide $Na_{0.5}Er_{0.5}Bi_4Ti_4O_{15}$: up-conversion luminescent, dielectric, and piezoelectric properties, Ceram. Int. 40 (8) (2014) 12477–12483, https://doi.org/10.1016/j.ceramint.2014.04.102. PART A.

[34] A. Banwal, R. Bokolia, Phase evolution and microstructure of $BaBi_2Nb_2O_9$ ferroelectric ceramics, Mater. Today Proc. 3 (2020) 2–5, https://doi.org/10.1016/j.matpr.2020.09.380.

[35] Z. Chen, L. Sheng, X. Li, P. Zheng, W.F. Bai, L. Li, F. Wen, W. Wu, L. Zheng, J. Cui, Enhanced piezoelectric properties and electrical resistivity in W/Cr co-doped $CaBi_2Nb_2O_9$ high-temperature piezoelectric ceramics, Ceram. Int. 45 (5) (2019) 6004–6011, https://doi.org/10.1016/j.ceramint.2018.11.252.

[36] H. Zou, Y. Yu, J. Li, Q. Cao, X. Wang, J. Hou, Photoluminescence, enhanced ferroelectric, and dielectric properties of Pr^{3+}-doped $SrBi_2Nb_2O_9$ multifunctional ceramics, Mater. Res. Bull. 69 (2015) 112–115, https://doi.org/10.1016/j.materresbull.2014.10.037.

[37] A. Banwal, R. Bokolia, Effect of Er^{3+} ion doping on structural, ferroelectric and up/down conversion luminescence in $BaBi_2Nb_2O_9$ ceramic, Mater. Today Proc. (2021) 3–6, https://doi.org/10.1016/j.matpr.2021.05.545.

[38] S. Kojima, R. Imaizumi, S. Hamazaki, M. Takashige, Raman scattering study of bismuth layer-structure ferroelectrics, Jpn. J. Appl. Phys. 33 (9) (1994) 5559–5564, https://doi.org/10.1143/JJAP.33.5559.

[39] J.D. Bobić, M.M.V. Petrović, B.D. Stojanović, "Aurivillius $BaBi_4Ti_4O_{15}$ based compounds: structure, synthesis and properties," *Process*, Appl. Ceram. 7 (3) (2013) 97–110, https://doi.org/10.2298/pac1303097b.

[40] S.F.L. Luis, U.R. Rodríguez-Mendoza, E. Lalla, V. Lavín, Chemical Temperature sensor based on the Er^{3+} green upconverted emission in a fluorotellurite glass, Sensor. Actuator. B (2011) 208–213, https://doi.org/10.1016/j.snb.2011.06.005.

[41] M.K. Mahata, T. Koppe, T. Mondal, C. Bru sewitz, K. Kumar, V.K. Rai, H. Hofsass, U. Vetter, Incorporation of Zn^{2+} ions into $BaTiO_3$:Er^{3+}/Yb^{3+} nanophosphor: an effective way to enhance upconversion, defect luminescence and temperature sensing, Phys. Chem. Chem. Phys. (2015) 20741–20753, https://doi.org/10.1039/C5CP01874A.

[42] L. Mukhopadhyay, V.K. Rai, R. Bokolia, K. Sreenivas, 980 nm excited Er^{3+}/Yb^{3+}/Li^+/Ba^{2+}:$NaZnPO_4$ upconverting phosphors in optical thermometry, J. Lumin. 187 (2017) 368–377, https://doi.org/10.1016/j.jlumin.2017.03.035.

[43] R. Ramaraghavulu, S. Buddhudu, Structural and dielectric properties of $BaBi_2Nb_2O_9$ ferroelectric ceramic powders by a solid state reaction method,

Ferroelectrics 460 (1) (2014) 57–67, https://doi.org/10.1080/00150193.2014.874924.
[44] H.C. Gupta, Archana, V. Luthra, Lattice vibrations of $ABi_2Nb_2O_9$ crystals (A = Ca, Sr, Ba), Vib. Spectrosc. 56 (2011) 235–240, https://doi.org/10.1016/j.vibspec.2011.03.002.
[45] Y.G. Abreu, A.P. Barranco, Y. Gagou, J. Belhadi, P.S. Grégoire, Vibrational analysis on two-layer Aurivillius phase $Sr_{1-x}Ba_xBi_2Nb_2O_9$ using Raman spectroscopy, Vib. Spectrosc. 77 (2015) 1–4, https://doi.org/10.1016/j.vibspec.2015.01.001.
[46] M.A. Basheer, G. Prasad, G.S. Kumar, N.V. Prasad, Dielectric studies on Sm-modified two-layered BLSF ceramics, Bull. Mater. Sci. 42 (3) (2019) 1–11, https://doi.org/10.1007/s12034-019-1776-6.
[47] W. Qi, Y. Wang, J. Wu, Z. Hu, C. Jia, G. Viola, H. Zhang, H. Yan, Relaxor behavior and photocatalytic properties of $BaBi_2Nb_2O_9$, J. Am. Ceram. Soc. 103 (1) (2020) 28–34, https://doi.org/10.1111/jace.16730.
[48] Y. Zhang, J. Roscow, R. Lewis, H. Khanbareh, V. Y. Topolov, M. Xie and C.R. Bowen, "Understanding the effect of porosity on the polarisation-field response of ferroelectric materials," Acta Mater., S1359–6454(18)30359-8, doi: 10.1016/j.actamat.2018.05.007.
[49] H. Zhang, H. Yan, M.J. Reece, Microstructure and electrical properties of Aurivillius phase $(CaBi_2Nb_2O_9)1\text{-}x(BaBi_2Nb_2O_9)x$ solid solution, J. Appl. Phys. 108 (1) (2010), https://doi.org/10.1063/1.3457229.
[50] B.S. Babu, S.N. Babu, G. Prasad, G.S. Kumar, N.V. Prasad, "Structural, electrical and photoluminescence properties of Er^{3+}-doped $Bi_4Ti_3O_{12}$ — $SrBi_4Ti_4O_{15}$ inter-growth ceramics, Front. Mater. Sci. 13 (1) (2019) 99–106, https://doi.org/10.1007/s11706-019-0454-3.
[51] N.A. Lomanova, Synthesis and thermal properties of nano-and macro-crystalline ceramic materials based on $Bi_5FeTi_3O_{15}$, Refract. Ind. Ceram. 59 (3) (2018) 301–305, https://doi.org/10.1007/s11148-018-0225-1.
[52] L. Yu, J. Hao, Z. Xu, W. Li, R. Chu, G. Li, Strong photoluminescence and good electrical properties in Eu-modified $SrBi_2Nb_2O_9$ multifunctional ceramics, Ceram. Int. 42 (13) (2016) 14849–14854, https://doi.org/10.1016/j.ceramint.2016.06.119.
[53] M. Chen, Study on the structure and luminescence quenching of Pr doped $Na_{0.5}Bi_{4.5}Ti_4O_{15}$ multifunctional ceramics, J. Mater. Sci. Mater. Electron. 30 (23) (2019) 20393–20399, https://doi.org/10.1007/s10854-019-02348-z.
[54] Z. Zhang, J. Li, L. Liu, J. Sun, J. Hao, W. Li, Upconversion luminescence and electrical properties of (K, Er) co-modified $Na_{0.5}Bi_{4.5}Ti_4O_{15}$ high-temperature piezoceramics, Phys. B Condens. Matter 580 (2020), 411920, https://doi.org/10.1016/j.physb.2019.411920. September 2019.
[55] W. Lv, Y. Jia, Q. Zhao, W. Lü, M. Jiao, B. Shao, H. You, " Synthesis, Structure, and luminescence properties of $K_2Ba_7Si_{16}O_{40}$:Eu^{2+} for white light emitting diodes, J. Phys. Chem. 118 (2014) 4649–4655, https://doi.org/10.1021/jp500662a.
[56] F. Liu, X. Jiang, C. Chen, X. Nie, X. Huang, Y. Chen, H. Hu, C. Su, Structural, electrical and photoluminescence properties of Er^{3+}-doped $SrBi_4Ti_4O_{15}$-$Bi_4Ti_3O_{12}$ inter-growth ceramics, Mater. Sci. 13 (1) (2019) 99–106, https://doi.org/10.1007/s11706-019-0454-3.
[57] A. Shandilya, R.S. Yadav, A.K. Gupta, K. Sreenivas, Effects of Yb^{3+} ion doping on lattice distortion, optical absorption and light upconversion in Er^{3+}/Yb^{3+} co-doped $SrMoO_4$ ceramics, Mater. Chem. Phys. 264 (2) (2021) 124441, https://doi.org/10.1016/j.matchemphys.2021.124441.
[58] J. Li, J. Sun, J. Liu, X. Li, J. Zhang, Y. Tian, S. Fu, L. Cheng, H. Zhong, H. Xia, B. Chen, Pumping-route-dependent concentration quenching and temperature effect of green up- and down-conversion luminescence in Er^{3+}/Yb^{3+} co-doped $Gd_2(WO_4)_3$ phosphors, Mater. Res. Bull. 48 (6) (2013) 2159–2165, https://doi.org/10.1016/j.materresbull.2013.02.009.
[59] P. Du, L. Luo, W. Li, Q. Yue, Upconversion emission in Er-doped and Er/Yb-codoped ferroelectric $Na_{0.5}Bi_{0.5}TiO_3$ and its temperature sensing application, J. Appl. Phys. 116 (1) (2014) 1–7, https://doi.org/10.1063/1.4886575.
[60] L.J. Li, Y. Tong, J. Chen, Y.H. Chen, G.A. Ashraf, L.P. Chen, T. Pang, Hai Guo, Up-conversion and temperature sensing properties of $Na_2GdMg_2(VO_4)_3$:Yb^{3+}, Er^{3+} phosphors, J. Am. Ceram. Soc. (2021) 1–8, https://doi.org/10.1111/jace.18070. ".
[61] Y. Liu, G. Bai, E. Pan, Y. Hua, L. Chen, S. Xu, Upconversion fluorescence property of Er^{3+}/Yb^{3+} codoped lanthanum titanate microcrystals for optical thermometry, J. Alloys Compd. 822 (2020) 153449, https://doi.org/10.1016/j.jallcom.2019.153449.

Journal of Luminescence 263 (2023) 120071

Contents lists available at ScienceDirect

Journal of Luminescence

journal homepage: www.elsevier.com/locate/jlumin

Full Length Article

Efficient tunable temperature sensitivity in thermally coupled levels of Er^{3+}/Yb^{3+} co-doped $BaBi_2Nb_2O_9$ ferroelectric ceramic

Ankita Banwal, Renuka Bokolia *

Delhi Technological University, Delhi, 110042, India

ARTICLE INFO

Keywords:
Thermal sensing
Time decay
Pump power
Upconversion luminescence
Ceramic
SEM
XRD

ABSTRACT

Er^{3+}/Yb^{3+} co-doped ferroelectric ceramic $BaBi_{2-0.04-y}Nb_2Er_{0.04}Yb_yO_9$ ($y = 0.00$, 0.02, 0.04, 0.06, 0.08, 0.10, and 0.12) are prepared by solid-state method and investigated for their structural and upconversion luminescence properties. High-resolution X-ray pattern investigation confirmed the ceramic's orthorhombic structure. Microstructure of sintered ceramic surface resembles plate-like structures and consists of non-uniform grains that are randomly oriented. Upconversion luminescence (UCL) spectra revealed two prominent green emission bands near 535 and 557 nm and a notable red band at 672 nm, corresponding to a 980 nm excitation wavelength. Decay time measurements support the effective energy transfer from Yb^{3+} to Er^{3+} ions. The average lifetime increases with increasing Er^{3+}/Yb^{3+} doping concentration up to the optimal concentration ($y = 0.10$). Pump power dependence demonstrates that two photons are required to generate green and red UC illumination. The absolute sensitivity, S_a (0.69% K^{-1} and 0.58% K^{-1}) and relative sensitivity, S_r (1.1% K^{-1} and 1.01% K^{-1}) have been recorded for the first time on Er^{3+}/Yb^{3+} co-doped $BaBi_{2-0.04-y}Nb_2Er_{0.04}Yb_yO_9$ ceramic at $y = 0.06$ and 0.10, respectively, suggesting it is a viable non-contact sensor ceramic whose sensitivity can be tuned by varying dopant concentrations.

1. Introduction

The ongoing investigations on trivalent rare earth (RE^{3+}) ion-doped ferroelectrics at nanoscale dimensions have attracted considerable interest [1–5]. The nanomaterials doped with optically active centres have enhanced structural, electrical, and sensor capabilities as well as better optical features. By taking advantage, near-infrared to visible upconversion luminescence in nanomaterials has lately received considerable interest for a variety of potential applications [6,7]. Most of these potential applications involve infrared quantum counter detectors, 3D displays, biological medicine, optic fibre communications, optical data storage, and others [2]. Furthermore, the need for low-cost and sustainable materials that can perform several functions led researchers to consider multifunctional and hybrid materials. Ferroelectrics are a non-toxic and environmentally benign alternative to lead-based ceramics, making them a superior replacement option. The selection of this material as a host is particularly promising because of its low phonon energy, which is important for decreasing radiative transitions to facilitate an efficient upconversion process [8–10]. Layered bismuth structure ferroelectric (BLSF) materials are steadily gaining prominence due to their favourable chemical and thermic immovability, excellent radiation shifts, decreased phonon power, and increased sensing capability over a broad thermal limit. The ferroelectrics (BLSF) are a unique class of ferroelectrics that follow a standard formula $(Bi_2O_2)^{2+}(A_{n-1}B_nO_{3n+1})^{2-}$. The quasi perovskite layer, designated by the formula $A_{n-1}B_nO_{3n+1}$, is surrounded by two bismuth oxide layers, $(Bi_2O_2)^{2+}$; n is the total octahedral sheets present within the perovskite unit. A is used to indicate ions with tripled, dual, or single valence ions (such as Sr^{2+}, Bi^{3+}, or Ba^{2+}), while B is used to represent ions with a higher valence (such as Nb^{5+}, Ta^{5+}, Ti^{4+}, or W^{6+}) [11–14].

According to the findings of the literature study, the electrical, optical, and sensing properties of BLSF materials were enhanced after being suitably doped with RE ions. Because of developments in the industry and technological advancements, temperature sensing has received significant attention in recent years. The necessity for a non-contact temperature sensor becomes apparent in areas such as electrical transformers in power plants, oil refineries, and coal mines where typical temperature measuring instruments are prohibited. It is challenging for today's researchers working in the field of RE-doped materials to create high-temperature sensing material with a significant level

* Corresponding author.
E-mail address: renukabokolia@dtu.ac.in (R. Bokolia).

https://doi.org/10.1016/j.jlumin.2023.120071
Received 15 May 2023; Received in revised form 5 July 2023; Accepted 15 July 2023
Available online 18 July 2023

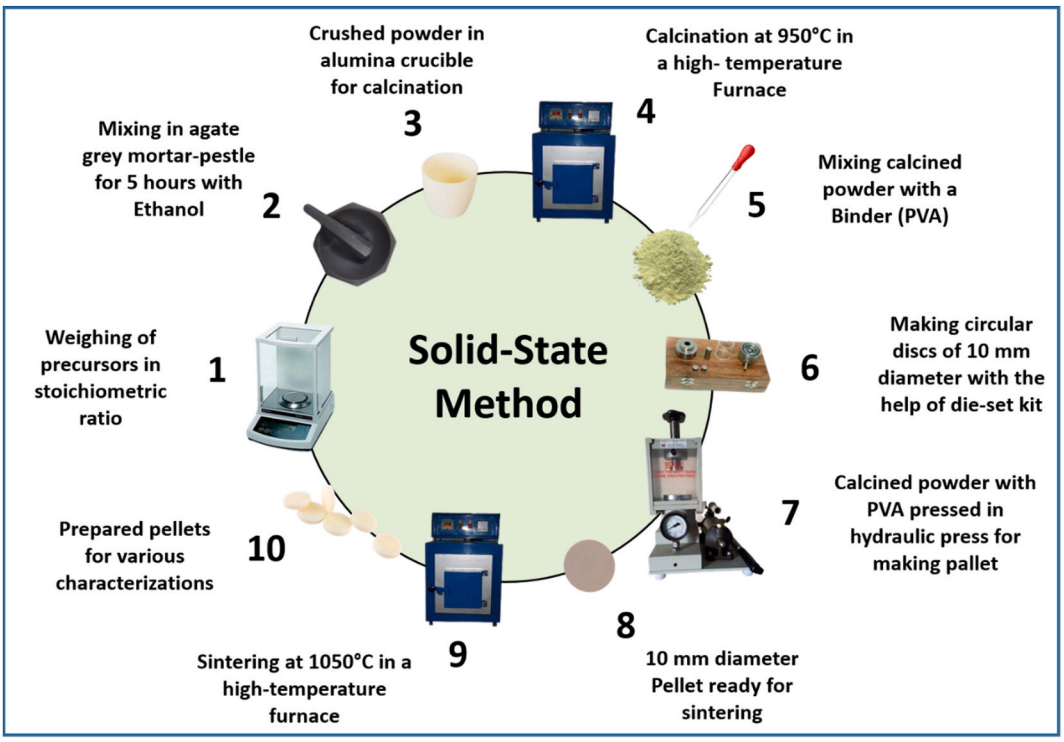

Fig. 1. Schematic diagram of the synthesis process.

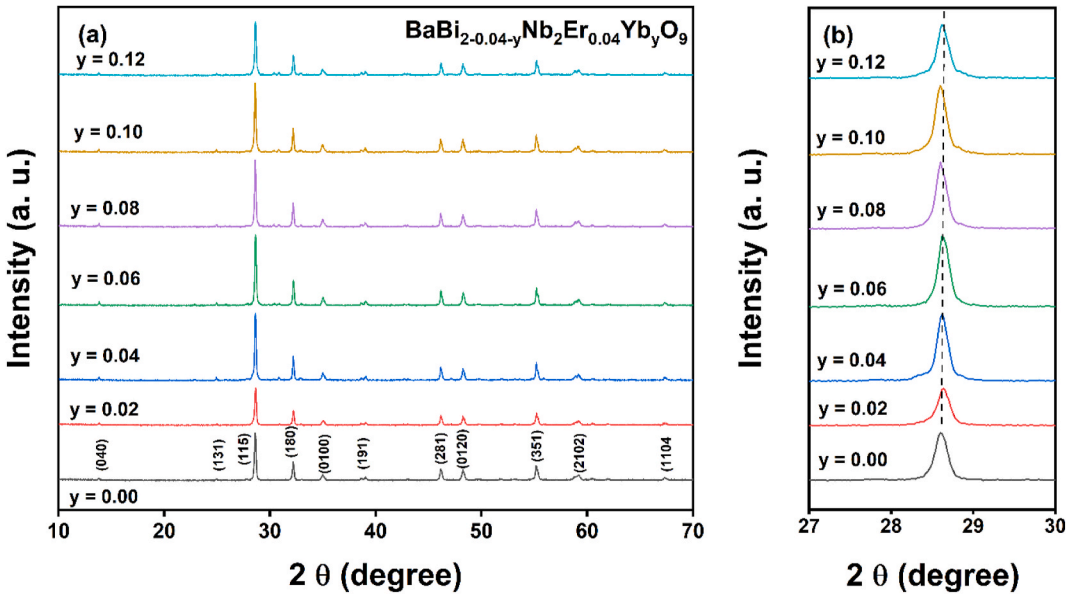

Fig. 2. (a) XRD spectra of $BaBi_{2-0.04-y}Nb_2Er_{0.04}Yb_yO_9$ ($y = 0.00$, 0.02, 0.04, 0.06, 0.08, 0.10, and 0.12) ceramic. (b) Peak displacement of (115) plane for various dopant concentrations.

of sensitivity. For instance, Luo et al. studied Er^{3+}/Yb^{3+} co-doped $Ba_2NaNb_5O_{15}$ glass ceramics for UC luminescence, thermal sensing, and energy storage performance [15]. Also, in a previous report, Er^{3+}/Yb^{3+} co-doped tungsten tellurite glass was used to make a temperature sensor with an absolute sensibility of around $28.72 \times 10^{-4}\ K^{-1}$ at 690 K along with decent green emission luminescence [16]. Swami et al. studied the luminescence intensity ratio of Yb^{3+}/Er^{3+} co-doped La_2TiO_7 ceramics and reported an absolute sensitivity value of around $0.0029\ K^{-1}$ at 498 K [17]. In addition, Peng et al. fabricated Yb^{3+}/Er^{3+} co-doped BNT across a wide temperature range and determined a sensitivity of approximately $0.0049\ K^{-1}$ at 363 K [18].

During our research, we concluded that the best dopants for us to use would be Er^{3+} and Yb^{3+}. This choice was made because Er^{3+} is the most prevalent and efficient activator for producing upconversion luminescence due to its extensive and long-lived intermediate energy levels. Er^{3+} acts as a luminescence upconversion activator. It is simpler to achieve the migration of electrons inside the 4f-4f energy level and generate a rich emission band in Er^{3+} because it has more unpaired 4f-layer orbital electrons than Sc^{3+}, Y^{3+}, La^{3+}, and Lu^{3+}. When Er^{3+} is put in an environment with a different matrix or ligand, there is a chance

Table 1
Lattice parameters for $BaBi_{2-0.04-y}Nb_2Er0_{0.04}Yb_yO_9$ compositions with constant Er^{3+} content (0.04) and varying Yb^{3+} content (y = 0.00, 0.02, 0.04, 0.06, 0.08, 0.10 and 0.12).

Parameters	$BaBi_{2-0.04-y}Nb_2Er_{0.04}Yb_yO_9$						
	y = 0.00	y = 0.02	y = 0.04	y = 0.06	y = 0.08	y = 0.10	y = 0.12
a (Å)	5.5439	5.5448	5.5450	5.5454	5.5479	5.5488	5.5497
b (Å)	5.5536	5.5551	5.5552	5.5561	5.5601	5.5612	5.5600
c (Å)	25.5975	25.5980	25.5989	25.5991	25.6178	25.6200	25.6219
V ($Å^3$)	788.111	788.467	788.537	788.728	790.229	790.581	790.597
Orthorhombic distortion (b/a)	1.00174	1.00185	1.00183	1.00192	1.00219	1.00223	1.00185
Experimental Density, ρ (g/cm^3)	7.00919	6.83796	6.72015	6.77289	6.47426	6.76007	6.0106
Theoretical density, ρ_0 (g/cm^3)	5.82447	5.88589	5.81015	5.9373	5.79818	5.94532	5.24095
Porosity ($1-\rho_0/\rho$) × 100%	16.90	13.92	13.54	12.33	10.44	12.05	12.80
Average grain size (μm)	1.39 ± 0.0278	1.54 ± 0.0125	1.67 ± 0.1365	1.78 ± 0.0889	1.89 ± 0.1129	1.92 ± 0.1761	1.45 ± 0.0295

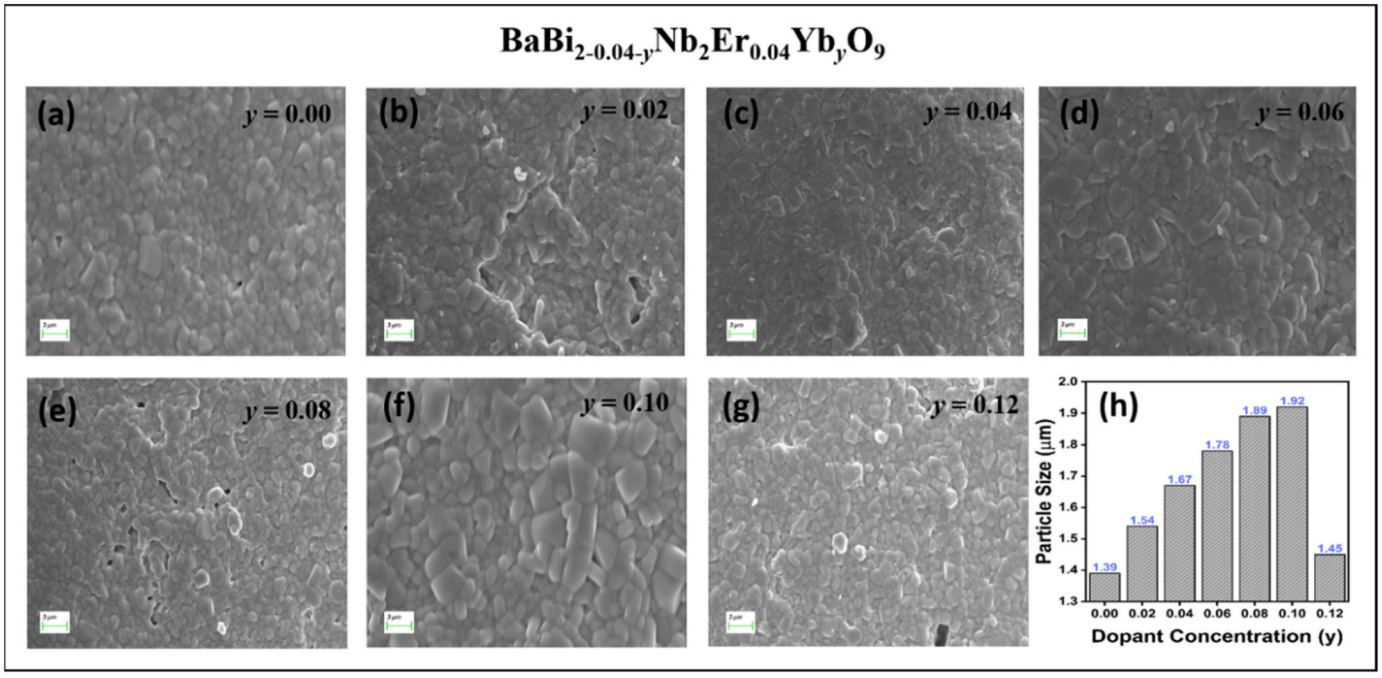

Fig. 3. (a–g) SEM micrographs of $BaBi_{2-0.04-y}Nb_2Er_{0.04}Yb_yO_9$ with y = 0.00 to 0.12 sintered at 1050 °C for 3 h. (h) Variation of particle size with all dopant concentrations.

that the crystal symmetry and crystal field of the matrix around Er^{3+} may change. This will, in turn, affect the photoluminescence emission [19]. In most cases, the Yb^{3+} ion is utilized as a sensitizer to raise the absorption cross-section to improve the upconversion efficiency. Therefore, we systematically replaced the bismuth ions in our host material $BaBi_2Nb_2O_9$ with erbium and ytterbium ions, and then we utilized X-ray powder diffraction to examine the resultant compound's configuration. For the UC emission investigations, a wavelength of 980 nm was selected as the excitation wavelength. Additionally, the pump power dependency on UC intensity was analyzed to determine the involvement of the number of photons in the UC process. The temperature sensing characteristics of a single Er^{3+} doped $BaBi_2Nb_2O_9$ ceramic system has been reported in our previous work [20]. The intense green emission occurs at x = 0.04 which is the optimum concentrationof Er^{3+} in $BaBi_2Nb_2O_9$ ceramic [20]. The decent sensitivity and upconversion luminescence behaviour of Er^{3+} doped $BaBi_2Nb_2O_9$ ceramic has motivated us to investigate it thoroughly, so we co-doped $BaBi_2Nb_2O_9$ with Yb^{3+} by keeping the Er^{3+} constant at optimum concentration (x = 0.04) throughout the synthesis. Also, as far as the author's knowledge, there is no study on the sensing behaviour of Er^{3+}/Yb^{3+} co-doped $BaBi_2Nb_2O_9$ host matrix system over a wide temperature range in thermally coupled levels ($^2H_{11/2}$ and $^4S_{3/2}$). In light of this, we investigated the fluorescence intensity ratio (FIR) approach for temperature sensing capabilities in the 303–573 K range to establish the applicability of the ceramic design suited for optoelectronic devices.

2. Synthesis and characterization descriptions

The solid-state approach synthesized the ceramics with the configuration $BaBi_{2-0.04-y}Nb_2Er_{0.04}Yb_yO_9$ (y = 0.02, 0.04, 0.06, 0.08, 0.10, and 0.12). Fig. 1 depicts a schematic representation of the fabrication of the ceramic. The initial precursors ($BaCO_3$, Bi_2O_3, Nb_2O_5, Er_2O_3, and Yb_2O_3) were obtained from Sigma Aldrich and had the greatest possible purity level (99.99%). The precursors were measured and weighed according to their stoichiometric proportions. The raw powders were manually crushed using a pestle and mortar in ethanol for 8 h before being sent to a regulated high-temperature furnace that operated at 950 °C for 3 h. After being calcined, the granules were combined with polyvinyl alcohol (PVA), which was used to form the pellets in a circular shape. The round pellets of 10 mm in diameter were constructed by applying a pressure of approximately 5 MPa for 1 min in a manual hydraulic press. After the pellets were made, they were sintered in two stages: firstly, rise to 500 °C/h to eliminate the PVA, then reach about 1050 °C and held there for 2 h. Cu-Kα radiations are used in conjunction with a sophisticated X-

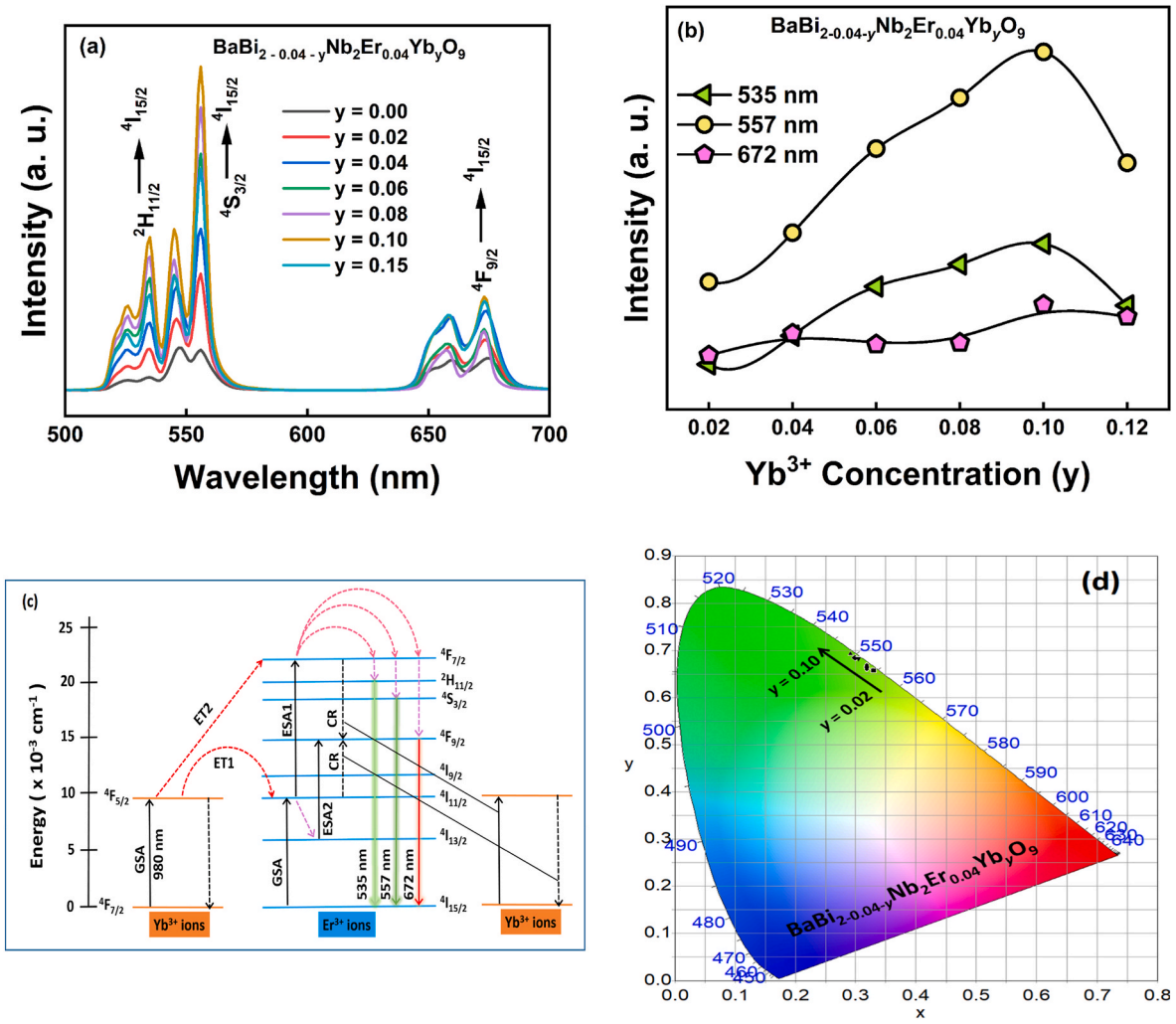

Fig. 4. (a) UC emission spectra of $BaBi_{2\text{-}0.04\text{-}y}Nb_2Er_{0.04}Yb_yO_9$ for various Yb^{3+} concentrations under 980 nm excitation. (b) Graph of intensity versus different concentrations of Yb^{3+}. (c) Schematic depiction of the energy pathways of Er^{3+}/Yb^{3+} ions doped in $BaBi_{2\text{-}0.04\text{-}y}Nb_2Er_{0.04}Yb_yO_9$ under the excitation of 980 nm. (d) CIE plot of $BaBi_{2\text{-}0.04\text{-}y}Nb_2Er_{0.04}Yb_yO_9$ for (y = 0.02, 0.04, 0.06, 0.08, 0.10, and 0.12).

ray diffractometer manufactured by Bruker to investigate the phase structure of the sample. The upconversion luminescence (UCL) spectra were acquired with the help of the HORIBA PTI Quanta-master under the wavelength of 980 nm laser. The SEM micrographs from the cracked pallet sample were obtained using a ZEISS scanning electron microscope. The thermally dependent UCL emitting spectra were studied by positioning the synthesized material on the heaters while using a thermocouple to measure the temperature. The handcrafted heater that was controlled by variable voltage and coupled with a thermocouple and multimeter was used for the thermal sensing, resolution, and stability studies that were carried out.

3. Results and analysis

3.1. Structural and microstructural analysis

The XRD pattern of the prepared composition $BaBi_{2\text{-}0.04\text{-}y}Nb_2Er_{0.04}Yb_yO_9$ (y = 0.00, 0.02, 0.04, 0.06, 0.08, 0.10, and 0.12) was exhibited in Fig. 2(a) after being sintered at a temperature of 1050 °C for 3 h. The detected XRD peaks show a good correlation, as stated in the JCPDF file no. 00-012-0403, and the lack of secondary peaks implies that the dopants are fully soluble in the host lattice without causing structural modifications or other drastic changes. The detected Bragg reflections showed that the prepared ceramic had a single phase with an orthorhombic geometry and belonged to the phase group Fmmm. Also, the maximum peak intensity of the (115) plane in $BaBi_{2\text{-}0.04\text{-}y}Nb_2Er_{0.04}Yb_yO_9$ ceramic reflects the BLSF with m = 2, according to previous reports, the (112 m + 1) plane relates to the high-intensity diffraction pattern for BLSF materials in the Aurivillius phase [21,22]. The ionic radii of Er^{3+} and Yb^{3+} are similar to one another such that the ions Yb^{3+} (1.22 Å) and Er^{3+} (1.25 Å) may favor occupying A-sites (Bi^{3+}) rather than B-sites (Nb^{5+}). This is because their effective ionic radii are the same as A site ions [6]. The density of sintered pellets was calculated using Archimedes' principle and recorded in Table 1. It was found that the density of the sintered pellets decreases with increasing dopant concentration. The tension within the host lattice due to the insertion of dopants causes the shifting of diffraction peaks slightly from their mean position and is given by Eq. (1) [20]:

$$\sigma = \frac{E}{2\upsilon}\left[\frac{\sin\theta_n}{\sin\theta_i} - 1\right] \quad (1)$$

where υ represents Poison's coefficient, E is the modulus of elasticity, θ_n is the displaced value of 2θ, and θ_i is the reference angle. Eq. (1) states that a positive σ indicates lattice compression, whereas a negative σ suggests lattice expansion after dopant substitution. Fig. 2(b) represents the shifting of peaks to slightly lower 2θ angles. In our case, $\theta_n < \theta_i$ (E and υ are constants). Therefore, σ comes out to be negative. This implies the expansion within the crystal lattice, which can also be verified from

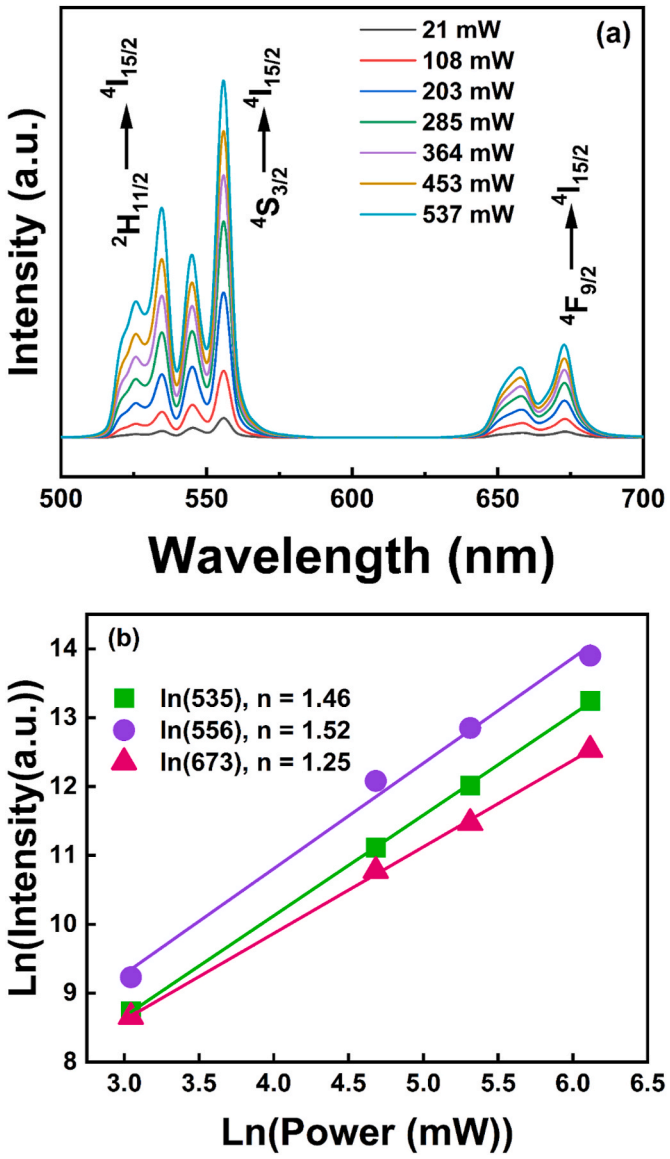

Fig. 5. (a) UCL emission spectra with different pump power ranging from 21 mW to 537 mW. (b) The plot of Ln(power) vs. Ln(UC intensity).

the increased cell volume parameters of the doped $BaBi_2Nb_2O_9$ ceramic, as shown in Table 1. This can also be explained by the constrained character of $6s^2$ lone-pair of Bi^{3+} ions in the host lattice which causes the expansion of unit cell volume and shifting of the peaks towards lower 2θ [6,8]. The increased cell volume parameters (a, b, c) suggest the increased interplanar spacing, which decreases the 2θ values. Although the ionic radius of Er^{3+}, Yb^{3+}, and Bi^{3+} varies, the cell volume and lattice parameters (a, b, c) of undoped $BaBi_2Nb_2O_9$ do not vary significantly. This could be ascribed to the formation of cationic vacancies, which maintain the lattice's electroneutrality and minimize crystal deformation [5].

The scanning electron microscopy images (SEIs) of the $BaBi_{2-0.04-y}Nb_2Er_{0.04}Yb_yO_9$ ceramics are shown in Fig. 3(a–g). These sintered ceramics possess a compact microstructure. These plate-like structures are composed of irregularly aligned non-uniform grains. This is consistent with the standard properties of BLSFs. In Table 1, the reduction in porosity suggests that as the dopant concentration rises, the ceramic becomes denser. ImageJ software performs the necessary calculations to estimate the average particle size. In Fig. 3(h), the average grain size increases up to the optimum dopant concentration ($y = 0.10$), and then there is a subsequent reduction in the average grain size. This grain size variation may result from a rise in the electron charge distribution on the interface of Er^{3+}/Yb^{3+}. Thie increase in electron charge density slows grain boundary diffusion and inhibits grain development, resulting in smaller grain sizes [23,24].

3.2. Upconversion luminescence analysis

To evaluate the effect of Yb^{3+} on the upconversion luminescence, the UC spectra for the ceramic $BaBi_{2-0.04-y}Nb_2Er_{0.04}Yb_yO_9$ with constant Er^{3+} content and variable Yb^{3+} content ($y = 0.02$, 0.04, 0.06, 0.08, 0.10, and 0.12) were measured. The UCL measurements were done under the illumination of 980 nm excitation, with a pumping power of 50 mW and an excitation source density of 3.25 W/cm^2, and are shown in Fig. 4(a). The transitions from $^2H_{11/2}$ to $^4I_{15/2}$ and $^4S_{3/2}$ to $^4I_{15/2}$ are responsible for the two strong green emission bands at 535 nm and 557 nm. Also, there is a notable red emission peak at 670 nm when the ions migrate from level $^4F_{9/2}$ to level $^4I_{15/2}$. The two partial bands near 672 nm are related to the split of the $^4F_{9/2}$ energy level by the crystal field that occurs due to the action of upconversion luminescence. Considering this, the collected UCL spectra of the prepared ceramic show a fair degree of consistency with previously published results [25,26]. The changing UCL intensity as a function of dopants is illustrated in Fig. 4(b). Initially, there is a rise in UCL intensity, and after reaching critical intensity at $y = 0.10$, it degrades with further insertion of dopants. This results from the concentration quenching effect, which occurs when dopant ions are so near to one another that energy transfer becomes easier, resulting in non-radiative emissions [1,21]. Furthermore, the distances between dopant ions may be calculated using the Blasse formula, as shown in Eq. (2) [23].

$$R_c \approx 2\left[\frac{3V}{4\pi X_c Z}\right]^{\frac{1}{3}} \quad (2)$$

Here, the amount for quenching is X_c ($0.04+y$), where V = 790.58 cm^3 is the volume of a unit cell in $BaBi_2Nb_2O_9$ ferroelectric ceramic, and Z = 4 shows the number of host cations. The R_c was calculated to be 13.92 Å. It was observed that in the absence of Yb^{3+} ions, the R_c value is 21.12 Å, whereas the R_c value is reduced in the presence of Yb^{3+} ions. This implies that the energy is efficiently transferring from Yb^{3+} to Er^{3+} ions. Notably, the upconversion emission process is often characterized by three processes, including ET (energy transfer), ESA (excited state absorption), and GSA (ground state absorption), along with CR and MPR (cross-relaxation processes and multi-phonon relaxation) [27–29]. In Fig. 4(c), the schematic diagram of upconversion luminescence is portrayed using these processes. The 980 nm laser is illuminated on Yb^{3+} ions, and it absorbs energy via GSA and transfers it to a higher level at $^4I_{11/2}$ via ET1 and $^4F_{7/2}$ through ET2. The Er^{3+} ions may also absorb photons through GSA. Thus, level $^4I_{11/2}$ is prepared for the ESA to reach a higher energy level, i.e., $^4F_{7/2}$. Thus, level $^4F_{7/2}$ is overpopulated by two processes, namely ET and ESA. The ions fall non-radiatively to levels $^2I_{11/2}$, $^4S_{3/2}$, and $^4F_{9/2}$ via MPR. From these levels, the ions transit to the lower level $^4F_{15/2}$, resulting in two green emission bands and one red emission band at 535 nm, 557 nm, and 672 nm, respectively. Another decay channel created by the cross-relaxation tracks (CR1 and CR2) is responsible for the increased red emission when the Yb^{3+} content increases. Besides, emission spectrum data from prepared ceramics were used to get the CIE chromaticity coordinates (x, y) for dopant concentrations ($y = 0.02$, 0.04, 0.06, 0.08, 0.10, and 0.12). The predicted CIE points, which are sited in the green region and then become bright green as dopant concentrations rise, are shown in Fig. 4(d).

3.3. Pump power dependency

To learn more about how upconversion luminescence works, we looked at transitions of levels $^2H_{11/2}$, $^4S_{3/2}$, and $^4F_{9/2}$ to level $^4I_{15/2}$ in

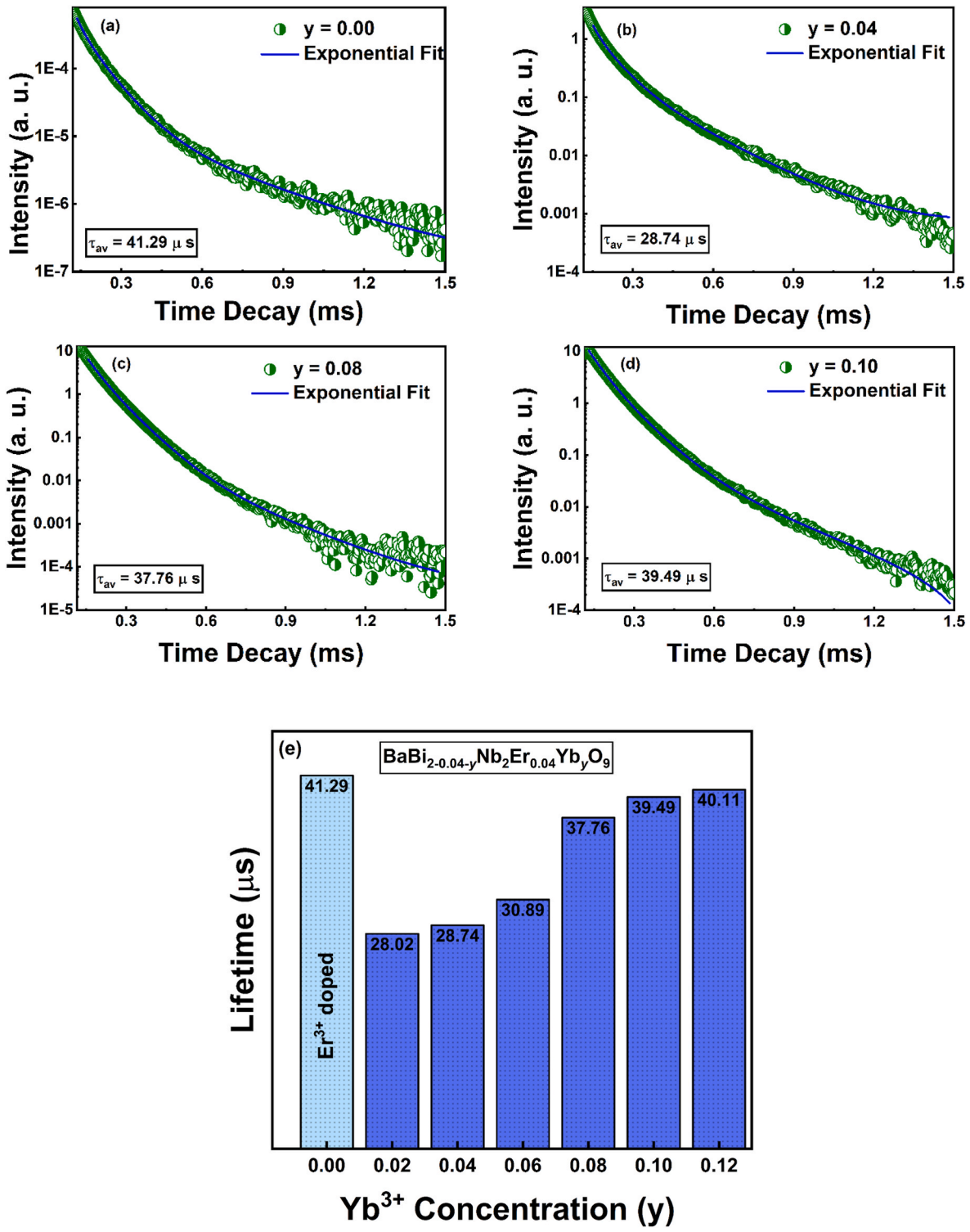

Fig. 6. (a–d) Time decay profile of $BaBi_{2-0.04-y}Nb_2Er_{0.04}Yb_yO_9$ composition for (y = 0.00, 0.04, 0.08, and 0.10) with an exponential fit. (e) Variation of an estimated lifetime of $BaBi_{2-0.04-y}Nb_2Er_{0.04}Yb_yO_9$ ceramic with varying concentrations of Yb^{3+}.

$BaBi_{2-0.04-y}Nb_2Er_{0.04}Yb_yO_9$ (y = 0.10) ceramic at six different pump powers (21, 108, 203, 285, 364, and 453 mW) as displayed in Fig. 5(a). It has been found that the UCL gets stronger as the pump power goes up. The relation between pump power and intensity demonstrates in Eq. (3) [30,31]:

$$I_{UP} \propto P^n \tag{3}$$

where n is the number of low-energy photons required for the UCL to proceed, P is the pump power, and I_{UP} refers to the intensity of UC luminescence. Fig. 5(b) depicts the log-log curve of the intensity vs. the excitation pump power. The magnitude of n for the green band near 535 and 557 nm and the red emissions band at 672 nm may be determined by the slope of the logarithmic plot. These values are 1.46, 1.52, and 1.25, respectively. In this research, the red and green UC bands are produced by the emission of two low-energy photons, which then produce radiation with higher energy that has a wavelength of 535, 557,

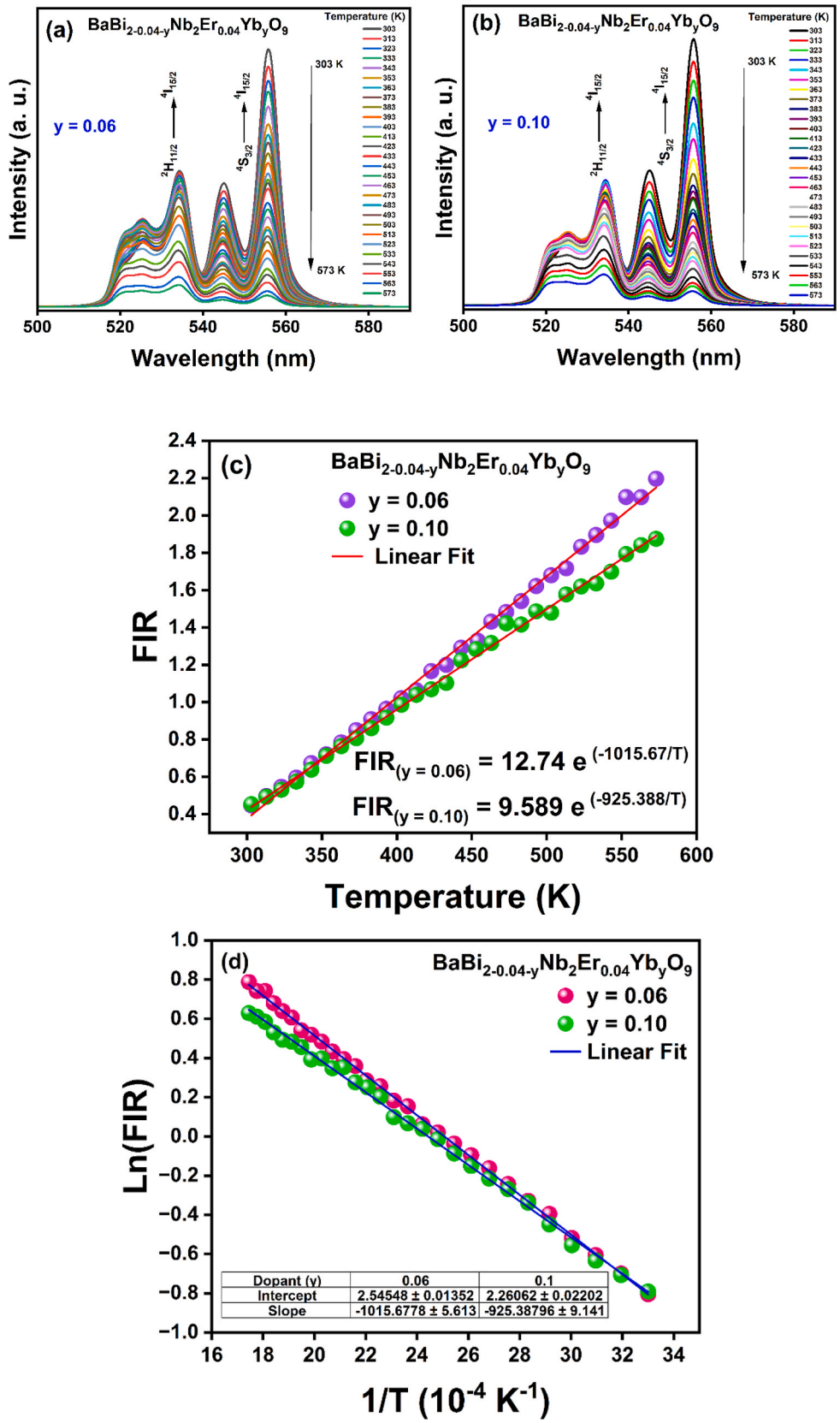

Fig. 7. (a, b) Time-dependent UC emission pattern of $BaBi_{2-0.04-y}Nb_2Er_{0.04}Yb_yO_9$ at $y = 0.06$ and 0.10 in the temperature range 303–573 K, respectively. (c) Evaluation of FIR vs. Temperature at two Yb^{3+} concentrations ($y = 0.06$ and 0.10). (d) The plot of Ln(FIR) with negative temperature for slope and intercept evaluations. (e) PRA values of thermally coupled levels ($^2H_{11/2}$ and $^4S_{3/2}$) at $y = 0.06$ and 0.10. (f) Absolute (S_a) and relative (S_r) sensitivity as a function of temperature for $BaBi_{2-0.04-y}Nb_2Er_{0.04}Yb_yO_9$ ceramic at $y = 0.06$. (g) 0.10 with operating temperature range (shaded region).

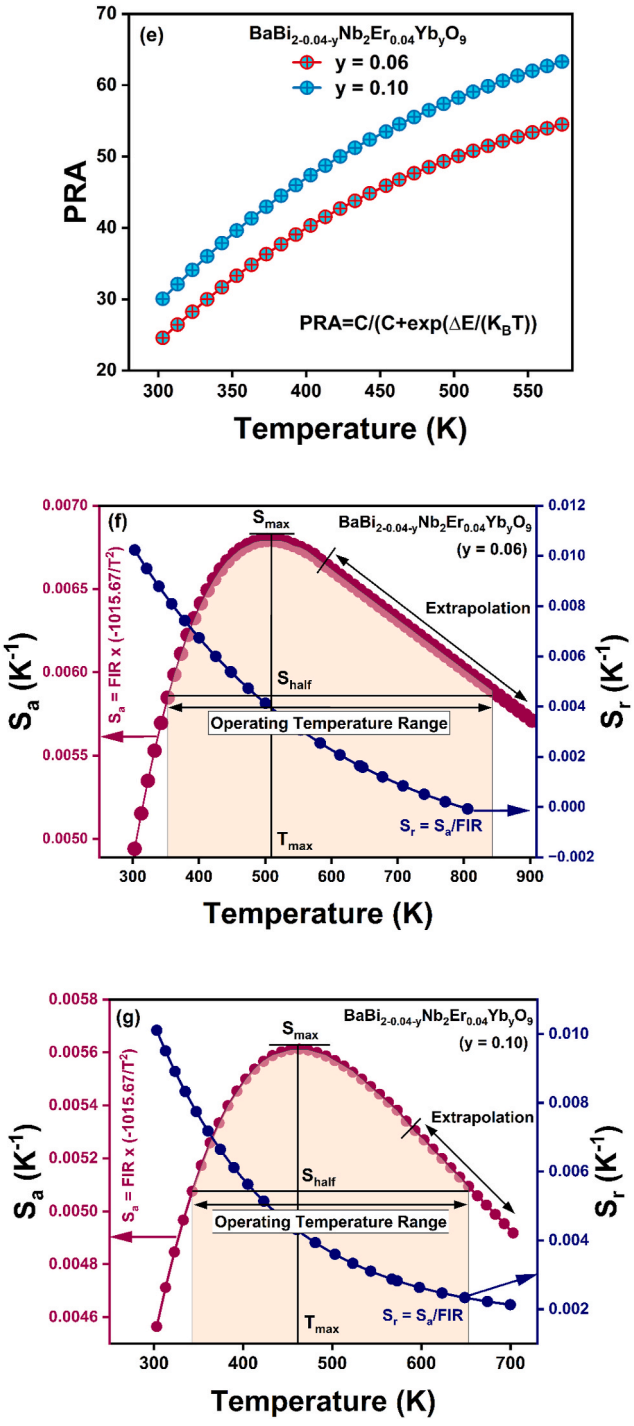

Fig. 7. (*continued*).

and 672 nm. The n values of both colors have been rounded to 2 because various upconversion processes are involved [15,17].

3.4. Time-resolved spectroscopy

A pulsed laser source was used to analyze the lifetime decay of $BaBi_{2-0.04-y}Nb_2Er_{0.04}Yb_yO_9$ ($y = 0.04$, 0.08, 0.10, and 0.12) ceramic for 557 nm transition from $^2S_{3/2}$ to $^4I_{15/2}$ energy level under 980 nm excitation wavelength. Fig. 6(a–d) depicts the decay overview of $BaBi_{2-0.04-y}Nb_2Er_{0.04}Yb_yO_9$ ceramics. The curves were fitted using Eq. (4) (tri exponential decay fit):

$$I(t) = I_0 + A_1 \exp\left(-\frac{t}{\tau_1}\right) + A_2 \exp\left(-\frac{t}{\tau_2}\right) + A_3 \exp\left(-\frac{t}{\tau_3}\right) \quad (4)$$

where I_0 corresponds to the intensity at the time $t = 0$ and A_1, A_2, A_3 are the fitting factors. Also, τ_1, τ_2, and τ_3 are luminescence decay times. The equation used to determine the mean lifespan is shown below in Eq. (5):

$$< \tau >= \frac{A_1\tau_1^2 + A_2\tau_2^2 + A_3\tau_3^2}{A_1\tau_1 + A_2\tau_2 + A_3\tau_3} \quad (5)$$

Fig. 6(e) depicts the predicted lifespan of Er^{3+} doped and Er^{3+}/Yb^{3+} doped $BaBi_{2-0.04-y}Nb_2Er_{0.04}Yb_yO_9$ ceramics. The calculated lifetime of

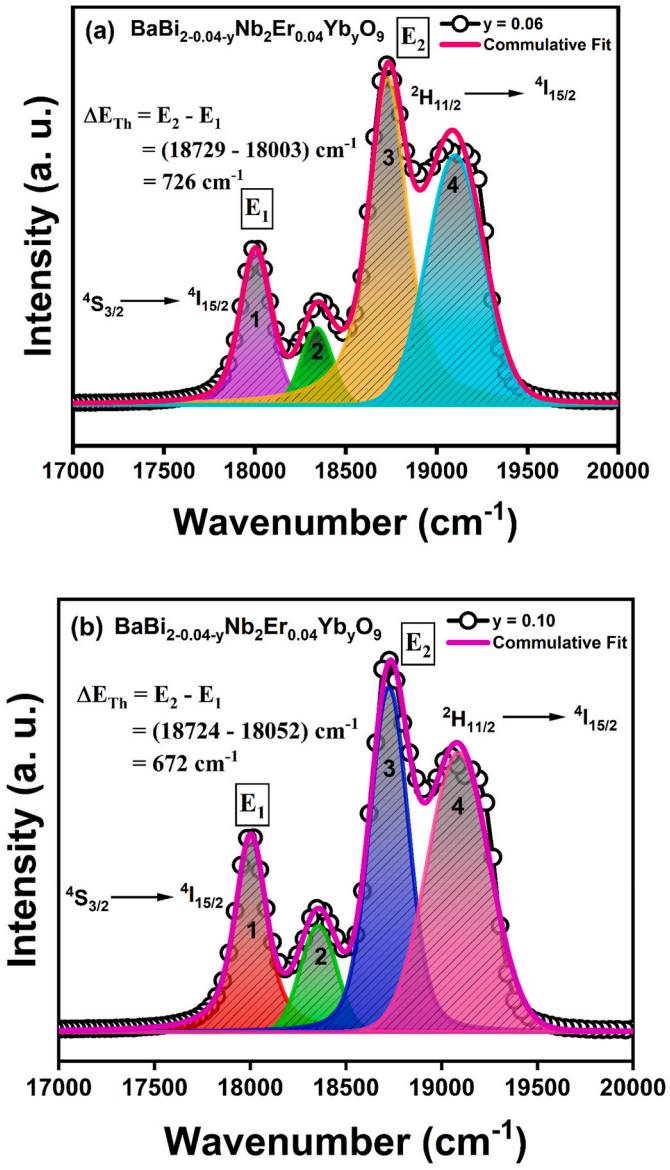

Fig. 8. (a, b) Deconvolution of time-dependent UC spectra by Voigt fit for $BaBi_{2-0.04-y}Nb_2Er_{0.04}Yb_yO_9$ at $y = 0.06$ and 0.10.

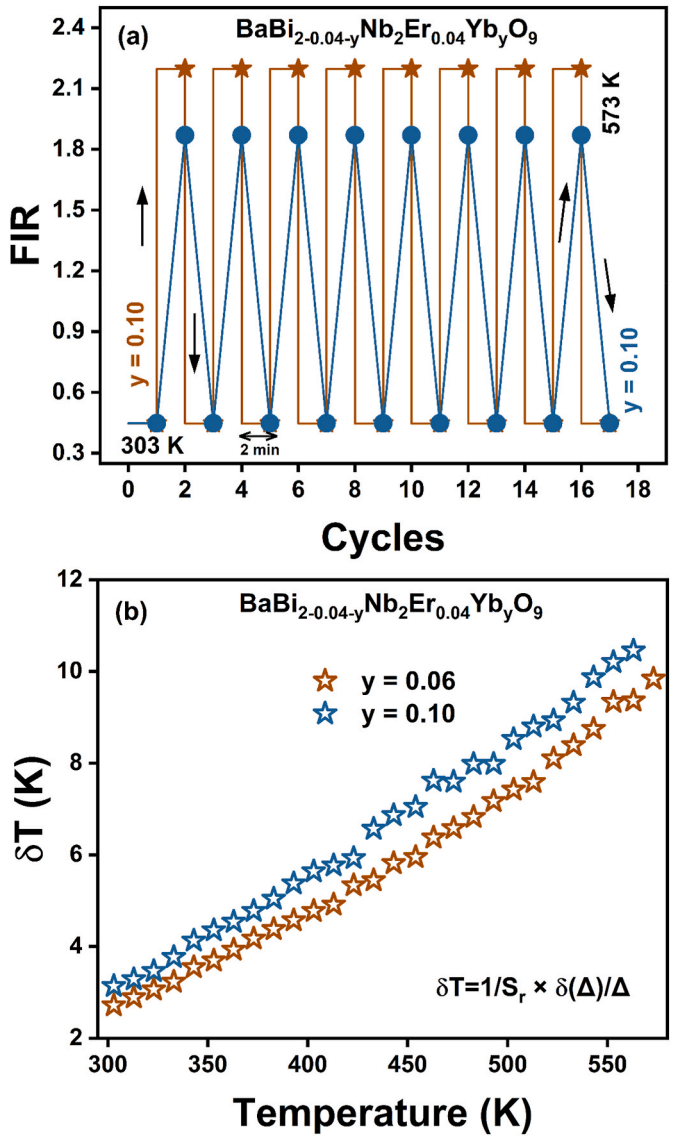

Fig. 9. (a) Reliablity test of $BaBi_{2-0.04-y}Nb_2Er_{0.04}Yb_yO_9$ ceramic in the temperature range (303–573 K) with a stabilization period of 2 min. (b) Resolution of temperature between 303 K and 573 K.

$BaBi_{2-0.04-y}Nb_2Er_{0.04}Yb_yO_9$ ceramic varies from 28.74 μs to 40.11 μs for the co-doped system. An increase in lifespan suggests effective energy transmission in dopant ions, leading to non-radiative transition at a higher doping content [20]. However, the time decay in Er^{3+} doped ceramic is 41.29 μs greater than co-doped ceramic. Thus, the efficiency of energy transfer (ET) in co-doped $BaBi_{2-0.04-y}Nb_2Er_{0.04}Yb_yO_9$ ceramic can be calculated by Eq. (6):

$$\eta = 1 - \frac{\tau_a}{\tau_b} \tag{6}$$

where τ_a is the mean lifetime for Er^{3+}/Yb^{3+} co-doped ceramic and τ_b is the average lifetime for Er^{3+} doped ceramic [20]. The efficiency of the energy transfer process is influenced by 32% by adding Yb^{3+} to the host lattice at a minimum Yb^{3+} concentration.

3.5. Contactless temperature sensing performance

In order to evaluate the possibility of using the present synthesized ceramic in optical temperature measurements, Fluorescence Intensity Ratio (FIR) approach is applied. For non-contact temperature measurements, the FIR is a basic approach that does not depend on variations in excitation intensity. This method was employed widely for temperature sensing in several host materials treated with RE^{3+} [31,32]. We selected the co-doped ceramic compositions with $y = 0.06$ and 0.10 in $BaBi_{2-0.04-y}Nb_2Er_{0.04}Yb_yO_9$ system to investigate the sensing behaviour with varying Yb^{3+} concentrations. This FIR technique compares the UC intensity of two thermocouple energy levels (green emission bands) during transitions $^2H_{11/2}$ to $^4I_{15/2}$ and $^4S_{3/2}$ to $^4I_{15/2}$. Fig. 7(a, b) represents the time-dependent UCL spectra for the $BaBi_{2-0.04-y}Nb_2Er_{0.04-}Yb_yO_9$ ($y = 0.06$ and 0.10) at temperatures ranging from 303 to 573 K. It can be seen that in both the co-doped systems ($y = 0.06$ and 0.10), the UC emission intensity decreases with increasing temperatures. But the FIR values follow the increasing trend, as demonstrated in Fig. 7(c). The mathematical expression of FIR is given by Eq. (7) [33,34]:

$$FIR = \frac{I_H}{I_S} = C \exp\left(-\frac{\Delta E}{K_B T}\right) \tag{7}$$

where I_H and I_S represent the integrated intensity of the green band at 535 nm and 557 nm, respectively, ΔE denotes the energy gap of levels $^4S_{3/2}$ and $^2H_{11/2}$, and C is the constant depending upon the transitions

Table 2
Temperature sensing parameters of various Er^{3+}/Yb^{3+} co-doped host materials in the different temperature ranges.

Host material	ΔE (cm^{-1})	Temperature range (K)	T_a (K)	S_a (K^{-1})	S_r (K^{-1})	T_r (K)	Published year	References
$CaBi_2Ta_2O_9$:Er/Yb	1181	153–603	590	0.39%	–	–	2014	[3]
$Na_{0.5}Er_{0.5}Bi_4Ti_4O_{15}$	500.1	175–500	380	0.17%	–	–	2014	[11]
La_2O_3:Er/Yb	566	303–600	303	0.91%	–	–	2014	[27]
$BaTiO_3$:Er/Yb	600	125–430	410	0.19%	–	–	2015	[2]
$Na_{0.5}Bi_{0.5}TiO_3$:Er/Yb	706.68	173–553	493	0.35%	–	–	2015	[26]
$La_2Ti_2O_7$:Er/Yb	683	93–773	493	0.29%	0.41%	300	2023	[17]
BNT-SBT:Er/Yb	–	303–573	363	0.49%	–	–	2022	[18]
$La_2Ti_2O_7$:Er/Yb	760	333–553	525	0.57%	0.63%	333	2020	[32]
$Na_{0.5}Bi_{2.5}Ta_2O_9$: Er/Yb	–	153–483	483	0.78%	5.99%	153	2023	[31]
$Sr_{0.75}Ba_{0.25}Nb_2O_6$: Er/Yb	–	310–470	410	0.54%	0.85%	310	2023	[37]
$(Bi_{0.5}Er_{0.1}Yb_{0.4})Ta_7O_{19}$	660.65	303–693	475	0.162%	1.04%	303	2021	[38]
$BaGd_2O_4$:Er/Yb	873.94	298–573	573	0.42%	–	–	2023	[32]
$Ba_2NaNb_5O_{15}$:Er/Yb	735.5	298–573	373	0.68%	0.90%	298	2022	[15]
$BaBi_{2-0.04-y}Nb_2Er_{0.04}Yb_yO_9$ ($y = 0.06$)	705	303–573	523	0.69%	1.10%	303	–	**This work**
$BaBi_{2-0.04-y}Nb_2Er_{0.04}Yb_yO_9$ ($y = 0.10$)	645	303–573	463	0.58%	1.01%	303	–	**This work**

and degeneracy factor of thermally coupled levels (TCLs). To calculate constant (C) and energy gap (ΔE), Eq. (7) can be put in linear form, as shown in Eq. (8):

$$\mathrm{Ln(FIR)} = -\left(\frac{\Delta E}{K_B}\right)\left(\frac{1}{T}\right) + \mathrm{LnC} \tag{8}$$

The curve of ln(FIR) and the negative of temperature are illustrated in Fig. 7(d). The slope of this graph analyzes the value of $\Delta E/K_B$ and the ln C intercept. For $y = 0.06$ and 0.10, $\Delta E/K_B$ is −1015.67 and −925.38, while C is 2.545 and 2.260, respectively. These FIR characteristics define the optical thermometric sensitivity of the fabricated ceramic $BaBi_{2-0.04-y}Nb_2Er_{0.04}Yb_yO_9$. The external temperature influences the population redistribution ability (PRA) of thermally coupled levels $^4S_{3/2}$ and $^2H_{11/2}$ and can be expressed by Eq. (9) [18]:

$$\mathrm{PRA} = \frac{C}{C + \exp\left(\frac{\Delta E}{K_B T}\right)} \tag{9}$$

The PRA values for $BaBi_{2-0.04-y}Nb_2Er_{0.04}Yb_yO_9$ ($y = 0.06$ and 0.10) ceramics are given in Fig. 7(e). It seems that the population of these thermally coupled levels increases with temperature. The absolute sensitivity (S_a) of a material is defined by Eq. (10) as the variation rate of FIR with temperature [18].

$$S_a = \frac{d(\mathrm{FIR})}{dT} = \frac{d\left(C\exp\left(-\frac{\Delta E}{K_B T}\right)\right)}{dT} = C\exp\left(-\frac{\Delta E}{K_B T}\right)\left(\frac{\Delta E}{K_B T^2}\right) \tag{10}$$

By multiplying the absolute sensitivity by the negative FIR, we get the relative sensitivity (S_r), employed by Eq. (11) [35]:

$$S_r = \frac{1}{\mathrm{FIR}} * S_a = \left(\frac{\Delta E}{K_B T^2}\right) \tag{11}$$

The S_a and S_r for $BaBi_{2-0.04-y}Nb_2Er_{0.04}Yb_yO_9$ ($y = 0.06$ and 0.10) are displayed in Fig. 7(f, g). In both cases, the absolute sensitivity increases with temperature up to the maximum T_a. For $y = 0.06$ and 0.10, S_a is 0.69% K^{-1} and 0.58% K^{-1} at T_a 523 K and 463 K, respectively. To check the operating temperature range for sensing application (denoted by the shaded region in Fig. 7(f, g)), the S_a values are extrapolated using Eq. (9), where the S_a is higher than half of its maximum value (S_{half}). It has been found that the sensitivity of lower dopant concentrations ($y = 0.06$) shows higher sensitivity than the optimal dopant concentrations ($y = 0.10$), and also the extrapolated data reveals the gradual decrease in the case of $y = 0.06$ whereas, in $y = 0.10$ the absolute sensitivity decreases exponentially. The operational temperature region is extended to a wider temperature range in $y = 0.06$ compared to $y = 0.10$, as shown in Fig. 7(f, g). These observations suggest that the sensing characteristics of the $BaBi_{2-0.04-y}Nb_2Er_{0.04}Yb_yO_9$ ceramic can be tuned by altering the dopant concentration. The material sensitivity is suitable if the theoretically calculated ΔE_{th} and the experimentally matched ΔE_{ex} are substantially comparable. The experimental value for ΔE_{ex} may be derived from Fig. 7(d), and the deconvolution of UC spectra using the Voigt fit yields the theoretical value for ΔE_{th}, shown in Fig. 8(a, b). According to Eq. (12), the inaccuracy (δ) in $BaBi_{2-0.04-y}Nb_2Er_{0.04}Yb_yO_9$ ceramic at $y = 0.06$ and 0.10 equals 2.89% and 4.01%, respectively.

$$\delta = \frac{|\Delta E_{th} - \Delta E_{ex}|}{\Delta E_{th}} * 100\% \tag{12}$$

A sensor's repeatability (R) and resolution (δT) are essential to determine its efficacy. The mathematical expression of these parameters is stated in Eqs. (13) and (14) [36]:

$$R = 1 - \frac{\max\left(\Delta_{Av} - \Delta_{Sp}\right)}{\Delta_{Av}} \tag{13}$$

$$\delta T = \frac{1}{S_r} \times \frac{\delta_\Delta}{\Delta} \tag{14}$$

where δ_Δ/Δ is the device's precision, Δ_{Av} and Δ_{Sp} are the mean and specific parameters of FIR with 17 cycles within temperature 303–573 K. The repeatability and resolution of the produced ceramic are shown in Fig. 9(a, b), respectively. Fig. 9(a) displays no discernible shift in the FIR values of both concentrations anywhere in the temperature range from 303 K to 573 K. In Fig. 9(b), the resolution improves from 2.74 to 9.72 and 3.13 to 10.45 for $y = 0.06$ and 0.10, respectively. Table 2 compares the sensitivity of prepared $BaBi_{2-0.04-y}Nb_2Er_{0.04}Yb_yO_9$ ceramic to that of currently published Er^{3+}/Yb^{3+}-codoped host materials. Our work demonstrates the ability of non-contact temperature sensors to function throughout a broad and high-temperature range, with a maximum temperature of 523 K, while maintaining excellent sensitivity. Consequently, we may conclude that the ceramic $BaBi_{2-0.04-y}Nb_2Er_{0.04}Yb_yO_9$ is a competent sensor material that has the potential to be further investigated for use in the applications area of optical temperature sensors.

4. Conclusion

The co-doped Er^{3+}/Yb^{3+} ferroelectric ceramic $BaBi_{2-0.04-y}Nb_2Er_{0.04}Yb_yO_9$ ($y = 0.00$, 0.02, 0.04, 0.06, 0.08, 0.10, and 0.12) is produced by the solid-state reaction technique at 1050 °C have been studied for upconversion luminescence and temperature sensing applications. The XRD investigation confirmed the ceramic's orthorhombic geometry. The microstructure seen by SEM resembles plate-like formations and comprises non-uniform grains with irregular orientation. An increase in grain size with Yb^{3+} content up to $y = 0.10$ was found to promote upconversion luminescence. Two bright green bands at 535 and 557 nm and a detectable red spectrum nearby 672 nm were observed in upconversion luminescence (UCL) spectra, corresponding to an excitation wavelength of 980 nm. The effective energy transfer process from Yb^{3+} to Er^{3+} ions is supported by decay time measurements, which

increases with increasing Er^{3+}/Yb^{3+} content because of the non-radiative transition at higher doping concentration. The pump power dependence upon the UC luminescence intensity for an optimum Yb^{3+} content $y = 0.10$ reveals that green and red UC emissions involve two photons. Er^{3+}/Yb^{3+} co-doped $BaBi_{2-0.04-y}Nb_2Er_{0.04}Yb_yO_9$ ceramic system with y = 0.06 and 0.10 exhibit a maximum absolute sensitivity (S_a) of 0.69% K^{-1} and 0.58% K^{-1} at $T_a = 523$ K and 463 K, respectively, and maximum relative sensitivity (S_r) of 1.10% and 1.01% at $T_r = 303$ K, suggesting a viable contactless temperature sensor with tunable sensitivity.

Author statement

We the undersigned declare that this manuscript is original, has not been published before and is not currently being considered for publication elsewhere. We confirm that the manuscript has been read and approved by all named authors and that there are no other persons who satisfied the criteria for authorship but are not listed. We further confirm that the order of authors listed in the manuscript has been approved by all of us.

We understand that the Corresponding Author is the sole contact for the Editorial process. He/she is responsible for communicating with the other authors about progress, submissions of revisions and final approval of proofs.

Declaration of competing interest

The authors declare that they have no known competing financial interests or personal relationships that could have appeared to influence the work reported in this paper.

Data availability

Data will be made available on request.

Acknowledgment

The authors would like to thank the Department of Applied Physics at Delhi Technological University for making all of the necessary resources and facilities available to carry out this study. One of the authors, AB, is thankful to CSIR-HRDG file no. 08/0133(15560)/2022-EMR-I for providing financial support.

References

[1] Z. Tianmin, Z. Yanqiu, W. Zhongli, C. Baojiu, Concentration effect and temperature quenching of upconversion luminescence in $BaGd_2ZnO_5:Er^{3+}/Yb^{3+}$ phosphor, J. Rare Earths 33 (7) (2015) 686, https://doi.org/10.1016/S1002-0721(14)60471-3.

[2] M.K. Mahata, T. Koppe, T. Mondal, C.B. Sewitz, K. Kumar, V.K. Rai, H. Hofsass, U. Vetter, Incorporation of Zn^{2+} ions into $BaTiO_3:Er^{3+}/Yb^{3+}$ nanophosphor: an effective way to enhance upconversion, defect luminescence, and temperature sensing, Phys. Chem. Chem. Phys. 17 (2015) 20741–20753, https://doi.org/10.1039/c5cp01874a.

[3] Q. Cao, D. Peng, H. Zou, J. Li, X. Wang, X. Yao, Up-conversion luminescence of Er^{3+} and Yb^{3+} co-doped $CaBi_2Ta_2O_9$ multifunctional ferroelectrics, J. Adv. Dielectr. 4 (3) (2014), 1450018, https://doi.org/10.1142/s2010135x14500180.

[4] V. Lojpur, G. Nikoli, M.D. Dramianin, Luminescence thermometry below room temperature via up-conversion emission of $Y_2O_3:Yb^{3+}$, Er^{3+} nanophosphors, J. Appl. Phys. 115 (2014), 203106, https://doi.org/10.1063/1.4880158.

[5] R. Bokolia, O.P. Thakur, V.K. Rai, S.K. Sharma, K. Sreenivas, Electrical properties and light up conversion effects in $Bi_{3.79}Er_{0.03}Yb_{0.18}Ti_{3x}W_xO_{12}$ ferroelectric ceramic, Ceram. Int. 42 (2016) 5718–5730, https://doi.org/10.1016/j.ceramint.2015.12.103.

[6] R.D. Shannon, Revised effective ionic radii and systematic studies of interatomic distances in halides and chalcogenides, J. Acta Cryst. A32 (2016) 751–767, https://doi.org/10.1107/S0567739476001551.

[7] C. Kornphom, K. Saenkam, T. Bongkarn, Enhanced energy storage properties of BNT–ST-AN relaxor ferroelectric ceramics fabrication by the solid-state combustion technique, Phys. Status Solidi A (2022), 2200240, https://doi.org/10.1002/pssa.202200240.

[8] M.X. Façanha, J.P.C. do Nascimento, M.A.S. Silva, M.C.C. Filho, A.N. L Marques, A. G. Pinheiro, A.S.B. Sombra, Up-conversion emission of Er^{3+}/Yb^{3+} co-doped $BaBi_2Nb_2O_9$ (BBN) phosphors, J. Lumin. 183 (2017) 102–107, https://doi.org/10.1016/j.jlumin.2016.08.011.

[9] T. Wei, C.Z. Zhao, Q.J. Zhou, Z.P. Li, Y.Q. Wang, L.S. Zhang, Bright green upconversion emission and enhanced ferroelectric polarization in $Sr_{1-1.5x}Er_xBi_2Nb_2O_9$, Opt. Mater. 36 (7) (2014) 1209–1212, https://doi.org/10.1016/j.optmat.2014.03.001.

[10] Z. Yao, R. Chu, Z. Xu, J. Hao, W. Li, G. Li, Processing and enhanced electrical properties of $Sr_{1-x}(K_{0.5}Bi_{0.5})_xBi_2Nb_2O_9$ lead-free piezoelectric ceramics, Ceram. Int. 42 (9) (2016) 10619–10623, https://doi.org/10.1016/j.ceramint.2016.03.156.

[11] X. Hui, D. Peng, H. Zou, J. Li, Q. Cao, Y. Li, X. Wang, X. Yao, A new multifunctional Aurivillius oxide $Na_{0.5}Er_{0.5}Bi_4Ti_4O_{15}$: up-conversion luminescent, dielectric, and piezoelectric properties, Ceram. Int. 40 (4A) (2014) 12477–12483, https://doi.org/10.1016/j.ceramint.2014.04.102.

[12] A. Banwal, R. Bokolia, Phase evolution and microstructure of $BaBi_2Nb_2O_9$ ferroelectric ceramics, Mater. Today Proc. 46 (20) (2021) 10121–10124, https://doi.org/10.1016/j.matpr.2020.09.380.

[13] Z. Chen, L. Sheng, X. Li, P. Zheng, W. Bai, L. Li, F. Wen, W. Wu, L. Zheng, J. Cui, Enhanced piezoelectric properties and electrical resistivity in W/Cr co-doped $CaBi_2Nb_2O_9$ high-temperature piezoelectric ceramics, Ceram. Int. 45 (5) (2019) 6004–6011, https://doi.org/10.1016/j.ceramint.2018.11.252.

[14] A. Banwal, R. Bokolia, Effect of Er^{3+} ion doping on structural, ferroelectric and up/down conversion luminescence in $BaBi_2Nb_2O_9$ ceramic, Mater. Today Proc. (2021) 3, https://doi.org/10.1016/j.matpr.2021.05.545. –6.

[15] F. Luo, J. Xing, Y. Qin, Y. Zhong, F. Shang, G. Chen, Up-conversion luminescence, temperature sensitive and energy storage performance of lead-free transparent Yb^{3+}/Er^{3+} co-doped $Ba_2NaNb_5O_{15}$ glass-ceramics, J. Alloys Compd. 910 (2022), 164859, https://doi.org/10.1016/j.jallcom.2022.164859.

[16] A. Pandey, S. Som, V. Kumar, V. Kumar, K. Kumar, V.K. Rai, H.C. Swart, Enhanced upconversion and temperature sensing study of Er^{3+}–Yb^{3+} co-doped tungsten–tellurite glass, Sensor. Actuator. B Chem. 202 (2014) 1305–1312, https://doi.org/10.1016/j.snb.2014.06.074.

[17] R. Swami, A. Shandilya, A.K. Shukla, P.S. Kumar, K. Sreenivas, Luminescence intensity ratio based wide range contactless temperature sensing properties of Er3+/Yb3+ ions co-doped La2Ti2O7 ceramics, J. Alloys Compd. 948 (2023), 169610, https://doi.org/10.1016/j.jallcom.2023.169610.

[18] P. Wang, X. Wang, G. Li, Y. Li, X. Yao, Z. Pan, Energy density capability and upconversion luminescence in Er^{3+}/Yb^{3+}-codoping BNT-based ferroelectric thin films, Ceram. Int. 48 (19) (2022) 28606–28613, https://doi.org/10.1016/j.ceramint.2022.06.174.

[19] X. Liu, G. Hu, H. Wu, S. Shi, H. Wang, J. Xu, L. Yang, W. Qiu, Transmittance, photoluminescence and electrical properties in Er-doped $0.98K_{0.5}Na_{0.5}NbO_3$-$0.02Sr(Yb_{0.5}Ta_{0.5})O_3$ ferroelectric ceramics, J. Electron. Mater. 51 (2022) 3476–3484, https://doi.org/10.1007/s11664-022-09626-3.

[20] A. Banwal, R. Bokolia, Enhanced upconversion luminescence and optical temperature sensing performance in Er^{3+} doped $BaBi_2Nb_2O_9$ ferroelectric ceramic, Ceram. Int. 48 (2) (2022) 2230–2240, https://doi.org/10.1016/j.ceramint.2021.09.314.

[21] R. Bokolia, O.P. Thakur, V.K. Rai, S.K. Sharma, K. Sreenivas, Dielectric, ferroelectric and photoluminescence properties of Er^{3+} doped $Bi_4Ti_3O_{12}$ ferroelectric ceramics, Ceram. Int. 41 (4) (2015) 6055–6066, https://doi.org/10.1016/j.ceramint.2015.01.062.

[22] L. Mukhopadhyay, V.K. Rai, R. Bokolia, K. Sreenivas, 980 nm excited $Er^{3+}/Yb^{3+}/Li^{+}/Ba^{2+}$: $NaZnPO_4$ upconverting phosphors in optical thermometry, J. Lumin. 187 (2017) 368–377, https://doi.org/10.1016/j.jlumin.2017.03.035.

[23] A. Banwal, R. Bokolia, Thermometric sensing performance in Erbium modified $SrBi_{2-x}Nb_2Er_xO_9$ ferroelectric ceramic for optoelectronic devices, Ceram. Int. 48 (23A) (2022) 34405–34414, https://doi.org/10.1016/j.ceramint.2022.08.019.

[24] F. Wang, Y. Han, C.S. Lim, Y. Lu, J. Wang, J. Xu, H. Chen, C. Zhang, M. Hong, X. Liu, Simultaneous phase and size control of upconversion nanocrystals through lanthanide doping, Nature 463 (2010) 1061–1065, https://doi.org/10.1038/nature08777.

[25] P. Du, L. Luo, W. Li, Q. Yue, Upconversion emission in Er-doped and Er/Yb-codoped ferroelectric $Na_{0.5}Bi_{0.5}TiO_3$ and its temperature sensing application, J. Appl. Phys. 116 (2014), 014102, https://doi.org/10.1063/1.4886575.

[26] P. Du, J.S. Yun, Effect of molybdenum on upconversion emission and temperature sensing properties in $Na_{0.5}Bi_{0.5}TiO_3$: Er/Yb ceramics, Ceram. Int. 41 (2015) 6710–6714, https://doi.org/10.1016/j.ceramint.2015.01.113.

[27] R. Dey, V.K. Rai, Yb^{3+} sensitized Er^{3+} doped La_2O_3 phosphor in temperature sensors and display devices, J Dalton Trans 43 (2014) 111, https://doi.org/10.1039/c3dt51773j.

[28] P. Du, L. Luo, W. Li, Upconversion emission in Er-doped and Er/Yb-codoped ferroelectric $Na_{0.5}Bi_{0.5}TiO_3$ and its temperature sensing application, J. Appl. Phys. 116 (2014), 014102, https://doi.org/10.1063/1.4886575.

[29] J. Shi, J. Suna, B. Fanga, Q. Dua, S. Zhanga, J. Ding, Photoluminescence performance of Er/Yb co-doped NBT ceramics prepared via hydrothermal method, J. Phys. Chems. 121 (2018) 228–235, https://doi.org/10.1016/j.jpcs.2018.05.031.

[30] R. Bokolia, M. Mondal, V.K. Rai, K. Sreenivas, Enhanced infrared-to-visible up-conversion emission and temperature sensitivity in (Er^{3+}, Yb^{3+}, and W^{6+}) tri-doped $Bi_4Ti_3O_{12}$ ferroelectric oxide, J. Appl. Phys. 121 (8) (2017), https://doi.org/10.1063/1.4977006.

[31] P. Li, Z. Zhang, Z. Xu, H. Sun, Q. Zhang, X. Hao, Photomodulated cryogenic temperature sensing through a photochromic reaction in $Na_{0.5}Bi_{2.5}Ta_2O_9$: Er/Yb multicolour upconversion, Opt Express 31 (5) (2023) 7047–7059, https://doi.org/10.1364/OE.469538.

[32] Y. Liu, G. Bai, E. Pan, Y. Hua, L. Chen, S. Xu, Upconversion fluorescence property of Er^{3+}/Yb^{3+} co-doped lanthanum titanate microcrystals for optical thermometry, J. Alloys Compd. 822 (2014), 153449, https://doi.org/10.1016/j.jallcom.2019.153449.

[33] Z. Guan, X. Li, R. Shen, Z. Tian, H. Yu, Y. Cao, Y. Wang, J. Zhang, S. Xu, B. Chen, Intense red up-conversion luminescence and temperature sensing property of Yb^{3+}/Er^{3+} co-doped $BaGd_2O_4$ phosphors, Spectrochim. Acta Mol. Biomol. Spectrosc. 284 (2023), 121805, https://doi.org/10.1016/j.saa.2022.121805.

[34] P. Du, L. Luo, W. Li, Q. Yue, Upconversion emission in Er-doped and Er/Yb-codoped ferroelectric $Na_{0.5}Bi_{0.5}TiO_3$ and its temperature sensing application, J. Appl. Phys. 116 (2014), 014102, https://doi.org/10.1063/1.4886575.

[35] J. Xing, F. Shang, G. Chen, Upconversion luminescence of Yb^{3+}/Er^{3+} co-doped $NaSrPO_4$ glass ceramic for optical thermometry, Ceram. Int. 147 (2021) 8330–8337, https://doi.org/10.1016/j.ceramint.2020.11.195.

[36] M.D. Dramićanin, Trends in luminescence thermometry, J. Appl. Phys. 128 (2020), 040902, https://doi.org/10.1063/5.0014825.

[37] J. Song, F. Luo, G. Chen, A new photoelectric niobate glass ceramic material: up-conversion optical thermometry and dielectric energy storage, Ceram. Int. (2023), https://doi.org/10.1016/j.ceramint.2023.05.281.

[38] H. Cui, Y. Cao, Y. Zhang, L. Cao, S. Ran, X. Wang, D. Wu, X. Li, X. Zhang, Baojiu Chen, Extremely intense green up-conversion luminescent and ultra-high temperature sensitivity in Er^{3+}/Yb^{3+} co-doped $BiTa_7O_{19}$ phosphors, J. Lumin. 241 (2022), 118484, https://doi.org/10.1016/j.jlumin.2021.118484.

Applied Physics A (2024) 130:334
https://doi.org/10.1007/s00339-024-07475-x

Applied Physics A
Materials Science & Processing

Temperature stability and improved energy storage efficiency of $BaBi_2Nb_2O_9$: Er^{3+}/Yb^{3+} relaxor ferroelectric ceramic under moderate electric fields

Ankita Banwal[1] · Manoj Verma[2] · Bharti Singh[1] · Renuka Bokolia[1]

Received: 17 December 2023 / Accepted: 24 March 2024 / Published online: 23 April 2024

Abstract
In this paper, undoped $BaBi_{2-x-y}Nb_2Er_xYb_yO_9$ (BBN), Er^{3+} doped BBN, and a series of Er^{3+}/Yb^{3+} co-doped BBN ferroelectric ceramic is synthesized by the solid-state method to study the structural, dielectric, ferroelectric, and energy storage behavior of the prepared ceramic. XRD spectra revealed orthorhombic geometry and Fmmm phase group of each prepared ceramic. SEM micrograph shows dense microstructures similar to square-shaped structures. Two FTIR bands at 619 and 822 cm^{-1} are observed, displaying the characteristic peaks of the Aurivillius phase. Four Raman bands are detected for undoped BBN, while twelve are visible in Er^{3+}/Yb^{3+} doped BBN compositions. Further, this work utilizes a comparable method to correlate Nb–O stretching frequencies with their corresponding bond lengths using Herschbach's exponential function. Temperature-dependent dielectric studies show considerable dispersion below and above maximum temperature (T_m), and the dielectric constant (ε') decreases with an increase in frequency. The dielectric loss (ε'') curves are quite diffused, and shifts in the maxima with frequency have been observed, thus validating the relaxor behavior of all the prepared BBN compositions. The slimmer PE curves were obtained under moderate electric fields ranging from 75 to 100 kV/cm. The energy storage parameters (W, W_{rec}, η) are improved with increasing applied electric field. The energy storage efficiency (η) obtained for undoped, Er^{3+} doped, and Er^{3+}/Yb^{3+} co-doped BBN ceramics are 78.25%, 83.39%, and 90.87%, respectively. The energy storage parameters revealed good temperature stability from 303 to 415 K, indicating that the synthesized material might aid in developing modern electronic equipment for energy storage applications.

Keywords Raman spectra · PE loops · Relaxor · Ceramic · Slim loops · Energy storage density

1 Introduction

Numerous applications, including mobile electronics, electric vehicles, and intermittent power technologies, immediately need high-energy storage materials. Ferroelectric ceramics based on lead, such as lead zirconate titanate and lead titanate, are well recognized for their piezoelectric properties and find widespread application in the fields of sensing, actuator, detector, and energy storage applications [1–3]. Peng et al. obtained a noticeable energy storage density in the $Pb_{0.8}Ba_{0.2}ZrO_3$ thin film. Even though lead-based materials are good at storing energy, they also cause a lot of damage to the planet when they disintegrate [4]. To achieve good energy storage in ferroelectrics, the following things should be checked: larger maximum polarization (P_m), lesser remnant polarization (P_r), and higher breakdown strength (BDS). Investigations are being conducted on alternative lead-free formulations, including barium titanate, bismuth perovskites, alkaline niobates, bismuth layered structured ferroelectrics (BLSFs), etc. [5–8]. The basic ferroelectric materials have larger P_m and P_r [9]. However, a relaxor ferroelectric has larger P_m and lesser P_r; consequently, we chose $BaBi_2Nb_2O_9$ relaxor ferroelectric, also a BLSF. BLSFs are advantageous substitutes for lead-based ceramics due to their non-toxic nature and ecologically beneficial characteristics, hence establishing their superiority as a replacement choice [10–12]. There is significant attention around lead-free BLSF materials because of their desirable characteristics,

✉ Renuka Bokolia
renukabokolia@dtu.ac.in

[1] CFMRL, Department of Applied Physics, Delhi Technological University, New Delhi, India

[2] Department of Physics, Hindu College, University of Delhi, New Delhi, India

including a low dielectric constant, fatigue-free properties, high transition temperatures, anisotropy in electromechanical coupling factors, and great temperature stability [13–15]. BLSFs have favorable chemical and thermal stability, decent radiative transitions, less phonon energy, and increased sensitivity over a wide temperature range. The BLSF is a unique category of ferroelectric materials that adhere to a defined chemical composition denoted as $(Bi_2O_2)^{2+}$ $(A_{n-1}B_nO_{3n+1})^{2-}$. The quasi-perovskite layer, represented as $A_{n-1}B_nO_{3n+1}$, is encompassed by two layers of bismuth oxide $(Bi_2O_2)^{2+}$. The number of octahedral layers inside the perovskite block is indicated by n. The ions such as Na^+, Ba^{2+}, Bi^{3+}, or Sr^{2+} having single, dual, or triple valance ions are denoted by A, while B signifies ions such as Nb^{5+}, Ta^{5+}, Ti^{4+}, or W^{6+} [16–19].

Literature studies revealed that due to the overconsumption of fossil fuels, there is a demand for developing green and sustainable energy like hydropower, wind or solar power, and many more. However, storing these kinds of energy is also challenging [20, 21]. In the last decade, ferroelectric-based capacitors have been used in energy storage applications because they have a rapid charge rate (less than a microsecond) and more extended charge–discharge periods than conventional cells to produce intense power pulses [22, 23]. In addition, these capacitors exhibit improved energy storage capabilities at higher temperatures. Few investigations have been conducted on using ferroelectric-based materials as energy storage devices. In one study, Huang et al. discussed the consequences of different RE ions on $BaTiO_3$ ceramic to examine its performance in energy storage applications [24]. The energy storage properties of $Ba_{0.5}Na_{0.5}TiO_3$ ceramic doped with $NaNbO_3$ were explored by Wan et al. [25]. Also, in other reports, a relaxor ceramic $Bi_{0.5}Na_{0.5}TiO_3$–$Sr_{0.7}Bi_{0.2}TiO_3$ and $Bi_{0.5}Na_{0.5}TiO_3$–$BaTiO_3$–$SrTi_{0.875}Nb_{0.1}O_3$ were investigated for their potential application in energy storage devices [1, 21]. The aforementioned studies served as a source of inspiration for our investigation into the energy storage potential of $BaBiNb_2O_9$ ceramic material co-doped with Er^{3+}/Yb^{3+}. As far as the author is aware, no previous study has yet been carried out on this material.

In our latest study, we doped $BaBi_2Nb_2O_9$ with Er^{3+}/Yb^{3+} and observed increased upconversion luminescence and decent thermal sensitivity (0.0069 K^{-1}) at 523 K [26]. However, the ferroelectric properties were not discussed, so we co-doped $BaBi_2Nb_2O_9$ with Er^{3+} and Yb^{3+} to investigate the ferroelectric properties. This study aims to check the versatility of the co-doped $BaBi_2Nb_2O_9$ ceramic for energy storage applications. In this paper, the P-E parameters obtained from P-E loops calculate energy density (W), rectifiable energy density (W_{rec}), and efficiency of the energy density (η). Figure 1 depicts the schematic representation of the basic approach to enhance the energy storage parameter.

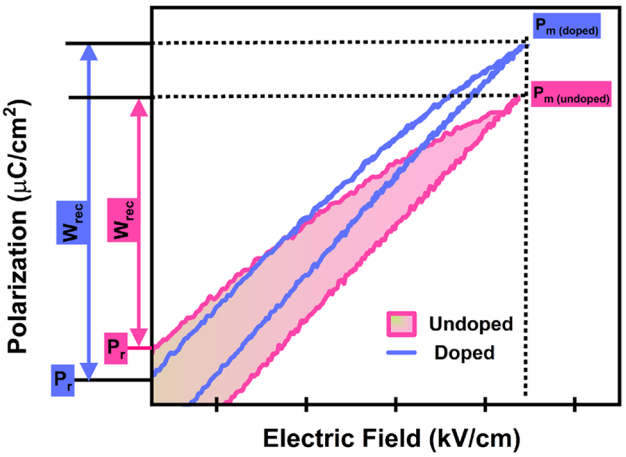

Fig. 1 Diagrammatic illustration of the basic strategy for improving energy storage density parameters

2 Synthesis and characterization description

The solid-state procedure is utilized to prepare the ceramics with the configuration of $BaBi_{2-x-y}Nb_2Er_xYb_yO_9$ (abbreviated BBN) doped with Er^{3+} and Yb^{3+}. The initial precursors ($BaCO_3$, Bi_2O_3, Nb_2O_5, Er_2O_3, and Yb_2O_3) were bought from Sigma Aldrich (99.99%). The raw powders were measured stoichiometrically, followed by mixing in ethanol for 5 h in a mortar pestle before heat treating at 950 °C for 3 h. The high-temperature cured calcined powder was added to the solution of PVA (polyvinyl alcohol) prepared in distilled water. After the complete mixing of PVA, the powder is pressed in circular shaped discs in a manual pelletizer. These pressed pellets (diameter = 10 mm, thickness = 1 mm) were heated at 1050 °C in a high-temperature furnace for a duration of 3 h. For the electrical measurements, these pellets were polished by rubbing with sandpaper to ensure good adhesion of the silver paste. The air-drying silver paste is used to prevent breaking while handling delicate pellets. The polarization against the applied electric field is measured by a high-end automated loop tracer. This measurement was done at room temperature under 20 Hz frequency. The phase of the material was investigated by examining the XRD spectra that use Cu-Kα radiations with a high-quality X-ray diffractometer produced by Bruker. The scanned images of the broken pellets were visualized from Zeiss SEM. The average particle size was measured using software named ImageJ. The Perkin Elmer spectrum-II was used to acquire the FTIR spectra. The Raman spectra were acquired with the Invia Raman spectrometer equipped with a laser source emitting light at a wavelength of 785 nm. The temperature-dependent dielectric studies were performed by an

Table 1 Coding of the prepared co-doped compositions of $BaBi_{2-x-y}Nb_2Er_xYb_yO_9$ ceramic

Compositions	Sample code	Er^{3+} (x)	Yb^{3+} (y)
$BaBi_{2-x-y}Nb_2Er_xYb_yO_9$	BBNE0Y0	0.00	0.00
$BaBi_{1.96}Nb_2Er_{0.04}Yb_{0.00}O_9$	BBNE4Y0	0.04	0.00
$BaBi_{1.94}Nb_2Er_{0.04}Yb_{0.02}O_9$	BBNE4Y2	0.04	0.02
$BaBi_{1.92}Nb_2Er_{0.04}Yb_{0.04}O_9$	BBNE4Y4	0.04	0.04
$BaBi_{1.90}Nb_2Er_{0.04}Yb_{0.06}O_9$	BBNE4Y6	0.04	0.06
$BaBi_{1.88}Nb_2Er_{0.04}Yb_{0.08}O_9$	BBNE4Y8	0.04	0.08
$BaBi_{1.86}Nb_2Er_{0.04}Yb_{0.10}O_9$	BBNE4Y10	0.04	0.10
$BaBi_{1.84}Nb_2Er_{0.04}Yb_{0.12}O_9$	BBNE4Y12	0.04	0.12

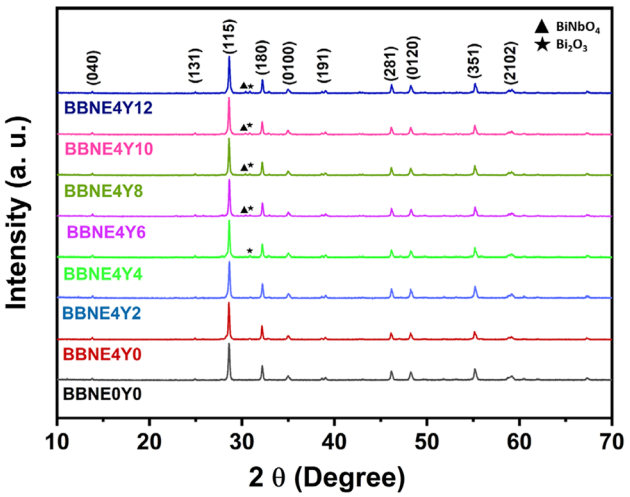

Fig. 2 XRD spectra of all the compositions of doped and undoped BBN ceramics (* depicts Bi_2O_3 and ▲: $BiNbO_4$ phase)

impedance analyzer from Keysight for different frequencies ranging from 1 kHz to 1 MHz. The sample coding for all the Er^{3+}/Yb^{3+} co-doped BBN ceramics is recorded in Table 1.

3 Outcomes and evaluations

3.1 XRD and SEM analysis

The X-ray diffraction profile of sintered Er^{3+}/Yb^{3+} co-doped BBN ceramic is provided in Fig. 2 for all the compositions. The XRD peaks are similar to JCPDF file number 00-012-0403, having orthorhombic geometry and Fmmm phase group. At lower dopant concentrations ($y < 0.04$), the absence of additional peaks in the XRD spectra serves as a confirmation of the complete solubility of the dopant inside the host lattice. However, at higher dopant concentrations ($y \geq 0.04$), there are minor additional peaks, which might be due to unreacted Bi_2O_3 (#00-002-0542) and $BiNbO_4$ (#00-016-0486) (represented by * and ▲). The refinement index and lattice parameters obtained from profile fit between observed and calculated XRD patterns using TOPAS software for all compositions of BBN are reported in Table 2. It can be seen that the goodness of fit (GoF) lies between 1 and 2, which shows the close matching of experimental and theoretical data. Furthermore, it is worth noting that the (115) plane in the BBN ceramic exhibits the most intense peak, which may be attributed to the BLSF of $m = 2$. Based on previous observations, it has been shown that the (112 $m + 1$) plane has a significant correlation with the high-intensity XRD peak in BLSF materials belonging to the Aurivillius phase [27]. The density of the synthesized pellets has been estimated via the Archimedes technique (Table 2). It has been found that the experimental density matches the theoretical density as reported in the JCPDF card with an accuracy of > 95%. The choice of Er^{3+}/Yb^{3+} doping ions to substitute A-site Bi^{3+} ions is based on the fact that doping ions and Bi^{3+} ions have the same charge valency and virtually identical radii [26]. The lattice parameters of doped BBN showed little variation compared to undoped BBN. Nevertheless, Table 2 reveals a slight increase in the cell volume, which can be explained by the $6s^2$ lone pair character of Bi^{3+}

Table 2 Refinement parameters, lattice parameters, experimental density, and grain size of all the compositions of BBN

Samples	Refinement parameters			Lattice parameters						
	R_{exp}	R_p	GoF	a (Å)	b (Å)	c (Å)	V (Å^3)	Orthorhombic distortion (b/a)	Exp. density, ρ (g/cm^3)	Average grain size (μm)
BBNE0Y0	10.76	12.84	1.02	5.5439	5.5536	25.5975	788.111	1.00174	7.00919	1.39 ± 0.0278
BBNE4Y0	11.57	13.59	1.05	5.5441	5.5550	25.5976	788.341	1.00196	6.87240	1.42 ± 0.014
BBNE4Y2	10.39	14.93	1.46	5.5448	5.5551	25.5980	788.467	1.00185	6.83796	1.54 ± 0.0125
BBNE4Y4	10.13	13.53	1.35	5.5450	5.5552	25.5989	788.537	1.00183	6.72015	1.67 ± 0.1365
BBNE4Y6	10.01	14.46	1.44	5.5454	5.5561	25.5991	788.728	1.00192	6.77289	1.78 ± 0.0889
BBNE4Y8	7.07	8.64	1.07	5.5479	5.5601	25.6178	790.229	1.00219	6.47426	1.89 ± 0.1129
BBNE4Y10	7.27	9.19	1.08	5.5488	5.5612	25.6200	790.581	1.00223	6.76007	1.92 ± 0.1761
BBNE4Y12	10.21	14.87	1.45	5.5497	5.5600	25.6219	790.597	1.00185	6.01060	1.45 ± 0.0295

ions. When Bi^{3+} ions are substituted with Er^{3+}/Yb^{3+} ions having smaller ionic radii than Bi^{3+}, the size of Bi^{3+} ions is dependent upon the extent of the $6s^2$ lone-pair character. In our $BaBi_2Nb_2O_9$ system, the volume increases with dopant substitution, possibly due to the constrained character of the $6s^2$ lone pair of Bi^{3+} in the host lattice. The lone-pair nature of Bi^{3+} causes slight distortion in the host lattice, thereby increasing the cell volume [6, 17, 26].

The SEM images of all the prepared compositions of BBN are represented in Fig. 3a–h. The pellets (sintered at 1050 °C) of all the compositions have dense microstructures similar to square-shaped structures. The grains in BLSF materials exhibit non-uniformity and arbitrary orientation that is characteristic of such materials [18, 28]. The grain size was estimated using software named ImageJ. The mean particle size is shown in Table 2. It has been observed that the size increases with dopant concentration up to BBNE4Y10 composition after it decreases. This difference in grain size may be attributed to the increase in the electron charge density on the surface of grains due to increasing dopant concentration, resulting in the slowing down of grain boundary diffusion and the inhibition of grain expansion, causing the reduction of grain size [29, 30].

3.2 IR spectroscopy

The Fourier transform infrared spectra of all the Er^{3+} and Yb^{3+} doped and undoped BBN are depicted in Fig. 4a. A broad and intense band can be seen at 619 and 822 cm^{-1}, which are the distinctive peaks of the Aurivillius phase [28, 31]. The stretching of the NbO_6 bond causes the frequency band at positions 619 and 822 cm^{-1}, and the degree to which this stretching occurs is extremely dependent on dopant concentration. The compositional dependency of dopants on the band positions is seen in Fig. 4b, and curves seem to be shifted towards higher values. The observed frequency shift may be ascribed to changing conditions near the NbO_6 bond. The changing condition near the NbO_6 bond means that the dopant ions affect the lattice structure, and this distortion causes the shifting of the FTIR bands. Therefore, it may be assumed that the FTIR spectra exhibit significant vulnerability to changes in the local structure of the host material by introducing dopants [28].

3.3 Raman spectra analysis

The Raman spectra of undoped and Er^{3+}/Yb^{3+} doped $BaBi_2Nb_2O_9$ ferroelectric ceramics were acquired using a laser source with a wavelength of 785 nm in the frequency range of 100–1000 cm^{-1}. The deconvoluted Raman plot of undoped BBN composition is provided in Fig. 5a. The four major peaks were obtained and positioned at 156 cm^{-1}, 215 cm^{-1}, 550 cm^{-1}, and 854 cm^{-1}. The spectra detected for all the prepared compositions are reported in Fig. 5b. According to the literature survey, there are 12 Raman modes, out of which only four Raman bands (156 cm^{-1}, 215 cm^{-1}, 550 cm^{-1}, and 854 cm^{-1}) are detectable in the

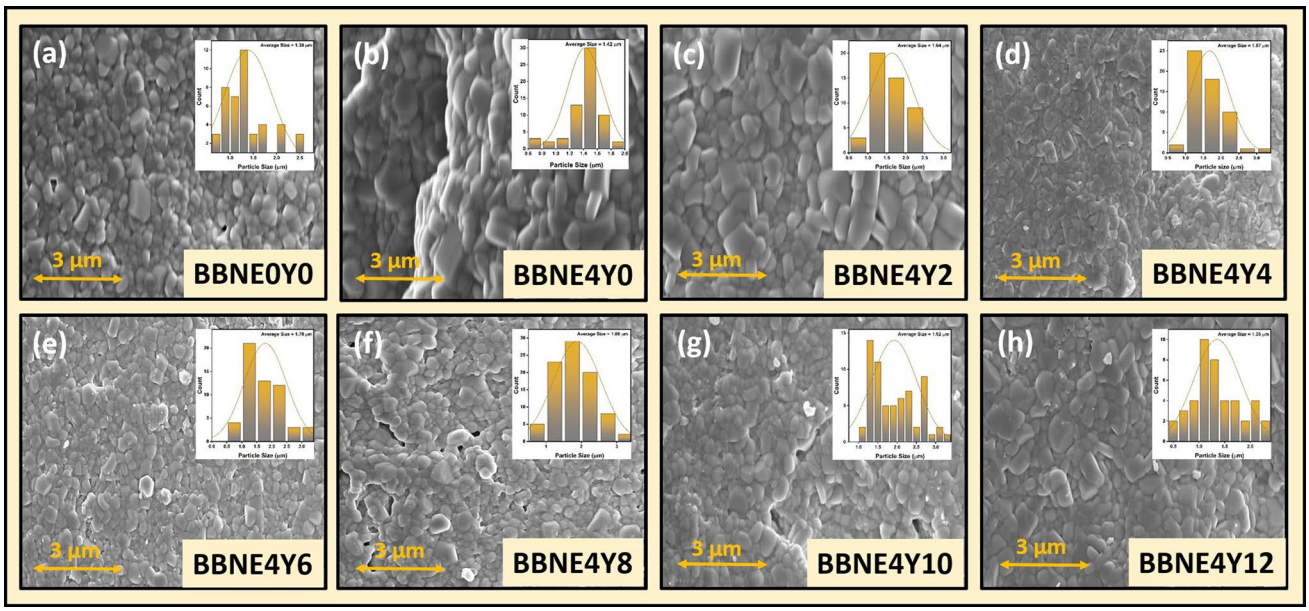

Fig. 3 **a–h** Scanning image micrographs of prepared undoped and doped BBN ceramics (Inset—histogram to evaluate the average grain size of the particle)

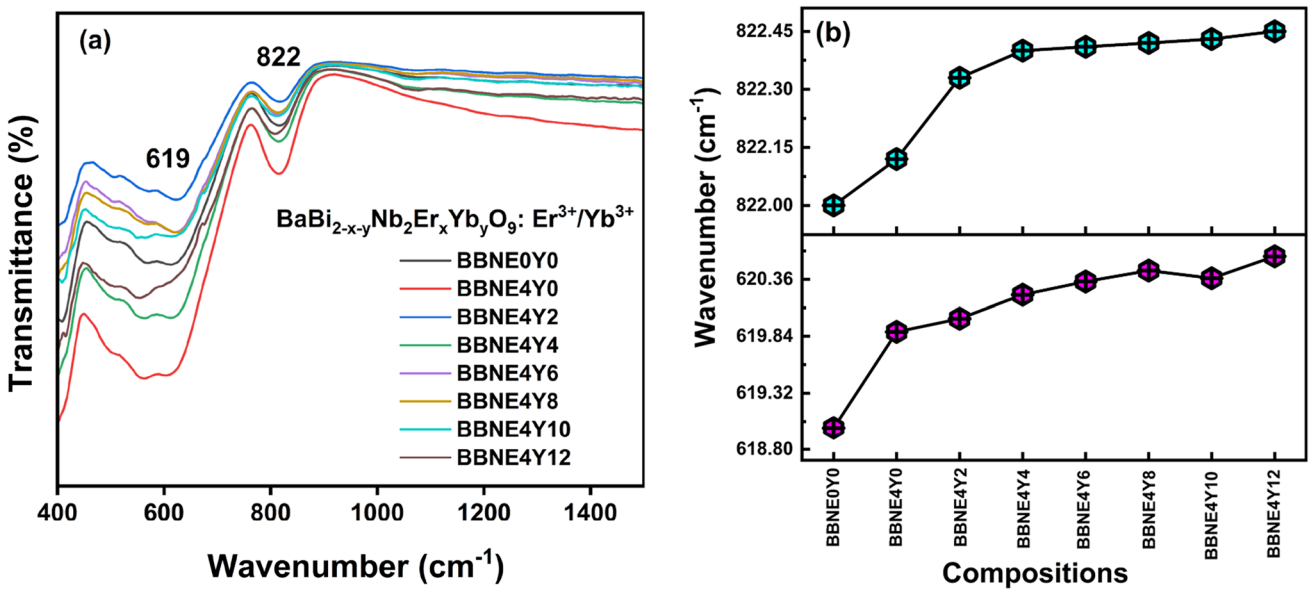

Fig. 4 **a** FTIR spectra obtained at room temperature for all the compositions of prepared BBN ceramic. **b** Shifting of FTIR modes (619 and 822 cm^{-1}) due to the insertion of dopants into the host material

case of undoped BBN ferroelectric ceramic [31–33]. The occurrence of these bands might be due to the coinciding of the same symmetrical vibrations or expansions of the vibration modes or the weakening of the vibrational mode's intensity. However, in Er^{3+}/Yb^{3+} BBN compositions, almost 12 experimental modes can be observed, which can be verified from deconvoluted Raman spectra (Fig. 5a). These modes are effectively reduced in undoped BBN ceramic, but they may be rapidly noticed in the case of Er^{3+}/Yb^{3+} doped BBN compositions. These suppressed modes are positioned at 289 cm^{-1}, 358 cm^{-1}, 379 cm^{-1}, 443 cm^{-1}, 681 cm^{-1}, 720 cm^{-1}, and 765 cm^{-1}. These modes might potentially be linked to the level of structural disorder present in materials belonging to the same family [15, 17, 27, 31]. As a result, the theoretically expected and experimentally observed Raman modes have a decent correlation. Figure 5c displays the Raman shift as a dependent variable of the dopant concentration, while Table 3 presents a comprehensive compilation of the observed frequency shifts with their corresponding band allocations.

The Raman spectra show four modes corresponding to the frequencies of 156 cm^{-1}, 215 cm^{-1}, 550 cm^{-1}, and 854 cm^{-1}. The Raman mode seen at a lower frequency (beneath 200 cm^{-1}) is related to the vibrational motions of Ba^{2+} ions present at the A-site. The higher frequency bands (beyond 200 cm^{-1}) result from the inner vibration of the NbO_6 octahedron. The observed mode with a frequency of 155 cm^{-1} has been ascribed to the vibrations of Bi^{3+} ions located on the A-site within the pseudo-perovskite structure. The A_{1g} mode at a frequency of 215 cm^{-1} in the NbO_6 group is due to the torsional bending of the O–Nb–O configuration. With the replacement of Bi^{3+} ions by dopant ions (Er^{3+}/Yb^{3+}), a little shift within the range of 215–217 cm^{-1} is recorded. The strong vibration mode seen at around 854 cm^{-1} may be attributed to the A_{1g} symmetry because of the symmetrical elongation of the Nb–O bonds in the NbO_6 in the z-axis of the crystal lattice [17, 31, 34]. The counter-directional movement in the apical oxygen atoms inside the NbO_6 octahedral structure, which arises from the B_{2g} mode, results in the Raman mode centered at 550 cm^{-1}. This mode exhibits a progressive decrease from 550 to 539 cm^{-1}, and it has been determined that the introduction of dopants results in its attenuation. This observation implies that the introduction of Er^{3+}/Yb^{3+} at Bi-sites leads to a decrease in compressive stress, indicating a relaxation in structural deformation. Meanwhile, the band at 854 cm^{-1} is due to the symmetrical stretching of Nb–O inside the NbO_6 octahedron, exhibiting a slight decrease in frequency to 852 cm^{-1}.

The bond length analysis of Nb–O at 854 cm^{-1} Raman band is crucial for investigating the impact of dopants on it. Badger's rule is the widely used expression that connects bond lengths to force constants in diatomic and polyatomic compounds [35]. The general form of this rule is expressed in Eq. (1) [36]:

$$k^{-\frac{1}{3}} = \left(a_{ij} - d_{ij}\right)^{-1}\left(R - d_{ij}\right) \quad (1)$$

Here, k stands for the force constant, R for the bond length, and a_{ij} and d_{ij} are constants for certain bonds between atoms in rows i and j of the periodic table. However, Badger's rule does not effectively account for the correlation between the Nb–O bond and force constants in niobate

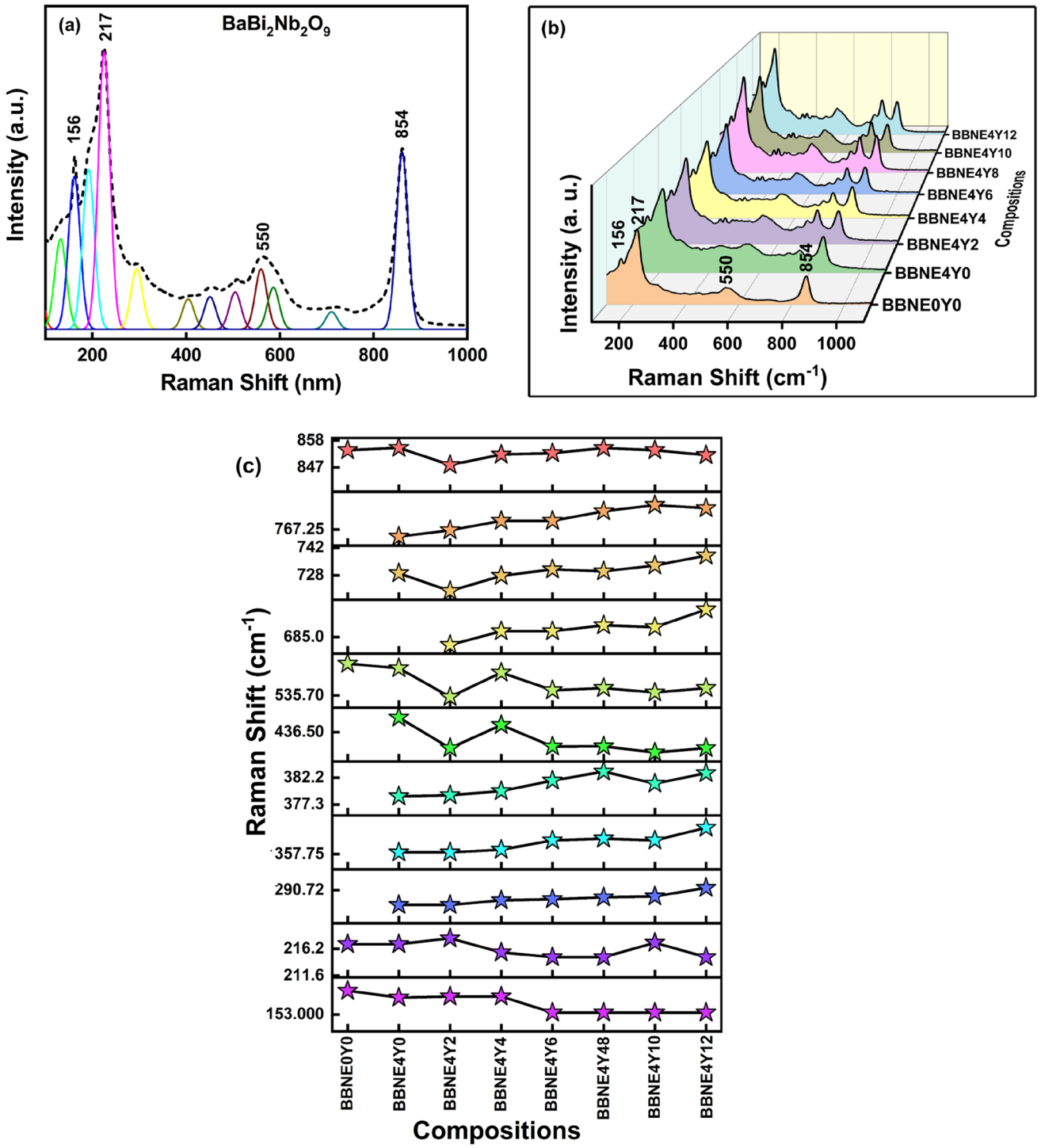

Fig. 5 **a** Deconvoluted Raman spectra of $BaBi_{2-x-y}Nb_2Er_xY-b_yO_9$ (x = 0.00, y = 0.00) ceramic under the excitation of 785 nm laser source. **b** Raman spectra of all the compositions of prepared $BaBi_{2-x-y}Nb_2Er_xYb_yO_9$ ceramics. **c** Dependency of dopant concentrations on various Raman modes

reference compounds. This is because $k^{-1/3}$ does not follow a linear relation with R but shows a minor curvature [35, 36]. Herschbach had a similar issue while attempting to fit cubic and quartic anharmonic force constants to internuclear distances for diatomic molecules [37]. Herschbach utilized an exponential fit to address the small curvature in the data accurately. Thus, following Herschbach's treatment, the current work utilizes a comparable method to correlate

Table 3 Assignment of various observed Raman bands in synthesized $BaBi_2Nb_2O_9$ compositions

Raman bands position (cm^{-1})	Band assignments	References
156	Vibration of Bi^{2+} ion	[17]
215	Torsion Bending of O-Nb–O bond	[17]
289	Vibration due to Bi-O_3 force constant	[31]
358	Vibration due to Bi-O_3 force constant	[31]
379	Vibration due to Bi-O_3 force constant	[31]
443	Vibration due to Bi-O_3 force constant	[31]
550	Opposite excursion of apical oxygen atom	[31]
681	Symmetric bending vibration of NbO_6 octahedron	[32]
720	Symmetric bending vibration of NbO_6 octahedron	[31]
765	Symmetric bending vibration of NbO_6 octahedron	[31]
854	Symmetrical stretching of Nb-O_6 group	[17]

Table 4 Bond length of Nb–O at 854 cm^{-1} Raman band for all the composition of $BaBi_2Nb_2O_9$

Sample	Band position (cm^{-1})	Bond length (Å)
BBNE0Y0	854.00	1.7805
BBNE4Y0	855.00	1.7799
BBNE4Y2	848.00	1.7842
BBNE4Y4	854.25	1.7803
BBNE4Y6	852.80	1.7812
BBNE4Y8	854.90	1.7799
BBNE4Y10	854.00	1.705
BBBNE4Y12	852.00	1.7817

Nb–O stretching frequencies with their corresponding bond lengths. The exponential function used is represented in Eq. (2) [38]:

$$\nu = A \exp(BR) \tag{2}$$

where ν is the Nb–O stretching frequency, R is the Nb–O bond length in Angstroms, and A and B are fitting parameters. The fitting parameters are determined from an exponential least squares fit of the crystallographic and the obtained Raman data from several niobium oxide reference compounds (Table 1 [35]). Then, Eq. (2) takes the form as shown in Eq. (3) [35]:

$$\nu = 25922 \exp(-1.9168\ R) \tag{3}$$

Using Eq. (3), the bond length of all the compositions of BBN is evaluated for the Raman band positioned near 854 cm^{-1} and is tabulated in Table 4. The variation in bond length shows that there is structural relaxation due to dopant introduction and can also be corroborated by XRD and FTIR spectra.

3.4 Dielectric studies

The dielectric constant (ε′) and dielectric loss (ε″) at various frequencies (1 kHz–1 MHz) for different BBN compositions are represented in Figs. 6a–d and 7a–d, respectively. The dielectric constant exhibits a wide anomaly around a temperature (T_m) associated with a diffuse ferroelectric phase transition, followed by a relaxation of the permittivity, consistent with previous findings [39–41]. There is a significant dielectric dispersion below and above the temperature T_m, displacement of T_m with increasing frequency, and a decrease in the value of ε' with increasing frequency. The ε″ curves are quite diffused, and shifts in the maxima with frequency have been observed. These observations validate the relaxor behavior of all the prepared BBN compositions. Additionally, in contrast to the Curie–Weiss law, which governs the dielectric permittivity of a typical ferroelectric material, a modified Curie–Weiss law is applied to relaxor ferroelectrics to define the variation in the reciprocal of the dielectric constant at high temperature and the diffuseness of the phase transition. It is given by Eq. (4) [41, 42]:

$$\frac{1}{\varepsilon'} - \frac{1}{\varepsilon_{m}'} = \frac{1}{C}\left(T - T_m\right)^{\gamma} \tag{4}$$

where ε'_m is the highest value of the dielectric constant, C is the Curie-like constant, and γ is the degree of diffuseness. The value of γ lies between 1 and 2. For normal ferroelectrics, the value is 1; for relaxors, it is 2 [43]. Figure 8a–d shows a linear relationship between the plot of ln(1/ε′ − 1/

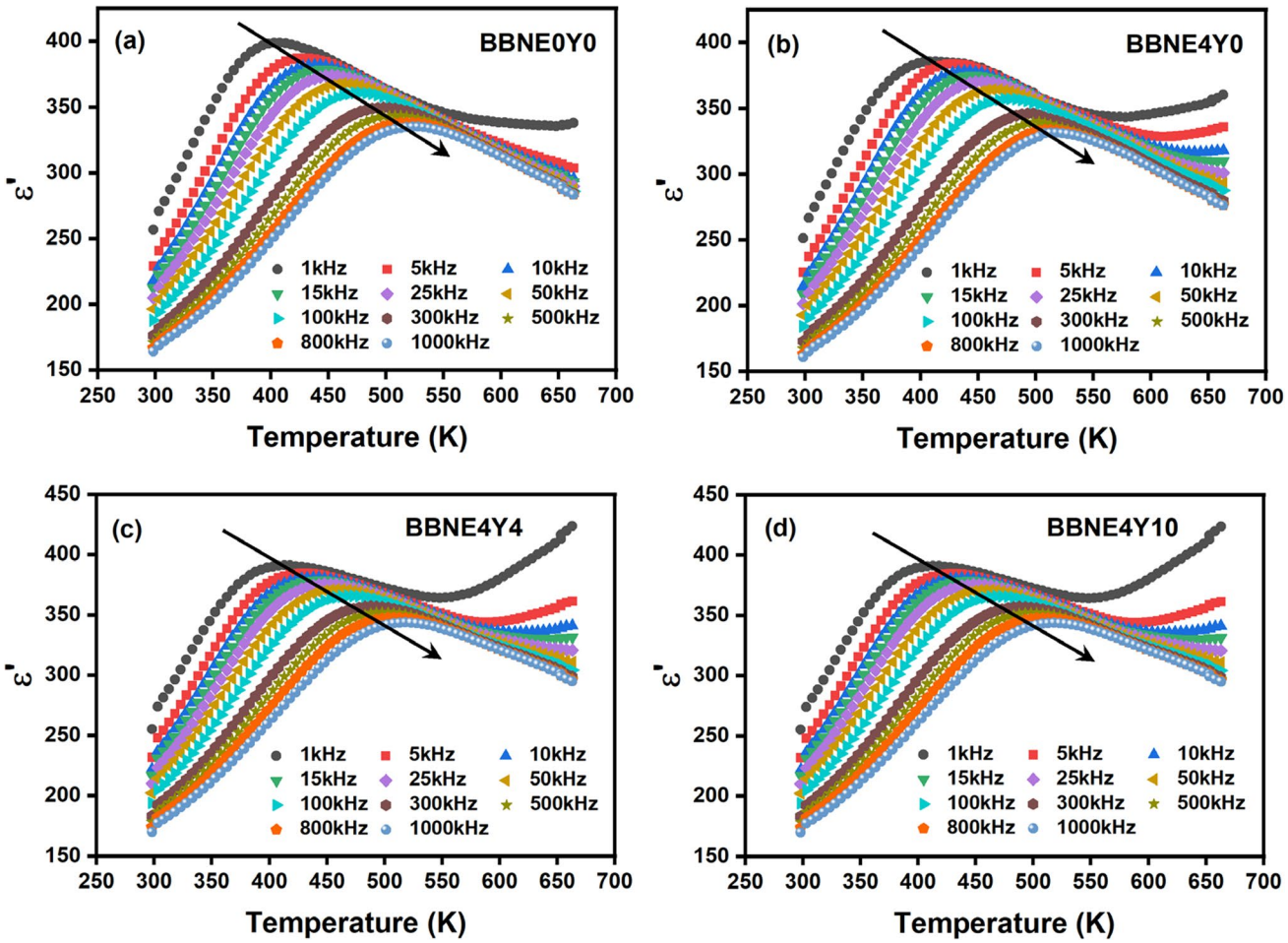

Fig. 6 Dielectric constant (ε′) at various frequencies (1 kHz–1 MHz) between the temperature range 303–673 K for **a** BBNE0Y0, **b** BBNE4Y0, **c** BBNE4Y4 and **d** BBNE4Y10 compositions

ε'_m) and $\ln(T - T_m)$ at 500 kHz for all prepared BBN compositions. The slope (γ) comes out to be 1.747, 1.727, 1.891, and 1.721 for BBNE0Y0, BBNE4Y0, BBNE4Y4, and BBNE4Y10, respectively. Thus proving the relaxor-type behavior of BBN ceramic. The dielectric measurement parameters at 500 kHz of all BBN compositions are tabulated in Table 5.

3.5 Polarization verus electric field loops and energy storage parameter analysis

The polarization versus electric field curves (PE loops) of undoped and doped compositions of BBN ceramic are represented in Fig. 9a–h for various applied electric fields ranging from 75 to 100 kV/cm. The PE loops are traced at room temperature at a 20 Hz frequency. The slimmer PE loops result in low remnant polarization of $BaBi_2Nb_2O_9$ (BBN) ceramic. In Table 6, it is seen that the PE loop parameters decrease with increasing dopant concentration. The P_m and P_r are obtained for undoped BBN (5.162–6.831 μC/cm^2) and (1.158–1.485 μC/cm^2) between the electric field range 75–100 kV/cm, respectively. In doped BBN compositions, the obtained P_m and P_r values increase with increasing electric field but are smaller than the undoped BBN. The decrease in P_m and P_r values may be elucidated by the incorporation of external ions into the host lattice, which results in the replacement of bismuth ions and the formation of oxygen vacancies. The oxygen vacancies tend to migrate toward the domain wall when subjected to a strong electric field, hence impeding the process of domain flipping. Nevertheless, the estimation of high-quality PE loops is subjected to several factors, including lattice strain, defects, grain size, density, and minimum sample thickness. The P_r, P_m, and applied electric field values were used to calculate the energy storage parameters: energy density (W), recoverable

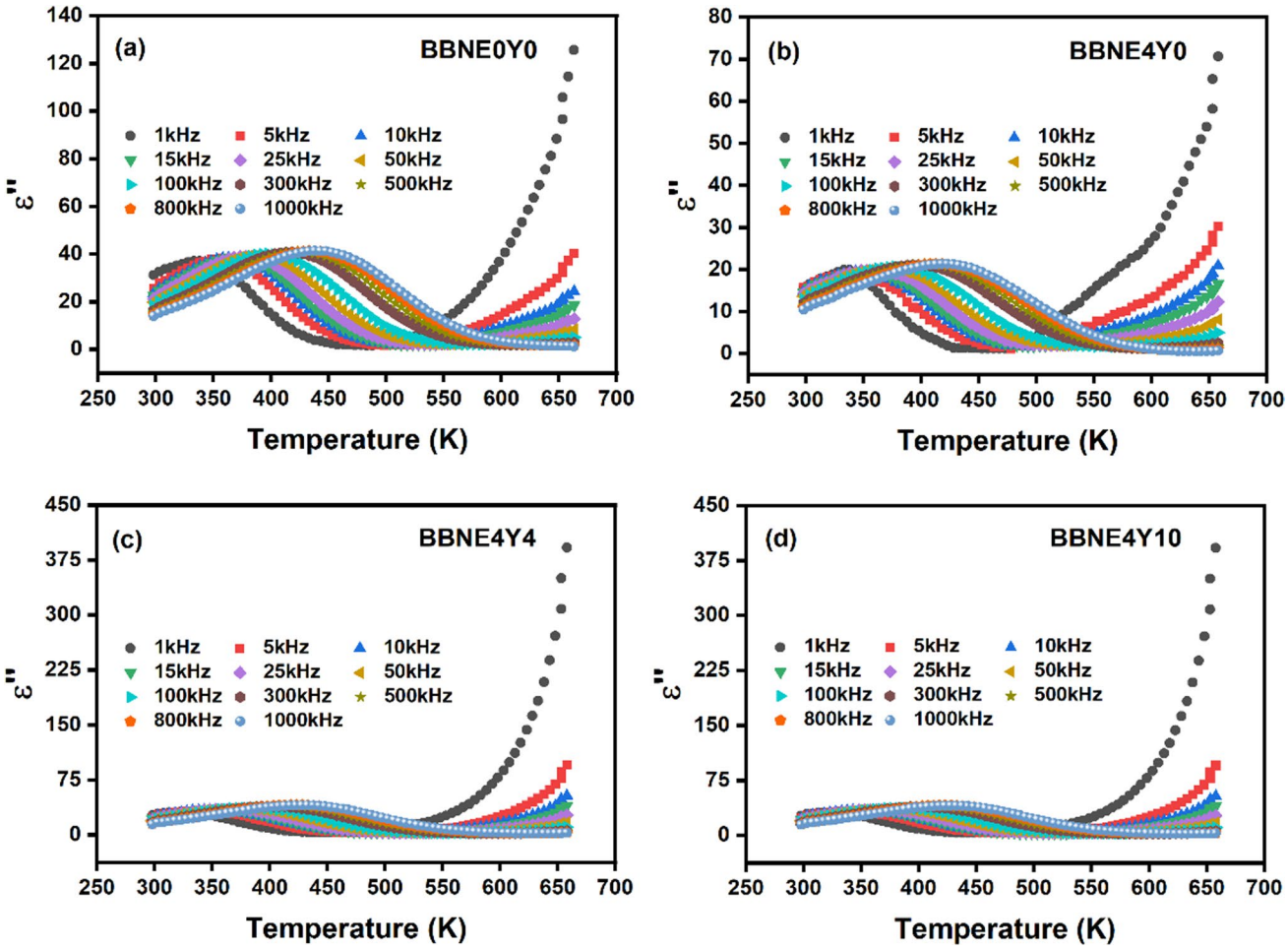

Fig. 7 Dielectric loss (ε″) at various frequencies (1 kHz–1 MHz) between the temperature range 303–673 K for **a** BBNE0Y0, **b** BBNE4Y0, **c** BBNE4Y4 and **d** BBNE4Y10 compositions

energy density (W_{rec}), and efficiency (η). Equations (5–7) give the mathematical expression [44, 45]:

$$W = \int_{0}^{P_m} EdP \tag{5}$$

$$W_{rec} = \int_{P_r}^{P_m} EdP \tag{6}$$

$$\eta = \frac{W_{rec}}{W} \times 100\% \tag{7}$$

Based on these expressions, it can be said that ceramic materials with a high energy density and efficiency should have a high maximum polarization, a low remnant polarization, and high BDS simultaneously. Table 6 tabulates the energy storage parameters W, W_{rec}, and η values for all the applied electric fields (75–100 kV/cm). The energy storage parameters improved with increasing electric field for all the compositions, as shown in Fig. 10a–c. For undoped BBN ceramic, the η varies from 77.59 to 79.76% within the electric field range. However, for doped BBN compositions, the overall efficiency increased within the aforementioned applied electric field. The highest value for η is obtained for BBNE4Y4 prepared composition and equals 91.28% at 80 kV/cm. The Weibull distribution function for BBNE4Y4 prepared composition is shown in Fig. 11. The determination of the maximum electric fields and energy storage capabilities for the practical application of energy storage ceramics relies on the important parameter known as the breakdown strength (BDS). BDS can be expressed by the Weibull distribution function given in Eqs. (8) and (9) [20, 22]:

$$X_i = Ln(E_i) \tag{8}$$

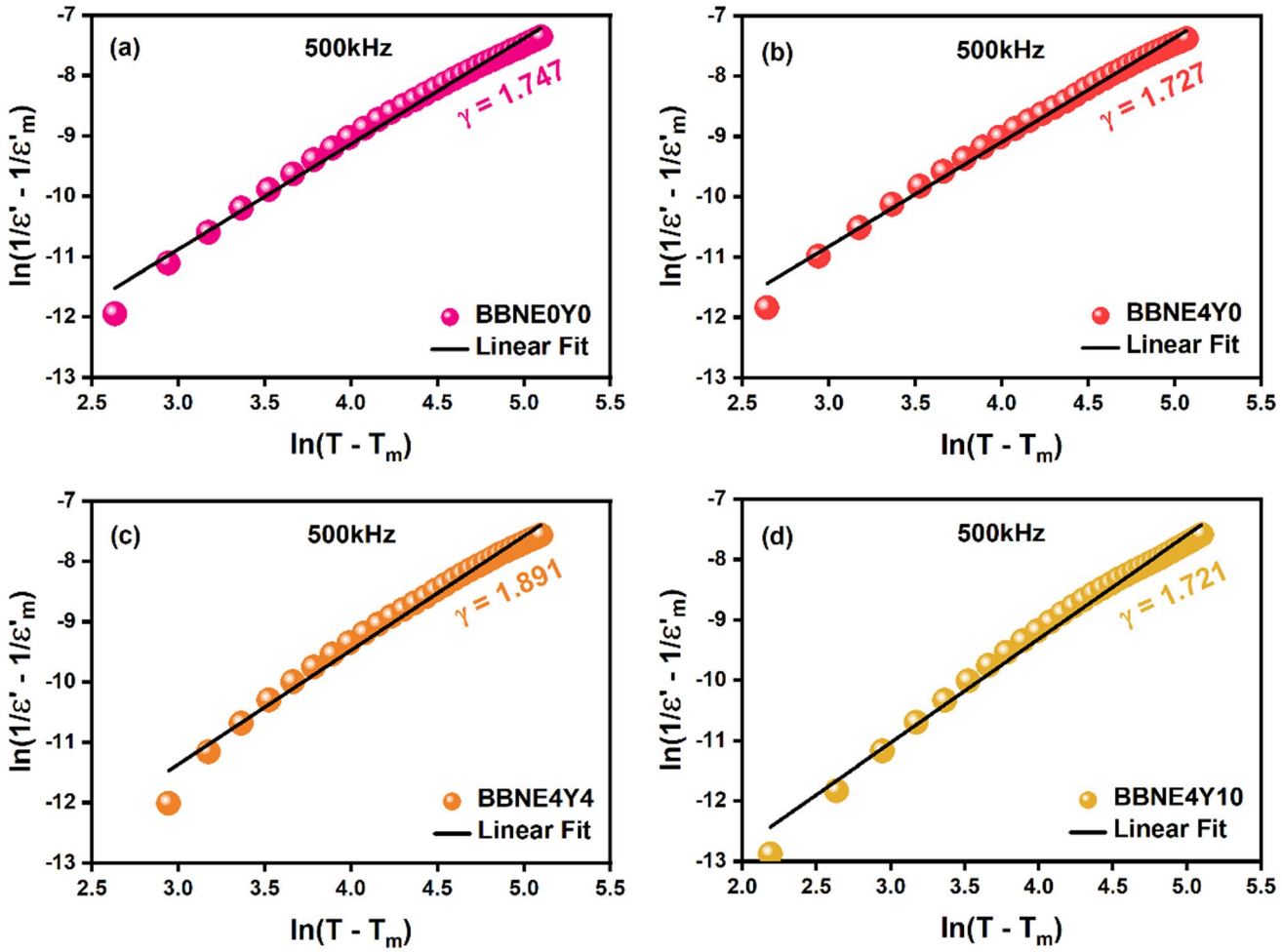

Fig. 8 Plot of $\ln(1/\varepsilon' - 1/\varepsilon'_m)$ and $\ln(T - T_m)$ at 500 kHz for **a** BBNE0Y0, **b** BBNE4Y0, **c** BBNE4Y4 and **d** BBNE4Y10 compositions

$$Y_i = \mathrm{Ln}\left(-\mathrm{Ln}\left(1 - \left(\frac{i}{1+n}\right)\right)\right) \tag{9}$$

where E_i is the BDS of the sample, i is the sequence of the sample, and n is the number of samples. To validate the experimental data, the Weibull shape parameter (β) is an important factor that can be calculated from the slope of the linearly fitted X_i and Y_i. The Weibull distribution model is appropriate for analyzing breakdown outcomes when the value of β exceeds 1 [24].

Table 5 Variation in dielectric measurement parameters at 500 kHz of all BBN compositions

Sample	ε'_{303K}	ε'_m	T_m (K)	γ
BBNE0Y0	175.94	343.26	503	1.747
BBNE4Y0	172.42	341.21	500	1.727
BBNE4Y4	196.94	353.22	489	1.891
BBNE4Y10	186.67	347.84	484	1.721

The temperature stability of prepared ceramic (BBNE4Y4) is studied between a wide temperature range (303–415 K), as shown in Fig. 12a. It has been observed that the energy storage density parameters (W, W_{rec}, η) of synthesized composition do not vary much with increasing temperature under 80 kV/cm applied electric field, as depicted in Fig. 12b. It is because of the transition of extensive diffusive phase in nonergodic and ergodic states of relaxor materials [22]. The W, W_{rec} increases with increasing temperature, and η remains constant. The change in W, W_{rec}, and η is 0.03%. A comparison of energy

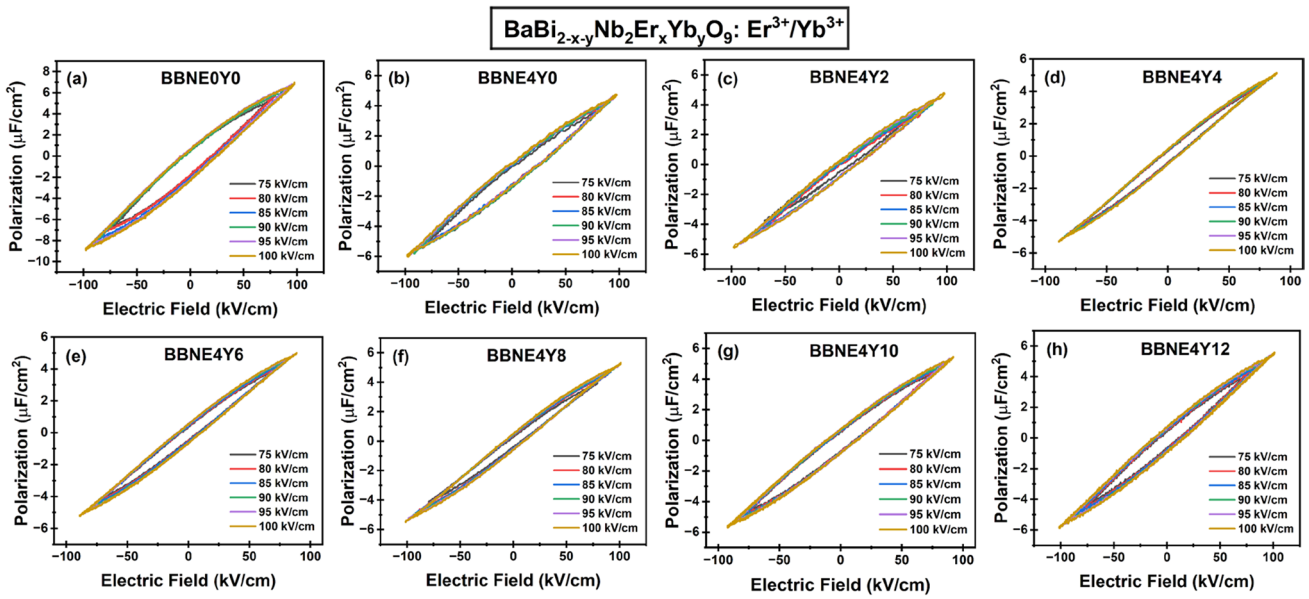

Fig. 9 **a**–**h** PE loops of all the compositions with varying applied electric fields ranging from 75 to 100 kV/cm

storage parameters of different host materials is given in Table 7.

4 Conclusion

The structural, dielectric, ferroelectric, and energy storage properties of undoped $BaBi_{2-x-y}Nb_2Er_xYb_yO_9$ (BBN), Er^{3+} doped BBN, and Er^{3+}/Yb^{3+} co-doped BBN ferroelectric ceramics have been investigated using the solid-state method. XRD analysis confirmed the orthorhombic geometry and Fmmm phase group for all prepared ceramics. SEM micrographs revealed dense microstructures with square-shaped features. FTIR spectra showed characteristic peaks of the Aurivillius phase at 619 and 822 cm^{-1}. In undoped BBN, four Raman modes are visible, whereas in doped BBN compositions, 12 modes have been observed. To calculate the bond length of Nb–O at 840 cm^{-1} Raman band, Herschbach's exponential function approach is utilized to establish a correlation between the stretching frequencies of Nb–O and the corresponding bond lengths. Temperature-dependent dielectric tests reveal significant dispersion below and above the maximum temperature (T_m), and the dielectric constant (ε') decreases with increasing frequency. The dielectric loss (ε'') values are diffused, and variations in the maxima with frequency have been detected, demonstrating the relaxor behavior of all produced BBN compositions. The thinner PE loops were achieved under applied electric fields between 75 and 100 kV/cm. The remnant polarization (P_r) and maximum polarization (P_m) were used to calculate the energy storage parameters (W, W_{rec}, η) of each ceramic composition. The energy storage parameters improve as the applied electric field increases. The energy density (W), recoverable energy storage density (W_{rec}), and energy storage efficiency (η) for undoped, Er^{3+} doped, and Er^{3+}/Yb^{3+} co-doped BBN

Table 6 Energy storage parameters of Er^{3+}/Yb^{3+} doped $BaBi_{2-x-y}Nb_2Er_xYb_yO_9$ ceramic composition

E_{Max} (kV/cm)	Parameters	Compositions							
		BBNE0Y0	BBNE4Y0	BBNE4Y2	BBNE4Y4	BBNE4Y6	BBNE4Y8	BBNE4Y10	BBNE4Y12
75	P_r (μC/cm^2)	1.158	0.711	0.324	0.380	0.425	0.365	0.654	0.624
	P_m (μC/cm^2)	5.162	3.780	3.278	4.315	4.060	3.955	4.424	4.038
	W (J/cm^3)	0.387	0.283	0.245	0.323	0.304	0.296	0.331	0.302
	W_{rec} (J/cm^3)	0.300	0.230	0.221	0.295	0.273	0.269	0.282	0.256
	η (%)	77.59	81.18	90.09	91.19	89.51	90.77	85.21	84.54
80	P_r (μC/cm^2)	1.172	0.738	0.464	0.395	0.490	0.465	0.713	0.680
	P_m (μC/cm^2)	5.786	4.059	3.532	4.539	4.209	4.598	4.689	4.458
	W (J/cm^3)	0.463	0.324	0.282	0.363	0.337	0.368	0.375	0.356
	W_{rec} (J/cm^3)	0.369	0.265	0.245	0.331	0.297	0.331	0.318	0.302
	η (%)	79.76	81.80	86.86	91.28	88.35	89.88	84.79	84.72
85	P_r (μC/cm^2)	1.314	0.684	0.438	0.434	0.511	0.497	0.728	0.670
	P_m (μC/cm^2)	6.308	4.296	3.782	4.689	4.410	4.719	4.811	4.767
	W (J/cm^3)	0.536	0.365	0.321	0.398	0.374	0.401	0.409	0.405
	W_{rec} (J/cm^3)	0.424	0.307	0.284	0.361	0.331	0.358	0.347	0.348
	η (%)	79.16	84.07	88.39	90.73	88.41	89.46	84.86	85.93
90	P_r (μC/cm^2)	1.403	0.754	0.507	0.448	0.602	0.492	0.744	0.782
	P_m (μC/cm^2)	6.426	4.348	4.094	4.900	4.682	4.882	5.014	5.110
	W (J/cm^3)	0.578	0.391	0.368	0.441	0.421	0.439	0.451	0.459
	W_{rec} (J/cm^3)	0.452	0.323	0.323	0.401	0.367	0.395	0.384	0.389
	η (%)	78.16	82.65	87.60	90.85	87.13	89.97	85.14	84.68
95	P_r (μC/cm^2)	1.395	0.743	0.540	0.459	0.640	0.560	0.790	0.792
	P_m (μC/cm^2)	6.768	4.535	4.477	5.102	4.818	5.080	5.221	5.348
	W (J/cm^3)	0.643	43.09	0.425	0.485	0.457	0.483	0.496	0.508
	W_{rec} (J/cm^3)	0.510	0.360	0.374	0.441	0.397	0.429	0.421	0.432
	η (%)	79.38	0.836	87.99	90.99	86.71	88.95	84.86	85.18
100	P_r (μC/cm^2)	1.485	0.781	0.638	0.463	0.636	0.566	0.780	0.802
	P_m (μC/cm^2)	6.831	4.708	4.712	5.080	4.949	5.288	5.359	5.474
	W (J/cm^3)	0.683	0.471	0.471	0.508	0.495	0.529	0.536	0.547
	W_{rec} (J/cm^3)	0.534	0.392	0.407	0.461	0.431	0.472	0.457	0.467
	η (%)	78.25	83.39	86.45	90.87	87.14	89.28	85.44	85.34

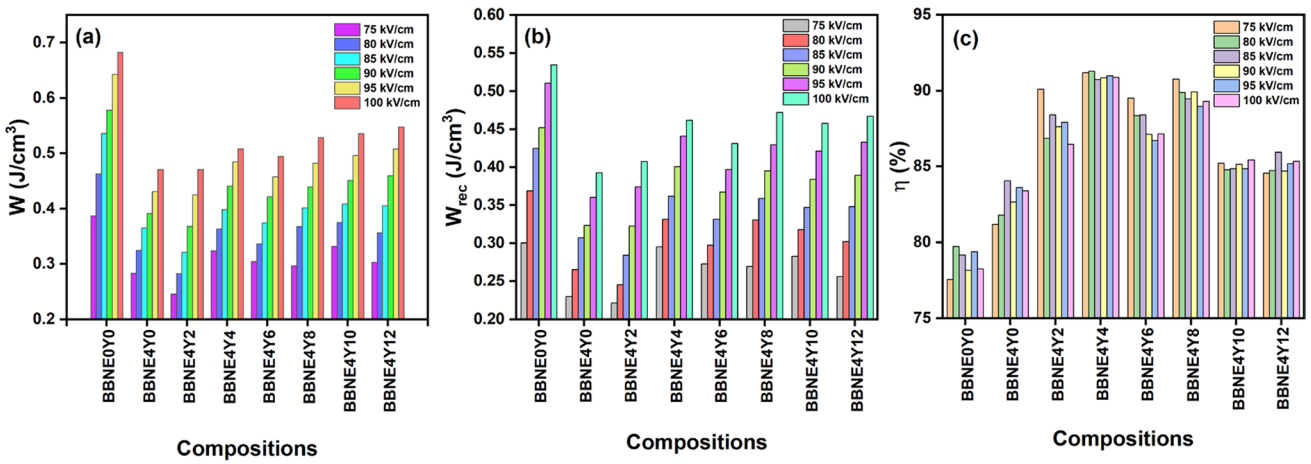

Fig. 10 **a–c** Energy storage parameters of all the prepared compositions of BBN with varying applied electric fields ranging from 75 to 100 kV/cm

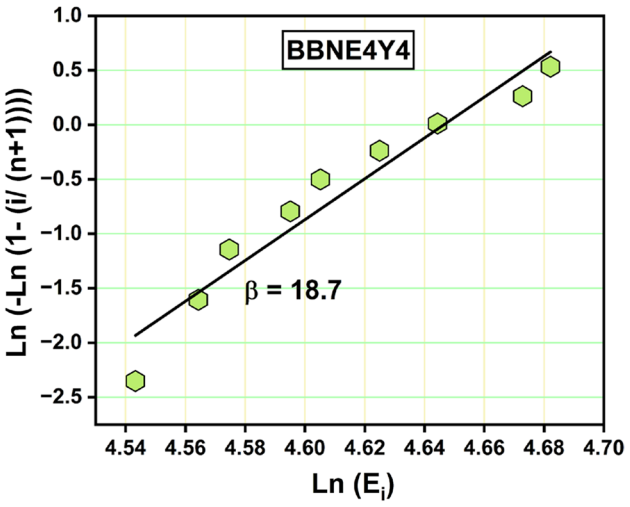

Fig. 11 Weibull distribution function for BBNE4Y4 prepared composition

ceramics were approximately (0.683 J/cm^3, 0.534 J/cm^3, and 78.25%), (0.471 J/cm^3, 0.392 J/cm^3, and 83.39%) and (0.508 J/cm^3, 0.461 J/cm^3, and 90.87%), respectively. The W, W_{rec}, η showed decent temperature stability between 303 and 415 K. The change in energy storage density parameters is only 0.03%. It can be concluded that the η of undoped, Er^{3+} doped, and Er^{3+}/Yb^{3+} co-doped $BaBi_{2-x-y}Nb_2Er_xYb_yO_9$ ceramics increased with doping concentrations. In contrast, the W and W_{rec} of Er^{3+} doped and Er^{3+}/Yb^{3+} co-doped BBN ceramic are comparable with undoped BBN. The dielectric constant at room temperature ($\varepsilon'_{303\ K}$), degree of diffuseness (γ), and energy storage efficiency (η) are superior in BBNE4Y4 compared to other BBN compositions, making this concentration the best among others. Therefore, all the above observations suggest that the prepared material may be helpful in the development of sophisticated electronic apparatus for applications involving energy storage.

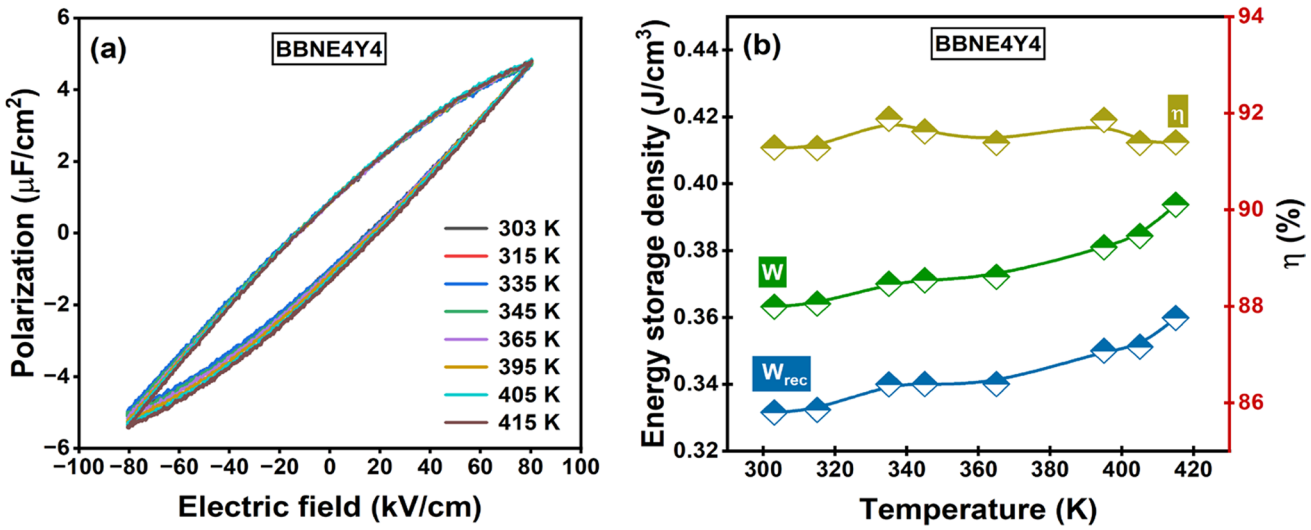

Fig. 12 **a** Temperature stability analysis of BBNE4Y4 ($Er^{3+}=0.04$ and $Yb^{3+}=0.04$) at various temperature ranges (303–415 K). **b** Variation of energy storage density parameters of the aforementioned ceramic

Table 7 Comparison of energy storage parameters of various ferroelectric ceramics

Host material	E_{max} (kV/cm)	W_{rec} (J/cm^3)	η (%)	References
$Bi_{0.5}Na_{0.5}TiO_3$–$BaTiO_3$–$SrTi_{0.875}Nb_{0.1}O_3$	105	1.17	91	[1]
$0.98(0.94Bi_{0.5}Na_{0.5}TiO_3$–$0.06BaTiO_3)$–$0.02BiAlO_3$	95	0.69	–	[2]
$(Na_{0.38}K_{0.12}Bi_{0.38}La_{0.12})TiO_3$	90	0.72	93	[11]
$Na_{0.5}Bi_{0.5}TiO_3$:Ho^{3+}	114	0.68	–	[44]
$BaBi_2Nb_2O_9$:ZrO_2	–	0.014	–	[45]
$BaBi_2Nb_2O_9$ ($Er^{3+}=0.00$, $Yb^{3+}=0.00$)	100	0.534	78.25	This work
$BaBi_2Nb_2O_9$ ($Er^{3+}=0.04$, $Yb^{3+}=0.00$)	100	0.392	83.39	This work
$BaBi_2Nb_2O_9$ ($Er^{3+}=0.04$, $Yb^{3+}=0.04$)	100	0.461	90.87	This work

Acknowledgements The authors would like to recognize the Computational and Functional Material Research Lab (CFMRL), Department of Applied Physics, Delhi Technological University, for providing all the facilities to conduct this research. Also, one of the authors thanks CSIR (08/0133(15560)) for their generous financial assistance.

Author contributions AB: Conceptualization, data curation, writing-original draft, made all the measurements. MV: XRD analysis, writing-editing, and Raman spectroscopy. BS: FTIR analysis, data curation, writing-editing. RB: Supervision, reviewing, and editing of the original draft.

Data availability The authors mentioned above have all the relevant data associated with this research work and will be dedicated to sharing that if they are asked to do so in the future.

References

1. J. Shi, X. Liu, W. Tian, High energy-storage properties of $Bi_{0.5}Na_{0.5}TiO_3$–$BaTiO_3$–$SrTi_{0.875}Nb_{0.1}O_3$ lead-free relaxor ferroelectrics. J. Mater. Sci. Technol. **34**(12), 2371–2374 (2018). https://doi.org/10.1016/j.jmst.2018.06.008
2. A. Manan, S. Khan, A. Ullah, A.S. Ahmad, Y. Iqbal, I. Qazi, A. Ullah, Z. Yao, H. Liu, H. Hao, M.A. Khan, M.U. Rehman, Improved energy storage characteristic of Yb doped $0.98(0.94Bi_{0.5}Na_{0.5}TiO_3$-$0.06BaTiO_3)$-$0.02BiAlO_3$ ceramics. Mater. Res. Bull. **137**, 111175 (2021). https://doi.org/10.1016/j.materresbull.2020.111175
3. Z. Peng, L. Chen, Y. Xiang, F. Cao, Microstructure and electrical properties of lanthanides-doped $CaBi_2Nb_2O_9$ ceramics. Mater. Res. Bull. **148**, 111670 (2022). https://doi.org/10.1016/j.materresbull.2021.111670
4. Z. Liu, P. Ren, C. Long, X. Wang, Y. Wan, G. Zhao, Enhanced energy storage properties of $NaNbO_3$ and $SrZrO_3$ modified $Bi_{0.5}Na_{0.5}TiO_3$ based ceramics. J. Alloys Compd. **721**, 538–544 (2017). https://doi.org/10.1016/j.jallcom.2017.05.162
5. T. Zhou, Y. Zhang, Z. Wu, B. Chen, Concentration effect and temperature quenching of upconversion luminescence in $BaGd_2ZnO_5$: Er^{3+}/Yb^{3+} phosphor. J. Rare Earths **33**(7), 686–692 (2015). https://doi.org/10.1016/S1002-0721(14)60471-3
6. R.D. Shannon, Revised effective ionic radii and systematic studies of interatomic distances in halides and chalcogenides. Acta Crystallogr. Sect. A **32**(5), 751–767 (1976). https://doi.org/10.1107/S0567739476001551
7. J. Zhang, Y. Lin, L. Wang, Y. Yang, H. Yang, Q. Yuan, Significantly enhanced energy storage density in sodium bismuth titanate-based ferroelectrics under low electric fields. J. Eur. Ceram. Soc. **40**(15), 5458–5465 (2020). https://doi.org/10.1016/j.jeurceramsoc.2020.06.059
8. Z. Chen, L. Sheng, X. Li, P. Zheng, W. Bai, L. Li, F. Wen, W. Wu, L. Zheng, J. Cui, Enhanced piezoelectric properties and electrical resistivity in W/Cr co-doped $CaBi_2Nb_2O_9$ high-temperature piezoelectric ceramics. Ceram. Int. **45**(5), 6004–6011 (2019). https://doi.org/10.1016/j.ceramint.2018.11.252
9. P. Ren, Z. Liu, X. Wang, Z. Duan, Y. Wan, F. Yan, G. Zhao, Dielectric and energy storage properties of $SrTiO_3$ and $SrZrO_3$ modified $Bi_{0.5}Na_{0.5}TiO_3$-$Sr_{0.8}Bi_{0.1}\square_{0.1}TiO_3$ based ceramics. J. Alloys Compd. **742**, 683–689 (2018). https://doi.org/10.1016/j.jallcom.2018.01.254
10. K. Wu, H. Wang, Z. Miao, S. Ding, Y. Qi, Y. Ming, W. Ding, H. Yuan, Q. Zheng, D. Lin, Improved energy storage properties of $Sr(Zr_{0.8}Nb_{0.16})O_3$-doped $Bi_{0.47}Na_{0.47}Ba_{0.06}TiO_3$ ceramics with excellent temperature/frequency stability. Ceram. Int. **46**(9), 13159–13169 (2020). https://doi.org/10.1016/j.ceramint.2020.02.090
11. A. Verma, A.K. Yadav, S. Kumar, V. Srihari, R. Jangir, H.K. Poswal, S. Biring, S. Sen, Enhanced energy storage properties in A-site substituted $Na_{0.5}Bi_{0.5}TiO_3$ ceramics. J. Alloys Compd. **792**, 95–107 (2019). https://doi.org/10.1016/j.jallcom.2019.03.304
12. F. Yan, X. Zhou, X. He, H. Bai, S. Wu, B. Shen, J. Zhai, Superior energy storage properties and excellent stability achieved in environment-friendly ferroelectrics via composition design strategy. Nano Energy **75**, 105012 (2020). https://doi.org/10.1016/j.nanoen.2020.105012
13. F. Luo, J. Xing, Y. Qin, Y. Zhong, F. Shang, G. Chen, Up-conversion luminescence, temperature sensitive and energy storage performance of lead-free transparent Yb^{3+}/Er^{3+} co-doped $Ba_2NaNb_5O_{15}$ glass-ceramics. J. Alloys Compd. **910**, 164859 (2022). https://doi.org/10.1016/j.jallcom.2022.164859
14. P. Wang, X. Wang, G. Li, Y. Li, X. Yao, Z. Pan, Energy density capability and upconversion luminescence in Er^{3+}/Yb^{3+}-co-doping BNT-based ferroelectric thin films. Ceram. Int. **48**(19), 28606–28613 (2022). https://doi.org/10.1016/j.ceramint.2022.06.174
15. A. Banwal, R. Bokolia, Enhanced upconversion luminescence and optical temperature sensing performance in Er^{3+} doped $BaBi_2Nb_2O_9$ ferroelectric ceramic. Ceram. Int. **48**(2), 2230–2240 (2022). https://doi.org/10.1016/j.ceramint.2021.09.314
16. A. Banwal, R. Bokolia, Effect of Er^{3+} ion doping on structural, ferroelectric and up/down conversion luminescence in $BaBi_2Nb_2O_9$ ceramic. Mater. Today Proc. (2021). https://doi.org/10.1016/j.matpr.2021.05.545
17. M.X. Façanha, J.P.C. doNascimento, M.A.S. Silva, M.C.C. Filho, A.N.L. Marques, A.G. Pinheiro, A.S.B. Sombra, Up-conversion emission of Er^{3+}/Yb^{3+} co-doped $BaBi_2Nb_2O_9$ (BBN) phosphors. J. Lumin. **183**, 102–107 (2017). https://doi.org/10.1016/j.jlumin.2016.08.011
18. R. Bokolia, O.P. Thakur, V.K. Rai, S.K. Sharma, K. Sreenivas, Electrical properties and light up conversion effects in $Bi_{3.79}Er_{0.03}Yb_{0.18}Ti_{3-x}W_xO_{12}$ ferroelectric ceramics. Ceram. Int. **42**(5), 5718–5730 (2016). https://doi.org/10.1016/j.ceramint.2015.12.103
19. A. Banwal, R. Bokolia, Phase evolution and microstructure of $BaBi_2Nb_2O_9$ ferroelectric ceramics. Mater. Today Proc. **46**, 10121–10124 (2021). https://doi.org/10.1016/j.matpr.2020.09.380
20. D. Hu, Z. Pan, Z. He, F. Yang, X. Zhang, P. Li, J. Liu, Significantly improved recoverable energy density and ultrafast discharge rate of $Na_{0.5}Bi_{0.5}TiO_3$-based ceramics. Ceram. Int. **46**(10), 15364–15371 (2020). https://doi.org/10.1016/j.ceramint.2020.03.080
21. X. Qiao, D. Wu, F. Zhang, M. Niu, B. Chen, X. Zhao, P. Liang, L. Wei, X. Chao, Z. Yang, Enhanced energy density and thermal stability in relaxor ferroelectric $Bi_{0.5}Na_{0.5}TiO_3$-$Sr_{0.7}Bi_{0.2}TiO_3$ ceramics. J. Eur. Ceram. Soc. **39**(15), 4778–4784 (2019). https://doi.org/10.1016/j.jeurceramsoc.2019.07.003
22. W. Ma, Y. Zhu, M.A. Marwat, P. Fan, B. Xie, D. Salamon, Z.G. Ye, H. Zhang, Enhanced energy-storage performance with excellent stability under low electric fields in BNT-ST relaxor ferroelectric ceramics. J. Mater. Chem. C **7**(2), 281–288 (2019). https://doi.org/10.1039/c8tc04447c
23. C. Kornphom, K. Saenkam, T. Bongkarn, Enhanced energy storage properties of BNT-ST-AN relaxor ferroelectric ceramics fabrication by the solid-state combustion technique. Phys. Status Solidi Appl. Mater. Sci. (2023). https://doi.org/10.1002/pssa.202200240
24. Q. Huang, F. Si, B. Tang, The effect of rare-earth oxides on the energy storage performances in $BaTiO_3$ based ceramics. Ceram. Int. **48**(12), 17359–17368 (2022). https://doi.org/10.1016/j.ceramint.2022.02.299
25. Y. Wan, N. Hou, P. Ren, M. Ma, K. Song, F. Yan, X. Lu, G. Zhao, High-temperature energy storage properties of $Bi_{0.5}Na_{0.5}TiO_3$

based ceramics modified by $NaNbO_3$. J. Alloys Compd. (2021). https://doi.org/10.1016/j.jallcom.2021.161591
26. A. Banwal, R. Bokolia, Efficient tunable temperature sensitivity in thermally coupled levels of Er^{3+}/Yb^{3+} co-doped $BaBi_2Nb_2O_9$ ferroelectric ceramic. J. Lumin. **263**, 120071 (2023). https://doi.org/10.1016/j.jlumin.2023.120071
27. R. Bokolia, O.P. Thakur, V.K. Rai, S.K. Sharma, K. Sreenivas, Dielectric, ferroelectric and photoluminescence properties of Er^{3+} doped $Bi_4Ti_3O_{12}$ ferroelectric ceramics. Ceram. Int. **41**(4), 6055–6066 (2015). https://doi.org/10.1016/j.ceramint.2015.01.062
28. A. Banwal, R. Bokolia, Thermometric sensing performance in Erbium modified $SrBi_{2-x}Nb_2Er_xO_9$ ferroelectric ceramic for optoelectronic devices. Ceram. Int. **48**(23), 34405–34414 (2022). https://doi.org/10.1016/j.ceramint.2022.08.019
29. A. Shandilya, R.S. Yadav, A.K. Gupta, K. Sreenivas, Effects of Yb^{3+} ion doping on lattice distortion, optical absorption and light upconversion in Er^{3+}/Yb^{3+} co-doped $SrMoO_4$ ceramics. Mater. Chem. Phys. **264**, 124441 (2021). https://doi.org/10.1016/j.matchemphys.2021.124441
30. F. Wang, Y. Han, C.S. Lim, Y. Lu, J. Wang, J. Xu, H. Chen, C. Zhang, M. Hong, X. Liu, Simultaneous phase and size control of upconversion nanocrystals through lanthanide doping. Nature **463**(7284), 1061–1065 (2010). https://doi.org/10.1038/nature08777
31. R. Ramaraghavulu, S. Buddhudu, Structural and dielectric properties of $BaBi_2Nb_2O_9$ ferroelectric ceramic powders by a solid state reaction method. Ferroelectrics **460**(1), 57–67 (2014). https://doi.org/10.1080/00150193.2014.874924
32. H.C. Gupta, Archana, V. Luthra, Lattice vibrations of $ABi_2Nb_2O_9$ crystals (A = Ca, Sr, Ba). Vib. Spectrosc.Spectrosc. **56**(2), 235–240 (2011). https://doi.org/10.1016/j.vibspec.2011.03.002
33. Y. González-Abreu, A. Pelaíz-Barranco, Y. Gagou, J. Belhadi, P. Saint-Grégoire, Vibrational analysis on two-layer Aurivillius phase $Sr_{1-x}Ba_xBi_2Nb_2O_9$ using Raman spectroscopy. Vib. Spectrosc. **77**, 1–4 (2015). https://doi.org/10.1016/j.vibspec.2015.01.001
34. A. Basheer, G. Prasad, G.S. Kumar, N.V. Prasad, Dielectric studies on Sm-modified two-layered BLSF ceramics. Bull. Mater. Sci. **42**(3), 1–11 (2019). https://doi.org/10.1007/s12034-019-1776-6
35. F.D. Hardcastle, I.E. Wachs, Determination of niobium-oxygen bond distances and bond orders by Raman spectroscopy. Solid State Ion. **45**, 201–213 (1991). https://doi.org/10.1016/0167-2738(91)90153-3
36. F.D. Hardcastle, I.E. Wachs, Determination of vanadium-oxygen bond distances and bond orders by Raman spectroscopy. J. Phys. Chem. **95**, 5031–5041 (1991). https://doi.org/10.1021/j100166a025
37. G.D. Chryssikos, Bond length-Raman frequency correlations in borate crystals. J. Raman Spectrosc. **22**, 645–650 (1991). https://doi.org/10.1002/jrs.1250221109
38. F.D. Hardcastle, I.E. Wachs, Determination of molybdenum-oxygen bond distances and bond orders by Raman spectroscopy. J. Raman Spectrosc. **21**, 683–691 (1991). https://doi.org/10.1002/jrs.1250221109
39. P. Keburis, J. Banys, A. Brilingas, J. Prapuolenis, A. Kholkin, M.E.V. Costa, Dielectric properties of relaxor ceramics BBN. Ferroelectr. **353**, 149–153 (2007). https://doi.org/10.1080/00150190701368109
40. J.D. Bobic, M.M.V. Petrovic, B.D. Stojanovic, Review of the most common relaxor ferroelectrics and their applications. Mag. Ferroelectr. Multiferr Meta Oxi. (2018). https://doi.org/10.1016/B978-0-12-811180-2.00011-6
41. P. Sun, H. Wang, X. Bu, Z. Chen, J. Du, L. Li, F. Wen, W. Bai, P. Zheng, W. Wu, L. Zheng, Y. Zhang, Enhanced energy storage performance in bismuth layer-structured $BaBi_2Me_2O_9$ (Me = Nb and Ta) relaxor ferroelectric ceramics. Ceram. Int. **46**, 15907–15914 (2020). https://doi.org/10.1016/j.ceramint.2020.03.139
42. A. Khokhar, M.L.V. Mahesh, A.R. James, P.K. Goyal, K. Sreenivas, Sintering characteristics and electrical properties of $BaBi_4Ti_4O_{15}$ ferroelectric ceramics. J. Alloys Compd. **581**, 150–159 (2013). https://doi.org/10.1016/j.jallcom.2013.07.040
43. A. Khokhar, P.K. Goyal, O.P. Thakur, K. Sreenivas, Effect of excess of bismuth doping on dielectric and ferroelectric properties of $BaBi_4Ti_4O_{15}$ ceramics. Ceram. Int. **41**, 4189–4198 (2015). https://doi.org/10.1016/j.ceramint.2014.12.103
44. A. Kumar, S. Asthana, Investigation on energy storage properties and thermally stable dielectric constant for high temperature electronic device applications in the holmium substituted $Na_{0.5}Bi_{0.5}TiO_3$. J. Mater. Sci. Mater. Elect. **32**, 20225–20239 (2021). https://doi.org/10.1007/s10854-021-06526-w
45. A. Chakrabarti, A.R. Molla, Zirconia assisted crystallization of ferroelectric $BaBi_2Nb_2O_9$ based glass-ceramics: kinetics, optical and dielectrical properties. J. Alloys Compd. **844**, 156181 (2020). https://doi.org/10.1016/j.jallcom.2020.156181